THE UNIVERSITY *of* EDINBURGH

This thesis has been submitted in fulfilment of the requirements for a postgraduate degree (e.g. PhD, MPhil, DClinPsychol) at the University of Edinburgh. Please note the following terms and conditions of use:

This work is protected by copyright and other intellectual property rights, which are retained by the thesis author, unless otherwise stated.
A copy can be downloaded for personal non-commercial research or study, without prior permission or charge.
This thesis cannot be reproduced or quoted extensively from without first obtaining permission in writing from the author.
The content must not be changed in any way or sold commercially in any format or medium without the formal permission of the author.
When referring to this work, full bibliographic details including the author, title, awarding institution and date of the thesis must be given.

Development of efficient hydrodynamic models for the simulation and optimisation of jointed wave energy converters

Alfred Cotten
School of Engineering
University of Edinburgh

A thesis submitted for the degree of
Doctor of Philosophy

2020

Lay Summary

As any experienced sailor would surely testify, there is a great amount of power contained in our seas and oceans, which is often most evident in the form of the waves. Given the ongoing pressures to switch to clean and renewable energy sources, it is of great importance to understand how best to extract this wave power. Assuming that we may one day require as much of this energy as possible in order to fuel the ever-increasing energy demands of humanity, it is also imperative to search for optimal solutions – i.e. those that would allow the most efficient extraction of a very large proportion of the available wave energy. Of the many hundreds of concepts that have been invented so far, many of the more promising designs involve collections of bodies interconnected with rotational joints. However, the extra complexity introduced by these joints often limits the scope of the design and testing processes.

In order to avoid the huge costs that would be incurred by carrying out the build-test-redesign cycle at full scale, it is commonplace to develop new wave energy conversion technologies using a mixture of computer models and small-scale physical models. The computer models aim to simulate the device as it would behave in a real sea or ocean, and are usually by far the quickest and cheapest way of exploring many design possibilities. However, because of the complicated ways in which a jointed device can move, the computer-based simulations of these devices often end up too slow to run and/or too expensive to construct. This is especially the case when thousands of potential designs require testing, in order to find a more optimal solution.

This work aims to solve this problem by first exploring and furthering an existing computer modelling methodology, motivated by the need for both efficiency (cheap and fast to run) and accessibility (easy to construct). This methodology is then applied to two concepts for wave energy extraction that involve rotational joints – the WaveTrain device, and a spine of Edinburgh Ducks. Both devices are freely-floating, which is essential for deployment far from shorelines in deep water, so require quite particular properties so that they do not undesirably sink or topple. Given these constraints, various geometries and mass distributions of the WaveTrain device are investigated, placing emphasis on achieving the highest possible energy extraction whilst minimising the chance of the joints being broken. In the case of the spine of Edinburgh Ducks, in order to extract as much energy as possible it will likely be necessary to actively control the device to make it resonate with the waves (just as a child on a swing must be pushed with the right timing in order to speed them up). With regards to this type of control of a wave energy device, there exists a mathematical technique can be used to determine the strategy that results in the highest possible power extraction. By applying this mathematical technique in various forms, the effects of extracting maximal power on the behaviour of the spine of ducks is investigated. For both applications, guidance for future designs is presented.

Abstract

Jointed wave energy converters are often conceived as an extension to a prior design in order to improve the efficiency of power extraction. However, by moving towards larger numbers of degrees of freedom, optimising their performance becomes increasingly constrained by the computational efficiency of the hydrodynamic numerical models. Metaheuristic optimisation methods, such as genetic algorithms, often provide a very effective search through the design space, but require many executions of the hydrodynamic analysis. Frequency-domain models based on linear hydrodynamics are reasonably accurate and fast enough to enable a suitably broad search for optimal designs. They also require the use of so-called generalised modes to account for types of body motion beyond the standard six degrees of freedom of a rigid body, as is the case in a jointed body. However, the scarcity of implementation details and simplicity of applications in the literature would suggest that there exist barriers to the widespread use of generalised modes for jointed bodies. Motivated by two distinct optimisation problems, the difficulties in constructing models using these modes are exposed in the present work, and a recommended approach is presented in a didactic manner. This approach is then applied to each of two applications in turn.

The first application is motivated by the fact that a wave energy device whose motion is confined to a sloped direction can efficiently absorb energy over a wide range of wave periods. However, sustaining this performance in a deep water environment would normally require a costly support structure. This problem has been addressed by a new device concept called the WaveTrain, which comprises a series of sloped modules, interlinked by struts and rotational joints. This configuration aims to restrict the module motion to the inclined plane, by enabling an exchange of restorative forces amongst neighbouring modules. Whereas the requirement for stable, sloped motion partly specifies the design, other aspects of the geometry and the mass distribution are best investigated through an optimisation study. Using bespoke genetic algorithms, the effects of the geometry and mass distribution on the power extraction are investigated herein, with additional consideration for the cyclic loadings in a multi-objective version. Since the objective functions are computed using a numerical hydrodynamic model (involving generalised modes), and due to the discontinuous nature of the search space that results from a set of nonlinear constraints, some specialised modifications are first required to ensure the correct and efficient operation of the genetic algorithms. Using four variants of the objective functions, a series of criteria have been found, which inform the design of the WaveTrain device.

The second application is a freely-floating spine of ten Edinburgh duck modules, whose two-degree-of-freedom spine joints aim to mitigate unwanted loadings, whilst increasing the efficiency of power extraction from a given area of sea or ocean. Whilst the shape of the duck is itself a result of careful design for energy absorption effi-

ciency, coordinated control of the moments imparted to the ducks about the joints is required for optimal performance of the full spine. Again exploiting an efficient model enabled by the use of generalised modes, several variants of a frequency-domain control strategy are used to investigate the dynamics and performance under conditions of optimal power extraction. In particular, the effects of constraining the motions of the five uncontrolled (not power-extracting) degrees of freedom in addition to the 28 controlled (power-extracting) degrees of freedom is investigated, by way of a theoretical development. The power extraction, motions, control moments and joint shear forces are analysed in a variety of monochromatic wave periods and heading angles, to provide a better understanding of the context for the full-scale design. A series of irregular seas based on a real wave climate are then used to infer how the scaling of the device affects the performance, along with obtaining further understanding of the effects of wave direction, directional spreading and the variant of the control strategy employed.

Declaration of Originality

I declare that I have composed this thesis myself, and that the work contained herein is my own, unless stated otherwise. This work has not been submitted for any other degree or professional qualification.

_____

Alfred Cotten

Acknowledgements

Whilst only one name stands on the front page of this thesis, such an endeavour has only been possible with the wealth of support and influences of innumerable acquaintances, colleagues, friends, and loved-ones. I am perhaps most indebted to David Forehand, firstly for inspiring my change of course towards the field of wave energy, but crucially, for his expert guidance and wisdom throughout my time in Edinburgh. No amount of words can really express how fortunate I feel to have been able to work with such a caring, committed and insightful supervisor. My thanks must also go to Nick Wells and Joe van' t Hoff for sending me into the daunting cavern of PhD solitude with a bright torch full of exciting ideas, technical know-how and a promising real-world application. I must also express my gratitude to Stephen Salter for the abundance of constructive comments and suggestions, often accompanied with arguments of such clarity. I would also like to thank Drew Smith for initially enticing me to Scotland with his Glaswegian charm, along with the whole team from the Wind and Marine CDT at the University of Strathclyde, for such a lively and character-building training year that ultimately equipped me with a very useful and relevant set of skills for the PhD and beyond. On that front, I must also thank the EPSRC for providing the funding that has enabled this whole venture.

I turn now to the countless friends and colleagues in both Glasgow and Edinburgh who have made all manner of positive contributions to my PhD journey. It would perhaps do me a disservice to list you all here, but I would not look back on the last four years with such awe and elation were it not for you! On a more academic note, Anna, thank you for the sometimes lengthy but always fruitful discussions regarding optimisation problems and the technicalities of WAMIT - certainly I found it comforting to know you shared at least some of my frustrations! James, our many evenings of

interesting conversation and chess definitely helped massively to calibrate my mindset for those daytimes full of maths, programming and thesis-writing. Ciaran, Bartek and the other Glasgow folk, it's been great to share and contrast our PhD experiences - I'm sure the football and beer enhanced that.

Mum, you have given me such support throughout and especially during my not-so-infrequent visits back to Bratton, for which I couldn't be more grateful. Dad, your eccentricity and stupid ideas for wave energy devices have not really been much help at all for the PhD, but there is something refreshing and reassuring about your general attitude towards life that has been of huge help to me. Barb, my vocabulary couldn't do justice to the amount of positive influence you've had on me in the past couple of years. You've helped me grow so much as a person and you certainly accelerated the flow of the PhD in a great way! Ryan, Dan, after so long you guys still provide such fun, entertainment and support, not to mention the midnight pies that have supposedly had such a lasting impact on our lives.

Contents

Nomenclature

The nomenclature used throughout the main body of this thesis is defined here. Nomenclature used only in Appendices will be introduced as and where it is required.

Abbreviations

2D	Two-Dimensional
3D	Three-Dimensional
CCC	Complex Conjugate Control
CWR	Capture Width Ratio
DoF	Degree of Freedom
GA	Genetic Algorithm
MOGA	Multi-Objective Genetic Algorithm
OWC	Oscillating Water Column
PTO	Power Take-Off
RAO	Response Amplitude Operator
SOGA	Single-Objective Genetic Algorithm
VFF	Vertical Float Face
WEC	Wave Energy Converter

Coordinates

(a, b, c)	Hinge location
$\hat{\mathbf{i}}, \hat{\mathbf{j}}, \hat{\mathbf{k}}$	Cartesian unit vectors
$\mathbf{x}' = (x', y', z')$	Displaced coordinates
$\mathbf{x} = (x, y, z)$	Cartesian coordinates
r	Radial distance from body

t	Time		

Constants

ρ	Water density		
i	Imaginary unit		$\sqrt{-1}$
C	Constant used in extended control theory		
g	Acceleration due to gravity	9.80665	ms^{-2}
h	Water depth		
n	Directional spectrum constant		

Mathematical symbols

$\angle$	Argument/phase angle
$\cdot$	Dot product
$\Gamma(\cdot)$	Gamma function
*	Complex conjugate
†	Complex conjugate transpose
^{T}	Transpose
$H(\cdot)$	Heaviside function
$Im\{\cdot\}$	Imaginary component
$Re\{\cdot\}$	Real component

Matrices

$\mathbf{\Gamma}$	Motion constraint matrix
$\hat{\mathbf{C}}$	Control matrix
$\hat{\mathbf{O}}$	Sea state occurrence
$\mathbf{\Lambda}$	Diagonalised matrix for extended control theory
$\mathbf{\Psi}$	Matrix introduced for extended control theory
$\mathbf{A}$	Added mass coefficients
$\mathbf{A}^\infty$	Infinite-frequency added mass coefficients
$\mathbf{B}$	Radiation damping coefficients
$\mathbf{B}^{pto}$	PTO damping coefficients
$\mathbf{C}$	Stiffness matrix

$\mathbf{c}$	Buoyancy force coefficients
$\mathbf{c}^g$	Gravitational restoring force coefficients
$\mathbf{K}$	Radiation impulse response functions
$\mathbf{K}^{pto}$	PTO stiffness coefficients
$\mathbf{M}$	Mass/inertia matrix
$\mathbf{V}$	Eigenvector matrix for extended control theory
$\mathbf{Z}^{\mathbf{m}}_{\mathbf{cc}}$	Modified impedance matrix
$\mathbf{Z}$	Intrinsic impedance matrix

Subscripts

$_{pto}$	Power take-off
$_{cap}$	Motion cap
$_{c}$	Controlled modes
$_{f}$	Uncontrolled ('free') modes; in context of WaveTrain, property of float
$_{g}$	Centre of gravity
$_{i,j,k,p,q}$	Indices
$_{LB}$	Lower bound
$_{l}$	To left side of hinge
$_{pm}$	Point mass
$_{P}$	Predominant wave direction
$_{p}$	Pitch
$_{rb}$	Rigid body
$_{rr}$	Roll
$_{r}$	To right side of hinge
$_{UB}$	Upper bound
$_{y}$	Yaw

Superscripts

^{b}	Buoyancy
^{g}	Gravitational restoring
^{lid}	Internal water column surface

^{opt}	Optimal
^{pto}	Power take-off
^{p}	Pressure
^{x}	'Fixed' generalised modes

Vectors

χ	Irregular body response (frequency-domain motions)
$\hat{\mathbf{n}}$	Unit normal to body surface
$\mathbf{\Omega}$	Body velocity (rotational)
$\mathbf{\Theta}$	Vector introduced for extended control theory
$\widetilde{\chi}$	Irregular body response (frequency-domain forces)
$\widetilde{\xi}$	Body response (frequency-domain forces)
$\mathbf{\Xi}$	Body response (time-domain motions, sinusoidal)
ξ	Body response (frequency-domain motions)
$\mathbf{F}^{b}$	Buoyancy forces
$\mathbf{F}^{g}$	Gravitational restoring forces
$\mathbf{F}^{p}$	Pressure forces
$\mathbf{F}^{x}$	Total forces acting on 'fixed' generalised modes
$\mathbf{F}_{c}$	Control forces
$\mathbf{G}$	Force impulse response functions
$\mathbf{P}$	Power
$\mathbf{Q}$	Auxiliary function for Lagrange optimisation
$\mathbf{S}$	Shape function
$\mathbf{U}$	Body velocities
$\mathbf{U}_{t}$	Body velocity (translational)
$\mathbf{X}$	Excitation force coefficients
$\mathbf{x}(t)$	Body response (time-domain)
$\mathbf{X}_{c}^{m}$	Modified excitation force vector

WaveTrain design parameters

ρ_f	Float density

ρ_t Tube wall density

θ Inclination angle

D Tube depth

h Waterline height

L Tube length

L_f Float length

t Tube wall thickness

W Tube width

W_f Float width

Other quantities

$\alpha(\cdot)$ Amplitudes of spectral components

$\bar{a}$ Empirical factor for Palmgren-Miner relation

$\bar{G}$ Mean 'damage' inflicted on WaveTrain joints

$\bar{P}$ Mean annual power

β Constraint weightings (in terms of displacement)

η Free surface elevation

$\forall$ Displaced water volume

γ Constraint weightings (in terms of velocity)

κ Wavenumber

λ Wavelength

$\mathbf{x}_b = (x_b, y_b, z_b)$ Centre of buoyancy

$\mathbf{x}_g = (x_g, y_g, z_g)$ Centre of gravity

μ Lagrange multiplier

ω Wave frequency (angular)

ϕ Fluid velocity potential

ϕ_0 Incident wave potential

ϕ_D Diffraction potential

ϕ_R Radiation potential

ϕ_s Scattering potential

ψ	Random phase
ρ_b	Body density
σ	Stress
τ	Dummy variable
θ	Phase angle
$\widetilde{\Psi}$	Added mass matrix symmetry metric
$\widetilde{x}(t)$	Time-series body response (forces)
A	Wave amplitude
A_i, B_i, C_i, D_i	Coefficients of polynomial equations
B_{pto}	PTO damping coefficient value
$D(\cdot)$	Directional spectrum
F	Force
$g(\cdot)$	Scalar function of the Lagrange multiplier
H_{m0}	Significant wave height
I_r	Set of indices associated with joint roll modes
I_y	Set of indices associated with joint yaw modes
J	Set of indices corresponding to the 'free' generalised modes of motion
K	Number of wave frequency components
L	Number of wave angle components
M	Mass
m	Palmgren-Miner relation exponent
N	Number of degrees of freedom; in context of genetic algorithm, number of generations
N_1	Number of modes analysed
N_2	Number of sample wave periods
N_i	Number of cycles to failure at stress magnitude, i
n_i	Number of cycles endured at stress magnitude, i
P	Power
p	Pressure

S	Waterplane moment
$S(\cdot)$	Spectral density function
S_b	Submerged body surface (mean)
$S_b^{(t)}$	Submerged body surface (instantaneous)
T_e	Energy period
T_z	Zero-crossing period
u	Fluid velocity
V_b	Total body volume (mean)
$V_b^{(t)}$	Total body volume (instantaneous)
$x(t)$	Time-series body response (motions)

List of Figures

List of Tables

Chapter 1

Introduction

Ocean waves provide a plentiful but technologically challenging source of energy. Since the 1970s and originally partly stimulated by UK government funding amidst the oil crisis, numerous device concepts have been conceived, spanning a variety of operational principles (e.g. [12]). Despite attempts to facilitate comparisons between different devices (e.g. Wave Energy Scotland's 'stage gate' process [13], U.S. Department of Energy Wave Energy Prize [14], a numerical benchmarking study by Babarit et al. [11]), there is still no unanimity on a single best device design. Of course, the truly optimal design at a particular moment in time will depend on deployment location, technological limitations, and will ultimately be influenced by the overarching political stance and will. Despite this complexity involved in the decision-making process, one can surmise that a potential for efficient power extraction ranks highly on the list of criteria for any candidate wave energy device. Exactly what constitutes 'efficient' power extraction is not totally clear but it can often be sufficiently surveyed during the development process of a device, using a combination of controlled tests, design refinement and evolution, and expert judgement of the engineering design. Two promising devices that mark the culmination thus far of expansive development timelines are the WaveTrain device, and long spines of Edinburgh ducks. Both of these entail complex operational principles, and do not easily fall within the conventional categories (e.g. [15]). To understand how and why such complexity is central to the

operation of these devices, some analysis is required of their design origins, stretching back through their developmental histories.

1.1 The WaveTrain device concept

The IPS Buoy is a heaving point absorber consisting of a hollow vertical tube with a piston inside (Fig. 1.1). The system was designed so that the piston would react against the inertial water mass inside the tube. The provision of a mass from the Wave Energy Converter (WEC) itself (or from the surrounding water) to act as a reaction mechanism for the Power Take-Off (PTO) system eliminates the need for rigid attachment to the seabed. This then avoids the use of costly support structures and reduces loading on the mooring system. This in turn is a practical requirement for the utilisation of the substantial offshore wave energy resource. The IPS Buoy also has the benefit of requiring no physical end-stops, as the tapered tubing allows water to rush around the piston as it nears its motion limits. This is a feature also of great importance for enabling smooth operation along with mimimal maintenance requirements.

However, for heaving buoys to be well-tuned to the waves in real sea conditions, either a large mass is required to counteract the hydrostatic forces, or an elaborate control system is needed to lengthen the natural period. An alternative solution is provided by tilting the axis of motion towards the horizontal, thus reducing the hydrodynamic stiffness, and lengthening the natural period without a significant increase in the device mass. Combining this operational principle with the aforementioned type of PTO led to the development of the Sloped IPS Buoy [16].

Early work on that device confirmed that constraining the motion of a WEC to an inclined axis can result in very high power absorption over a wide range of frequencies [7]. For deep water deployment, the device must maintain these benefits without the rigid constraint on the axis of motion. Unfortunately, testing of freely-floating versions of the device revealed a collapse of that high and broad power absorption profile [17], as the resulting pitching motion tended to cause dissipation of much of the energy [18].

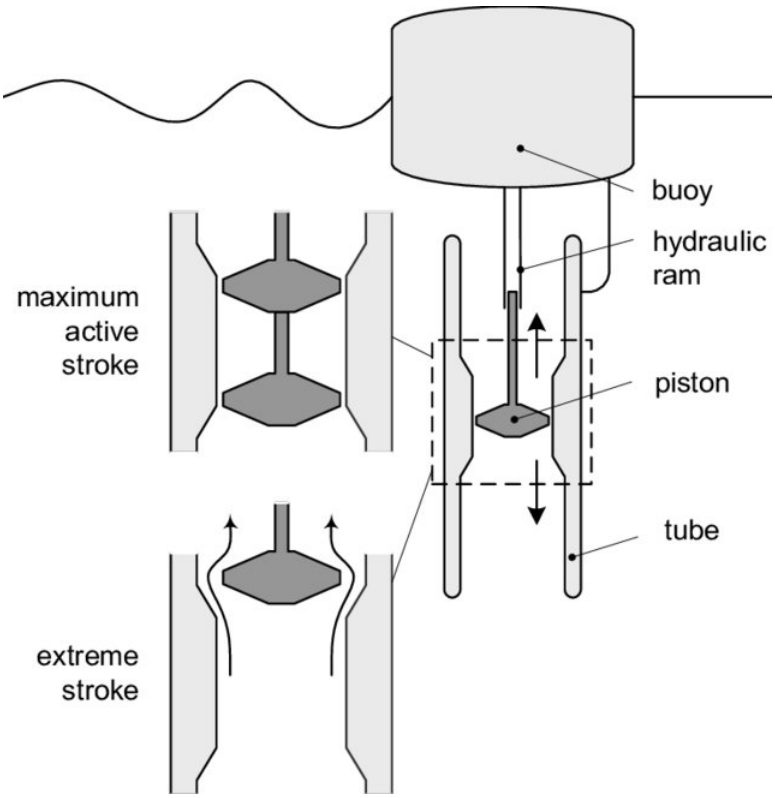

Figure 1.1: Schematic of the IPS buoy. Courtesy of [1].

The WaveTrain concept [19],[20] (not to be confused with a research training network under the name of 'WAVETRAIN' [21]) provides a potential solution to this problem, enabling retention of the good power absorption characteristics, whilst avoiding the need for any kind of rigid connection to the seabed.

The key innovation of the WaveTrain concept is to mechanically interlink multiple sloped buoy modules, so that free motion along the inclined plane is retained, whilst restricting the counterproductive pitch motions (Fig. 1.2; of course, to minimise vortex losses, edges would be rounded in practice). To this end, rotational joints at each end of the connecting struts enable the exchange of restorative forces between neighbouring sloped modules, which enforces the desired restrictions on the device motions. Those forces are best provided when the struts lie perpendicular to the modules. Hence, with each module orientated at its intended inclination angle, the struts are connected so as to form right-angles with the module surfaces when the device is floating in its

equilibrium position.

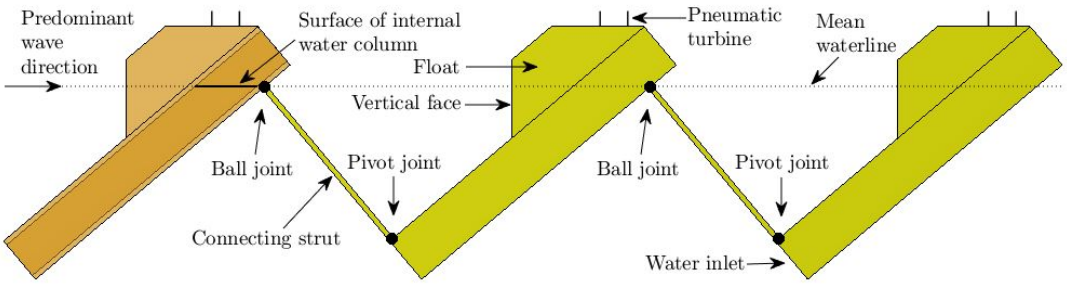

Figure 1.2: Equilibrium configuration of a three-module WaveTrain device, 'in-plane' view. The modules are arranged in an attenuator configuration.

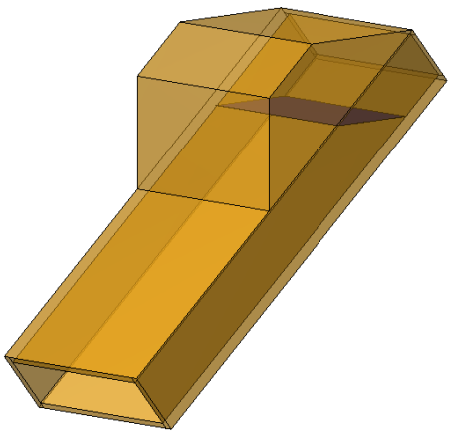

Figure 1.3: 3D transparent view of a single module of the WaveTrain device in its equilibrium position, showing the internal free surface.

Though only in-plane motions are desired for power extraction, employing all three rotational degrees of freedom (DoFs) in just the uppermost joints (see the ball joints in Fig. 1.2) allows some limited out-of-plane motions to alleviate loadings. Each module incorporates a hollow tubular section, which is open at its bottom end (see Fig. 1.3), and the motion of the internal free surface is then used to force air through a pneumatic turbine. These separate PTOs are situated atop each module, and the

whole device resembles a series of floating oscillating water column devices, albeit with each wave-activated body acting in unison with its internal water column in order to provide the power extraction. The internal water columns are primarily a means by which to react against the inertial mass of the surrounding water. Each module also utilises a float of lower density material, in order to both provide buoyancy, and present a vertical face to the incoming waves, so that a sufficient surge component of motion can result.

The orientation of the device is such that the waves propagate towards the float-side of the modules. Under linear wave theory, the water motion is cyclic, and so one may object to the orientation (frontwards or backwards) having any influence on the dynamics. However, the correct orientation is imperative in achieving the correct phase separation between the surge and heave forces acting on the modules. These forces need to be in-phase with one another for a given WaveTrain module, if the device is to effectively exhibit sloped motion. Reversing the wave direction would alter the phase of the surge forces so as to shift them out of phase with the heave motions. In practice also, drift forces may provide a further reason for such orientation of the device.

Originally developed by Dr. Nicholas Wells, the WaveTrain concept recently underwent physical and numerical model testing as part of Wave Energy Scotland's Novel WEC programme [2] (see also Figs. 1.4, 1.5, 1.6). The key recommendation from that work for driving the concept forward was to optimise the geometric and mass properties of the device.

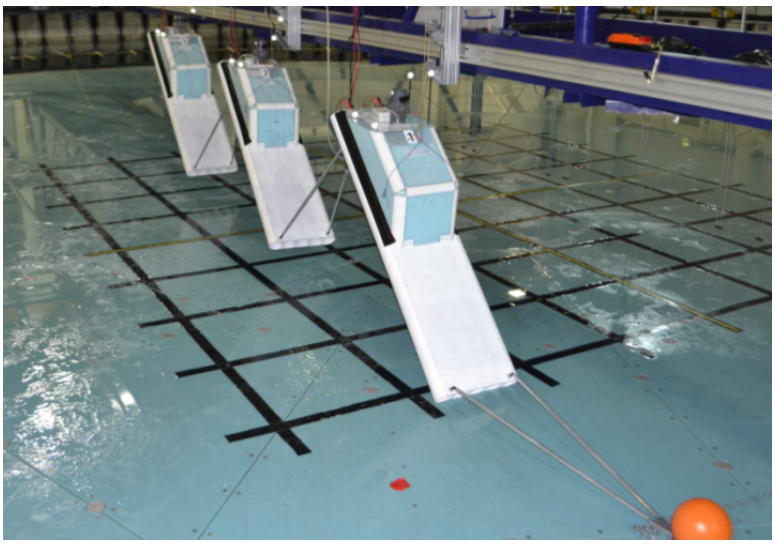

Figure 1.4: Angled view of the WaveTrain device in its static, unsubmerged configuration prior to 1:35 scale model testing in 2016 [2].

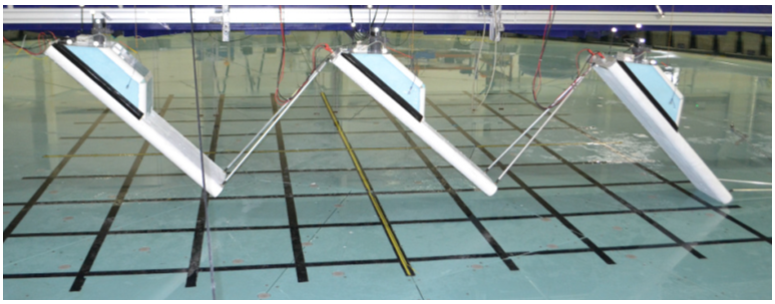

Figure 1.5: Side view of the WaveTrain device in its static, unsubmerged configuration prior to 1:35 scale model testing in 2016 [2].

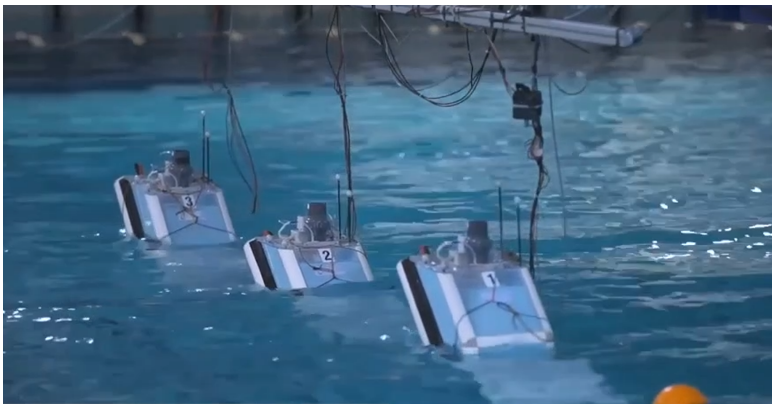

Figure 1.6: Snapshot of the WaveTrain device during dynamic testing [2].

1.2 The Edinburgh duck

The Edinburgh duck started life as the culmination of trialling a selection of shapes, with the goal of maximising the fraction of the incident wave energy that was absorbed. The duck is shaped in cross-section somewhat like a symmetrical teardrop, but with the two surfaces curving all the way to the vertex (see the shape in Fig. 6.2). In practice, this vertex should be rounded off so as to avoid destructive turbulent effects. This cross-section protrudes along the third axis, in which the incoming wavefronts would lie. As wave crests pass through its field of influence, the duck is free to rotate about an axis parallel to the wave fronts. The curved surfaces either side of the duck ensure that very little of the wave energy can transmit beyond the duck. Early indications suggested that for the 2D case in a narrow wave tank, at least 90% of the energy could be absorbed [3] (Fig. 1.7).

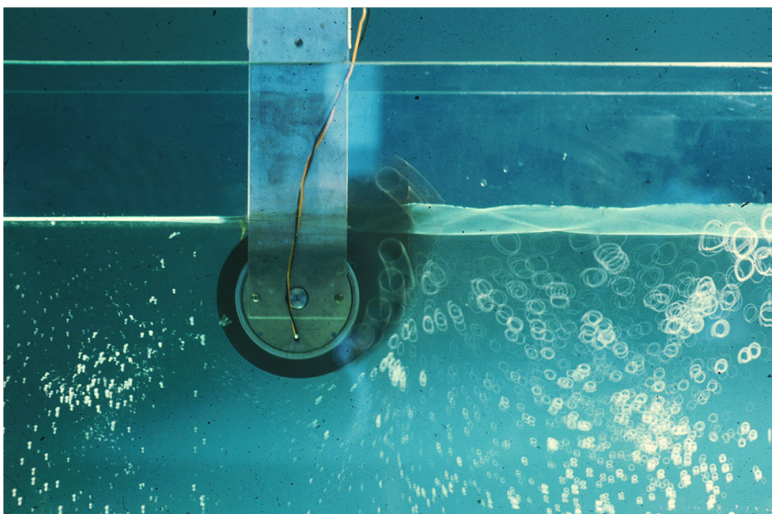

Figure 1.7: Model of an early Edinburgh duck being used to prove its high efficiency in absorbing wave energy. Courtesy of [3].

When first proposed as a concept to extract large amounts of energy from sea or ocean waves, long spines comprising many tens of 'duck' devices were envisioned, in order to take advantage of the common reference structure [22]. Since then, many stages of investigation have led to multiple design refinements. With a view to deep-water deployment, the flexibility afforded by rotational joints is necessary between the

ducks to avoid significant damage by bending moments [3]. Given the subsequent lack of rigidity of the spine, effective designs for a power take-off system were required to be housed inside each duck. These were initially provided with the use of a gyroscopic reference frame [23], and more recently by purely hydraulic technology, after indications that gyroscopes without vacuum conditions could struggle to allow sufficient torque. These designs, crucially, retain the absence of a rigid reference point, and enable power conversion that can be continuously controlled. It is also proposed for the hydraulic technology to allow power extraction through the joints, giving full control over most of the degrees of freedom associated with a full spine of ducks. It is this type of integrated, freely-floating system that is required to enable truly significant levels of wave energy extraction from our seas and oceans. Perhaps more importantly, this kind of spine-based system is able to maximally exploit the available sea or ocean space, given the demands of other users. Designated shipping lanes perforating a well-marked spine of ducks also provide advantages for ship navigation.

Figure 1.8: Artist's impression of a full spine of Edinburgh ducks. Courtesy of [4].

In addition to the efficient geometric design, maximal power extraction necessitates active control of the system during operation. Devising and understanding the implications of such a control strategy is complicated by the large number of degrees of freedom involved.

In light of the scale and cost of a deployment of long spines of Edinburgh ducks, potentially spanning an entire sea, solo ducks have also been investigated (e.g. [24], [8], [25], [26]), with various configurations of the degrees of freedom in which the duck is allowed to move.

1.3 Numerical modelling of wave energy devices

Since the inception of the fundamental theory for wave energy converters in the 1970s (e.g. [27]), it became commonplace to use the foundations of linear wave theory to explore the performance and dynamics of various device concepts. During the mid-seventies, numerical studies were generally infeasible, as computing hardware with around 16 Kilobytes of memory and a processor of perhaps a few MegaHertz would have cost somewhere around three times the annual research associate salary. By the mid-1990s, the vastly increased levels of available computing resources (by then at least in the order of Megabytes of RAM, processors providing hundreds of Megahertz, and costing well below a research associate's annual salary) made it possible to compute the hydrodynamic behaviour of arbitrary shapes, by way of numerical solvers. As computer power has increased in the subsequent years up to the present day (details of the computational resources used in this work are provided in Appendix H), not only have increasingly complex body shapes and array sizes become amenable to these techniques, but additional nonlinear techniques have widened the range of modelling approaches. (In addition to more affordable and powerful personal computers, widespread remote access to supercomputers has greatly contributed to this.) Nonlinear potential flow methods retain the assumption of potential flow, but allow more complete representations of the free surface and body boundary conditions. Computational fluid dynamics can also incorporate the effects of viscosity, and opens the

possibility of rotational flow fields. With the associated increase in computational expense, many complex phenomena seen in real wave conditions can be simulated, such as wave-breaking. Whilst these techniques allow more accurate models, particularly applicable to understanding dynamics in storm conditions or turbulent flows around sharp edges, typically only a small number of scenarios can be simulated, which places the majority of optimisation problems out of their reach.

1.4 Optimisation of wave energy devices

The optimisation of a wave energy device can be viewed as having two types of variable - those that are inherent to the engineering design of the device and are largely fixed after construction ('design' parameters), and those that can be easily changed or recalibrated during operation ('control' parameters). Whilst ideally the two would be optimised simultaneously, computational limits often prohibit this.

1.4.1 Design configuration

In the design of a system with many variables, a thorough optimisation study based on numerical models can help to avert the costly processes of trial and improvement using physical models. Whilst current computing resources still severely limit the applicability of nonlinear wave energy converter models in this regard, models based on linear potential flow theory often offer sufficient insight into the physics and dynamics of certain concepts to be able to explore various design parameters. Time-domain models allow augmentation with nonlinear terms, either empirically determined or provided through the reevaluation of the linear hydrodynamic coefficients at each time step. However, fully linear frequency-domain techniques tend to be far more efficient, maximising the amount of design space that can be explored with a given computational resource. It is for this reason that these models are often utilised for optimisation problems that require a large quantity of simulations. In summary, the choice of approach is somewhat problem-specific, dependent both on the nature of the optimisation goals and the modelling requirements of the device. For example, for a

heaving body with a largely constant waterplane area under changes in free surface position, a fully linear model may be well justified, leaving ample computational resource for optimisation. Even devices with more complex geometry and not clearly unchanging hydrodynamic behaviour with the body motions may be amenable to a fully linear frequency-domain model, as long as these factors exert minimal influence on the results of the optimisation study. Of course, clearly determining the validity of the model for a particular optimisation study is a difficult task, but given the vastly lower cost than their practical counterparts, the endeavour is usually a worthwhile one. Even if the optimisation procedures do not lead conclusively to a single optimal design, the design process can often be usefully informed and sculpted by the learned insight into physical behaviour and trends in performance. Whilst it could be risky to take all of the findings at face value, even a small amount of relevant physical testing results can greatly improve the confidence in the outputs from such optimisation studies.

1.4.2 Control strategy

Once deployed, an efficient wave energy converter must adapt to its surrounding conditions in order to perform optimally. Whereas this could involve adaptive control of the device shape, usually the actuator for real-time control is the power take-off system. A well-designed control system can strategically impart forces on a device in order to shift the resonance profile of the body, so as to meet a variety of dynamics-related goals - e.g. to maximise extracted power or to minimise shear forces at a joint. The challenge to implement such a strategy is complicated by the need for knowledge of the future wave profile. Complex conjugate control is a strategy originally derived analytically, by treating a device interacting with regular waves as modelled by a linear, second order differential equation, and then considering which combination of external stiffness and damping forces leads to the optimal power absorption. Whilst a more adaptable strategy, such as one based upon machine learning techniques, may be able to perform better in real-world unpredictable sea conditions, complex conjugate

control can still give a good idea of the upper limit on performance. And despite the lack of nonlinear effects accounted for with this technique (in fact still a limitation of many other strategies too), it can be better placed to gauge the likely operational characteristics and performance of a device at an earlier, design stage. A further benefit is realised through the lack of computational requirements, especially when seeking to control devices of high functional complexity, whose models already demand the majority of processing power.

1.5 Aims, objectives and chapter summaries

This thesis aims to extend the range of available optimisation techniques, primarily towards the ultimate goal of better assessing the arguably higher potential of complex, jointed wave energy converters. With regards to two applications, efficient numerical hydrodynamic models are first developed, exploiting the concept of 'generalised modes'. Aided and largely enabled by their efficiency, those models are then applied towards optimising aspects of wave energy converter design and performance. Single- and multi-objective genetic algorithms are specially tailored to investigate aspects of the geometric and inertial design of the WaveTrain device, with a view to maximising power and minimising the cyclic loadings on the joints. By imposing various forms of a motion constraint on an optimal control strategy, the performance and dynamics of a long spine of Edinburgh ducks under conditions of optimal power extraction are explored.

The present chapter has already introduced the WaveTrain and Edinburgh duck spine wave energy devices, along with some background, both on the numerical modelling of WECs and on their optimisation with regards to both the design configuration and control strategy.

Chapter 2 surveys the literature on a number of key areas related to the work presented in the subsequent chapters. Firstly covered is the shortage of implementation details and model complexity involved in published applications of generalised modes

to jointed bodies, exposing the need for a detailed but also somewhat didactic explanation of the construction of such models. The remaining four subsections then focus on the approaches used towards optimising various aspects of wave energy converters. Existing studies involving the optimisation of the geometry and/or mass distribution are presented, with a focus on the few studies that utilise genetic algorithms. Though none of these are applied specifically to sloped devices, more primitive approaches have enabled some conclusions about the required design features for optimal performance. Also surveyed in this chapter are the variants of the complex conjugate control strategy, and studies investigating the effects of different combinations of degrees of freedom.

With this context set out, Chapter 3 lays the groundwork for Chapters 4 - 6 by detailing the common aspects of the underpinning theory and methodology. By briefly setting out the hydrodynamic problem in the context of linear wave theory, the concept of generalised modes is clearly defined, isolating the troublesome aspects, particularly with regards to their application to jointed bodies in modelling their motions and loadings. Whilst frequency-domain models are employed to obtain the majority of the insight in this thesis, time-domain models are also defined, with regards to their use as a verification tool.

Building upon the established theory of generalised modes, Chapter 4 then covers the three potentially troublesome aspects of applying generalised modes to jointed bodies - defining appropriate shape functions, the computation of the mass/inertial properties and the computation of the gravitational restoring forces and moments. This treatment is designed to be somewhat didactic, using appropriate examples to clarify the key details. And whilst the information is presented in a theoretical manner, there is some allusion to the commercial software package, WAMIT [28], that is used for the applications in Chapters 5 and 6, which form the bulk of the thesis. The benefits of using generalised modes to model jointed bodies are also discussed.

Chapter 5 is centred around the optimisation of the geometric and mass/inertial properties of the WaveTrain device. Beginning with a thorough account of the construction of the hydrodynamic models, the development of the bespoke optimisation routines is then explored in detail, with particular emphasis on handling the complexities introduced by the nature of the search space - balancing the compromise between computational resources, model accuracy and the breadth of the algorithmic search. It is also stressed that the primary goal of this study is to provide improvements in the available knowledge regarding optimal device design, with the performance of the search algorithm itself of lower priority. Key findings relating to the optimal design features are then presented using both the single- and multi-objective genetic algorithm runs.

Chapter 6 provides a second case study of a jointed wave energy device, focussing on investigating the dynamics and performance of a long spine of Edinburgh ducks, under conditions of optimal power extraction. Following the development of the hydrodynamic model, a form of complex conjugate control in which only the controlled degrees of freedom are constrained is then applied to the ten-duck spine. The motion constraint is then extended to encompass a restriction on all degrees of freedom, and the resulting theory is applied to the duck spine to investigate the impact on the dynamics and performance. Since this new theory involves some intricacies, a solo duck is first used to demonstrate its utility, along with the limitations, and is applied to investigate optimal combinations of controlled degrees of freedom. Finally, the performance of the duck spine in uni- and multi-directional irregular seas is investigated, using a realistic wave climate.

The main conclusions from Chapters 5 and 6 are then presented in Chapter 7, along with suggestions for further work on these topics based on the limitations of the work contained in this thesis.

Chapter 2

Literature Review

2.1 Application of generalised modes to jointed bodies

Generalised modes of motion can provide an efficient description of body motions for any number of degrees of freedom in a single body or in a collection of bodies. The term, 'generalised modes', is used widely within the field of multibody dynamics, but in the context of wave energy modelling is often also associated with their method of implementation within a radiation-diffraction code, such as WAMIT [28]. Generalised modes can be viewed as an extension to the standard six degrees of freedom of a single rigid body - surge, sway, heave, roll, pitch and yaw. Some examples of applications are provided in [29] and [28], and Section 3.3 provides more complete description and definition of generalised modes, but this section solely focuses on the published literature with regards to generalised modes applied to jointed bodies.

Generalised modes have previously been applied to jointed bodies, including multi-body WECs, in order to model their interactions with (linear) waves. Examples found in the literature tend to involve simple geometries and mass distributions, often with implementation details kept brief, despite the potential complexity involved in constructing such models.

After introducing the theory and approach for the general case of deformable bodies disturbed by linear water waves, Newman [29] presents the case of two identical cuboidal barges, connected by a central, equidistantly located hinge. By also using a symmetric definition of the rotational motions about the hinge, complexity in the

inertia and gravitational restoring forces coupling the modes of motion with one another, is minimised. McNatt et al. [5] applied similar, symmetrical definitions of the hinge motions (Fig. 2.1) to three cylindrical barges with spherical ends, with symmetry along the length of the body retained, using equidistantly spaced hinge locations. Mathai [30] does likewise for three hinge-connected cuboidal barges. Newman [31] introduces an alternative choice of generalised modes that can be applied to an ensemble of hinge-connected floating bodies, to analyse only the vertical motions. Afforded by symmetry about the plane perpendicular to the length of the ensemble, symmetric and antisymmetric variants of the generalised modes are presented, enabling a reduction in runtime. This approach is also applied to a hinged assembly of semi-submersible structures by Lee and Newman [32], but a uniform distribution of mass and stiffness is assumed to avoid any further complexity introduced by the geometry. Symmetry along the axis threading the hinges is also present, as is the case in the four other aforementioned studies. Following Newman's approach [31], Li et al. [33] apply generalised modes to analyse the vertical motions of the two hinges of the SeaWEED device. That device's modules are asymmetric in the axial direction, likely the reason why symmetric and antisymmetric modes are not used, yet whilst the shape used for the WAMIT mesh is not presented, the device design suggests at still relatively simple geometry and hinge layout. A generalised mode is also used by Xu et al. [34] to represent the rotational motion about the hinge connecting two floating bodies. The device does not possess symmetry either side of the hinge, but the geometry is nonetheless rather simple, comprising mainly cylindrical body components, and forming simple rafters either side of the hinge.

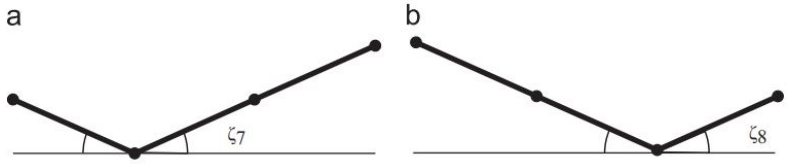

Figure 2.1: Depiction of the two symmetric hinge modes used in [5].

In summary, to the author's knowledge, the published studies on this topic only present cases with relatively simple geometries and hinge arrangements, with many also providing only brief details of the implementation. When applying generalised modes to jointed bodies with a more complex geometry, the implementation can be far from straightforward. The various difficulties to this end are treated in a somewhat didactic fashion in Chapter 4.

2.2 Optimisation of geometry/mass distributions

In two of the studies whose models utilise generalised modes, Xu et al. [34] and Li et al. [33] both apply their models towards optimising aspects of device geometry, relying on an initial assessment of a sufficiently sized batch of designs, then used directly to extract the optimal parameters. However, with larger and/or more complex parameter spaces, more advanced heuristic algorithms, such as those based on evolutionary principles, are often more appropriate. In particular, genetic algorithms (GAs) have been combined with frequency-domain WEC models, in order to optimise device geometry. McCabe et al. [35] use a genetic algorithm to optimise the shape of a 'surge-and-pitch' wave energy absorber. Control points that define the geometry via a B-spline representation are used to form the set of optimisation variables, and the resulting geometry is then used to compute linear hydrodynamic coefficients that characterise the device behaviour in regular seas. A later study by McCabe [6] extends the analysis to an irregular wave climate, optimising the shape of a WEC free to oscillate only in surge, for a prospective site in the North East Atlantic Ocean. This approach is further extended by Garcia-Teruel and Forehand [36], analysing the effects that the unlocked degrees of freedom have on the optimal shape and performance. Babarit and Clément [37] used a multi-objective genetic algorithm to optimise the parameters associated with the SEAREV device, whilst maintaining one of three fixed hull shapes. For each given geometry to be assessed by the GA, an inner optimisation loop based on a gradient-descent method was used to find the optimal pendulum design, reducing the number of variables required in the GA. Hard constraints were imposed on the

candidate designs for this freely-floating device, to ensure static stability in pitch and roll.

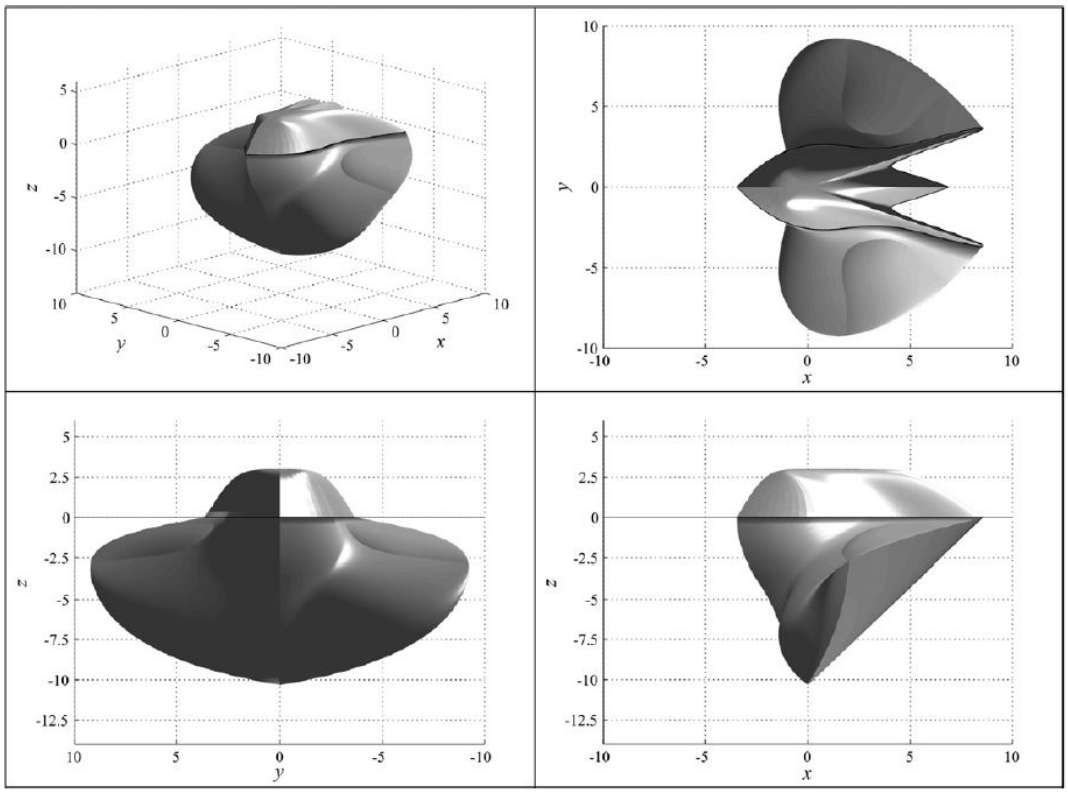

Figure 2.2: Best shape obtained from the optimisation study in [6], using a cost function of mean annual power extraction divided by volume, a power limit of 2.5MW and a motion limit of 5m.

2.3 Towards optimal design of sloped motion devices

To the author's knowledge, there are currently no published studies that use a genetic algorithm to optimise a WEC whose operational principle requires motion along a slope. However, a small number of studies have investigated the impact of design parameters on the performance of sloped motion WECs. Lin [7] used a mechanical rig (Fig. 2.3) to restrict the motion of a buoy to a fixed, sloped axis. Of the four inclination angles tested in monochromatic waves, 45° was selected for further testing due to its broad-banded high efficiencies. It is also evident from this data that the closer to vertical the slope angle lay, the narrower the efficiency peak was as a function

of wave period. Payne et al. [38] used a numerical model to investigate the effects of four parameters on the performance of a freely-floating buoy with inclined-plane power take-off (PTO). A cylindrical float linked through a damper to a point mass was adopted as a simplified representation of the Sloped IPS Buoy. The point mass and damper was used in place of the internal piston reacting against the surrounding water inertia, and the float as a simplified version of the more detailed sloped buoy shape. This efficient model enabled the performance of 4000 combinations of the four parameters to be assessed, based on three weighted combinations of two metrics associated with capture width ratio. By fitting an analytical model to the data, the mass and vertical position of the point mass, and the inclination angle and damping coefficient of the PTO were optimised within bounds. It was found that the point mass should be at least as massive as the buoy mass, and should be located at least half a cylinder draught below the cylinder centre. The optimal angle in this study was found to be 40° to the horizontal. More recently, López et al. [39] investigated the impact of five inclination angles (15°, 30°, 45°, 60°, and 75°) on the performance of a nearshore WEC, comprising a floating body whose motion is constrained by a sloped mechanical rig. Using a model based on linear hydrodynamic coefficients to simulate the device performance in a range of wave climates along the west coast of the Iberian Peninsula, it was determined that for most locations, 30° yielded the most power, with second most obtained by the 45° configuration.

Whilst the nature of these applications differs somewhat to that of the WaveTrain, these results are useful to bear in mind with regards to the work presented in Chapter 5.

2.4 Optimal control strategy

A variety of techniques have been explored with regards to controlling WECs (see e.g. [40]). The first of these was complex conjugate control (see e.g. [41]), which followed from mathematical considerations of the original fundamental theory of wave energy

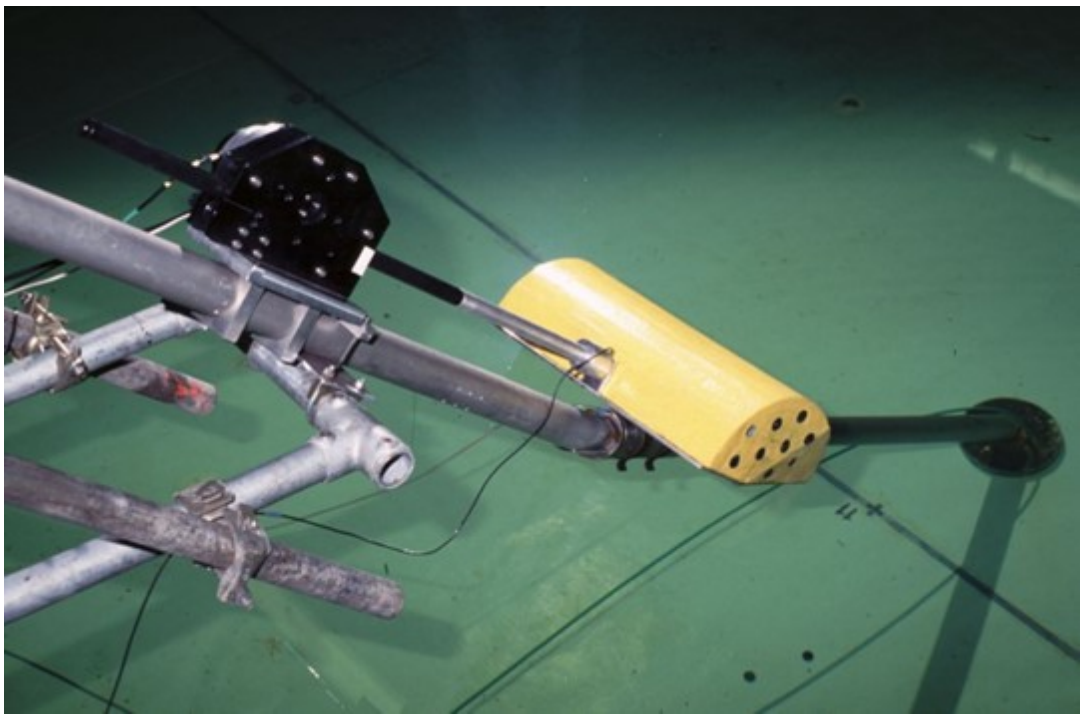

Figure 2.3: The mechanical rig used by C.P. Lin [7] to investigate the performance of a buoy constrained to motion along a sloped axis.

extraction. Under the assumptions of linear wave theory, this method yields the optimal power in terms of the hydrodynamic coefficients. For purposes of achieving the body motions necessary for optimal power, the required control forces can also be expressed in terms of the hydrodynamic properties of the absorber (e.g. [42]). However, for wavelengths large relative to the body, the demanded excursions can greatly exceed the bounds of validity of the linear theory. In order to maintain results in accordance with the linearity assumptions, Evans [43] used a method of Lagrange multipliers to optimise the absorbed power subject to a global constraint (proportional to the wave amplitude) on the body motions. Pizer [8] then extended that method so that the global constraint can encompass different weightings for each degree of freedom, each of which are independent of the wave amplitude. Pizer [44] then extended the theory further to allow uncontrolled DoFs, though the motion constraint still applied to only the controlled DoFs. This leaves the possibility of unrealistic motions in the uncontrolled DoFs that violate the assumptions of the linear theory.

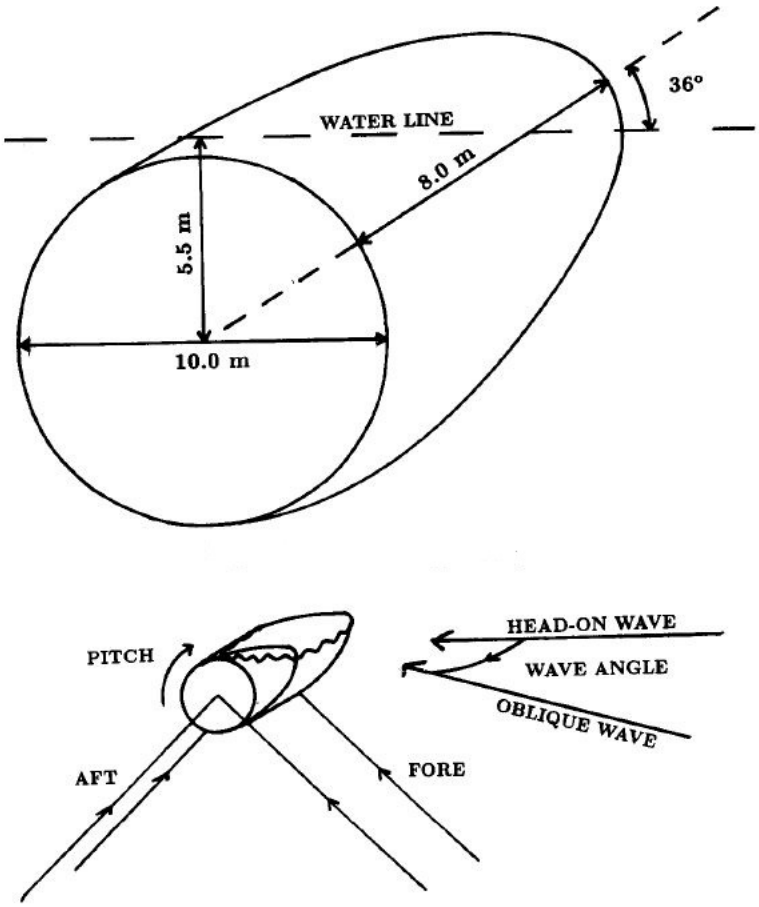

Figure 2.4: The solo duck configuration to which Pizer [8] applied a constrained form of complex conjugate control algorithm.

2.5 Optimal combinations of degrees of freedom

With the large potential of reducing overall cost through the structural design, freeing or fixing (and even conceding control of) certain degrees of freedom may be beneficial if performance is not diminished significantly. Garcia-Teruel and Forehand [36] investigated the effects of the allowed degrees of freedom on both the optimal shape of a single body wave energy converter, and its resulting power capture. Each shape was optimised for a wave climate in the North East Atlantic Ocean. Complex conjugate control was used to simulate the body responses under a range of regular wave periods, which were then superimposed to generate the irregular body responses in each sea state. Four combinations of the in-plane DoFs were tested: surge, pitch, surge and

heave, and surge, heave and pitch. As expected, all three degrees of freedom led to the greatest power, but that was closely followed by surge and heave, which significantly outperformed the two single degree of freedom configurations. This even held with the objective function normalised with respect to volume. And between those two single DoF cases, pitch enabled greater extraction than surge, especially so with the objective function modified to penalise high volumes.

Pizer [8],[44] used a form of constrained complex conjugate control to investigate the impact of the degrees of freedom on the performance of a single Edinburgh duck. In these cases, the duck shape was fixed and the power (or efficiency/capture width ratio) computed for regular waves. In the earlier of the two studies [8], Pizer investigated different sets of controlled degrees of freedom, with motions prohibited (DoFs 'locked') in the other directions. Under head-on waves where the system can be simplified to just three degrees of freedom, locking a degree of freedom was found to cause only a very small reduction in performance. Also under head-on waves, the later study [44] looked at the effect of releasing various DoFs to leave a combination of controlled and uncontrolled modes of motion. It was discovered that from a two degree of freedom system, releasing the third degree of freedom (changing it from fixed to free but uncontrolled), results in a loss in power, which is much greater when it is surge released rather than heave or pitch. It was also evident that with all three DoFs free, when relinquishing control of surge, the reduction in power is much greater than if control of heave or pitch is conceded. However, as noted by Pizer, the duck of its original shape is likely to be most efficient in oblique waves [8], and neither of these two studies investigated the impact of conceding control of degrees of freedom under these conditions. Of course, these studies also left open the possibility of unrealistic motions in the uncontrolled DoFs.

Chapter 3

Common Methodology

In the subsequent chapters, there are several common branches of theory which underpin the development of the frequency-domain models and the optimisation studies. Broadly, these regard the use of a radiation-diffraction panel code (specifically, WAMIT), the concept of 'generalised modes', and both time- and frequency-domain models. This section gives an overview of these methodologies, along with the key technical details that are most relevant to their subsequent use in this thesis.

3.1 Fundamental hydrodynamics theory

Consider an inviscid fluid of constant density. If the fluid flow is irrotational, the fluid velocity can be expressed in terms of a scalar potential, $\phi(x, y, z, t)$ (Eq. 3.1).

$$u = \nabla\phi \tag{3.1}$$

If, additionally, the fluid is incompressible, it follows that the velocity potential satisfies the Laplace equation (Eq. 3.2).

$$\nabla^2\phi = 0 \tag{3.2}$$

In the context of a body interacting with waves, any solution for ϕ must also satisfy a number of boundary conditions at: 1) The interface between air and water; 2) The submerged surface of the body; 3) The seabed; 4) The side boundaries of the body of water, perhaps approximated as being infinite in extent.

The *dynamic boundary condition* specifies that pressure must be balanced either side of the interface between air and water - that is, the fluid pressure must equal the atmospheric pressure at the free surface, $\eta(x, y, t)$. The fluid pressure is produced by both the fluid velocity field and the effect of gravity, whilst air pressure, p, is taken to be atmospheric pressure. Eq. 3.3 is the Bernoulli equation for unsteady, irrotational flows [45].

$$\frac{\partial \phi}{\partial t} + \frac{1}{2}(\nabla \phi)^2 + \frac{p}{\rho} + gz = 0 \text{ on } z = \eta(x, y, t) \tag{3.3}$$

With $z = 0$ at the mean free surface, considering the still water case allows this to be simplified.

$$\frac{\partial \phi}{\partial t} + \frac{1}{2}(\nabla \phi)^2 + gz = 0 \text{ on } z = \eta(x, y, t) \tag{3.4}$$

The *kinematic boundary condition* specifies that the water at the surface must track the surface - that is, fluid velocity normal to the surface must equal the surface velocity (Eq. 3.5).

$$\frac{\partial z}{\partial t} + \frac{\partial \phi}{\partial x}\frac{\partial z}{\partial x} + \frac{\partial \phi}{\partial y}\frac{\partial z}{\partial y} + \frac{\partial \phi}{\partial z} = 0 \text{ on } z = \eta(x, y, t) \tag{3.5}$$

Applying the boundary conditions just at the free surface equilibrium position, and combining the linearised forms of Eqs. 3.4 and 3.5, yields a single, linearised free surface boundary condition (Eq. 3.6).

$$\frac{\partial^2 \phi}{\partial t^2} + g\frac{\partial \phi}{\partial z} = 0 \text{ on } z = 0 \tag{3.6}$$

Fluid at the boundary with the submerged body surface must track the body's movements normal to the surface (Eq. 3.7).

$$\frac{\partial \phi}{\partial n} = \mathbf{U}_t \cdot \hat{\mathbf{n}} + \boldsymbol{\Omega} \cdot (\mathbf{x} \times \hat{\mathbf{n}}) \text{ on } S_b^{(t)} \tag{3.7}$$

where $\frac{\partial}{\partial n} = \hat{\mathbf{n}} \cdot \nabla$ and $\hat{\mathbf{n}} = (n_x, n_y, n_z)$ denotes the unit normal to the body surface, $\mathbf{U}_t$ is the three-dimensional vector of the translational body velocity, and $\boldsymbol{\Omega}$ is the three-dimensional vector of the angular velocity of the body.

Similarly, at the depth of the static seabed (assumed flat), water must not move vertically (Eq. 3.8).

$$\frac{\partial \phi}{\partial z} = 0 \text{ on } z = -h \tag{3.8}$$

Finally, for a unique solution to exist, a further condition must be imposed, to ensure that the scattered and radiated waves decay as the distance from the body increases (Eq. 3.9).

$$\phi \propto \frac{e^{-\mathrm{i}\kappa r}}{\sqrt{r}} \text{ as } r \to \infty \tag{3.9}$$

where r is the radial distance from the body.

Thus equations 3.2, and 3.6-3.9 define the boundary value problem for a floating body interacting with an incident wave field, with a unique solution for ϕ.

With sinusoidal incident waves, the body responses will also be of sinusoidal form (Eq. 3.10), which can be differentiated to obtain the body velocities and accelerations.

$$\Xi_j(t) = Re\{\xi_j e^{\mathrm{i}\omega t}\} \tag{3.10}$$

where $\xi_j = \xi_a e^{\mathrm{i}\theta}$ are complex amplitudes of $\Xi_j(t)$, and j denotes the particular mode of motion.

In this context, each Response Amplitude Operator (RAO), defined as the body motions normalised by the wave amplitude, ξ_j/A, contains the phase (θ) and amplitude (ξ_a) information of the sinusoidal body response. ξ_a may also be referred to as the RAO *magnitude*. The velocity potentials can be treated analogously, meaning that the boundary value problem can be used to instead obtain the complex amplitudes of the body.

$$\phi(x, y, z, t) = Re\{\hat{\phi}(x, y, z)e^{\mathrm{i}\omega t}\} \tag{3.11}$$

Exploiting the linearity of the problem, the complex amplitude of the velocity potential, $\hat{\phi}$ can be decomposed to more readily facilitate a solution (Eq. 3.12).

$$\hat{\phi} = \phi_R + \phi_0 + \phi_s \tag{3.12}$$

The incident potential, ϕ_0, represents the incident wave in the absence of a body. The scattered potential, ϕ_s, is the velocity potential generated by the interaction

between the incident wave and the stationary body. Often, these two are grouped together as a diffraction potential, $\phi_D = \phi_0 + \phi_s$. The radiation potential, ϕ_R, is the total velocity potential resulting from motions of the body, as if it were initially in still water. It is useful to decompose this further, to yield a velocity potential corresponding to a unit amplitude motion of each degree of freedom (Eq. 3.13). In the case of a single, freely-floating rigid body, with six degrees of freedom, $N = 6$.

$$\phi_R = \sum_{j=1}^{N} \xi_j \phi_j \tag{3.13}$$

With the decomposition of the velocity potential, we now have three separate problems. Solving for the incident wave potential is simplest, since conditions 3.7 and 3.9 are not applicable in the absence of a body. For deep water (where $A << \lambda$) and regular incident sinusoidal waves parallel to the x-axis, this is given by Eq. 3.14.

$$\phi_0 = \frac{gA}{\omega} e^{\kappa z} sin(\kappa x - \omega t) \tag{3.14}$$

The scattered and radiation potentials satisfy boundary conditions 3.6, 3.8, and 3.9. Since the scattering potential and the incident potential are independent of the body motions, Eq. 3.7 can be reexpressed for the *diffraction problem* (Eq. 3.15).

$$\frac{\partial \phi_s}{\partial n} = -\frac{\partial \phi_0}{\partial n} \text{ on } S_b^{(t)} \tag{3.15}$$

Returning to the submerged body surface boundary condition, substituting Eq. 3.13 and $\mathbf{U} = \mathrm{i}\omega\xi$ into Eq. 3.7 yields the equivalent condition for the *radiation problem* (Eq. 3.16).

$$\frac{\partial \phi_j}{\partial n} = \mathrm{i}\omega n_j \text{ on } S_b^{(t)} \tag{3.16}$$

where n_j is the component of $\hat{\mathbf{n}}$ in the jth coordinate direction, for j = 1,2,3, and $n_j = \mathbf{x} \times \hat{\mathbf{n}}$ for the rotations about each coordinate axis, where j = 4,5,6. Together, these form $\mathbf{n}$ - an extended version of the normal vector, $\hat{\mathbf{n}}$.

Whereas the incident wave potential can usually be obtained analytically, the radiation and scattering potentials are complicated by the presence of a potentially arbitrarily-shaped body. Analytical solutions are known for only very specific shapes.

However, the system can often be solved numerically for these potentials using a radiation-diffraction code, such as WAMIT [28].

3.2 Frequency-domain models

Working with the complex amplitudes of the body motions and velocity potentials (Eqs. 3.10 and 3.11), for a given frequency of incident wave, the system can be solved within the frequency domain. However, in order to derive the equations of motion, the pressure forces first need to be derived in terms of the velocity potentials.

Substituting Eqs. 3.12, 3.13 and 3.11 into Eq. 3.3, discarding nonlinear terms, and rearranging for p, gives the total pressure acting on the body (Eq. 3.17).

$$p = -\rho Re\Big\{ \big(\sum_{j=1}^{N} \xi_j \phi_j + A(\phi_0 + \phi_s) \big) \mathrm{i}\omega e^{\mathrm{i}\omega t} \Big\} - \rho g z \tag{3.17}$$

In order to yield the total resultant forces/moments in each degree of freedom, the pressure is used to weight the extended normal vector, $\mathbf{n}$, which is then integrated over the submerged body surface. $\mathbf{n}$ can also be rewritten in the case of the radiation and diffraction forces/moments, using Eq. 3.16.

$$F_i^p = Re\big\{ \sum_{j=1}^{N} \xi_j e^{\mathrm{i}\omega t} f_{ij} \big\} + Re\big\{ \mathrm{i}\omega A e^{\mathrm{i}\omega t} X_i \big\} - \rho g \iint_{S_b^{(t)}} n_i z dS \tag{3.18}$$

where f_{ij} are the coefficients of the radiation forces/moments (Eq. 3.19), and X_i are the wave excitation force/moment coefficients (Eq. 3.20). Due to their independence of the coordinate frame, the integrals in both of these terms can be taken over the mean submerged body surface, S_b - i.e. the submerged body surface of the static body.

$$f_{ij} = -\rho \iint_{S_b} \frac{\partial \phi_i}{\partial n} \phi_j dS \tag{3.19}$$

$$X_i = -\rho \iint_{S_b} n_i (\phi_0 + \phi_s) dS \tag{3.20}$$

The first term in Eq. 3.18 is the radiation force/moment acting on mode i, due to a motion in mode j of complex amplitude ξ_j. The coefficients, f_{ij}, are more conveniently decomposed into the *added mass coefficients,* A_{ij} and *radiation damping*

coefficients, B_{ij} (Eq. 3.21). Added mass represents the increased inertia provided by the surrounding water, which must also be accelerated with the body. Radiation damping defines the waves that are generated purely due to the body motions, and radiate energy away from the body. These coefficients together quantify the strength of the hydrodynamic coupling between the modes of motion.

$$f_{ij} = \omega^2 A_{ij} - \mathrm{i}\omega B_{ij} \tag{3.21}$$

The second term in Eq. 3.18 represents the force/moment acting on mode i, due to an incident, diffracted wave of amplitude, A (and of zero phase angle). The excitation force is the only hydrodynamic quantity dependent on the incident wave direction.

Whereas the first two terms are both oscillatory, the third term in Eq. 3.18 describes a constant force/moment due to the effect of buoyancy, acting on mode i. Further, the buoyancy force is dependent on the distinction between the *fixed* coordinate system and the *displaced* coordinate system, meaning the integral must be taken over the instantaneous submerged body surface, $S_b^{(t)}$. This integral can alternatively be expressed as an integral over the submerged body volume, then by approximating the volume between the displaced and static submerged body surfaces as a thin strip, it can be expressed as a surface integral over the static submerged body surface (see section 6.16 of [46], and [29]). This last step incorporates a second index, j, so that the buoyancy force, F_i^b, can be resolved into components describing the force or moment imparted on mode i, due to a motion in mode j of complex amplitude ξ_j (Eqs. 3.22 and 3.23).

$$F_i^b = \sum_{j=1}^{N} c_{ij}\xi_j \tag{3.22}$$

$$c_{ij} = \rho g \iint_{S_b} n_j \left(\frac{\partial n_i}{\partial n_z} + z\nabla \cdot \left[\begin{pmatrix} \frac{\partial}{\partial n_x} \\ \frac{\partial}{\partial n_y} \\ \frac{\partial}{\partial n_z} \end{pmatrix} n_i \right] \right) dS \tag{3.23}$$

In addition to the forces and moments due to the water pressure acting on the body, there are also gravitational forces and moments that result from a displacement about the equilibrium position. In this context, they are conveniently subsumed along

with the buoyancy forces in a stiffness matrix, C_{ij}. Finally, a measure of the body's inertial properties via matrix, M_{ij}, permits the computation of the body motions, ξ_j (Eq. 3.24). (More details are given in Section 3.3 regarding the gravitational restoring forces and the mass/inertia matrix.)

$$\sum_{j=1}^{N}[-\omega^2(M_{ij}+A_{ij})+\mathrm{i}\omega B_{ij}+C_{ij}]\xi_j = X_i \tag{3.24}$$

Whilst this describes the motions of a body resulting from an incident wave field, for wave energy applications, external forces or moments are applied by a power take-off system (PTO), in order to extract some of the energy. These mechanical forces can be represented by a damping matrix, $\mathbf{B}^{pto}$, and a stiffness matrix, $\mathbf{K}^{pto}$.

$$\sum_{j=1}^{N}[-\omega^2(M_{ij}+A_{ij})+\mathrm{i}\omega(B_{ij}+B_{ij}^{pto})+C_{ij}+K_{ij}^{pto}]\xi_j = X_i \tag{3.25}$$

As mentioned earlier, the velocities and accelerations of each mode of motion can be obtained by differentiating Eq. 3.10 with respect to t - the complex amplitude of the velocity is $\mathrm{i}\omega\xi_j$, and that of the acceleration is $-\omega^2\xi_j$. Given the sinusoidal nature of the system's motions, the mean power extracted over a full wave cycle is then given by Eq. 3.26. Net power is extracted only through the damper; the energy exchanged through the mechanical spring is conserved over a full wave period, despite contributing to the instantaneous power.

$$P = \frac{1}{2}\omega^2\xi^{\dagger}\mathbf{B}^{pto}\xi \tag{3.26}$$

In order to extend the analysis to irregular waves, the body responses under a range of incident wave frequencies can be superimposed according to a wave spectrum to generate an irregular body response. This time series can then be used to compute the power using Eq. 3.27.

$$P(t) = \dot{\mathbf{x}}^T(t)\mathbf{B}^{pto}\dot{\mathbf{x}}(t) \tag{3.27}$$

3.3 Generalised modes of motion

Thus far, little mention has been made of the exact nature of the body motions. A single freely-floating rigid body has six degrees of freedom - 3 translational (*surge*, *sway* and *heave*) and 3 rotational (*roll*, *pitch* and *yaw*). In the present work, we define surge motion along the x-axis, sway along the y-axis, and heave along the vertical z-axis. When relating to the rigid body modes, roll denotes rotation about the x-axis, pitch denotes rotation about the y-axis, and yaw denotes rotation about the z-axis. To account for multiple rigid bodies that are hydrodynamically- but not mechanically- or hydrostatically-interacting (such as in a WEC array), additional radiation potentials can be defined in the same manner as the original six rigid body modes. This results in a greater number of linear equations of motion, but only the added mass and radiation damping matrices incorporate terms coupling the motions of one body to the motions of another. However, for bodies whose motions are more complex than those of a single rigid body, another approach is required.

Generalised modes of motion allow the specification of extra types of body motion. To clarify, when referring to generalised modes in the remainder of this thesis, it is not only to provide the physical description, but also with the more specific association to their implementation in WAMIT, for a body undergoing wave loadings. In order to define the necessary additional radiation potentials that correspond to the new types of motion, the boundary condition on the body surface (Eq. 3.16) requires a generalisation so that n_j is defined for each mode of motion, j. The same extension is required for the hydrostatic force (Eq. 3.23). A convenient way to do this is to express n_j in terms of a *shape function*, $S_j(\mathbf{x})$, which contains the components of the body motion in each of the three axial directions, for the mode j.

$$n_j = \mathbf{S}_j \cdot \hat{\mathbf{n}} = s_1 n_x + s_2 n_y + s_3 n_z \tag{3.28}$$

For the rigid body modes, with n_j defined as previously, the shape functions are given in Table 3.1. Note the implied distinction between 'modes (of motion)' and 'degrees of freedom' - whilst these are equivalent in a maximally efficient model, the

motions that the defined 'modes' describe need not necessarily be independent of one another.

Mode index	s_1	s_2	s_3
1 - surge	1	0	0
2 - sway	0	1	0
3 - heave	0	0	1
4 - roll	0	$-z$	y
5 - pitch	z	0	$-x$
6 - yaw	$-y$	x	0

Table 3.1: Definitions of the shape functions of the six rigid body modes.

Specifying the shape function for each generalised mode completes the definition of the radiation problem. Given the solution for the additional radiation potentials, the radiation coefficients are naturally given by Eqs. 3.19. The wave excitation coefficients and the hydrostatic (or buoyancy) coefficients are also given naturally for the generalised modes by way of the appropriate shape functions (Eqs. 3.20 and 3.23, or, more clearly, by Eqs. 3.29 and 3.30).

$$X_i = -\rho \iint_{S_b} \mathbf{S}_i \cdot \hat{\mathbf{n}} (\phi_0 + \phi_s) dS \tag{3.29}$$

$$c_{ij} = \rho g \iint_{S_b} \mathbf{S}_j \cdot \hat{\mathbf{n}} \Bigg(\mathbf{S}_i(3) + z \nabla \cdot \mathbf{S}_i \Bigg) dS \tag{3.30}$$

The gravitational restoring forces and moments are given by Eq. 3.31. In general, the body density is a function of the spatial coordinates. The integral is taken over the instantaneous volume since the quantity itself is dependent on the body displacement, which means the shape function must be expressed in the displaced coordinate system in order to compute F_i. (This will be explored further in Chapter 4.) An analogous version of Eq. 3.22 can then be used in conjunction with Eq. 3.31, to obtain the coefficients that describe the gravitational force or moment acting on mode i, due to a unit motion in mode j. These coefficients are then added to those due to the buoyancy forces, to form matrix, C_{ij}.

$$F_i = -g \iiint_{V_b^{(t)}} \rho_b(\mathbf{x}) \mathbf{S}_i \cdot \hat{\mathbf{k}} dV \tag{3.31}$$

Up to this point, we have considered only the buoyancy and gravitational restoring forces that are first-order in the body motions. Both have zeroth-order contributions, but these cancel for a body oscillating about its equilibrium position, where its centre of gravity lies on the same vertical line as its centre of buoyancy and its mass is equal to the mass of displaced water.

The mass matrix is defined in Eq. 3.32, and quantifies the inertial coupling amongst the modes of motion.

$$M_{ij} = \iiint_{V_b} \rho_b(\mathbf{x}) \mathbf{S}_i \cdot \mathbf{S}_j dV \tag{3.32}$$

Note that the shape functions of the generalised modes may be non-zero only on a subset of the total body surface or volume. In order to avoid this type of discontinuity from being introduced to the shape functions, the integral limits can instead be altered. With this approach, Eqs. 3.19 and 3.29 involve integrals over the submerged body surface associated with mode i; the integration surface of Eq. 3.30 is the intersection of the two submerged body surfaces associated with modes i and j; the integration volume of Eq. 3.31 is the total body volume associated with mode i; and finally, the integration volume of Eq. 3.32 is the intersection of the two total body volumes associated with modes i and j.

Since these last two integrals (Eqs. 3.31 and 3.32) are dependent upon the mass distribution and the unsubmerged portion of the body, commercial radiation-diffraction codes, such as WAMIT, tend not to be able to compute them. Hence, they must be provided by the user. For complex body shapes and with many generalised modes, this is not necessarily straightforward. This subject is again encountered in Chapter 4. For the reason that the user must provide the shape functions for the generalised modes, which could take a variety of forms, the second of the two terms in Eq. 3.30 also tends to require manual input.

The body motions for all of the modes, including any generalised modes can then be computed using Eq. 3.24, or Eq. 3.25, given appropriate extension of the $\mathbf{B}^{pto}$ and $\mathbf{K}^{pto}$ matrices, using a standard matrix inversion technique.

Since the only restriction on the shape functions is that they are a piecewise differentiable function of the body coordinates, with the divergence term in Eq. 3.30 well-defined, there are numerous applications (see e.g. [29], [28]). Even internal water columns, which are traditionally not considered part of the body, can be modelled using generalised modes [47].

3.4 Modelling forces/moments using generalised modes

Under incoming monochromatic waves, the body will be subject to loadings due to the hydrodynamic, hydrostatic and inertial forces and moments. It is possible to specify additional *'fixed'* generalised modes in order to compute these forces/moments. The shape function should describe the direction or manner in which the forces/moments act. From another perspective, they should describe the components of the body motion that would result, were the body free to move in the manner specified by the shape function. In exactly the same way as before, the radiation potentials are then solved for these extra, fixed modes, enabling the computation of the associated hydrodynamic coefficients. The stiffness (buoyancy and gravitational restoring) and mass/inertia matrices can also be computed in the same way. Eq. 3.24 or Eq. 3.25 can then be used exactly as before to obtain the body motions; the 'fixed' generalised modes are used to model forces so are excluded from this set of equations. The total forces/moments acting on the body in the manner specified by each 'fixed' generalised mode, i, can then be obtained by summing the inertial, hydrodynamic, hydrostatic and gravitational restoring forces/moments (Eq. 3.33). Since these resulting complex amplitudes describe the force response due to the incident wave, they could equally be labelled a 'response amplitude operator', when normalised by the wave amplitude. However, to avoid confusion with RAOs describing the response in terms of body motions, the complex amplitudes describing the total forces will be referred to as 'force RAOs'. 'RAO' will continue to refer to the complex amplitude associated with

the body motions.

$$\widetilde{\xi}_i = \sum_{j \in J} X_i + [\omega^2(M_{ij} + A_{ij}) - \mathrm{i}\omega B_{ij} + C_{ij}]\xi_j \tag{3.33}$$

where J denotes the set of indices corresponding to the 'free' generalised modes of motion.

Note that the forces/moments, $\widetilde{\xi}_i$, are only a function of the matrix entries that correspond to a force/moment acting on fixed mode i, due to a body motion in mode j. This means that the elements coupling fixed modes to fixed modes are not required. A further point to note is that Eq. 3.33 is not directly a function of the PTO damping and stiffness matrices, because these are only populated with non-zero entries where $i \in J$ and $j \in J$. However, the body motions, ξ_j, are functions of B_{ij}^{pto} and K_{ij}^{pto}.

3.5 Time-domain models

Eq. 3.25 can also be solved in the time-domain, using the same hydrodynamic outputs based upon the linear wave theory. For a single frequency, the transformation of the equations into the time domain is trivial (Eq. 3.34), since the hydrodynamic coefficients are constants.

$$\sum_{j=1}^{N}(M_{ij} + A_{ij}))\ddot{x}_j(t) + (B_{ij} + B_{ij}^{pto})\dot{x}_j(t) + (C_{ij} + K_{ij}^{pto})x_j(t) = X_i \tag{3.34}$$

In order to simulate the exposure of the body to irregular waves, a superposition of many monochromatic waves provides an incident wave elevation, from which the excitation force can be obtained. Since the body must now respond to the superposition of these different wave frequency components, the hydrodynamic coefficients are frequency-dependent, and necessitate a convolution integral. A convolution integral can also be used to represent the wave excitation force. Eq. 3.35 gives a typical form of the equations, that can then be solved by a numerical ordinary differential equation

solver to obtain the body motions.

$$\sum_{j=1}^{N}(M_{ij}+A_{ij}^{\infty}))\ddot{x}_j(t)+\int_0^t K_{ij}(t-\tau)\dot{x}_j(\tau)d\tau+B_{ij}^{pto}\dot{x}_j(t)+(C_{ij}+K_{ij}^{pto})x_j(t) = \int_{-\infty}^{\infty} G_j(\tau)\eta(t-\tau)d\tau \tag{3.35}$$

where A_{ij}^{∞} is the infinite-frequency added mass, $K_{ij}(t)$ is the radiation impulse response function, $G_j(t)$ is the force impulse response function, and $\eta(t)$ is the surface elevation. More information on these coefficients and time-domain modelling in general is given in [48]. For completeness, the time-dependent power is given by Eq. 3.27.

Besides allowing easy incorporation of nonlinearities, the equations of motion are often formulated in the time domain in order to be more readily compatible with multibody codes (e.g. WEC-Sim [49], Edinburgh Wave Systems Simulation Toolbox [50]).

3.6 Modelling jointed devices

Wave energy devices involving rotational joints are often modelled in the time-domain, where a multibody code can be exploited to handle the joints. The quantities defined by Eqs. 3.19, 3.29, 3.30, 3.31 and 3.32 are computed for each of the bodies as if they were mechanically independent, but with hydrodynamic interactions. Those quantities are then transformed into the time domain, where additional equations are defined to impose the spatial constraints provided by the joints. Multibody codes often reduce the difficulty in defining the joints - the SimScape Multibody package [51] contains a series of pre-defined joints, which can easily be assembled in a graphical form within Simulink. Whereas this method allows nonlinear behaviour of the joints, the full model still has the restriction of the linear wave theory that the hydrodynamic behaviour is based upon. With a small wave amplitude, the system is fully linear, and may be modelled at much lower computational expense using generalised modes to

approach the problem in the frequency domain. In addition to the increased computational effort in solving differential equations (time domain) instead of algebraic equations (frequency domain), the time-domain model also requires the solution of more radiation potentials than there are degrees of freedom in the system.

Jointed devices can be linearly modelled in the frequency domain using generalised modes by defining appropriate shape functions (see Chapter 4 for more detail), such that the entire range of body motions can be represented by a combination of the modes of motion. However, since the computation of the inertial and gravitational properties is not straightforward for complex body configurations, a time-domain model may be useful in verifying the frequency-domain approach that uses generalised modes. The time-domain model can be solved for the body motions, using small incident wave amplitudes to ensure dynamics are within the linear regime. Given enough settling time to reach a steady state, the Response Amplitude Operators (RAOs) can then be extracted from the time series, to facilitate comparison between the two methods.

Chapter 4

Modelling Jointed Bodies using Generalised Modes

Despite generalised modes providing an efficient modelling approach for jointed bodies, the implementation is often not straightforward. To first recap the problem, generalised modes can be used to specify extra types of motion, in addition to the standard six rigid body modes (surge, sway, heave, roll, pitch and yaw). An additional radiation potential is introduced for each generalised mode, given definitions of the corresponding velocity components that are normal to the body surfaces, provided via the shape functions. Solving for the diffraction potential and all of the radiation potentials then enables computation of the hydrodynamic (radiation and excitation) coefficients (A_{ij}, B_{ij}, X_i) using the geometry of the submerged body surface, in the same manner as for the rigid body modes. In order to solve the N equations of motion (Eq. 3.24 if no power is extracted, otherwise Eq. 3.25), corresponding to both the rigid body and generalised modes, the inertial and gravitational restoring properties (M_{ij} and c^g_{ij}) are first required. Since the elements in these two matrices are dependent upon the overall mass distribution and the geometry of the unsubmerged portion of the body, commercial radiation-diffraction codes (such as WAMIT) typically lack the inputs required to compute them. Given their dependence in part on the gradient of the shape functions (Eq. 3.30), the buoyancy forces (c_{ij}) also require computation, but as will be revealed by the shape functions associated with joints, these do not require any special treatment. Thus, there are three quantities that can pose some difficulties in

modelling joints, especially for bodies with a high level of geometric or configurational complexity:

1. Shape functions, $\mathbf{S}_i(\mathbf{x})$
2. Mass/inertia matrix elements, M_{ij}
3. Gravitational restoring force/moment coefficients, c^g_{ij}

Each of these are treated in turn in the following three sections, outlining a recommended approach whilst emphasising the key conceptual details. Whilst the treatment is, in general, not specific to any particular radiation-diffraction software, this chapter also includes remarks relating specifically to WAMIT, which is the software used throughout this thesis.

The shape functions enabling the modelling of shear forces at the joints are also considered, in addition to a short summary of the advantages this modelling approach brings. A further selection of related miscellaneous points of a 'troubleshooting' nature are documented in Appendix B, some of which relate specifically to the implementation of the generalised modes within WAMIT.

4.1 Shape functions

The choice of shape function must simply allow for representation of the desired type of body motions. More specifically, all desired configurations of the body elements must be representable as a superposition of the rigid body and generalised modes. Hence, the choice of generalised modes is not unique, and as well as differences in efficiency, some configurations may be better suited towards certain applications than others. For instance, defining only the vertical component of the shape function to more conveniently allow analysis of the vertical motions of a hinged body, as in [31] (this study is also mentioned in Section 2.1). In the case of the jointed wave energy converters studied in Chapters 5 and 6, both the horizontal and vertical motions at and about the joints are required to capture the device behaviour correctly. In the

case of the duck spine system, power is also extracted through the joint motions. With these considerations, a natural choice of generalised mode is one that models a conventional angular rotation around the joint. For the body segment connected to each joint arm, this is similar to a rigid body rotation. In order to derive the appropriate shape functions, we first consider the motions of a single, rigid body. (This part is also relevant to the construction of c_{ij}^{g} later in this chapter.)

Assuming both small body motions and retaining only first order terms, Eq. 4.1 relates a body coordinate, $\mathbf{x}_{rb} = [x, y, z]^T$ expressed in a fixed coordinate system to the same body coordinate $\mathbf{x}' = [x', y', z']^T$ expressed in a displaced coordinate system ([46], p.290).

$$\mathbf{x}_{rb} = \begin{bmatrix} 1 & -\xi_6 & \xi_5 \\ \xi_6 & 1 & -\xi_4 \\ -\xi_5 & \xi_4 & 1 \end{bmatrix} \mathbf{x}' + \begin{bmatrix} \xi_1 \\ \xi_2 \\ \xi_3 \end{bmatrix} \tag{4.1}$$

We now consider dividing the body into two components and connecting them by a hinge joint, located at $[a, b, c]^T$, about which the body is free to rotate in the x-z plane. We will refer to the body component connected to one hinge arm as the 'left part', and to the other component as the 'right part'. For ease of visualisation, the body shape may be such that the 'left part' is situated mainly or entirely leftward of the hinge, and that the 'right part' is mainly or entirely rightward of the hinge. The analysis still holds for the general body shape, however. To operate as a hinge, the angle between the two parts of the body must change from their equilibrium angle - it may be that the 'left part' moves clockwise about the hinge, whilst the 'right part' rotates in an anticlockwise direction (as viewed from the same side of the body). Now focus on a point on the 'left part' where clockwise rotation is positive, as it is for pitch rotation of the entire body. In order to express its displaced coordinate in the fixed coordinate system, accounting for this extra type of rotation, we must first shift to the hinge location, then apply the rotation about the y-axis, before shifting back to the origin of the fixed coordinate system (Eqs. 4.2, 4.3). Again, the rotation matrix

is defined for small motions and only linear terms are retained.

$$\mathbf{x} = \begin{bmatrix} 1 & 0 & \xi_7 \\ 0 & 1 & 0 \\ -\xi_7 & 0 & 1 \end{bmatrix} \cdot \left(\mathbf{x}_{rb} + \begin{bmatrix} -a \\ -b \\ -c \end{bmatrix} \right) + \begin{bmatrix} a \\ b \\ c \end{bmatrix} \tag{4.2}$$

$$\mathbf{x} = \begin{bmatrix} x' + \xi_1 - \xi_6 y' + \xi_5 z' + \xi_7 (z' - c) \\ y' + \xi_2 - \xi_4 z' + \xi_6 x' \\ z' + \xi_3 + \xi_4 y' - \xi_5 x' - \xi_7 (x' - a) \end{bmatrix} \tag{4.3}$$

An appropriate shape function for this type of motion about the hinge is given by the components of $\mathbf{x}$ proportional to ξ_7. Defining the rotation oppositely would just result in opposite signs of the ξ_7 terms, and additional hinges would simply yield additional analogous terms due to the linearity of the transformation. At this stage, a further decision must be made regarding the form of the shape function; all desired body positions must be achievable using a superposition of the rigid body and generalised modes. To reiterate an earlier point, this is not a unique decision. Here, a symmetric form is opted for, where the rotation of the 'right part' is defined oppositely to that of the 'left part' (Eq. 4.4). Note that $\pm$, $\mp$ and $\lessgtr$ are used as shorthand to denote two separate equations - one taking the upper symbols, the other taking the lower symbols. Appendix A verifies the appropriateness of this definition. Note also that $x < a$ and $x > a$ are used as shorthand to denote the 'left part' and 'right part' of the body, respectively. Often these are equivalent, but this is not true in general, as the mass connected to one hinge arm may surround the hinge (i.e. including x coordinates both greater than and less than a).

$$\mathbf{S}_p(\mathbf{x}) = \begin{bmatrix} \pm(z - c) \\ 0 \\ \mp(x - a) \end{bmatrix} \text{ for } x \lessgtr a \tag{4.4}$$

Similarly, if ξ_8 denotes symmetric rotation about the x-axis, substituting the appropriate rotation matrix into Eq. 4.2 yields the shape function defined in Eq. 4.5.

$$\mathbf{S}_{rr}(\mathbf{x}) = \begin{bmatrix} 0 \\ \mp(z - c) \\ \pm(y - b) \end{bmatrix} \text{ for } x \lessgtr a \tag{4.5}$$

In the same manner, the shape function given by Eq. 4.6 defines symmetric rotation about the z-axis, denoted by ξ_9.

$$\mathbf{S}_y(\mathbf{x}) = \begin{bmatrix} \mp(y-b) \\ \pm(x-a) \\ 0 \end{bmatrix} \text{ for } x \lesseqgtr a \tag{4.6}$$

Implicit in the wording used so far in this section, the 'rigid body' modes have been applied to the assembly of two connected bodies, as if they were a single, rigid body. The generalised mode has then been defined relative to this 'rigid body', in order to permit the relative motion about the hinge. This is the default convention for modelling generalised modes in WAMIT, and is particularly convenient if an external torque were to be applied at the hinges by some 'on-board' mechanism (e.g. by a power take-off system), since the 'equal-and-opposite' reaction torque would naturally be applied to the rest of the body (see Appendix E for more details). However, one could alternatively define the six rigid body modes over just the first body, yet preserve the correct dynamics by way of altered coefficients in Eq. 3.25. In WAMIT, this can be achieved by 'locking' the rigid body modes, in order to supplant them with the appropriate generalised modes. In the standard case with a hinge, this has no obvious benefit, but this is a useful insight when considering other types of wave energy converter, particularly where power extraction is translational (see Section 5.2.6), or where an internal mechanism is used to extract power as if the body were seabed-fixed (see Section 6.2.3).

4.2 Mass and inertial properties

The mass and inertia couplings between each pair of modes are computed using Eq. 3.32, where the integration volume is the total body volume (in the fixed coordinate system, that defines the body equilibrium position) in the case of using the joint modes as defined in this Chapter. For a simple geometry (e.g. a series of uniform density, cuboidal barges), evaluating these integrals for the terms involving joint modes reduces to a series of easily computable moments. However, for complex body geometries and mass distributions, and where many generalised modes are involved, these integrals

can require substantial computational resources, and can also require significant work on the part of the user to define. More details are given with respect to the two applications of the WaveTrain device and a spine of Edinburgh ducks in Sections 5.2.5 and 6.2.3.

4.3 Gravitational restoring forces and moments

The gravitational forces/moments acting on each mode, due to a motion of each other mode, are found by Eq. 3.31. The integral is taken over the instantaneous volume, $V_b^{(t)}$, since the quantity itself is dependent on the distinction between the fixed and displaced coordinate systems. This means that the shape functions, $\mathbf{S}_i$, ordinarily (and for the purposes of WAMIT) defined in the fixed coordinate system, must be reexpressed in the displaced coordinate system if the integration is to be more conveniently performed over the equilibrium volume, V_b. This is done by substituting the appropriate version of the coordinate transformation (in a form similar to Eq. 4.3) into Eq. 3.31 with the appropriate shape functions (such as those given by Eqs. 4.4, 4.5 or 4.6). Combining this with the version of Eq. 3.22 that involves gravitational restoring forces allows determination of the coefficients, c_{ij}^g, that are first-order in the body motions. Some simplification can also be provided by expressing the centre of gravity as a volume integral over the body (Eq. 4.7). The zeroth-order forces are not considered as these are cancelled by the buoyancy forces for a body freely floating about its equilibrium position (see p.293-4 of [46] for the analogous case involving the rigid body modes).

$$m\mathbf{x_g} = \iiint_{V_b} \mathbf{x}\rho_b dV \tag{4.7}$$

Returning to the earlier example involving the six rigid body modes and a single hinge, Eqs. 4.8 - 4.10 illustrate an example case for c_{57}^g, the gravitational restoring moment acting on the rigid body pitch mode, due to a unit motion of the symmetric hinge mode. In the displaced coordinate frame, $V_b^{(t)} = V_b$. The discontinuity of the shape function leads to two force terms, one due to the body either side of the hinge. In physical terms, the coupling force is zero if there are equal moments about either

side of the hinge, which is as expected, since a pitching of the body requires an uneven distribution of moments about its centre of rotation.

$$\begin{aligned} F_5 &= -g \iiint_{V_b^{(t)}} -x\rho_b dV \\ &= -g \iiint_{V_b} -(x' + \xi_1 - \xi_6 y' + \xi_5 z')\rho_b dV \\ &\qquad - g \iiint_{V_{b,l}} -\xi_7 (z' - c)\rho_b dV \\ &\qquad - g \iiint_{V_{b,r}} \xi_7 (z' - c)\rho_b dV \end{aligned} \tag{4.8}$$

$$F_{57} = (m_l g z_{g,l} - m_r g z_{g,r})\xi_7 \tag{4.9}$$

$$c^g_{57} = m_r g z_{g,r} - m_l g z_{g,l} \tag{4.10}$$

where m_r denotes the mass to the right of the hinge (in this example, where $x > a$), and $z_{g,r}$ denotes the z-coordinate of the centre of gravity of the mass to the right hand side of the hinge, expressed relative to the hinge location. V_b is the equilibrium volume, and $V_{b,l}$ denotes the component of V_b residing to the left of the hinge (where $x < a$).

4.4 Shear forces

One of the key concerns with a jointed wave energy converter, or indeed any jointed body, involves the forces and moments that act at the joints in directions in which motions are not permitted. For a ball joint with three rotational degrees of freedom, the shear forces are crucial in estimating the likelihood of failure of a joint. In order to compute these using Eq. 3.33, suitable shape functions are required. In the same manner adopted by Mathai [30] to model cross-structural loads, the shape functions for the shear forces along the x, y and z axial directions are given by Eq. 4.11.

$$\mathbf{S}_{i_1} = \pm\hat{\mathbf{i}} \text{ for } x \gtrless a \; ; \; \mathbf{S}_{i_2} = \pm\hat{\mathbf{j}} \text{ for } x \gtrless a \; ; \; \mathbf{S}_{i_3} = \pm\hat{\mathbf{k}} \text{ for } x \gtrless a \tag{4.11}$$

Remember that only the M_{ij} and c^g_{ij} terms with 'fixed' (shear force) modes, i, and 'free' modes, j, are required to obtain the total shear forces. And due to the

shape functions for the shear forces being independent of the body coordinates, $\mathbf{x}$, the relevant components of c_{ij}^{g} are all zero.

Again, the divergence of these shape functions is zero, and so the required buoyancy force coefficients, c_{ij}, are computed automatically by WAMIT.

4.5 Advantages of this approach

Despite the implementation difficulties, a jointed body with many degrees of freedom is much more efficiently modelled in the frequency-domain, for two reasons. Firstly, resources are not used by redundant modes of motion; the number of modes of motion is equal to the number of degrees of freedom. Whilst this is also possible in a time-domain model, it is more common that the hydrodynamic coefficients are computed for the collection of bodies as if they were mechanically independent, followed by imposing the mechanical constraint afterwards. In this way, the hydrodynamic coefficients are computed for more modes of motion than the final, jointed system has degrees of freedom. Secondly, the solution of frequency-domain equations is far more computationally efficient than solving their time-domain equivalents is. Whilst a frequency-domain model does not easily allow for the incorporation of nonlinearities, often the fully linear model is sufficient for gaining insight into the underlying physics and dynamics of a device, and for heuristic optimisation studies, where only the relative ordering of performance amongst different designs matters (not the absolute accuracy of each result). An additional benefit of formulating the model entirely within the linear boundary value problem is that complex conjugate control (see Ch. 6 of [52]) is applicable.

Chapter 5

The WaveTrain Device

5.1 Introduction

As part of Wave Energy Scotland's Novel Wave Energy Converter programme, the WaveTrain device underwent a range of physical and numerical model testing during the calendar year of 2016 [2]. The programme began with an optimisation study, using a linear model of a single module, restricted to a single degree of freedom along the inclined plane, in order to investigate the effect of the inclination angle on power production. Based on the preferred angle, the mass of entrained water was tuned using the length and depth of the water column, and the effect of the linear damping coefficient was analysed. Consideration of optimal power-producing behaviour occurring when the modules are separated by half a wavelength was also utilised to select an appropriate module spacing for the three-module WaveTrain device - another driver for setting the length of the entrained water column. This was followed by the development of a time-domain numerical model of the full WaveTrain device, which enabled simulation of the device extracting power from irregular waves. Two phases of physical model testing were then carried out, firstly using models with ramp-constrained motions in the University of Edinburgh's Curved Tank [53], followed by more extensive testing of a freely-floating WaveTrain device in FloWave Test Tank [54]. In the latter phase of testing the freely-floating model, amongst the multitude of physical tests, some test data was used in order to calibrate the numerical model, by tuning a quadratic drag coefficient.

Whilst the early optimisation study gave some insight into the effects of a few parameters, these insights were based on a simplified, linear model of just a single module interacting with monochromatic waves, with each variable investigated in turn. In the case of the physical, freely-floating model, additional design constraints are imposed by the underlying physics. For example, the device must reside at a suitable height in the water, and each module at the correct inclination angle when the device is in its equilibrium position. Especially when compounded by practical engineering constraints (available materials, etc.), the restrictions on the design can be significant. In order to prevent perceived underachievement of the WaveTrain concept, an appropriate optimisation study must better incorporate these constraints. A few results from the testing programme of 2016 illustrate the potential for improvement that such an optimisation study could aim to exploit.

Firstly, further testing of an updated design in polychromatic waves suggested a better power capture would result from a module spacing larger than that originally concluded from the early optimisation work. Secondly, early studies investigating the effect of module inclination angle were not conclusive. Some suggested use of a value 5° to 10° below the chosen inclination angle of 40° to the horizontal. Further regular wave tests using the Mean Capture Width Period as a metric, to select more favourably for designs that performed better in more energetic longer waves, concluded that 35° leads to a better performance than 40°. However, only four inclination angles were tested, and no tests were conducted in irregular waves. Thirdly, early WaveTrain models adopted a rectangular water column cross-section (as opposed to the row of adjoined cylindrical columns used later), with which much better results were found in a comparison using both designs with the tuned full numerical model in irregular seas. This finding was also later reproduced in further tank tests. It was suspected that perhaps some part of this difference in performance could be attributed to the differing ratios of the WaveTrain module mass to the water column mass, as this parameter also differed between the two cases.

Consequently, a key recommendation to progress the development of the Wave-Train device was to carry out a full optimisation study, focussing on the mass/inertial and geometric parameters, with particular emphasis on the inclination angle and the ratio of the module mass to the entrained water mass. The calibrated time-domain model was originally proposed for use in such a study. However, an heuristic tool is necessitated by the lack of available information on the gradient of the objective function with respect to the optimisation variables. Heuristic (or often 'metaheuristic') tools can require a large number of design evaluations, and could cause excessive runtimes using the time-domain model.

Fortunately, frequency-domain models provide a much faster alternative for such optimisation schemes, though they cannot readily incorporate nonlinear behaviour. However, on the basis of only small differences in terms of power captures (in a range of irregular seas) between two variants of the numerical model (with and without quadratic drag terms) and the physical model, it was noted that a fully linear, frequency-domain model could be sufficient for an optimisation study [20] (the full paper is reproduced in Appendix I). To add further weight to this, the nonlinear drag term was proportional to the square of the velocity for each mode of motion, so will be greater under conditions in which a larger power capture would be expected. Add to that the success of this single nonlinear term in enabling calibration of the model to the physical tests, and it follows that the relative ranking of devices in terms of power capture should be maintained when using a fully linear model. On this basis of these arguments, all of the device dynamics can be more efficiently accounted for in the frequency-domain, permitting a faster and broader search for optimal design candidates.

Note that a spectral-domain model (see Ch. 4 of [48]) could allow the incorporation of nonlinear mechanisms (e.g. quadratic drag forces) at little runtime expense for an optimisation study. However, the specification of the empirical coefficients required for these models (just as with the equivalent nonlinearities that may be incorporated into a time-domain model), would warrant additional attention, since these may need

to be adjusted for different candidate designs within the optimisation scheme. For this reason, along with the reduced awareness of the author to this modelling technique, spectral domain models were not considered for use in this work.

5.2 Development of an efficient hydrodynamic model

The WaveTrain can be efficiently modelled in the frequency-domain using generalised modes, by viewing the collection of three modules as a single, rigid body, augmented by extra rotations about the joints, and by relative motions of the internal water columns. In this section, the development of this hydrodynamic model and its implementation within WAMIT are detailed. See [55] or [28] for more detail on the methods related to WAMIT that are described herein.

5.2.1 Modelling assumptions

Each device considered during this study comprises three modules, as this provides the simplest case that is representative of the complete system dynamics (i.e. it includes a module with neighbours on either side). It is assumed that the interconnecting mechanical struts will have negligible hydrodynamic effect compared to the modules themselves. Thus in determining the device motions, the model needs to account for the connections, but the hydrodynamic interactions need only involve the three modules (including their internal water columns). It is also assumed that these struts will not significantly impact the dynamics through their mass and inertia, so this is also disregarded. Nevertheless, each strut is to be connected from the base of one module, to a position coinciding with the waterline on the underside of the module in front (Fig. 1.2). Since the device is intended for deep-water deployment, it is assumed that its slack-mooring will have a negligible effect on the dynamics relevant for power absorption. As observed in previous wave tank tests, the chain of WaveTrain modules tends to align itself perpendicular to the incoming wavefronts. Consequently, the model only needs to capture the in-plane dynamics, which means only a single degree of freedom is required to model each joint. Considering also that each module

contains an internal body of water, this leads to a 10 DoF model - the 3 in-plane rigid body DoFs (surge, heave and pitch), 4 DoFs due to the four hinges, and 3 DoFs corresponding to the sloped translational motions of the three internal water columns. (In practice, the compressibility of the internal air chambers may affect the power extraction, which could be modelled using additional DoFs, but this is assumed insignificant for the current application and not considered further in this work. See Section 5.2.6 for further justification of this.)

As the power take-off system is expected to be small compared to each module, its effect on the device dynamics through its own mass and inertia is not considered. Indeed, the only contribution of each PTO is via a linear damping coefficient, to account for the effects of removing energy from the system.

The complexity of this WEC concept necessitates that some base assumptions are also made about the physical structure of each module. Each comprises a trapezium-shaped float of uniform density, the base of which is attached to the top of a hollowed-out cuboid, which is open to the surrounding water at the bottom, and whose walls are also of uniform density (Fig. 5.1). These two components are supplemented by a 'point mass', situated at the leftmost edge of the module (see also Fig. 5.1), whose role is to enable the desired mass distribution with maximal simplicity (primarily to allow satisfaction of Eq. 5.1 for a wide range of designs). (See Appendix C for further justification of this approach.) All of the surfaces are to be flat, and each of the three modules identical in form. Whilst the sharp edges resulting from these flat surfaces would lead to losses through vortex shedding in practice, the models considered in this thesis do not account for viscous effects, and differences in the linear hydrodynamic coefficients are assumed to be negligible between the cases with sharp and rounded edges.

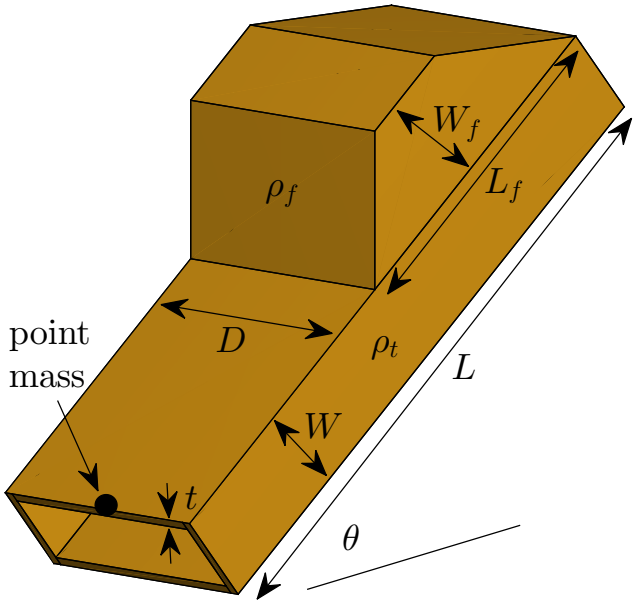

Figure 5.1: Schematic of a single WaveTrain module, with the defining parameters labelled. θ is the angle between the horizontal plane and the length, L.

5.2.2 Physical constraints

There are a number of constraints that need to hold to ensure physical feasibility. Firstly, the centre of buoyancy of a given module must lie on the same vertical line as the centre of gravity, for the desired inclination angle to be achieved at equilibrium (Eq. 5.1).

$$x_b = x_g \tag{5.1}$$

It is also imperative that the device as a whole does not capsize when displaced, and instead returns to its equilibrium position - i.e. static stability is observed. Additionally, each individual module must be statically stable, to maintain the intended device configuration. The stability of the entire chain of modules is implied by each individual module being statically stable, and just considering in-plane motions, each module must be statically stable in pitch. This is equivalent to requiring positive

metacentric heights (Eq. 5.2).

$$(S_{11}/\forall) + z_b - z_g > 0 \tag{5.2}$$

S_{11} denotes a waterplane moment associated with pitch rotation (see [46], p.292), $\forall$ denotes the displaced water volume. In order for the vertical float face to correctly influence the device dynamics, the equilibrium water level should be no lower than the bottom of this vertical surface. The fact that the device should not be fully submerged enforces an upper constraint on the waterline. In fact, in order for all designs explored to remain robust when tested in real seas, it seems sensible to enforce this limit at the uppermost edge of the base of the tubes (Fig. 5.2). This also affords greater simplicity in the model. Since the height at which the module rests in equilibrium is dependent on its mass distribution, these waterline limits correspond to upper and lower limits of the module mass (Eq. 5.3).

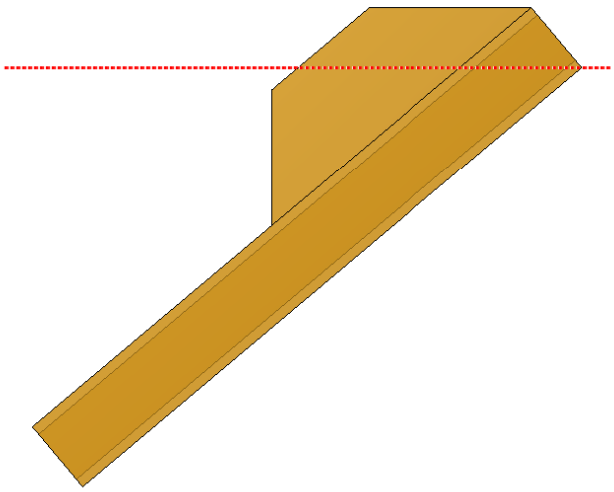

Figure 5.2: Side view of a single WaveTrain module. Red dotted line denotes the maximum waterline height.

$$M_{LB} \leq M \leq M_{UB} \tag{5.3}$$

To constrain the model complexity, a further limit is imposed on the vertical float face. The top of this face must be at a vertical position below the uppermost edge of the module base (see the red dots in Fig. 5.3). This can be expressed in terms of the float dimensions, tube width and angle of inclination (Eq. 5.4).

$$L_f sin(\theta)cos(\theta) - W_f - Wcos^2(\theta) > 0 \tag{5.4}$$

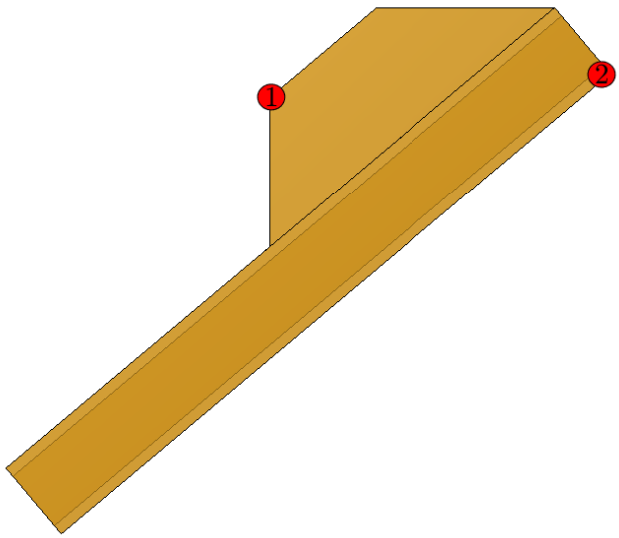

Figure 5.3: Side view of a single WaveTrain module. Red dots denote the constraint given by Eq. 5.4; the vertical position of dot 1 must be below that of dot 2.

Two further physical constraints are imposed by the float configuration (Eq. 5.5). Firstly, the float must be shorter than the tubes. Secondly, due to the lower and upper side surfaces of the float being vertical and horizontal, respectively, the float width must be less than than its value in the extreme case where the top of the trapezium has zero length (i.e. where the float is triangular in shape).

$$L_f < L \text{ and } W_f < L_f sin(\theta)cos(\theta) \tag{5.5}$$

This forms a set of seven constraints, which any feasible design must satisfy.

5.2.3 General approach and geometry representation

As described in detail in Chapter 3, the problem involves solving a boundary value problem describing the wave-body interaction, which is governed by linear potential flow theory. In order to obtain the velocity potentials that correspond to the system behaviour, a series of integral equations are to be solved numerically, using WAMIT [28]. The form of those equations depends on the representation of the velocity potentials. The preferred approach in this study is to use WAMIT's 'higher-order method', which uses B-splines to represent the variation of the velocity potentials on the body. This method is known to usually give a more efficient and accurate solution than the case in which a piecewise constant description of the velocity potentials is used (i.e. WAMIT's 'low-order method') [55].

5.2.4 Thin tube walls

Each WaveTrain module comprises thin tube walls, which can lead to large runtimes if the mesh is constructed with their true thickness. An alternative approach involves their approximation as walls of zero thickness. WAMIT facilitates this by using a modified form of the integral equations, to represent the velocity potentials by a distribution of dipoles over the double-sided surfaces. The mesh is then defined with 'dipole patches' in place of the walls. The suitability of this approximation must be ensured for all designs considered; if the walls are thin enough, the change in the hydrodynamic and hydrostatic properties relating to the infinitely thin representation of the tube walls will be small. Note that the inertial and gravitational restoring properties remain associated with the walls of their true, finite thickness.

The RAOs corresponding to each water column of a model scale test device have been compared for the finite-thickness and zero-thickness cases, over a range of wall thicknesses (see Appendix D). It can be observed that for wall thicknesses above 5mm, the approximation begins to significantly break down. Considering that the dominant cause of the discrepancies is the difference between the true water column

cross-sectional area and that represented by the dipole-walled model, this figure can be generalised for any module design (Eq. 5.6).

$$t_{limit} = \frac{2t}{min\{W, D\} - 2t} \tag{5.6}$$

With $t = 0.005$, $W = 0.15$ and $D = 0.8$, this gives a limit of $\frac{1}{14}$, which defines a restriction on the wall thickness, t, in terms of W and D (5.7).

$$t \leq \frac{1}{30} min\{W, D\} \tag{5.7}$$

5.2.5 Hinge joints

The shape functions for the four in-plane hinge joints are those specifying rotation about the y-axis (which runs parallel to the wavefronts), of the form given by Eq. 4.4, with hinge locations $(a_i, b_i, c_i)^T$ for i = 1,2,3,4. The presence of four joints leads to a coordinate transformation between the fixed and displaced reference frames that contains four discontinuities. This complicates the construction of the $\mathbf{c}^g$ matrix as the integrals must be performed over the entire body volume. But, as an example, for volume elements lying to the right of the hinges indexed 7 and 8 ($x > a_1$ and $x > a_2$) and to the left of the hinges indexed 9 and 10 ($x < a_3$ and $x < a_4$), the coordinate transformation is given as in Eq. 5.8.

$$\mathbf{x} = \begin{bmatrix} x' + \xi_1 - \xi_6 y' + \xi_5 z' - \xi_7(z' - c_1) - \xi_8(z' - c_2) + \xi_9(z' - c_3) + \xi_{10}(z' - c_4) \\ y' + \xi_2 - \xi_4 z' + \xi_6 x' \\ z' + \xi_3 + \xi_4 y' - \xi_5 x' + \xi_7(x' - a_1) + \xi_8(x' - a_2) - \xi_9(x' - a_3) - \xi_{10}(x' - a_4) \end{bmatrix} \tag{5.8}$$

Over the complete body, care must be taken to preserve the correct signs with the correct set of volume elements, when computing the $\mathbf{c}^g$ matrix. However, considering each element, c^g_{ij}, in turn, yields at most a dependence on two discontinuities, giving at most three separate integrals requiring evaluation. For example, consider two hinges, p and q, with hinge p located at $(a_p, b_p, c_p)^T$ and hinge q further rightwards ($a_q > a_p$) at $(a_q, b_q, c_q)^T$. Using Eq. 3.31 with the coordinate transformation (shown here for just the rigid body modes and these two hinges) yields three separate terms that comprise the moment on mode p due to motion in mode q (Eqs. 5.9 - 5.11). The total moment

is the difference between the moment around hinge q due to the mass in between the two hinges, and the moment around hinge q due to the mass outside the two hinges.

$$\begin{aligned}
F_p^g &= -\rho_b g \iiint_{V_{b,l(p)}} -x dV - \rho_b g \iiint_{V_{b,r(p)}} x dV \\
&= -g \iiint_{V_{b,l(p)}} -(x' + \xi_1 - \xi_6 y' + \xi_5 z' + \xi_p(z' - c_p))\rho_b dV \\
&- g \iiint_{V_{b,r(p)}} (x' + \xi_1 - \xi_6 y' + \xi_5 z' - \xi_p(z' - c_p))\rho_b dV \\
&- g \iiint_{V_{b,l(p)}} -(\xi_q(z' - c_q))\rho_b dV \\
&- g \iiint_{V_{b,m}} (\xi_q(z' - c_q))\rho_b dV \\
&- g \iiint_{V_{b,r(q)}} (-\xi_q(z' - c_q))\rho_b dV
\end{aligned} \tag{5.9}$$

$$F_{pq}^g = (m_{l(p)} g z_{g,l(p)}^q + m_{r(q)} g z_{g,r(q)}^q - m_m g z_{g,m}^q)\xi_q \tag{5.10}$$

$$c_{pq}^g = m_m g z_{g,m}^q - (m_{l(p)} g z_{g,l(p)}^q + m_{r(q)} g z_{g,r(q)}^q) \tag{5.11}$$

where m_m denotes the mass in between the two hinges, and $z_{g,m}^q$ denotes the z-coordinate of the centre of gravity of the mass in between the two hinges, expressed relative to the position of hinge q.

The inertial terms, M_{ij}, require that the body is broken down into regions with continuous boundaries. The cross-section of each WaveTrain module is broken down into eleven regions, two on the float and nine on the tube walls. Along with the point mass, this allows expression of each M_{ij} element as a summation of these twelve volume integrals, for each module. These terms comprise at most two discontinuities due to the hinges, as with the c_{ij}^g terms. These integrals were expressed analytically in terms of the nine fundamental parameters (see Fig. 5.1) in the interests of computational efficiency.

5.2.6 Internal water columns

The WaveTrain device extracts power through the relative motion between each solid module and its internal water column, and so a linear damping force needs to be

applied between these two reference frames. In reality, the compressibility of the air between the internal free surface and the point of power extraction may introduce an added stiffness, and hence a phase difference between the water column motion and the power extraction. One way to model these effects would be to include an additional degree of freedom for each air volume, most importantly with an associated stiffness (e.g. see [56], [57]). However, since the volumes of entrained air are likely to be relatively small in the case of the WaveTrain, it is henceforth assumed that the effects on power capture would be marginal. In fact, for designs with particularly large internal water columns, their natural period may be greater than the periods of the majority of the incoming waves, which could actually increase power capture in practice [57]. Additionally, the small phase shift which may be introduced by air compressibility could in practice be mitigated by exploiting a design parameter that is related to natural frequency - e.g. the module inclination angle could be slightly reduced to counteract the reduction in natural period caused by the additional stiffness. In any case, the effects of air compressibility are not considered further in this work.

By adding an extra patch to the mesh of each WaveTrain module on the internal free surface, generalised modes can then be used to define various types of motion of this surface (see [47] for more details, [28] also contains an example of this method used to model a body with a moonpool). By treating each of these patches as a massless 'lid', damping can then easily be applied to the relative motion of the water column. Since the water column width is small compared to the wavelength of incoming waves for the designs considered in this study, just a single, translational 'piston' mode defined over each lid is sufficient (Eq. 5.12). Even if there were small distortions of the internal free surface that cannot be accounted for by the piston mode, it is expected that the power would not be greatly affected since it is dependent on the motion of the entire internal free surface.

$$\mathbf{S}_i^{lid}(\mathbf{x}) = \begin{bmatrix} cos(\theta) \\ 0 \\ sin(\theta) \end{bmatrix} \text{ for } \mathbf{x} \in S_i^{lid} \tag{5.12}$$

where $\mathbf{S}_i^{lid}$ denotes the shape function of lid i, defined over its surface, S_i^{lid}.

Because of their massless nature, these generalised modes make no contribution to the inertial or gravitational restoring matrices.

As alluded to in Section 4.1, particularly when translational motions are involved, it can be useful to consider whether the system is more conveniently modelled with the rigid body modes within WAMIT 'locked' or 'free'. The WaveTrain extracts power through the relative motion of the internal water column with respect to the module body, by way of an 'on-board' PTO system (a pneumatic turbine such as a Wells turbine). Thus, maintaining 'free' rigid body modes defined over the entire device allows provision of just a single damping coefficient associated with the generalised 'lid' mode. In this way, the relative motion is damped, by imparting equal and opposite forces on the water column surface and the surrounding module. However, if the rigid body modes were redefined over just the solid body panels (in WAMIT, by locking the rigid body modes and defining new generalised modes), damping the relative water column motion would require additional damping coefficients. Nonetheless, other types of device, whose power is extracted via a seabed-mounted PTO system, may benefit from this model formulation (see Appendix E for more details).

5.2.7 Irregular frequency removal

Spurious irregular frequency effects can be removed by extending the set of integral equations to include the interior free surface [58]. This option is employed in WAMIT and necessitates adding extra patches on the interior free surface of each float, whose surface normal orientation must be defined oppositely to that of the massless 'lid' patches used in modelling each internal water column. An example of the complete form of the mesh, comprising all patches, is given in Fig. 5.4. Note that the symmetry of the device is also exploited to reduce runtime, thus only half the device is shown.

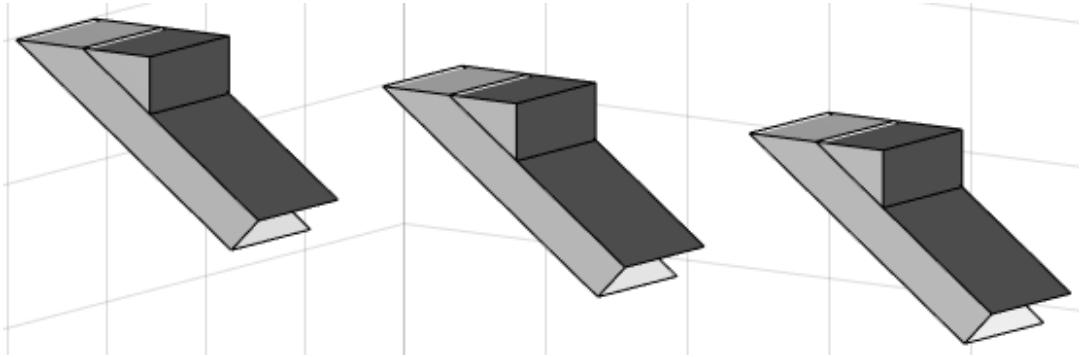

Figure 5.4: Example mesh used for input to WAMIT.

5.2.8 Verification of modelling approach

The computation of the inertial and gravitational properties in particular are not straightforward for complex body configurations such as the WaveTrain. Since a time-domain model is more easily constructed (see Section 3.6), it is useful in verifying the frequency-domain approach that uses generalised modes for the joints. The time-domain model can be solved for the body motions, using small incident wave amplitudes to ensure dynamics are within the linear regime. Given enough settling time to reach a steady state, the Response Amplitude Operators (RAOs) can then be extracted from the time series, to facilitate comparison between the two methods.

Figure 5.5 shows a good match between the magnitudes of the undamped Response Amplitude Operators (RAOs) derived from both modelling approaches, for the three lids and four hinges of a prototype WaveTrain design. Note that the RAOs are particularly unrealistic for the massless water column lids when undamped.

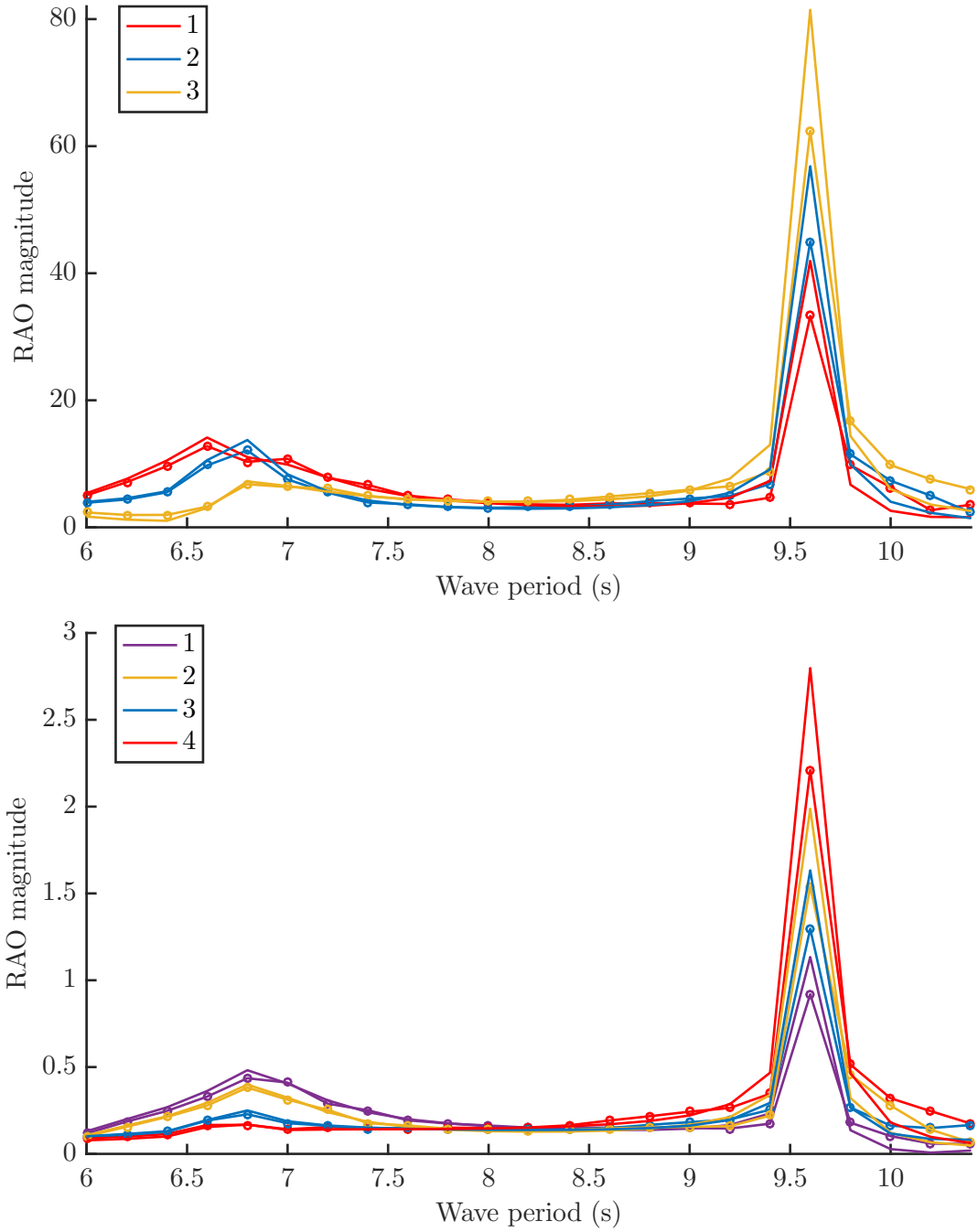

Figure 5.5: Verification of the modelling approach (upper plot: lids; lower plot: hinges). Solid lines with circles: time-domain approach. Solid lines: frequency-domain approach using generalised modes. Lids and hinges are numbered left to right from the perspective of Fig. 1.2. The RAO magnitudes of the lower plot are measured in radians per metre of incident wave amplitude.

5.3 Development of single-objective optimisation routines

A genetic algorithm is used to optimise the power extraction of the WaveTrain with respect to 6 geometric variables (θ, W, D, L_f, W_f, L) and 2 densities (ρ_t, ρ_f) (Fig. 5.1), in addition to the linear PTO parameters. The tube wall thickness, t, is held constant. The objective function is based on the hydrodynamic model introduced in Section 5.2, and is used to compute the yearly mean power extraction in a West Shetland Shelf wave climate (see Appendix G). In order to reduce the number of optimisation variables involved in the outer loop of the GA, an inner optimisation loop is used to compute the optimal PTO parameters for each candidate design specified by the other eight variables.

5.3.1 Ensuring physically feasible designs

If supplemented with bounds on the optimisation parameters, the seven physical constraints applying to a single WaveTrain module (see Section 5.2.2) form a closed section of parameter space from which candidate designs must be selected, during the optimisation process. The equality (Eq. 5.1) warrants the most attention and should be solved for directly to ensure the equilibrium inclination angle of any physical incarnation would be as intended. (The inequalities are more flexible, and are dealt with using a trial-and-error method of replacement - see Section 5.3.3.) The point mass can be used to this effect by adjusting the locations of the centre of gravity and centre of buoyancy.

The centre of gravity is the combined centre of mass of the float, tube and point mass. Quantifying the dependence of the centre of buoyancy on the point mass also requires knowledge of the volume distribution of the module, which is discontinuous as a function of height. Also bearing in mind the restrictions on waterline position, it is therefore useful to split the module cross-section into two zones, in each of which this volume function is continuous. This will yield a separate version of equation 5.1 for each zone. Zone 1 spans the waterline locations that intersect the vertical float

face. Zone 2 spans the regions between the top of zone 1 and below the maximum waterline height (Fig. 5.2).

In determining how x_b depends on the mass of the point mass, m_{pm}, it is useful to notice that x_b depends on the waterline height, h (defined from the lowest part of the module), which in turn depends on m_{pm}. Equating the displaced water mass with the total module mass (Archimedes' principle), h can be determined as a function of m_{pm} for each zone, i (Eqs. 5.14, 5.16). By substituting the upper and lower limits of h into these relations, the bounds for each zone can be reexpressed in terms of m_{pm} (Eq. 5.13).

$$m^i_{pm_{LB}} \leq m_{pm} \leq m^i_{pm_{UB}} \tag{5.13}$$

This then allows equation 5.1 to be expressed (for each zone) as a function of a single variable, and solved for m_{pm}.

For zone 1, this gives a fifth order polynomial equation in h, and a second order equation relating m_{pm} to h (Eqs. 5.14, 5.15). Equation 5.15 can then be solved numerically, and its solution substituted into Eq. 5.14 to obtain the m_{pm} that solves the constraint expressed by Eq. 5.1, should one exist. Only solutions that also fall within one of the pairs of zone boundaries (Eq. 5.13) are taken to represent physical solutions. For many parameter sets there will exist no physical solutions in either zone.

$$m_{pm} = A_1 h^2 + A_2 h + A_3 \tag{5.14}$$

$$B_1 h^5 + B_2 h^4 + B_3 h^3 + B_4 h^2 + B_5 h + B_6 = 0 \tag{5.15}$$

The corresponding two equations for zone 2 are of lower order (Eqs. 5.16, 5.17), due to the differing module cross-section shapes in each region - zone 1 includes a triangular element, zone 2 does not. These can be solved in a similar manner to equations 5.14 and 5.15.

$$m_{pm} = C_1 h + C_2 \tag{5.16}$$

$$D_1 h^3 + D_2 h^2 + D_3 h + D_4 = 0 \tag{5.17}$$

The constant coefficients of these polynomial equations are functions of the nine fundamental geometric and density parameters that are known for a given device (see Fig. 5.1).

5.3.2 Inner optimisation loop

It is assumed that only damping, and not stiffness, provision is feasible by each pneumatic PTO, and only the three diagonal damping matrix elements are considered (i.e. there is no cross-coupling control between the three PTOs). Similar to the approach used by McCabe [6], the damping coefficients are optimised for power extraction at the energy period, ω_e, of each sea state, giving 14 sets of 3 coefficients. (This is because the energy period is virtually independent of the significant wave height, and each sea state corresponds to 1 of 14 mean wave periods.)

Optimising the damping coefficients in an inner loop serves at least three purposes. Firstly, because the dependence of the power on these variables is likely to be convex (at least for single-frequency power), vast computational expense can be saved by reducing the number of variables involved in the main loop of the genetic algorithm. Secondly, the performance of each design is maximised with respect to these variables (with the caveat of being optimised for regular waves of period equal to the energy period of each sea state). This enables a fair comparison between encountered designs, regardless of which generation they were encountered in. Thirdly, the effect of the eight geometric and mass-related variables can be more clearly separated, in the context of the GA performance.

Since it is assumed that the PTO systems cannot provide stiffness, complex conjugate control is not applicable. However, it is an interesting problem as to whether the optimal damping coefficients can be obtained analytically, in terms of the fundamental system characteristics (the elements X_i, M_{ij}, A_{ij}, B_{ij}, c_{ij} and c^g_{ij}). It is relatively simple to find the optimal damping coefficient for a bottom-fixed Oscillating Water Column (OWC) device with just a single degree of freedom ([59], p.192), but the problem is complicated by the presence of other degrees of freedom, and by

additional PTO systems. Even without cross-coupling (off-diagonal) PTO damping coefficients, the problem is still complicated by the hydrodynamic, hydrostatic and mechanical coupling between the degrees of freedom of the device. A further analysis of this problem is given in Appendix F, but the key finding is that it is only possible to solve for the optimal damping coefficient if power is extracted only via one mode of motion. For systems with greater numbers of PTO systems, such as the WaveTrain, attempting analytical optimisation results in polynomial equations of high degree, which may in theory be numerically soluble with acceptable computational effort, but would likely require extensive work to derive the coefficients. Therefore, in order to find the water column surface damping coefficients that provide the optimal power, a gradient-based numerical solver is used.

Whilst allowing different values within each trio of damping coefficients can result in higher powers at the energy period, lower powers often result at nearby wave periods, as the device becomes too specifically tuned. Since each trio of damping coefficients is used to generate the body response in all 98 wave periods in order to compute the annual mean power, the three coefficients are instead set to always be of the same value as one another.

5.3.3 Outer optimisation loop

A genetic algorithm (GA) is a metaheuristic optimisation technique, especially suited to problems involving analytically-intractable relationships between the *optimisation variables* and the *objective function(s)*. Initially, a *generation* of randomly chosen *individuals* is tested (i.e. their objective functions are evaluated), but subsequent stages of learning about the better- and worse-performing regions of the parameter space help to then direct the search more strategically through the later generations. Based on evolutionary principles from the natural world, a GA must comprise two key components: *heritable genetic variation* and *differential reproductive success*. More explicitly, the implications of these two terms are as follows. The identity of a given individual must be completely encoded within its 'genetic code', a list of the defining values of

the optimisation variables. As in the natural world, where the phenotypic expression (observable characteristics) of the genetic code is also dependent on environmental interactions, the objective function defines how the genetic code translates into 'performance' of the given individual. It is this 'performance' (in the natural world, analogous to the aspects of the phenotypic expression relating to sexual selection) that governs that individual's chances of successfully 'reproducing'. 'Higher-performing' individuals more successfully reproduce than their 'lower-performing' counterparts. The act of 'reproduction' then enables the inheritance of 'phenotypic characteristics' by members of the subsequent generation, through their 'genetic code'. In the context of a genetic algorithm, this could occur as a random selection of variables from each of two 'parent' individuals, in order to create the 'offspring'. Finally, the entire evolutionary process must maintain variety amongst the individuals of each population, commonly implemented by randomly 'mutating' individuals as part of the process of reproduction (i.e. transferring from one generation to the next). In the context of the WaveTrain device, an 'individual' is defined by a particular set of the design variables, and the 'phenotypic expression', by which the level of 'reproductive success' is determined, corresponds to the objective function(s) - in the current section of this chapter, just the annual mean power extraction in the West Shetland Shelf wave climate.

For an accessible introduction to genetic algorithms and their range of application, see [60].

A single-objective GA developed at the University of Sheffield [61], augmented with extra adaptations to handle the constraints, forms the basic structure of the outer optimisation loop. Since all feasible individuals must satisfy Eqs. 5.1 - 5.5, the majority of which are nonlinear functions of the optimisation variables, a trial-and-error approach is taken to impose these as hard boundaries on the search space. The implementation of this is simpler with the initial population than for subsequent generations.

Initially, a population is generated at random and each individual is screened to check for violation of the physical constraints. Those that pass are retained, and those

that fail are discarded. The process is then repeated, each time attempting to generate feasible individuals in place of the discarded ones, until all are feasible. Evaluation of the objective functions for this initial population then follows in the usual manner.

In setting up each subsequent generation, a breeding stage takes place, consisting of three processes - selection, crossover and mutation. On the first run-through, the three processes are carried out as usual, first selecting the parents fit enough to reproduce, then crossing over pairs of these chromosomes to create new individuals, to whom random mutations are then applied. Some combination of repeated stages of selection, crossover and mutation is then required to replace the infeasible individuals with feasible ones. In order to allow efficient rectification of individuals close to the boundary of the feasible design space, up to five further mutations are first applied. Individuals that are then still infeasible are likely to lie further from the feasible space, so in those cases, the crossover process is repeated, followed by the same repeated mutation procedure. Since each parent is feasible by definition of the previous generation, this is a much more efficient approach for individuals resistant to the repeated mutation procedure. Because the same parents are used for the repeated applications of the crossover process, the method is still based on the same selection procedure of the original algorithm.

Figure 5.6 gives an overview of the full optimisation process.

5.3.4 Objective function - power-based

Superpositions of the motion responses for each of the internal water column lids are used to estimate the power extraction in each sea state, based on the method used by McCabe [6], which calculated the mean annual power production of WEC shapes in the West Shetland Shelf wave climate, subject to motion and power constraints.

5.3.4.1 Wave climate

The wave climate is for the same West Shetland Shelf site used by McCabe [6], and is located around 40km west of the Shetland Islands. Each (unidirectional) sea state within the climate is described by a spectral density function, $S(\omega_k)$, defined by the

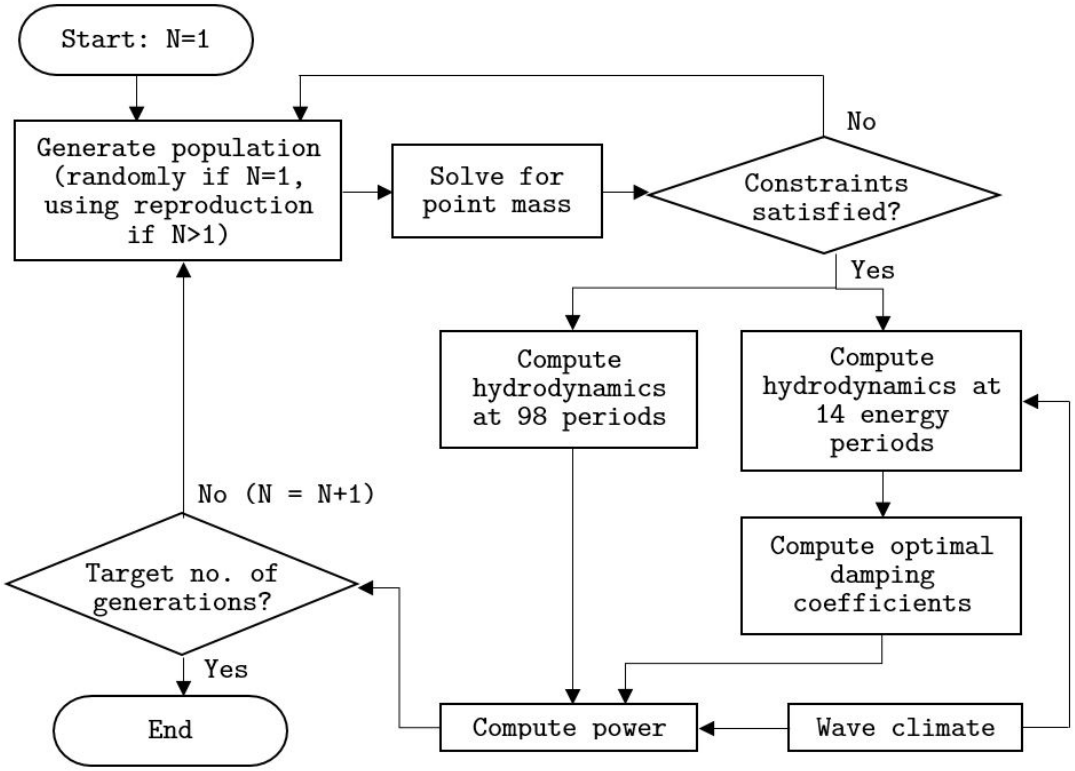

Figure 5.6: Outline of the structure of the full optimisation process. N is the generation number.

mid-point values of the significant wave heights and mean zero-crossing periods within the occurrence matrix (see Appendix G). The spectral density function is based on a modified Pierson-Moskowitz wave spectrum, given by Eq. 5.18 ([62], p. 24).

$$S(\omega_k) = \frac{0.11}{2\pi} H_{m0}^2 T_z \big(\frac{\omega_k T_z}{2\pi}\big)^{-5} exp\Big[-0.44\big(\frac{\omega_k T_z}{2\pi}\big)^{-4}\Big] \tag{5.18}$$

The wave amplitudes of the frequency components within the spectrum are given by Eq. 5.19.

$$\alpha(\omega_k)^2 = 2S(\omega_k)\Delta\omega_k \tag{5.19}$$

In order to construct the irregular wave profiles, a random phase, ψ_k, is assigned to each frequency component, ω_k, for each of the 173 sea states. Ten sets of these random phases enable the construction of ten incident wave and body response time series, over which the power can later be averaged. The incident irregular wave profile

of a given sea state, for one of the ten sets of random phases, q, is given by the superposition of wave profiles over all K frequencies.

$$\eta_q(t) = \sum_{k=1}^{K} \alpha(\omega_k) cos(\omega_k t + \psi_{k,q}) \tag{5.20}$$

5.3.4.2 Body response

The response of the body, $x_{j,q}(t)$, in a particular degree of freedom, j, with a set of random phases denoted by q, is related to the irregular incident wave profile by the response amplitude operators (Eqs. 5.22, 5.23). These are obtained from the equations of motion for each frequency (Eq. 5.21). (Note, C_{ij} includes both buoyancy and gravitational restoring contributions.)

$$\sum_{j=1}^{N} [-\omega_k^2 (M_{ij} + A_{ij}) + \mathrm{i}\omega_k (B_{ij} + B_{ij}^{pto}) + C_{ij}]\xi_j = X_i \tag{5.21}$$

$$\chi_j(\omega_k) = \alpha(\omega_k)\xi_j(\omega_k) \tag{5.22}$$

$$x_{j,q}(t) = \sum_{k=1}^{K} |\chi_j(\omega_k)| cos(\omega_k t + \psi_{k,q} + \angle\chi_j(\omega_k)) \tag{5.23}$$

5.3.4.3 Motion cap

A motion cap is used to truncate the time series, based on practical considerations of the internal free surface for a given design candidate. The shorter of the distances from the surface to either end of the tube (in the equilibrium configuration) is used as the upper limit on the relative water column position (Fig. 5.7 and Eqs. 5.24, 5.25 and 5.26).

$$X_1 = h/sin(\theta) - W/tan(\theta) \tag{5.24}$$

$$X_2 = L - h/sin(\theta) \tag{5.25}$$

$$X_{cap} = \min(X_1, X_2) \tag{5.26}$$

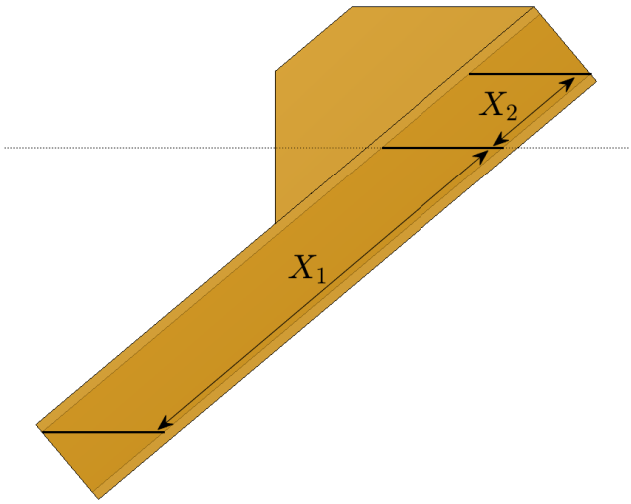

Figure 5.7: Definition of the motion cap.

5.3.4.4 Mean annual power extraction

Given the absence of cross-coupling components within the PTO damping matrix and that the three non-zero elements are equal to one another, the instantaneous power extracted by the relative motion of water column (or 'lid'), j, is given by Eq. 5.27.

$$P_{j,q}(t) = \begin{cases} B_{pto}(\omega_e)\left(\dot{x}_{j,q}(t)\right)^2 & \text{for } |x_{j,q}(t)| \leq X_{cap} \\ \\ 0 & \text{otherwise} \end{cases} \tag{5.27}$$

Since the optimisation variables allow a range of device sizes and shapes in this study, any cap on instantaneous power capture must fairly represent the complex decision making process that would lead to the determination of rated power for each design's PTO system. Given also that different modes (or types) of resonance may govern different design candidates - i.e. it is not necessarily just a case of scaling the rated power with the scale of the device - this study uses no power cap so as to avoid introducing additional bias.

For each time series of the instantaneous power, the average power is obtained by

integrating over the total duration of 314s (Eq. 5.28).

$$\bar{P}(H_{m0}, T_z, j, q) = \frac{1}{314} \int_{t=0}^{t=314} P_{j,q}(t) dt \tag{5.28}$$

Averaging over the ten sets of random phases and summing the power extracted by each of the three water column 'lids', gives the mean power extracted by the WaveTrain device in a given sea state (Eq. 5.29).

$$\bar{P}(H_{m0}, T_z) = \sum_{j=1}^{3} \frac{1}{10} \sum_{q=1}^{10} \bar{P}(H_{m0}, T_z, j, q) \tag{5.29}$$

Weighting the power in each sea state by its annual occurrence gives the mean annual power (Eq. 5.30).

$$\bar{P} = \frac{1}{|\hat{O}(H_{m0}, T_z)|} \sum_{H_{m0}} \sum_{T_z} \hat{O}(H_{m0}, T_z) \bar{P}(H_{m0}, T_z) \tag{5.30}$$

The mean annual power, $\bar{P}$, is the objective function used in the single-objective genetic algorithm.

5.3.4.5 Computational notes

The genetic algorithm relies upon the numerical solution of the hydrodynamic problem concerning the interaction between the waves and the wave energy converter, for each candidate design. In order to most thoroughly search the parameter space with minimal compromise, the efficiency in all aspects of the model should be maximised. Since the solution for the radiation potentials and the integration of the power time series dominate the computational resources, all drivers of complexity in these areas should be heavily scrutinised.

The smallest timestep is required in the sea states with smallest T_z, since they contain the most significant contributions of the smallest wavelength components. Plotting a sample time series of the motions associated with a water column surface in the sea state of lowest T_z reveals that an integration timestep as large as 1s is sufficient (Fig. 5.8). In fact, a 1s timestep may even be conservative, given both the infrequent occurrence of these sea states, and the fact that the majority of devices

assessed by the GA will be tuned towards sea states in which much larger wavelengths dominate. Hence, sea states containing the very shortest wavelengths likely do not make a significant contribution to the extracted power for most designs anyway.

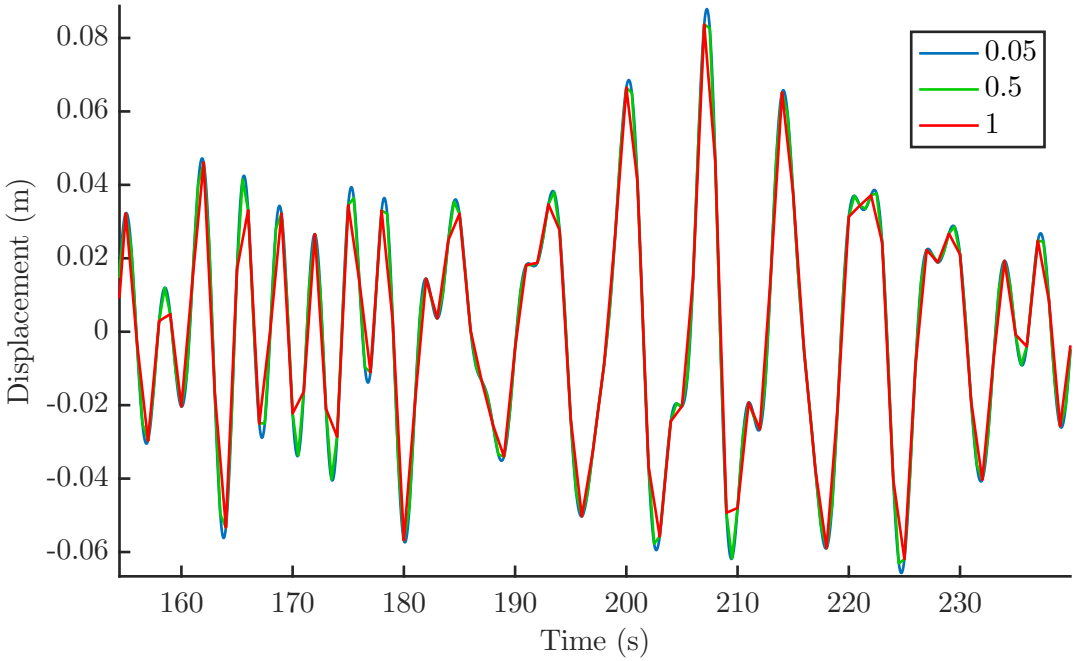

Figure 5.8: Sample time series of the water column response in a sea state with $T_z = 4.5$s, generated using the spectrum defined by Eq. 5.18, for various sizes of timestep, ΔT, measured in seconds.

The radiation and diffraction potentials should only be solved at wave periods that contribute significantly to the power generation. In particular, ensuring that the higher end of the frequency range makes significant contributions to the power is essential, as the shortest wavelengths necessitate the smallest patch subdivisions and increase the required computational effort. By plotting the spectral density functions for the highest and lowest T_z values encountered in the West Shetland Shelf wave climate, it becomes evident that angular frequencies above 2.12rads^{-1} and below 0.18rads^{-1} contribute minimally to the irregular wave profiles (Fig. 5.9). In order to determine these bounds, an arbitrary cut-off of $S_\omega = 0.005$ has been used, but this is still thought to be conservative. For the same reasons given above for the integration timestep, this

could likely be further narrowed without any degradation of accuracy in the power calculation.

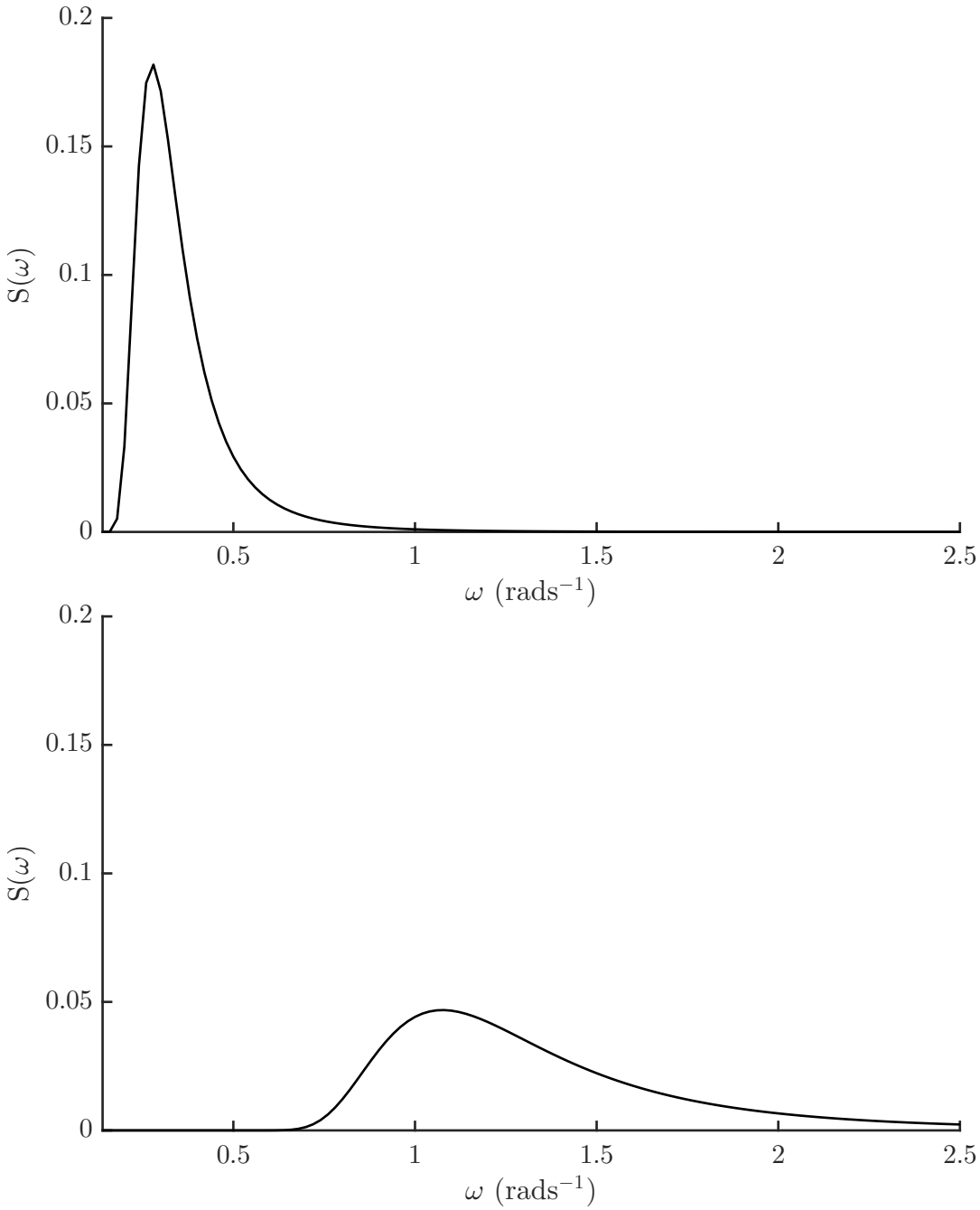

Figure 5.9: Wave spectrum defined by Eq. 5.18, for $T_z = 17.5$s (top) and $T_z = 4.5$s (bottom).

However, the integration timestep of 1s and angular frequency range of 0.18 –

2.12rads^{-1} (in increments of 0.02rads^{-1}) results in a manageable runtime for this application.

5.3.5 Variable bounds

The bounds on the optimisation variables (Table 5.1) are chosen to encompass a wide range of possible designs, whilst only allowing values that can lead to physically feasible designs. The tube wall thickness is set to 0.075m. Whilst the structural integrity of the longest modules with this thickness is perhaps questionable, it is believed that this value is at least in the correct ballpark. As with the other variables used in this study, it is accepted that adaptations would be required for a practical implementation, but that the optimisation study results can act strongly as a guide. Additionally, the tube wall density can always be reinterpreted as the product of the tube wall density and the wall thickness, so that the tube mass is preserved. Regardless of the exact thickness required for structural soundness in practice, it is almost certain that the tube walls will be thin enough for the hydrodynamic properties of their thickness to be dwarfed by those of their length.

Variable	Lower bound	Upper bound	Units
θ	20	60	$^\circ$
W	3.5	25	m
D	3.5	30	m
L	50	150	m
L_f	13	90	m
W_f	1.75	35	m
ρ_t	1000	6500	kgm^{-3}
ρ_f	50	900	kgm^{-3}

Table 5.1: Variable ranges used for the single-objective genetic algorithm runs.

The bounds on L and θ allow for a wide range of module spacings. Since the majority of the tube length L will be submerged, the position of the hinge on the underside of the tube will be situated perhaps around three-quarters of the way along towards the upper end of the tube. With this in mind, and considering that resonant behaviour will occur at least near to the case where the modules are separated by

half a wavelength (i.e. in anti-phase with one another), the linear dispersion relation for deep water ($\lambda = gT^2/2\pi$) can be used to conclude that the bounds are suitable. Under these assumptions, $L = 150$m and $\theta = 60°$ give a resonant period of 17s, and $L = 50$m and $\theta = 20°$ a period of 7.1s. Given the climate's occurrence matrix and the fact that the other variables may be able to extend this range, these ranges are deemed to permit a wide enough range of designs.

The lower bounds on W and D are informed by the tube thickness limits, discussed in Section 5.2.4. The tube density lower bound deliberately lies significantly below what is thought to be currently manufacturable at reasonable cost, in order to allow for the possibility of novel materials that may be developed in the coming years. The upper limit of W remains small enough that no significant distortion of the free surface within the tubes is expected. Finally, variable ranges that only allow for a negligible quantity of feasible designs should be avoided. Justification of the parameter bounds selected on that basis is given in Section 5.6.

5.4 Development of multi-objective optimisation routines

In practice, the power extraction is also dependent on the availability of the device, which itself has many drivers, including weather conditions, structural health, network connectivity, amongst others. In particular, the connecting joints provide a potential vulnerability, which may somewhat offset the benefits provided through the increased power-extracting capability. If the joints are too prone to failure, less power would be extracted. This section aims to address this concern by extending the analysis to include an extra objective function, based on the cyclic loadings at the joints during operation.

5.4.1 Multi-objective genetic algorithms

5.4.1.1 Managing conflicting objectives

The most straightforward way to handle multiple objectives is to combine them into a single objective function, to which an algorithm akin to the one introduced in Section

5.3.3 can then be applied. However, this relies on knowledge of the relative importance of the two objectives, or on the two objectives aligning with one another so that optimising one automatically optimises the other. In cases with conflicting objective functions, even if the conflict is well-understood, choosing the relative weightings attached to each objective function can lead to a solution that is too specific. In order to defer the decision of the relative importance of the two objectives, the Pareto front can be sought - a continuum of the optimal solutions for all possible sets of weightings. Whilst this could be investigated with multiple runs of a single-objective genetic algorithm (SOGA), a well-configured multi-objective genetic algorithm (MOGA) has the potential to more efficiently obtain an accurate approximation of the Pareto front.

5.4.1.2 Exploring the Pareto front

The main differences between single-objective GAs and multi-objective GAs are the fitness functions, and the need to maintain diversity in a MOGA. In a SOGA, the solutions can easily be ranked by their objective function values. This is not applicable to a MOGA, but analogous ranking-based procedures can be formulated to similar effect. For example, non-domination sorting involves assigning a rank to each individual, based on how many other individuals it is outperformed by on *all* objective functions. This results in groups of individuals with different ranks (the current approximation to the Pareto front is defined by the individuals of rank 1), but extensions to this approach may also assign different ranks within each non-dominated front, linking with the concept of maintaining diversity. There are many alternative approaches, including weighted sum approaches or even changing objective functions (for more information, see [63]).

In a MOGA, since multiple optimal solutions are sought, the algorithm requires some additional incentive to maintain evenly and widely spaced individuals in the Pareto subset. Without this, the population tends to cluster around a small number of points. Again, many possible approaches exist (see [63]). For example, fitness sharing can enforce penalisation of individuals in densely populated regions (of the Pareto

front or the parameter space), reducing the likelihood that any one of those individuals will be selected to reproduce, therefore balancing the likelihood of reproducing between densely and sparsely populated regions. This concept could also link with the choice of fitness function and ranking procedure. As another example, crowding distance approaches attach to each individual a measure of the distance of the nearest neighbours within the best-known Pareto front. This 'crowding parameter' is then used to influence the selection or reproduction processes in a diversity-maintaining fashion. For example, the algorithm NSGA-II [64] uses this measure of crowding as a tie-breaker in its selection technique, essentially providing a way to bias the selection process more in favour of individuals with a lower surrounding population density.

As with SOGAs, there are many more options to configure within a MOGA, such as elitism, crossover algorithms, selection algorithms, etc., and finding the optimal optimisation routine set-up for particular problems constitutes an entire field of research in itself. Konak et al. [63] give a more widely accessible overview of the approaches used within multi-objective genetic algorithms.

NSGA-II [64] is an algorithm with a fast non-dominated sorting approach, and is widely regarded as an efficient and versatile multi-objective optimisation algorithm. In this light, NSGA-II constitutes the basis of a bespoke MOGA, used for optimising the WaveTrain concept.

5.4.1.3 Application to the WaveTrain

As with the single-objective algorithm, the same trial-and-error method from Section 5.3.3 is required to enforce the physical constraints, replacing the constraint handling facilities of NSGA-II. This necessitates the separation of the crossover and mutation stages, from the default configuration of NSGA-II. Additionally, the crossover function used by NSGA-II (Simulated Binary Crossover) uses two parents to produce two offspring [65]. Due to the nature of the trial-and-error method used to find feasible WaveTrain individuals (see Section 5.3.3), an even number of parents cannot always be

assured. Hence the MOGA used in the present work is adapted to allow any number of parents - if odd, the final parent is simply cloned to create the final child.

5.4.2 Objective function - force-based

5.4.2.1 Establishing a method

Focusing on just physical mechanisms, a wave energy device could fail through repeated cyclic loading on the structure, or through a single extreme event causing failure through a lack of mechanical strength. Of course in the latter case, the specific survival strategy employed will also affect the likelihood of failure, and in some cases may reduce the chances so that the dominant failure mode is by far the repeated cyclic loading under normal operational conditions. Since WECs are designed to resonate under commonly occurring wave conditions, fatigue loading can be particularly pertinent when considering structural design, etc. Wave Energy Scotland suggests that both modes of failure are important for consideration for generic hinged barge-type devices (p. 65, [66]). Although the WaveTrain does not fit completely in this category, it is expected that similar loadings will affect the structure, and particularly through the cyclic loading on the rotational joints. Assuming that a suitable survival strategy can be devised to reduce the loading in extreme sea conditions (perhaps utilising internal chambers to reduce the buoyancy and submerge the device), operational cyclic loads may be the dominant cause of failures. Given that the weak points on the device are likely to be the rotational joints, the shear forces acting at these locations should be analysed.

In practice, the fatigue life of a structure can depend on the frequency of its cyclic loading. However, under conditions where neither high temperatures nor high levels of corrosion are encountered, stress cycling can be taken as frequency-independent (p. 294, [67]). Assuming the WEC is relatively resistant to corrosion, this holds true for a wave energy converter, given the surrounding body of water and the low frequencies of oscillation.

Rainflow counting is an established method with which to find the number of stress cycles of each stress magnitude from a given irregular time series, enabling use of the Palmgren-Miner relation (Eq. 5.31) to assess the fatigue life. However, in order to absolutely quantify the expected lifetime, either the total number of cycles to failure, N_i, must be known for each frequency component, or the intercept of the corresponding S-N curve must be known. (An S-N curve gives the number of cycles required for failure, at each stress value) Both of these quantities require empirical determination. To the author's knowledge, no formal guidance is currently available with regards to these empirical factors in the context of WECs.

$$G = \sum_i \frac{n_i}{N_i} = \frac{1}{\bar{a}} \sum_i n_i (\sigma_i)^m \tag{5.31}$$

Wave Energy Scotland [66] performs a fatigue analysis on a two-body heaving point absorber to highlight the difficulty in performing a fatigue analysis without any specific practical data. In this case, the fatigue life is predicted using empirical factors that assume the connection between the mooring line and spar to be analogous to a category W3 welded joint, that carries the load perpendicularly to the weld line (pp. 99-100, [66]). Of course, this is a crude approximation but it allows a representation of the fatigue life in absolute terms. Cases with and without cathodic protection are analysed, and lead to wildly different estimates of the fatigue life - 149 and 1200 years.

In the absence of empirical stress cycling data specific to the WaveTrain device, a measure of the total damage across a range of encountered frequencies can still be obtained, using the time-series of the loadings and the exponent representing the slope of the S-N curve, m (Eq. 5.32). Whilst the empirical factors would be required to obtain an absolute measure of the damage in terms of the device's lifetime, this method still allows a determination of the ranking order of different designs in terms of the accumulated fatigue damage. It is assumed that for all devices tested during the optimisation process, the same joints are employed. This means that the stresses, σ_i, can be replaced by forces, F_i (Eq. 5.32). In practice, more robust joints may be used for designs that would be likely to incur higher amounts of fatigue damage, so

this measure can be alternatively viewed as the costliness resulting from the cyclic loadings on the joints.

$$G = \sum_{i=1}^{K} F_i^m n_i \tag{5.32}$$

The exponent, m, is advised to be very similar for a range of design cases [68]. For all types of listed weld joint undergoing cyclic loading in seawater, with some form of cathodic protection, and a high number of cycles ($> 10^6$), the exponent is given as $m = 5$ (p.19, [68]). A constant wave period of 10s would result in 6.3 x 10^7 cycles over the course of 20 years, meaning a wave energy device almost certainly falls under the category of 'high cycle'. It seem also a reasonable assumption that the loading on a rigid, welded joint is likely to be similar to the loading in the degrees of freedom not allowed by the WaveTrain joints.

Given $m = 5$, F_i and n_i can be obtained from the time series, whose construction is detailed next, along with the computation of the objective function.

5.4.2.2 Implementation

The method involving generalised modes described in Section 3.4 is used to obtain the forces acting at the hinges for each of the 98 wave periods. There are four hinges in the WaveTrain device, yet because the struts are modelled as massless and not hydrodynamically interacting, each pair at either end of a strut experience the same loadings. Hence the shear forces are only analysed at one hinge of each strut. Since only in-plane dynamics are modelled, only the vertical and in-plane horizontal shear forces are analysed, using the first and third shape functions of those defined in Eq. 4.11. Following the method described in Sections 3.4 and 4.4, the complex amplitudes of the shear forces are computed (for each frequency) using Eq. 3.33.

The time-series of each of the four types of shear force are generated in much the same way as with the body motions, using the force RAOs with the frequency component wave amplitudes to synthesise the force responses in an irregular sea, expressed as a superposition of regular wave responses (Eqs. 5.33 and 5.34). Again,

ten time series are generated in each of the 173 sea states, using different sets of random phases.

$$\widetilde{\chi}_j(\omega_k) = \alpha(\omega_k)\widetilde{\xi}_j(\omega_k) \tag{5.33}$$

$$\widetilde{x}_{j,q}(t) = \sum_{k=1}^{K} |\widetilde{\chi}_j(\omega_k)| cos(\omega_k t + \psi_{k,q} + \angle\widetilde{\chi}_j(\omega_k)) \tag{5.34}$$

A rainflow counting algorithm [69] is used to convert each time series to a set of stress cycles of particular stress magnitudes. The measure of 'damage' (relating to the predicted lifespan of the device, or how costly repairs or structural reinforcement would be) of each generalised force mode, $\widetilde{j}$, can then be computed using Eq. 5.32, for each 314s time series. For each sea state, the damage can then be averaged over the ten sets of random phases (Eq. 5.35).

$$\bar{G}_{\widetilde{j}}(H_{m0}, T_z) = \frac{1}{10}\sum_{q=1}^{10} G(H_{m0}, T_z, \widetilde{j}, q) \tag{5.35}$$

Weighting the measure of damage in each sea state by its annual occurrence gives an indication of the mean amount of damage incurred in a 314s time period, based on a yearly description of the wave climate (Eq. 5.36). This could easily be scaled to a measure of damage endured through a time period of one year, but that is irrelevant without any conversion to absolute lifespan.

$$\bar{G}_{\widetilde{j}} = \frac{1}{|\hat{O}(H_{m0}, T_z)|}\sum_{H_{m0}}\sum_{T_z} \hat{O}(H_{m0}, T_z)\bar{G}(H_{m0}, T_z) \tag{5.36}$$

Averaging over the four 'fixed' generalised modes gives the second objective function - a total measure of the damage endured by a single WaveTrain design over a fixed period of time (Eq. 5.37). (Strictly, a summation would be more appropriate if an absolute lifetime were to be calculated, but taking the mean achieves the same effect here.)

$$\bar{G} = \frac{1}{4}\sum_{\widetilde{j}=1}^{4} \bar{G}_{\widetilde{j}} \tag{5.37}$$

5.5 Model accuracy and testing philosophy

Of much greater concern than the comprehensiveness of the GA search is the accuracy of the hydrodynamic models, which are used to compute the performance of each design candidate. Whilst the numerical method can enable an efficient assessment of many design candidates, there are other associated problems which must be mitigated by the optimisation algorithm in order to obtain sufficiently accurate outputs. These are manifested in two ways.

Firstly, the numerical solvers employed by WAMIT may be deemed to have failed to converge. The complex geometry of the WaveTrain device and the accompanying interaction between the closely spaced modules make this phenomenon more likely than with simpler WEC designs. Whilst WAMIT's direct solver is the most robust option offered [28], use of the block-iterative solver provides easily accessible information on the level of convergence. Experience dictates that three blocks is most appropriate for this application. If the maximum number of iterations (of 35) is reached for more than 10 of the 98 frequencies, then the power is set to zero for that individual. Below this limit of 10, the power is set to zero at just at the unconverged frequencies. [It is known that smaller panels are needed to achieve accuracy at lower wave periods, and experience suggests these poorer convergence properties at low periods extend to the solver convergence.] In order to save on computational expenses and to ensure fewer 'zero-power' individuals in each GA generation, a preliminary check for solver convergence is carried out for each individual, at a range of frequencies biased towards lower wave periods (3, 4.5, 6, 9, 12 and 30s). If the maximum number of iterations is reached for more than one of these frequencies, the individual is removed and replaced by another, before computing the full objective function.

The second way in which numerical problems can arise is through a lack of accuracy resulting from insufficient patch subdivisions (or 'panels') and/or orders of the B-splines. In applications focussing on a single WEC design, this is often handled by performing tests of the convergence of the hydrodynamic outputs with increasing

numbers of panels (e.g. [1]). In an optimisation study where thousands of designs may be analysed, it is inefficient and impractical to adopt that approach. The rest of this section details the tools used to mitigate this difficulty, taking into account the objectives of the GA.

5.5.1 Maximising the utility of the GA

The purpose of this GA is to explore the features that lead to more optimal configurations of the WaveTrain device. Since only the best-performing designs are of interest, it is not essential that all devices tested have sufficiently accurate hydrodynamic results, just that those with inaccuracies do not skew the search enough to prevent the discovery of the optimal designs. If multiple GA runs are to be used to infer trends, then it is also not necessary that each GA run converges on a specific design, just that enough GA runs get close enough to the best designs (of which there may be many) to elucidate useful trends. In fact, if perfect knowledge of the search space were to be available, it may subsequently be discovered that these trends do not hold globally, but only for a subset of the design space. A partial and potentially incomplete solution to the optimisation problem may sound treacherous, but from an engineering standpoint, design improvement marks a success, especially given the difficulties (the treatment of which is described in this chapter) that arise due to the hydrodynamic model. Just as any candidates for improved performance should later be physically tested, so too should a further stage of optimisation be carried out, but with more emphasis on the performance of the GA, and less on the accuracy of the hydrodynamic models and size of the available search space. With this in mind, the aim of such an optimisation scheme is to strike a compromise between computational demands and the thoroughness of the search, whilst maintaining both enough accuracy of the hydrodynamic outputs used to compute the objective functions, and enough convergence of each GA run. Thus, any tools that aim to improve the model accuracy of the designs encountered through the GA searches should be computationally efficient, and should

not exclude so much of the search space that too little of it remains for a thorough investigation.

5.5.2 Tools for achieving maximal GA utility

When using the higher order method, the level of accuracy is dependent on both the number of panels and the order of the B-splines used to represent the velocity potentials. Whilst increasing the spline order from constant to linear results in greater accuracy, it is not always the case that all subsequent increases in the order will increase accuracy [70]. In fact, it is advised that quadratic B-splines are usually appropriate for relatively complex geometries [28], and so these are employed for the genetic algorithms. The panel size is set here to $0.2L$, where the proportionality to the length of the device ensures that panels are sized independently of scale.

The presence of very thin patches can worsen the accuracy of the hydrodynamic model. These arise when the waterline is just above the lower limit of either zone (see the second paragraph of Section 5.3.1 for their definitions), and can be rectified by adapting the mesh design (Fig. 5.10).

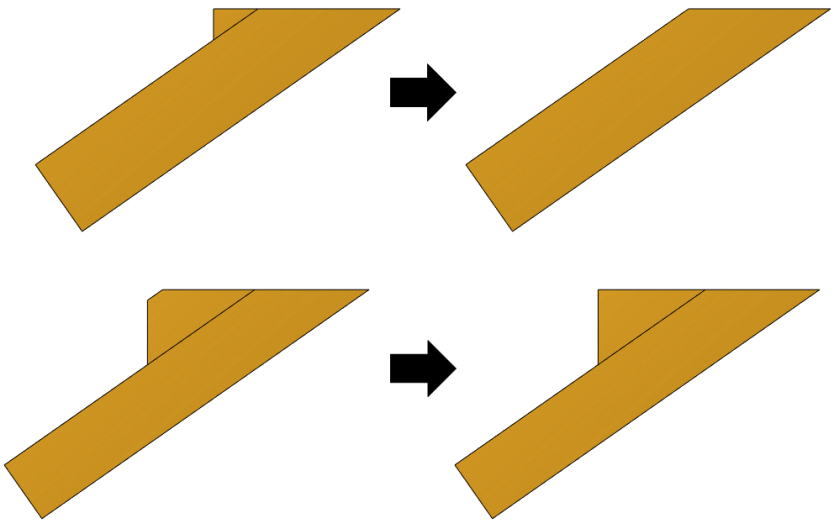

Figure 5.10: The geometry modifications applied to meshes that initially comprise a float patch deemed too thin to enable an accurate hydrodynamic analysis. Left: original meshes selected by the algorithm. Right: modified meshes.

As with the panel size, it is logical to set the threshold for thin patches proportional to L. Based on empirical observations, should the uppermost float patch have a dimension less than $L/75$, the alteration is made to the mesh. Because of the small patch dimension required to trigger this procedure, no significant impact on the hydrodynamic behaviour specified by the mesh is expected.

A spurious peak can also sometimes occur in the Response Amplitude Operators (RAOs) at high wave frequencies, due to a small wavelength to panel size ratio. Often the accuracy can be sufficient in the rest of the frequency range and so it would be wasteful to discard these designs based on this symptom. If the RAO magnitude of any of the three water column lids takes a value greater than unity for a wave frequency above 1.24rads^{-1}, this RAO magnitude is set to zero.

Whereas the previous two tools modify an existing model to remove sources of inaccuracy, a direct check is also required as a final safeguard against the proliferation of inaccurate models. Theoretically, the added mass and radiation damping matrices are symmetric, but this does not hold if an insufficient number of panels (or an inappropriate spline order) is used. Hence, by using just a single discretisation (the number of panels and the spline order), a measure of the amount of symmetry in these matrices can act as a proxy for the model accuracy. Such a metric does not need to correspond perfectly with the level of accuracy of the hydrodynamic model, but must correlate enough to ensure that a high enough fraction of sufficiently accurate models are encountered by the GA search. In this study, we consider only the added mass coefficients coupling the lid mode at the rear of the device (denoted by index 10) to: the lid mode at the front of the device, each of the four hinge modes, and the surge, heave and pitch rigid body modes (denoted by indices $i = 1 - 8$). From experience, these were some of the coefficients most likely to differ significantly from their symmetric counterparts. As with testing for solver convergence, a preliminary test over the same six test wave periods (mentioned in the first part of Section 5.5) is carried out in order to catch inaccurate designs early and at reduced computational expense (Eq. 5.38). For one of the mode pairs, at each wave period, the absolute difference

between the pair of symmetrically located (within the matrix) added mass components is divided by the maximum of the two values, to yield a percentage difference. If the two coefficients have different signs, the absolute difference is instead divided by the largest added mass value over all six wave periods. This aims to prevent very large percentages developing, that are not reflective of a large difference in the device dynamics. These percentages are then summed over the six wave periods, then over all eight mode pairs. If the resulting number exceeds a threshold (see Eq. 5.38), the candidate design is discarded, to be replaced by another.

$$\widetilde{\Psi} = \frac{1}{N_1}\sum_{i=1}^{N_1}\frac{1}{N_2}\sum_{j=1}^{N_2}\left[\frac{H(-A_{[i,10],j}A_{[10,i],j})abs(A_{[i,10],j}-A_{[10,i],j})}{\max_{j\in[1,N_2]}(A_{[i,10],j},A_{[10,i],j})} + \frac{H(A_{[i,10],j}A_{[10,i],j})abs(A_{[i,10],j}-A_{[10,i],j})}{\max(A_{[i,10],j},A_{[10,i],j})}\right] \tag{5.38}$$

$A_{[i,k],j}$ is the added mass coefficient of mode i due to mode k, at wave period j. N_2 is the number of sample wave periods (six), N_1 is the number of modes analysed (eight). $H(\cdot)$ denotes the Heaviside function.

Setting the threshold is an empirical task and is also dependent on the nature of the objective function, since this will skew the search towards certain kinds of design more than others. In this study, a threshold value of 0.17 was found to give a good compromise between the accuracy of the hydrodynamic models and the size of the available search space. Bearing in mind the discussion in Section 5.5.1, there should still be areas of the search space in which model accuracy is less than perfect. These can be addressed with more thorough convergence studies on a subset of the best performing designs (see Section 5.7). This test of added mass matrix symmetry is also applied as a further safeguard over the full range of wave periods before performing the power calculation.

5.6 Parameter space exploration

It is not straightforward to visualise the eight-dimensional search space with its feasible regions enclosed by the set of physical constraints (Eq. 5.1 - 5.5), variable bounds

(Table 5.1) and the 'computational' constraints due to the numerical solver limitations (see Section 5.5). However, the success of the genetic algorithms in searching for optimal WaveTrain designs ultimately depends on being able to traverse this search space.

In order to obtain some insight into the search space, 2000 feasible individuals were sought using the same procedure used to randomly generate the initial generation of a GA run, whilst keeping track of the further 5762 individuals that passed the physical constraints but failed the computational constraints. Since only six of these failed due to a lack of numerical solver convergence, we can draw information about the impact of the added mass symmetry check, $\widetilde{\Psi}$ (Eq. 5.38), from the total of 7762 individuals, by assessing the features of the group of 5762 relative to the group of 2000.

Each variable range is broken down into 10 sub-ranges (Table 5.2), displaying the number of designs that occupy each variable range. Whilst this does not allow direct insight into the effects of the interdependencies between the variables, indirect knowledge of the search space can be extracted, along with direct information about the potential biases that the GA should circumvent when attempting to draw trends about the optimal designs.

Variable	Lower limit	Upper limit	Increment
θ (°)	20	65	4.5
W (m)	3.5	25	2.15
D (m)	3.5	30	2.65
L (m)	50	150	10
L_f (m)	13	90	7.7
W_f (m)	1.75	35	3.325
ρ_t (kgm^{-3})	1000	6500	550
ρ_f (kgm^{-3})	50	900	85

Table 5.2: Definitions of the parameter sub-ranges used to present the distribution of the set of 7762 randomly-selected designs.

From the 7762 designs satisfying only the physical constraints (Fig. 5.11), only for the lowest L_f values were a very small number of devices discovered. This is likely because too small a float increases the likelihood that the device will sink. Thus,

besides the lowest L_f subranges, the variable bounds are such that computational expense is not misdirected in the process of generating new individuals. As may be expected from their increased likelihood of sinking or having inappropriately high water levels, fewer designs satisfy the physical constraints with higher ρ_t or ρ_f values. The highest W_f values are only achievable in the presence of high L_f and relatively low ρ_f values, as evidenced by the declining number of devices towards the upper limit on W_f. Devices with the lowest θ values also appear slightly less likely to satisfy the physical constraints.

Considering only the 2000 designs that satisfy both the physical and computational constraints, it becomes evident that there are biases against potentially the best-performing devices. Whilst there are not drastic changes imposed by the computational constraints (compare Fig. 5.12 with Fig. 5.11), far fewer devices of high L and very low θ (within the lowest two sub-ranges) pass the computational constraints. And from geometrical considerations, as θ decreases, greater L values are required to achieve a given separation. Therefore, in order to match the module separation to half the predominant wavelength (an assumed beneficial characteristic), devices of low θ require high L, the discovery of which is biased against by the constraints. This is more clearly visualised in Fig. 5.13, where data points above the dotted line represent the cases where, given a random device (that satisfies the physical constraints) within a certain variable range, there is a greater chance it will not satisfy the computational constraints than would be expected based on the average across the full variable ranges (i.e. the likelihood is greater than 5762/7762). Designs with very low W or D values also tend to fail the computational constraints, likely because of the thin patches introduced to the mesh. Unexpectedly, designs with D close to its upper limit also exhibit a lower likelihood of satisfying the computational constraints.

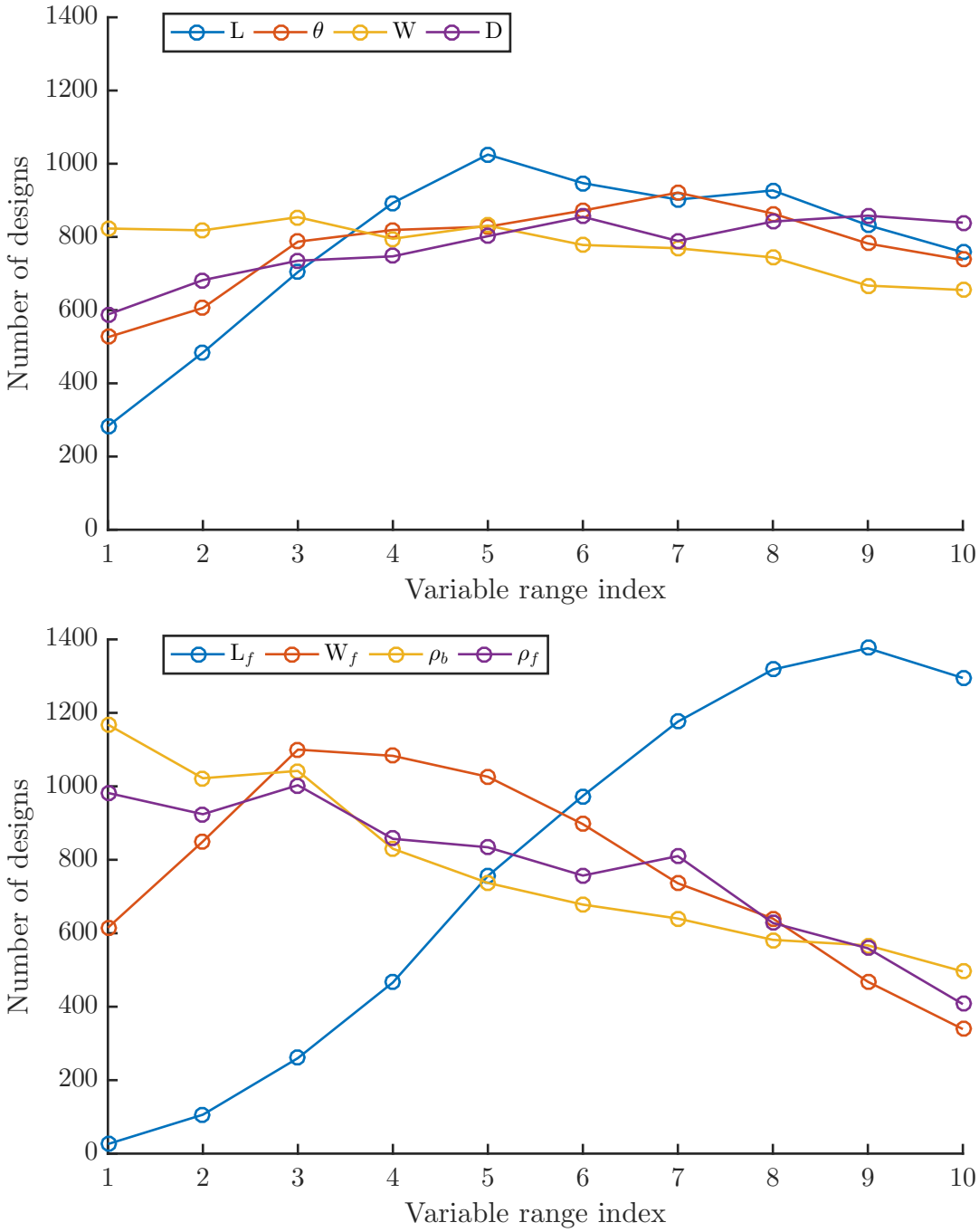

Figure 5.11: Parameter sets satisfying only the physical constraints.

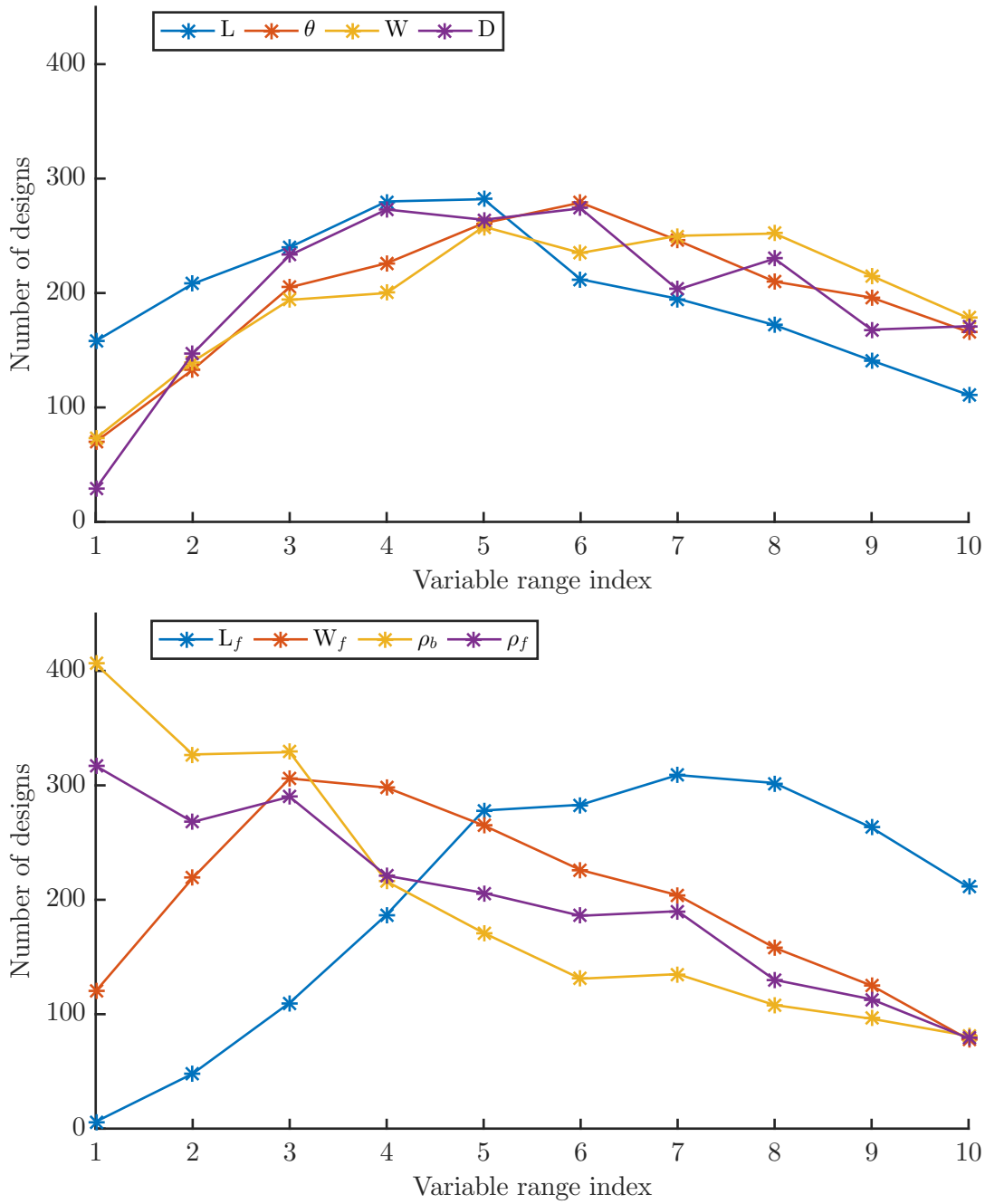

Figure 5.12: Parameter sets satisfying the physical and computational constraints.

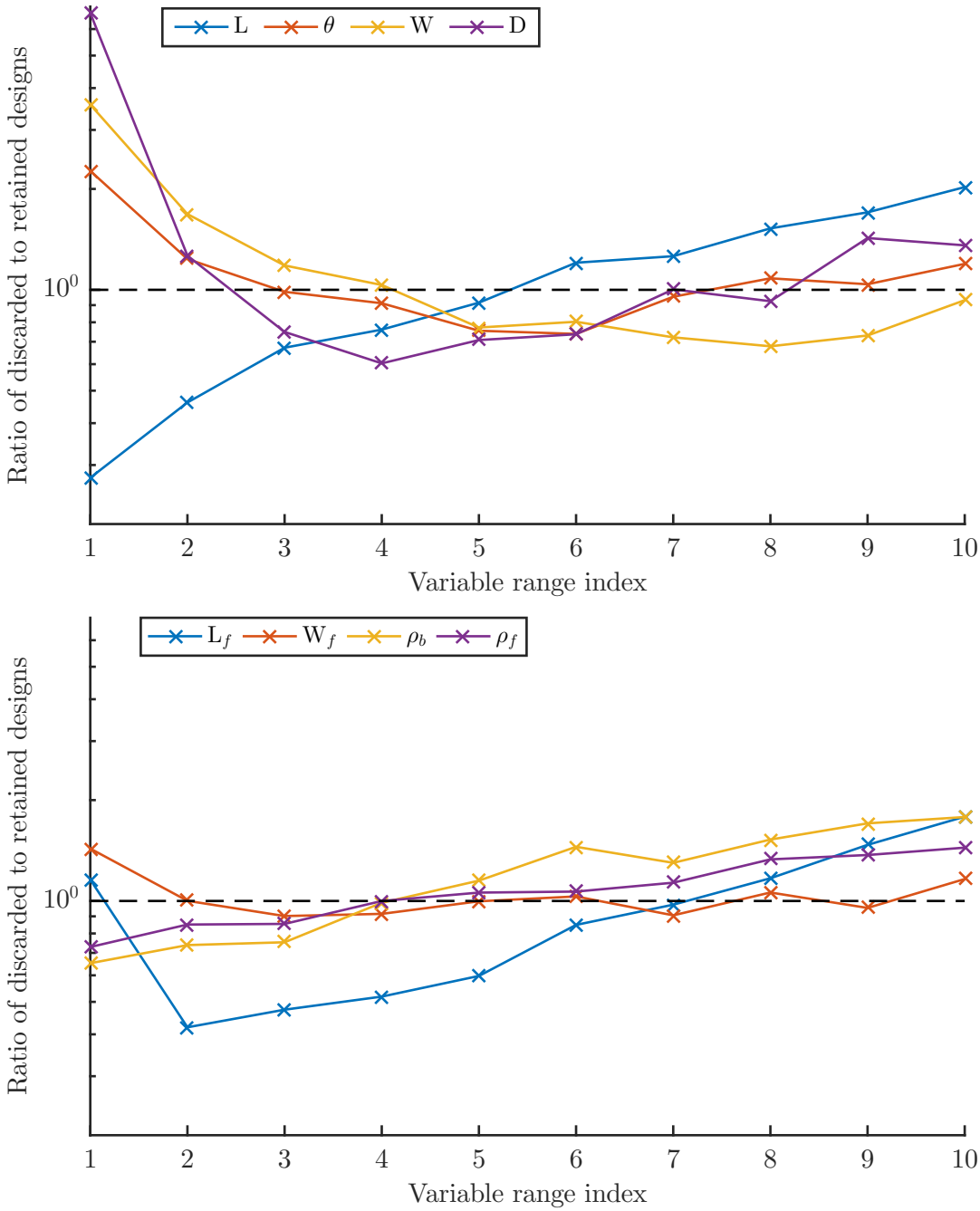

Figure 5.13: The ratio of the number of discarded (infeasible) designs to the number of retained (feasible) designs, normalised by the ratio of the total numbers of each.

Since the inclination angle is a variable of particular interest (see Section 5.1), it is imperative that the bias against the discovery of designs of low θ is counteracted, either, most easily by running the GA over multiple angle ranges, or by increasing the

population sizes.

A further deduction from these studies is that the parameter space is quite sparse, consisting of closely separated regions of feasibility. Overall, the parameter space is well-populated with feasible designs, yet also reliably interspersed with infeasible regions too. Additionally, it takes many more attempts to randomly populate the initial generation than subsequent ones; once in a feasible region, designs created through the breeding process are likely to remain feasible. This suggests a parameter space consisting of medium-sized continuous feasible regions, interspersed by infeasible regions of a similar nature. For variable sub-ranges with whom designs are less likely to satisfy the constraints - for example, θ for the lowest sub-ranges - the infeasible regions are likely much larger than the feasible ones.

5.7 Results and discussion

5.7.1 Single-objective GA

The series of GA runs performed in this section is motivated by the nature of the search space and its impact on the performance of the GA. The WaveTrain concept is subject to physical constraints (Eqs. 5.1 - 5.5), overlaid with constraints due to the difficulties in finding sufficiently accurate numerical solutions to the hydrodynamic equations (i.e. the 'computational constraints' discussed in Section 5.5). A key consequence of this is that designs of lower inclination angle, θ, are not as readily discovered and assessed as designs of greater θ (Section 5.6). It is also unclear whether there will be just one optimal design. Especially given the discontinuous nature of the search space, the GA may well be predisposed to find multiple candidates for optimal performance. For these reasons, the GA is run multiple times within specific angle ranges. This allows the bias against lower angle devices to be overcome, and for multiple design candidates for optimal performance to be discovered. Each GA run uses 31 generations (including the initial population) of 16 individuals (twice the number of variables). 24 GA runs were made, three for each five degree range between 20 and 60°. To confirm the accuracy of the final results, the hydrodynamic model for each of the final

generation individuals (most of which are near-optimal solutions) is compared for two discretisations: quadratic splines with a panel size of 20% of L, and cubic splines with a panel size of 10% of L. If the power differs by less than 5% between these two cases, the model is deemed to be suitably converged. Whilst power was used as the objective function, the computational constraints can sometimes restrict the GA's ability to increase the dimension, D, of a given design (see Fig. 5.13), which tends to increase power capture. Hence, Capture Width Ratio (CWR) can be better placed to elucidate the pertinent design trends.

Amongst the total of 11904 individuals assessed by the GA, several design trends become apparent. Firstly, it appears important that the mass of entrained water within each module is sufficiently large relative to the module mass. In this context, the ratio of these two masses is a necessary but not sufficient condition for high power extraction (Fig. 5.14). In order to maintain a broad power absorption bandwidth, the resonant response of the entrained water columns and the modules must be sufficiently spaced in wave period. There is an upper limit on module mass (relative to the module size) due to the physical constraints (in particular, the device must not sink), whereas the mass of entrained water can be increased more freely. This provides an explanation as to why the mass ratio is a necessary condition. However, it is not seen as a sufficient condition in this context, partly because the search space permits a range of device sizes; simply scaling down a device will reduce its power capture. More conclusively though, since the mass ratio does not completely embody the other design features presented hereafter, it cannot be a completely sufficient condition for high power capture, even with some form of module size restriction. The data set comprising green squares in Fig. 5.14 shows the optimal mass ratio to be around 10. On top of the dependency on the constraints imposed by the problem definition (e.g. module shape, joint locations, parameter bounds, etc.), the results shown in this figure are also dependent on the wave climate. Climates encompassing a wider range of wave periods are likely to require higher values of the mass ratio, in order to achieve a broader profile of resonant response.

Figure 5.14: The mass ratio is defined as the mass of entrained water, divided by the mass of the module. Each data point represents one set of design parameters encountered by the GA. Green squares - original design; blue circles - after design change (introduced later in this section).

Another parameter on which power capture (or CWR) depends strongly is the module inclination angle, θ. Fig. 5.15 shows that the highest performance can be attained with devices whose inclination angles are around 36°, but that relatively high performance can also be sustained with inclination angles as low as 30° and as high as 50°. By highlighting the individuals (orange data set in Fig. 5.15) for which convergence has been more rigorously tested and verified, the trend is further justified, confirming that it is not simply an artefact. Again, this condition is necessary for optimal performance, but not sufficient, due to the dependency on other parameters such as the mass ratio.

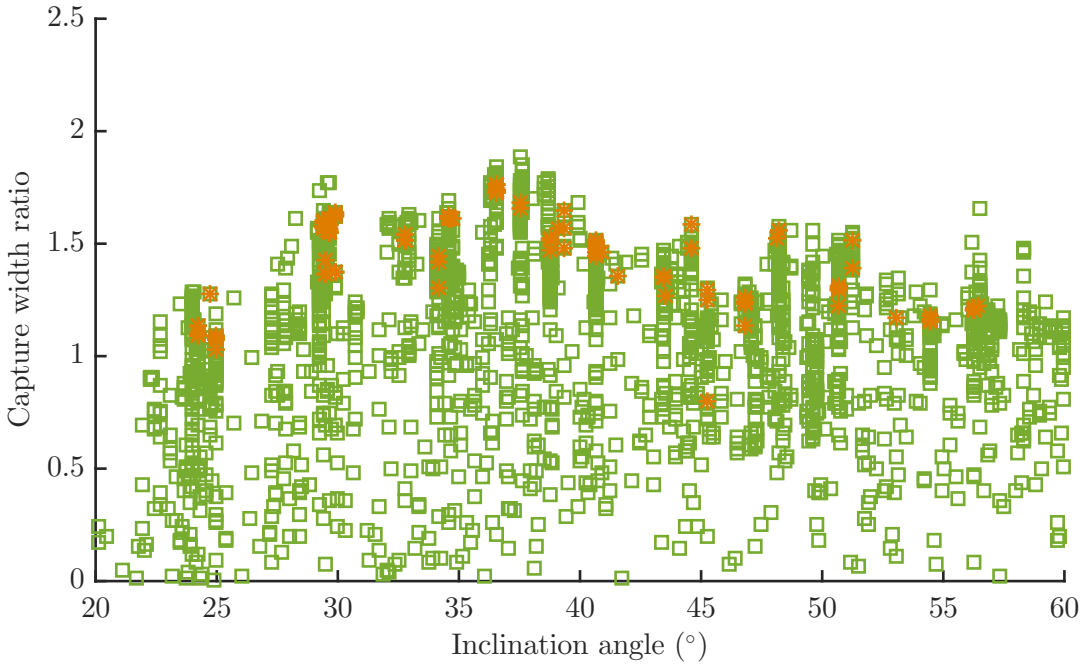

Figure 5.15: The dependence of capture width ratio on the module inclination angle. Green squares represent every parameter set encountered by the GA. Orange stars represent only parameter sets from the final generations, whose hydrodynamic models have been deemed suitably converged ($<$ 5% difference in power between the two model discretisations).

However, the aforementioned requirement on the mass ratio brings the optimality of the results presented thus far into doubt. In order to achieve high mass ratios, the physical constraints dictate that the water column mass must be high, which is most readily achieved by increasing the dimensions of the tube cross-section, W and D. However, Eq. 5.4 imposes a restriction on W, relative to the float width (W_f) and length (L_f). It is known that a sufficient length of vertical float face (VFF) is required to produce the desired sloped motion, and this correlates with the float width. Thus to achieve optimal performance, both sufficiently high W and W_f values are required, whereas Eq. 5.4 ensures that this can only be achieved if L_f is increased - i.e. if the float is lengthened, pushing the VFF further beneath the water surface than is desired. Too long a float is also likely to negatively affect the mass distribution. Hence, a suitable measure of the severity of this restriction is proportional to W and W_f (since these should both attain high values), and inversely proportional to

L_f (since a corresponding increase in L_f should be avoided). This restriction also tightens for decreasing inclination angle. Removing the influence of this constraint is most easily done by extending the top of the tubes so that they lie horizontally, in line with the top of the float. Repeating the 24 GA runs with this alteration leads to the exploration of a much expanded parameter space, with the effects most pronounced on W, and W_f relative to L_f (Fig. 5.16).

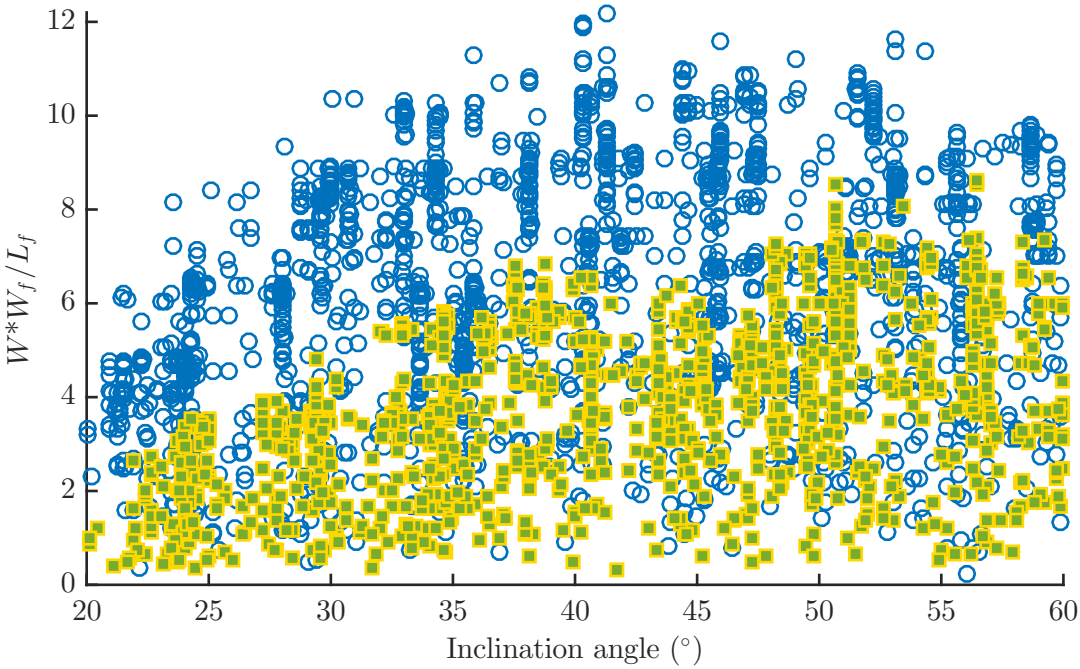

Figure 5.16: The effect of removing the constraint given by Eq. 5.4 on the severity of the restriction of W, and W_f relative to L_f. Green squares represent parameter sets explored by the GA with the constraint active. Blue circles represent parameter sets explored after removal of the constraint.

It is also evident that this expansion of the feasible parameter space brings significant increases in power extraction and CWR (Fig. 5.17). Significant increases in CWR are seen for inclination angles below around 45°, but the peak performance still occurs around 36°. Indeed, whilst the best performing devices in this region with the original geometry had float lengths (L_f) around half the body length (L), with the updated geometry, the top performers have float lengths of less than a third of the body length. This reduced float length leads to further increased mass ratios for

some of the devices with greatest CWRs. Designs with predicted CWRs above 2 are characterised by mass ratios ranging between 9 and 40 (Fig. 5.15). A new region of perhaps more physically realisable designs has also opened up with mass ratios around 5. The greatest improvements in CWR have been made for the lowest θ values. Due to the nature of the search space and the operation of the GA, there are certain angle ranges in which high performing devices have not been discovered. The GA was rerun between angles of 25 and 32° to confirm that the trend of CWR with angle was simply perforated by the bias against the discovery of low angled devices (see the orange data set of Fig. 5.17). Given this evidence, θ values between 27 and 37° lead to the highest CWRs. However, it is possible that the shape of the float is constraining the performance below 27° somewhat. This is supported by the uppermost values in Fig. 5.16 falling significantly towards the lowest angles. This is a reflection of the upper limit on float width falling with reducing inclination angle - floats can only be as wide as is needed for a triangular float shape. Also from geometrical considerations, for lower angles, greater float widths are required in order to yield a given length of VFF. In any case, since very low angled devices likely inhabit isolated regions of feasibility (just considering the physical constraints), practical difficulties could result in aiming to maintain feasibility of the physical device.

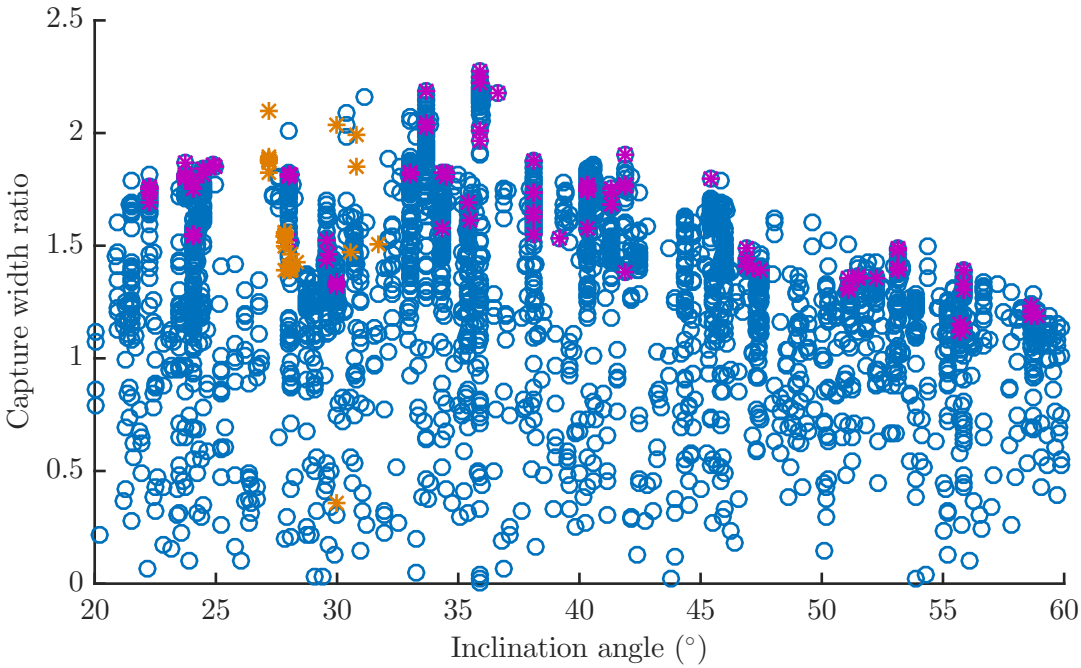

Figure 5.17: The dependence of capture width ratio on the module inclination angle, given the removal of the constraint given by Eq. 5.4 - see Fig. 5.15 for comparison. Blue circles represent all parameter sets encountered by the GA. Magenta stars represent only parameter sets from the final generations, whose hydrodynamic models are deemed suitably converged ($< 5\%$ difference in power between the two model discretisations). Orange stars represent designs found through repeated GA runs, specifically targeting low angles.

It was largely expected that the dimensions of the tube (L, D, W) would approach their upper bounds to maximise performance, based on simply achieving an increase in the scale of the device. However, this is not necessarily the only driver of L. At least in regular seas, or irregular conditions in which one wavelength is relatively dominant, it is beneficial for the horizontal spacing between successive modules to be around half a wavelength. This encourages adjacent pairs of modules to move in anti-phase with one another, providing maximal restoring forces to prevent unwanted pitching. From geometrical considerations, the lower the value of θ, the greater the required L value in order to achieve a given separation between the CoGs of adjacent modules. This means that increasing L will not always be beneficial for performance, though L values close to the upper bound of 150m lead to best performance in this study. Similarly, greater W and D values also do not necessarily lead to increased performance, if they

were to increase the resonant response of the device beyond the range of wave periods present in the encountered wave climate.

There is more variability of the other variables amongst the best performing designs, but some ranges are evident in which performance is better. Considering just devices with power extraction in excess of 3.5MW: L_f lies between 30 and 65m, ranging from 0.22 to 0.45 of the module length; W_f ranges from 10 to 28m; ρ_t ranges between the lower bound of 1000kgm^{-3}, up to values approaching 4000kgm^{-3}; ρ_f values remain towards the lower end of the allowed range, somewhere between 90 and 300kgm^{-3}. The spread of these variables increases further if lower power captures are considered. From this evidence, there are likely to be many near optimal designs, which could allow extra flexibility in construction without compromising on performance.

Despite the spread in many of the variables seen amongst the optimal devices, various combinations of them are required to fulfil other criteria necessary for high power capture. Firstly, the waterlines intersect the highest power extracting ($>$ around 3.5MW) designs below the top of the VFF (Fig. 5.18). The waterlines intersect the very highest power designs halfway down the VFF. Again, this is not a sufficient condition, because variation of the other parameters can reduce power extraction but retain the waterline position.

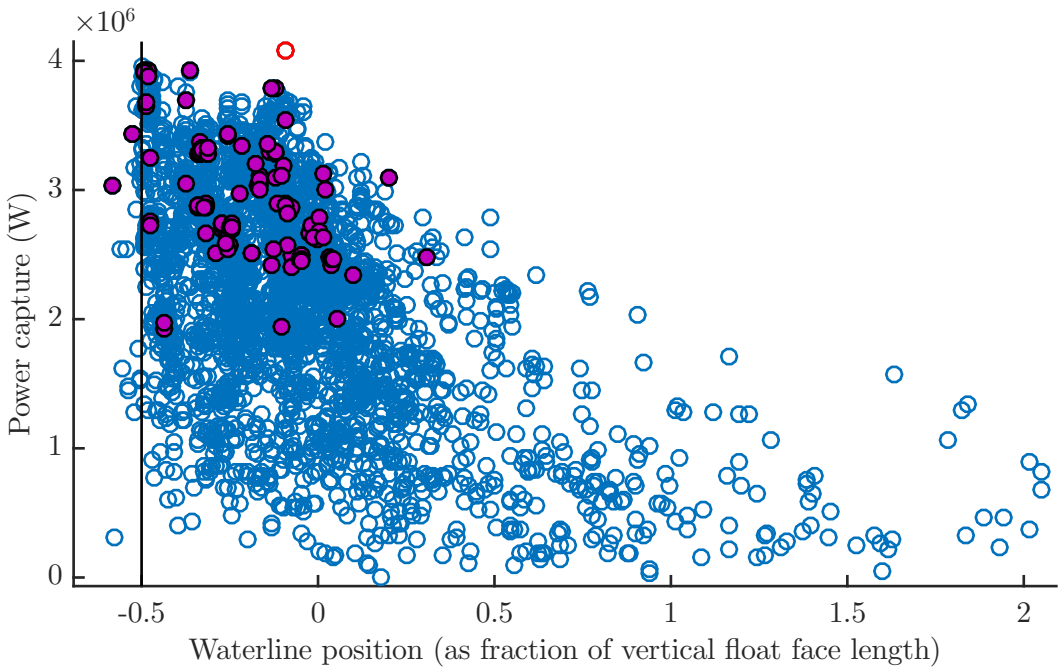

Figure 5.18: The relationship between the waterline position and the power capture. Blue circles represent all parameter sets encountered by the GA. Magenta circles represent parameter sets from the final generation, whose hydrodynamic models are deemed suitably converged. Red circles (very closely spaced) denote two final generation devices for which the hydrodynamic model accuracy is too low to be considered. A waterline position of zero corresponds to the top of the vertical float face, and a positive or negative value denotes the waterline position above or below this point, as a fraction of the total height of the vertical float face.

A similar criterion exists for the thickness of the float (W_f) employed in the group of high power extracting designs (again, $>$ around 3.5MW), where W_f is not less than half the maximum allowed value (Fig. 5.19). In fact, the very highest power extracting designs have W_f much closer to the maximum value (defined by the second relation of Eq. 5.5), which would correspond to a triangular float shape. This bears great similarity to the trends observed for the waterline position, and is no coincidence, as shown by the relation between the two (Fig. 5.20).

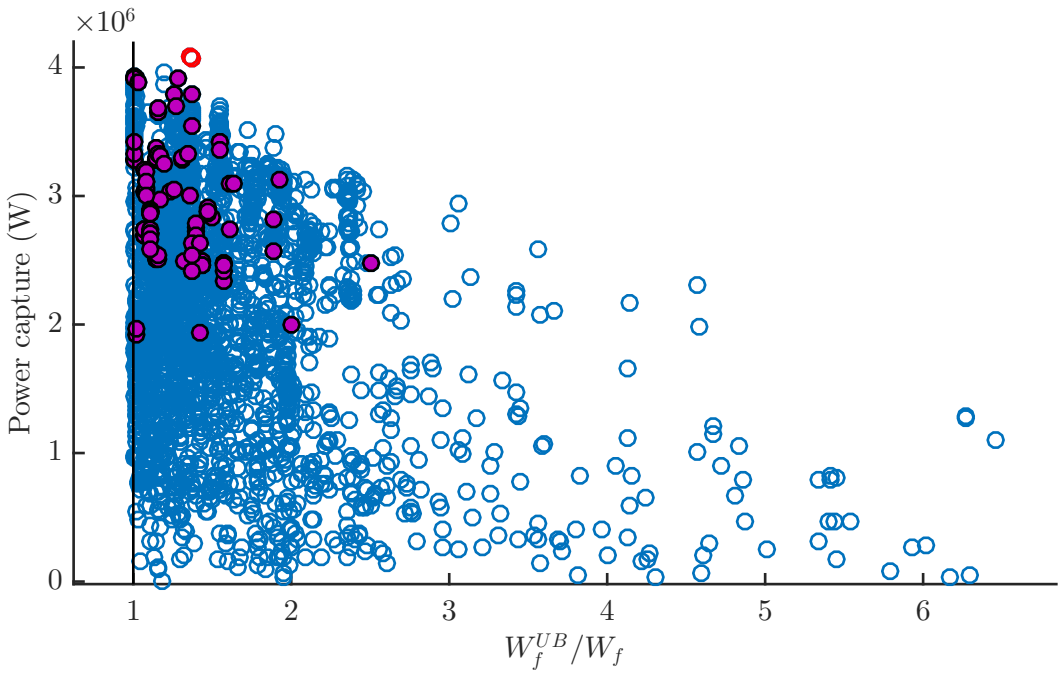

Figure 5.19: The relationship between the float width relative to the upper bound, and the power capture. Blue circles represent all parameter sets encountered by the GA. Magenta circles represent parameter sets from the final generation, whose hydrodynamic models are deemed suitably converged. Red circles (very closely spaced) denote two final generation devices for which the hydrodynamic model accuracy is too low to be considered.

Enforced by the physical constraints, all data points lie within a band that expands in thickness as it approaches thinner floats and higher relative waterline positions, but becomes sparser. The density of encountered parameter sets towards thicker floats and lower relative waterline positions reflects the convergence of the GA runs towards the higher performing individuals. It makes physical sense that for floats at the triangular limit, waterlines cannot lie above the VFF, since this would correspond to the device being fully submerged. Whilst there are no limits imposed through this linear model on how close to full submergence the device can be, there are signs that being close to this region is actually detrimental to the performance. In other words, not having enough mass above the water level, in general results in lower power capture, even when neglecting the changes in waterline that would occur in the physical system. This is reflected in the set of suitably converged ($< 5\%$ difference in power between

the two test discretisations) individuals from the final generations of the GA runs (Fig. 5.20). These individuals are some of the highest power extractors, and always allow a significant amount of the body to lie above the water surface. Though not the strongest correlation, designs with thicker floats tend to benefit from a lower relative waterline position, which retains a significant amount of the device above water. Conversely, amongst these higher power designs, a higher relative waterline position is only beneficial if the float is thinner. One may also expect a larger L_f value to exacerbate this effect, perhaps one reason why correlation with W_f is weaker.

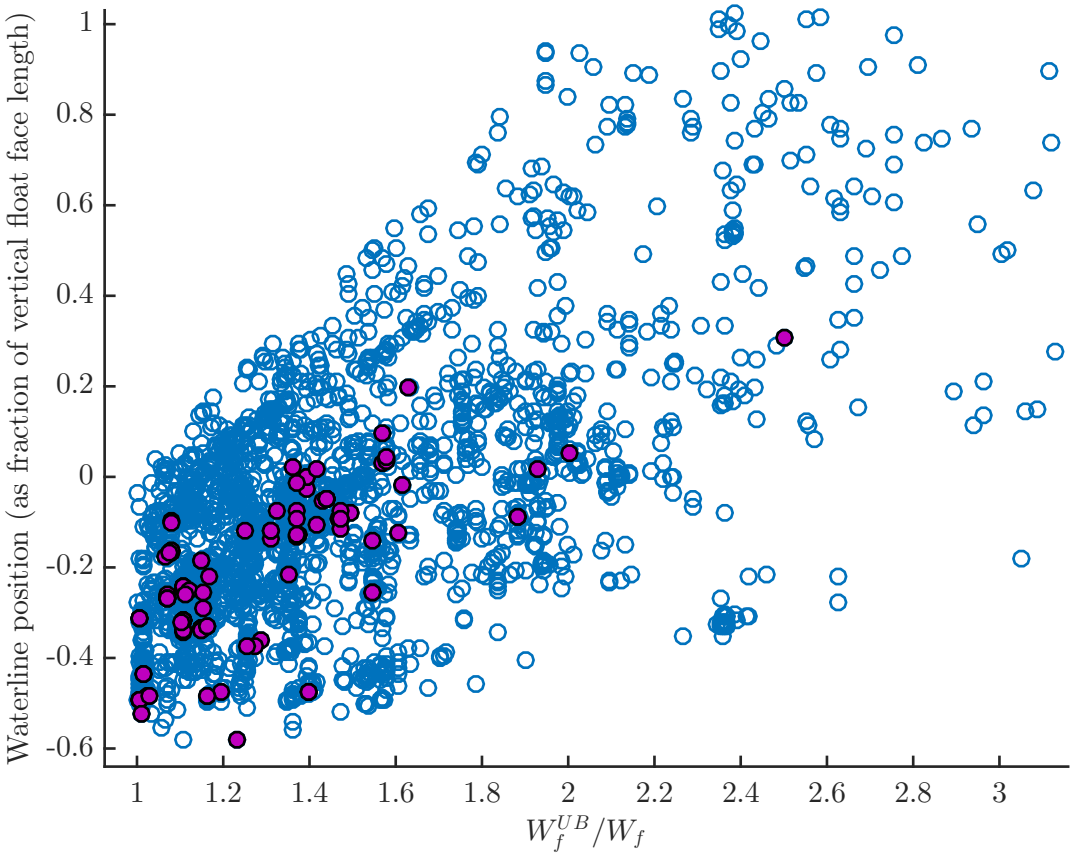

Figure 5.20: The relationship between the waterline position and the float width relative to the upper bound. Blue circles represent all parameter sets encountered by the GA. Magenta circles represent parameter sets from the final generation, whose hydrodynamic models are deemed suitably converged. A waterline position of zero corresponds to the top of the vertical float face, and a positive or negative value denotes the waterline position above or below this point, as a fraction of the total height of the vertical float face.

5.7.2 Multi-objective GA

This section presents the results regarding optimal WaveTrain designs, obtained using the multi-objective genetic algorithm with three variations of the objective functions - the standalone power and force-based objective functions, those normalised by the characteristic device width, D, and those normalised by the module mass, M. Normalising by D gives objective functions not dissimilar to capture width ratio, and was seen to clarify some of the physical trends seen in the previous section. Normalising by M has the aim of also minimising the material cost, with the idea that longer modules will no longer simply be favoured by their increased size with which to interact with the waves. Other normalisation factors could provide useful insights: for example, the device surface area is often instead used to reflect the structural costs, and a more complete monetary cost model could even be used to better estimate this. However, in the current scope of work, only the three above mentioned cases are investigated.

The power-based objective function is negated by convention, so that both objective functions are to be minimised. Since the joint force objective function involves a large exponent ($m = 5$), very steep Pareto fronts can result, meaning the results are viewed more clearly with this objective function given a logarithmic scale. Continuing from the slight design change implemented along with the removal of the constraint defined by Eq. 5.4, all results in this section use the updated geometry (see Section 5.7.1 for details).

5.7.2.1 Objective functions $\bar{P}$ & $\bar{G}$

Though the damage measure cannot take absolute values, it is useful in this section to take the m^{th} root of the quantity so that the resulting measure is proportional to stress. Thus purely in this subsection, Eq. 5.32 is to be replaced with Eq. 5.39. This allows the results in this subsection to be more easily interpreted with relation to material costs (under the assumption that material costs will be proportional to the stresses).

$$G = \sqrt[m]{\sum_{i=1}^{K} F_i^m n_i} \tag{5.39}$$

Within the variable bounds specified by Table 5.3, the genetic algorithm was run for 61 generations of 100 individuals - deemed to give a high enough level of convergence of the Pareto front. In order to verify sufficient accuracy of the designs on the resulting Pareto front, two discretisations were used as in the previous subsection: quadratic splines with a panel size of $0.2L$ and cubic splines with a panel size of $0.1L$. Figure 5.21 shows that only a small level of distortion is introduced to the Pareto front under the switch to a finer discretisation, which indicates a high level of accuracy. For 80% of the designs, the difference in $\bar{P}$ is less than 10%, and the difference in $\bar{G}$ is less than 10% for 87% of the designs.

The Pareto front can be viewed as several continuous regions, separated by discontinuous jumps. These discontinuities can be attributed to both the inability of the GA to locate some sections of the front, and the innate nature of the problem, which embodies the underlying physics and the constraints (physical and computational). In the results presented here, most often the groups of designs either side of a discontinuous region are seen to be of distinct types, whilst designs within each continuous band are more similar to one another. This suggests that the underlying physics of the problem (including the nonlinear set of physical constraints) is the dominant factor, and that the discontinuous regions are indeed features of the true Pareto front. (Computational constraints have not been observed to significantly impact the feasible search space - see Section 5.6.) A purely vertical or horizontal discontinuous jump can occur if there exist regions in which the two objectives are not in conflict with each other - i.e. where one objective function can be altered independently of the other. The non-existence of feasible designs with certain pairings of the two objective function values can also result in discontinuous jumps. This is more likely to explain jumps through which both objective functions change in value; by smoothly changing

a particular combination of variables, it may in principle be possible to move continuously along the Pareto front, until a bound or constraint is hit, at which point there must be a step change in the design to transition to the next continuous region of the front.

Variable	Lower bound	Upper bound	Units
θ	20	65	$^\circ$
W	3.5	25	m
D	3.5	30	m
L	50	150	m
L_f	13	90	m
W_f	1.75	35	m
ρ_t	1000	6500	kgm^{-3}
ρ_f	50	900	kgm^{-3}

Table 5.3: Variable ranges used for the multi-objective genetic algorithm runs that use $\bar{P}$ and $\bar{G}$, and $\bar{P}/D$ and $\bar{G}/D$ as the objective functions.

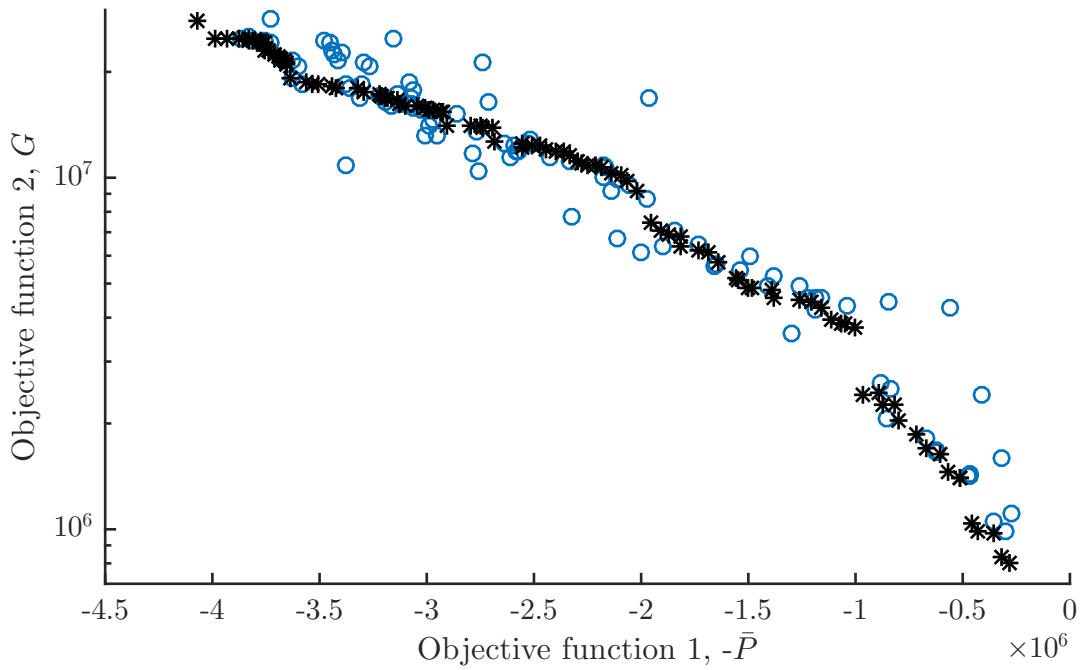

Figure 5.21: The Pareto front with $\bar{P}$ and $\bar{G}$ as objective functions. Black stars - spline order = 3, maximum panel size = $0.2L$; blue circles - spline order = 4, maximum panel size = $0.1L$.

Some degree of wider context is necessary to select from the optimal design candidates along the Pareto front. However, without knowing the real-world implications

(for example, in terms of monetary cost) of the various designs, two aspects of the shape of the front can be used to narrow the selection to a few candidates. This rests on the tacit assumption that the force-based objective function is proportional to the overall cost (monetary or otherwise) of energy extraction. Firstly, the discontinuous regions can be exploited: at a vertical jump, the lower of the two designs should be chosen, where the same power can be obtained at lower expense, whilst for analogous reasons, the leftmost of the two designs at a horizontal jump should be chosen. Secondly, continuous regions in which the gradient of the Pareto front appears to be close to zero often provide an easy selection: again, the leftmost design should be selected since it provides more power with minimal increases in likely structural damage. Figure 5.22 displays the Pareto front with both axes logarithmically scaled, along with a few of the best designs based on these selection principles (see also Table 5.4).

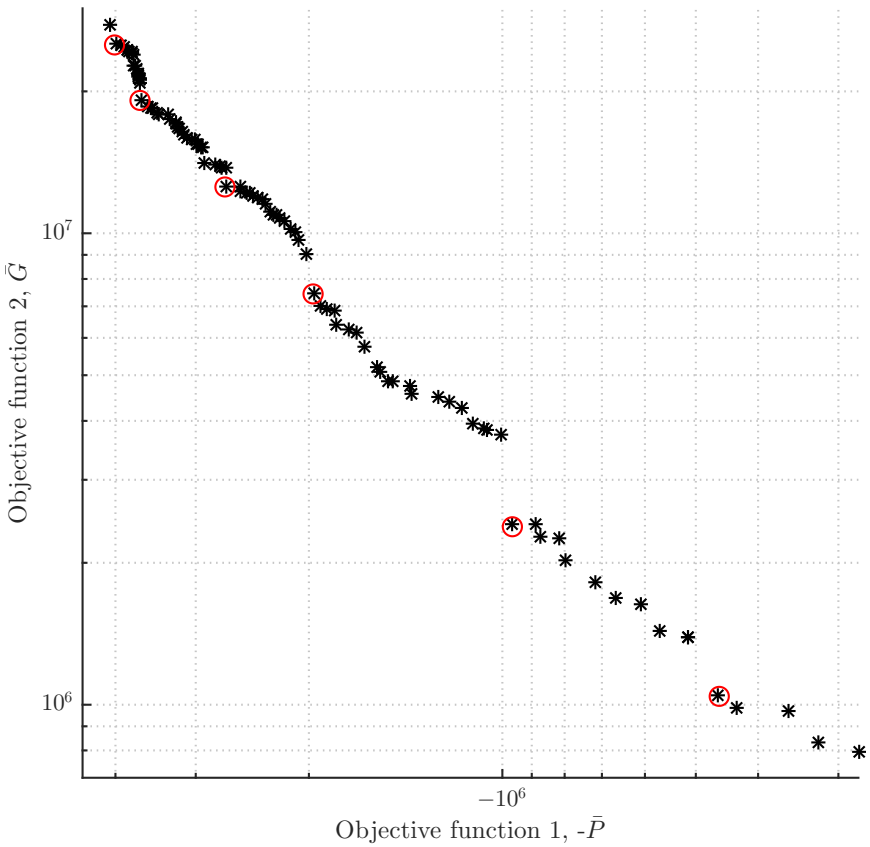

Figure 5.22: The Pareto front from Fig. 5.21, with a selection of the most favourable design candidates circled in red. $\bar{P}$ is measured in Watts.

Design	θ	W	D	L_f	W_f	ρ_t	ρ_f	L	$\bar{P}$ (W)	$\bar{G}$
1	35.67	24.90	29.70	57.01	24.82	1135.56	190.70	148.16	3.98 x 10^{6}	1.03 x 10^{37}
2	42.62	23.65	29.80	55.57	24.65	1408.17	270.78	149.55	3.64 x 10^{6}	2.58 x 10^{36}
3	43.43	23.40	19.90	50.22	24.46	2492.71	336.60	146.94	2.68 x 10^{6}	3.16 x 10^{35}
4	42.43	21.52	16.50	36.86	16.28	3416.62	72.57	98.26	1.96 x 10^{6}	2.32 x 10^{34}
5	51.08	14.53	12.99	33.72	13.67	2349.64	93.19	67.21	9.68 x 10^{5}	8.33 x 10^{31}
6	49.32	14.45	5.15	38.10	15.45	2049.95	125.80	71.50	4.62 x 10^{5}	1.24 x 10^{30}

Table 5.4: The defining parameters and objective function values of the designs circled in red in Fig. 5.22.

Device	θ	W	D	L_f	W_f	ρ_t	ρ_f	L	$\bar{P}/D$ (Wm^{-1})	$\bar{G}/D$
1	33.70	24.91	9.04	43.33	18.40	1107.48	175.37	149.63	1.93 x 10^{5}	5.51 x 10^{33}
2	39.56	24.68	9.31	46.06	19.61	1022.37	145.85	149.84	1.70 x 10^{5}	6.24 x 10^{32}
3	47.06	24.95	5.85	59.82	22.18	1645.97	404.97	97.09	1.46 x 10^{5}	1.46 x 10^{31}
4	51.88	20.40	4.89	54.28	23.77	1539.07	212.93	85.07	1.28 x 10^{5}	3.14 x 10^{30}
5	51.14	19.14	4.53	54.02	25.54	1589.03	213.19	83.41	1.15 x 10^{5}	8.07 x 10^{29}

Table 5.5: The defining parameters and objective function values of the designs circled in red in Fig. 5.26.

Device	θ	W	D	L_f	W_f	ρ_t	ρ_f	L	$\bar{P}/M$ (Wkg^{-1})	$\bar{G}/M$
1	47.34	11.31	11.04	20.68	5.21	1742.65	80.37	65.64	1.42	6.83 x 10^{25}
2	55.08	5.54	5.83	16.89	5.72	1710.20	81.04	50.12	1.12	3.06 x 10^{23}

Table 5.6: The defining parameters and objective function values of the designs circled in red in Fig. 5.28.

As is hinted at by the six selected designs (see Table 5.4), the Pareto front individuals also exhibit some trends. In general, as one traverses the front from high to low powers, θ increases from 35° through to around 54°, and L decreases from the maximum of 150m down to around 62m. W and D also vary from their maximum values with the highest power individuals, through to W around 13m and D of just above 4m for the lowest power designs. Whilst L_f broadly appears to increase towards the higher power regions of the front, the ratio of L_f to L decreases, with a division into two clumps of data points: for designs with power extraction lower than 1.6 x 10^6W, $0.5 < L_f/L < 0.62$, and for powers above 1.6 x 10^6W, $0.3 < L_f/L < 0.44$. W_f increases (with some spread) from 12m up to 27m from low to high power extracting designs. However, the extracted power exhibits little correlation with the ratio of W_f to L_f, though that ratio is found to lie between 0.32 and 0.5 for all devices on the Pareto front. For designs with $\bar{P} > 3.5$ x 10^6W, the mass ratio lies between 10 and 15. ρ_t is found to take values spanning almost the full range allowed by the bounds, yet as higher powers are approached along the front, ρ_t values decrease towards the lower bound. There is also some indication that lower ρ_t values are required for the lowest power regions too, whilst it is free to adopt higher values in between. ρ_f values tend to be somewhat independent of ρ_t, yet the two cannot both take large values simultaneously, since the device must float. ρ_f is split into two distinct clumps of data points, with designs extracting powers below 2MW taking values ranging between 50 and 125kgm^{-3}, and designs with powers above 2MW taking value between 200 and 380kgm^{-3}. Thus, at one extreme, the designs with greatest power have low ρ_t with relatively high ρ_f, whilst at the other extreme, the designs optimised most heavily for low damage due to stress cycling have low ρ_t and low ρ_f. The trend in ρ_t is somewhat mirrored by the trend in waterline height (Fig. 5.23), which is perhaps of little surprise since the waterline height is in part dependent on ρ_t. As for the devices optimised solely for high power (see Section 5.7.1), the highest power designs require a waterline position extending to around halfway down the vertical float face. However, with the extra force-related objective function, the lowest power designs (also those subject to

lowest damage) also require a lowering waterline height, towards a similar limit of half the vertical float face length. This is most clearly illustrated by using capture width ratio in place of power (Fig. 5.23). In contrast to the highest $\bar{P}$ designs, which are also accompanied by a maximal float width, it is just sufficient that the float width of the lowest $\bar{G}$ designs is greater than around two-thirds of its maximal value. In between the two ends of the Pareto front, the waterline heights generally do not exceed the top of the vertical float face - almost all optimal design candidates have a waterline intersecting the upper half of the vertical float face.

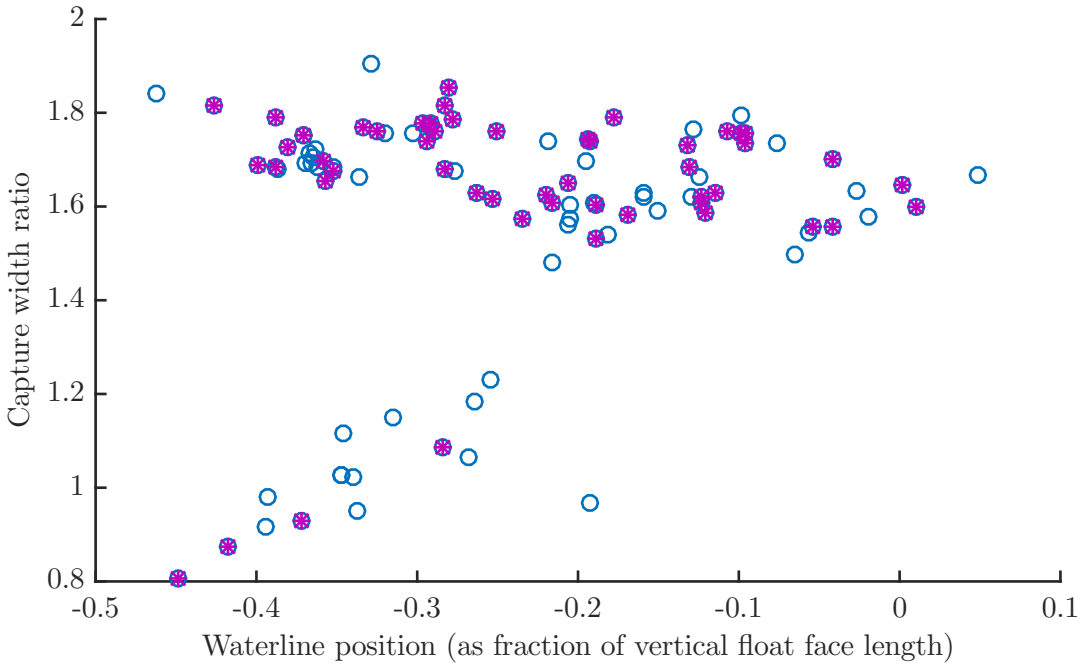

Figure 5.23: Capture width ratio with waterline position. Blue circles represent all parameter sets in the Pareto front shown in Fig. 5.22, magenta stars just those sets whose hydrodynamic models are deemed suitably converged. A waterline position of zero corresponds to the top of the vertical float face, and a positive or negative value denotes the waterline position above or below this point, as a fraction of the total height of the vertical float face.

Since high power devices exist with angles either side of the peak with θ around 35° (see Fig. 5.17), the implication from the results in this section is that higher forces must result on designs with angles much lower than 35°, otherwise the Pareto front would include designs from that range. A rerun of the multi-objective genetic

algorithm with a 35° upper limit on θ confirms this, with the Pareto front designs undergoing greater forces for a given power (Fig. 5.24), with one exception. As expected, no results achieved greater power than in the original run, but one new kind of device has been found that does improve upon the original front, and it is amongst the highest power designs (Table 5.7). As discussed previously (Section 5.6), with lower angles, in general there are fewer feasible regions as the search itself is more severely restricted by the physical and computational constraints. When larger angles are permitted, this biases the search against the discovery of designs with very low θ values. Figure 5.25 again shows that the hydrodynamic modelling outputs for the Pareto front individuals are sufficiently accurate.

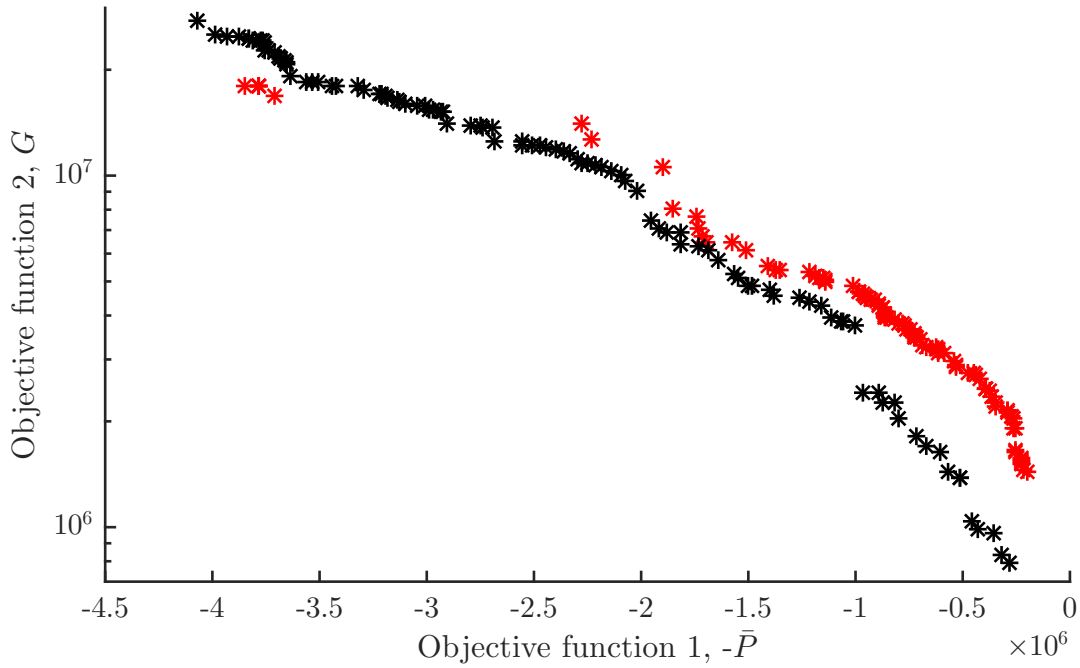

Figure 5.24: The Pareto fronts of the GA runs with the full θ range (black) and with the restricted θ range (red).

θ	W	D	L_f	W_f
28.84	24.60	25.14	57.97	12.10
ρ_t	ρ_f	L	$\bar{P}$	G
3087.68	95.92	136.30	3.71 x 10^6	1.40 x 10^{36}

Table 5.7: The defining parameters and objective function values of the new type of design encountered by the GA run restricted to low θ. $\bar{P}$ is measured in Watts.

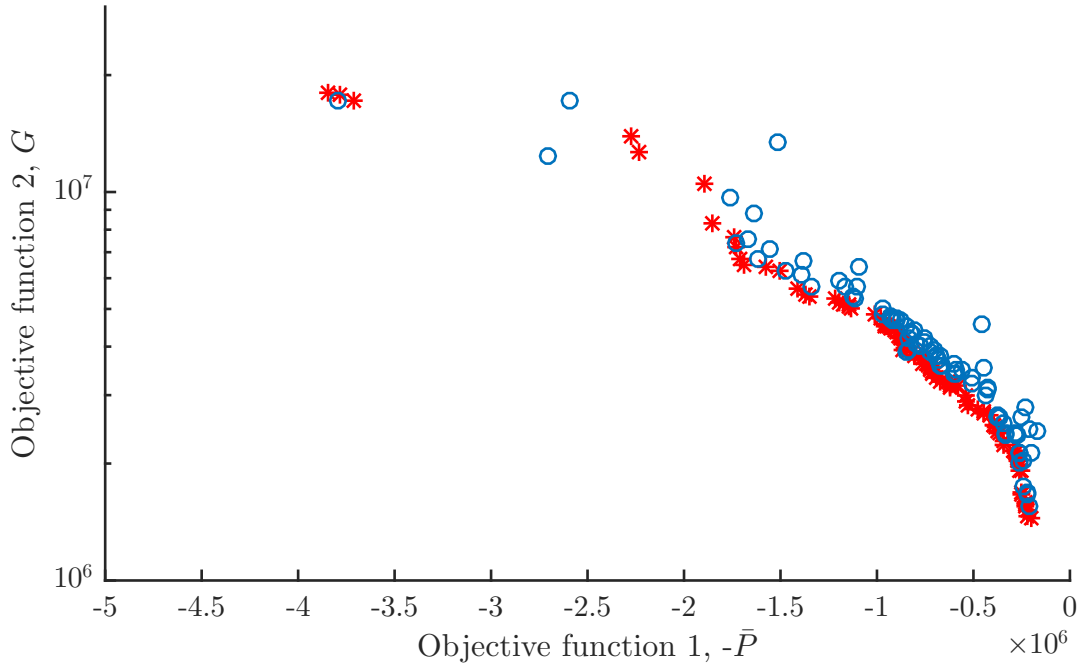

Figure 5.25: The Pareto front with $\bar{P}$ and $\bar{G}$ as objective functions, and the upper bound of θ reduced to 35°. Red stars - spline order = 3, maximum panel size = $0.2L$; blue circles - spline order = 4, maximum panel size = $0.1L$.

5.7.2.2 Objective functions $\bar{P}/D$ & $\bar{G}/D$

Within the variable bounds specified by Table 5.3, the genetic algorithm was run for 121 generations of 100 individuals - twice as many generations as were required in Section 5.7.2.1, due to the altered nature of the search (this is discussed again in a later paragraph). Whilst the level of accuracy of the hydrodynamic models of the Pareto front designs is not as strong as in Section 5.7.2.1, a similar kind of clustering is seen amongst the designs. Figure 5.26 shows that even when only considering designs for which the power difference is less than 20% between the two discretisations, the Pareto front remains well-represented. Additionally, in some cases, the difference in predicted power stems from the zeroing of power for frequencies at which the solver fails to converge, and since this tends to occur more often with the finer of the two discretisations, the difference in power is sometimes not actually representative of insufficient accuracy. In any case, omitting from consideration those designs for which accuracy is

disputed, five of the specific designs that strike the best compromise between the two objectives are presented in Table 5.5.

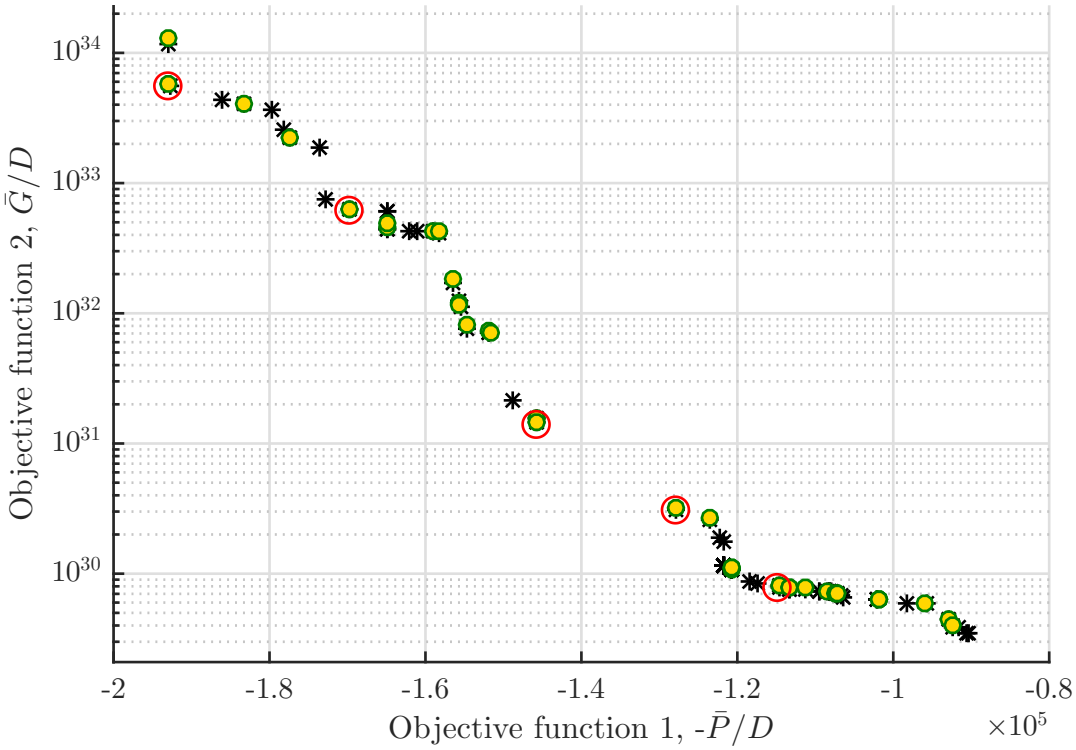

Figure 5.26: The Pareto front (black stars), with designs for whom the difference in power is less than 20% overlaid (green circles, filled in yellow). A selection of the most favourable design candidates are circled in red.

Noticeably, the trend of increasing θ with reducing power-based objective function value is retained, spanning a similar range of angles from 32° to 54°. The correlation is far stronger in this case (Fig. 5.27) than with the unnormalised objective functions. Similarly, at the top left of the Pareto front, L pushes up against the upper bound of 150m, and decreases down to about 70m in the bottom right. W also shares a similar trend, ranging from the upper limit of 25m down to 14m as the front is traversed from left to right. As before, the lower values of D taken by the designs in the bottom right of the front is the same as before, lying around 4m. This is enforced by the computational constraints. However, the individuals with highest $\bar{P}/D$ have a maximum D of around 9m, indicating that the designs may be exploiting some sort of beneficial diffraction of the waves around the front module, in order to attain a higher

capture width ratio. Further, the requirement for a greater number of generations in order for the GA to reach a sufficient level of convergence is largely due to this feature of the Pareto front individuals; small D values can lead to worsened hydrodynamic model accuracy with a given panel size, and worsened solver convergence properties.

Despite the absolute value of L_f not showing any obvious correlation with the objective functions, its ratio to L is again, broadly divided into two regions - $0.25 < L_f/L < 0.36$ for $\bar{P}/D$ values greater than 1.6 x $10^5 \mathrm{Wm}^{-1}$, and $0.54 < L_f/L < 0.72$ for $\bar{P}/D$ values less than 1.5 x $10^5 \mathrm{Wm}^{-1}$. These ranges stretch to both higher and lower extreme values of L_f/L than with the unnormalised objective functions. Again, there is little correlation between the objective functions and W_f/L_f, though this ratio has been found to lie between 0.25 and 0.5. As before, the designs furthest leftward on the Pareto front display a tendency towards lower ρ_t values, but the lowest $\bar{P}/D$ designs actually have the highest ρ_t values - around $3000 \mathrm{kgm}^{-3}$. ρ_f values show no clear correlation with $\bar{P}/D$ but are clustered in four groups, which span from around $150 \mathrm{kgm}^{-3}$ to $400 \mathrm{kgm}^{-3}$. The mass ratio lies between 15 and 20 for all designs with $\bar{P}/D > 1.6$ x $10^5 \mathrm{Wm}^{-1}$.

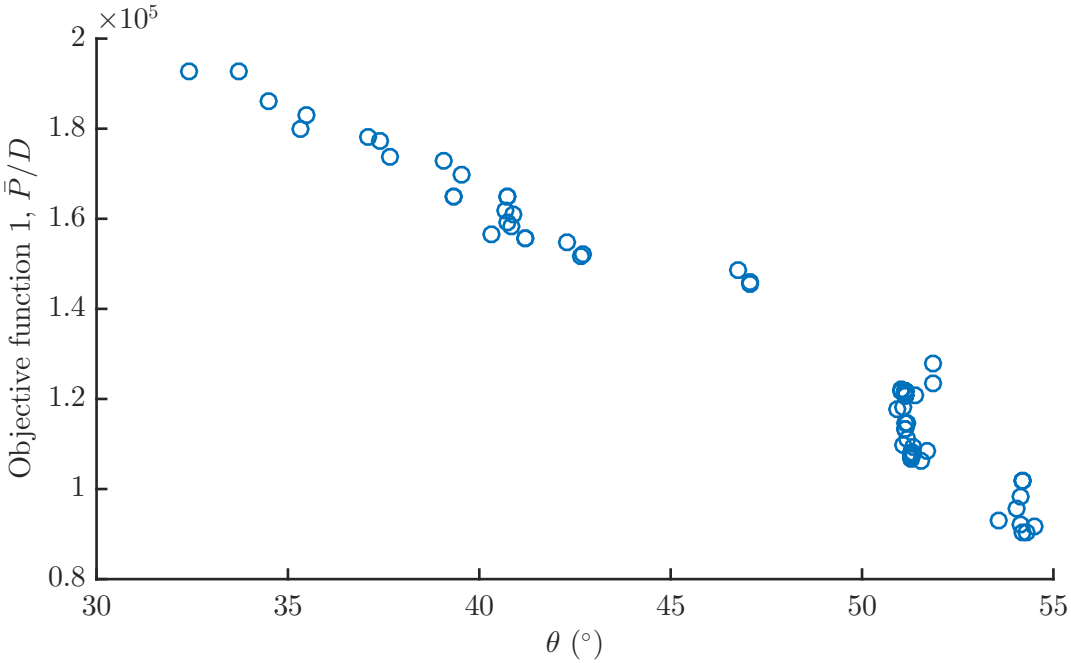

Figure 5.27: Correlation of the power-based objective function with the module inclination angle.

5.7.2.3 Objective functions $\bar{P}/M$ & $\bar{G}/M$

When normalising both objective functions by the module mass, there is a tendency of the GA search to veer towards values of W_f small enough to cause accuracy issues, with the enforced spline order and panel size. Thus the lower limit of W_f was raised to 5m. These objective functions also encourage minimisation of the densities involved, but practically, it may be difficult to achieve $\rho_t < 1700\text{kgm}^{-3}$ or $\rho_f < 80\text{kgm}^{-3}$, so these were enforced as lower limits. L was found to always lie towards the lower end of the range, so the upper limit was adjusted accordingly (Table 5.8), to save computational effort. The genetic algorithm was again run with 121 generations of 100 individuals.

Variable	Lower bound	Upper bound	Units
θ	20	65	$^\circ$
W	3.5	25	m
D	3.5	30	m
L	50	75	m
L_f	13	90	m
W_f	5	35	m
ρ_t	1700	6500	kgm^{-3}
ρ_f	80	900	kgm^{-3}

Table 5.8: Variable ranges used for the multi-objective GA run that uses $\bar{P}/M$ and $\bar{G}/M$ as the objective functions.

Computing the objective functions a second time for each Pareto front individual, using a finer discretisation and increased spline order, does not result in an identical front. However, as the 45 individuals are split broadly into two types of design, the 29% of these with differences in $\bar{P}/M < 10\%$ is enough to justify the performance of those two design types. The best performing of these designs are highlighted on the Pareto front (Fig. 5.28) and are defined in Table 5.6. Both have inclination angles above 45°. W is almost equal to D, giving a square cross-section of the internal water column in both cases. Peak $\bar{P}/M$ is achieved with a value of L_f/L around 0.3, and the mass ratio increases from 5 to 7.3 traversing leftwards along the lowest section of the front, and then from 11 up to 14 along the second, upper branch of the front.

Whilst the $\bar{P}/M$ value of device 1 (Table 5.6) is a quarter higher than that of device 2, $\bar{G}/M$ increases by two orders of magnitude. Most interestingly, with the small variation present amongst the 45 Pareto front designs, there is a clear trend relating to the waterline position (Fig. 5.29). There is direct proportionality between the degree to which a float is triangular in cross-section, and the waterline position relative to the vertical float face. The design with the float closest in cross-sectional shape to a triangle has a waterline intersecting the module just less than a third of the way down the vertical float face. As the float shape further departs from this upper (and triangular) limit, the waterline shifts closer to the edge at the top of the vertical float face. This could perhaps be interpreted in terms of a retention of the amount of mass/inertia above water.

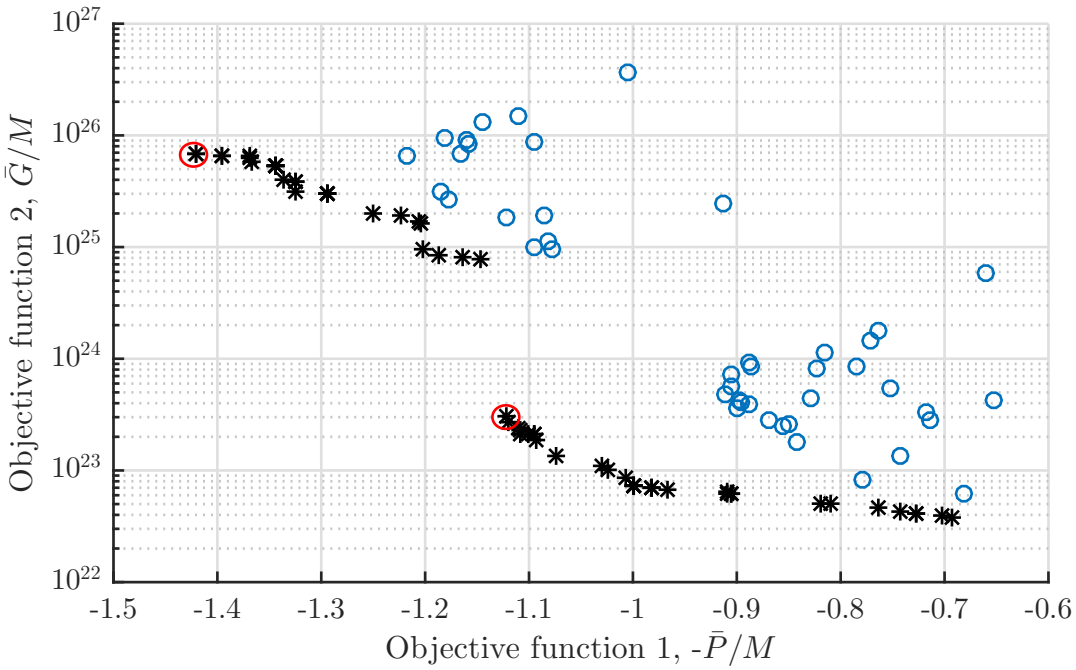

Figure 5.28: The Pareto front with two discretisations: spline order = 3, max. panel size = $0.2L$ - black stars; spline order = 4, max. panel size = $0.1L$ - blue circles. A selection of the most favourable design candidates are circled in red.

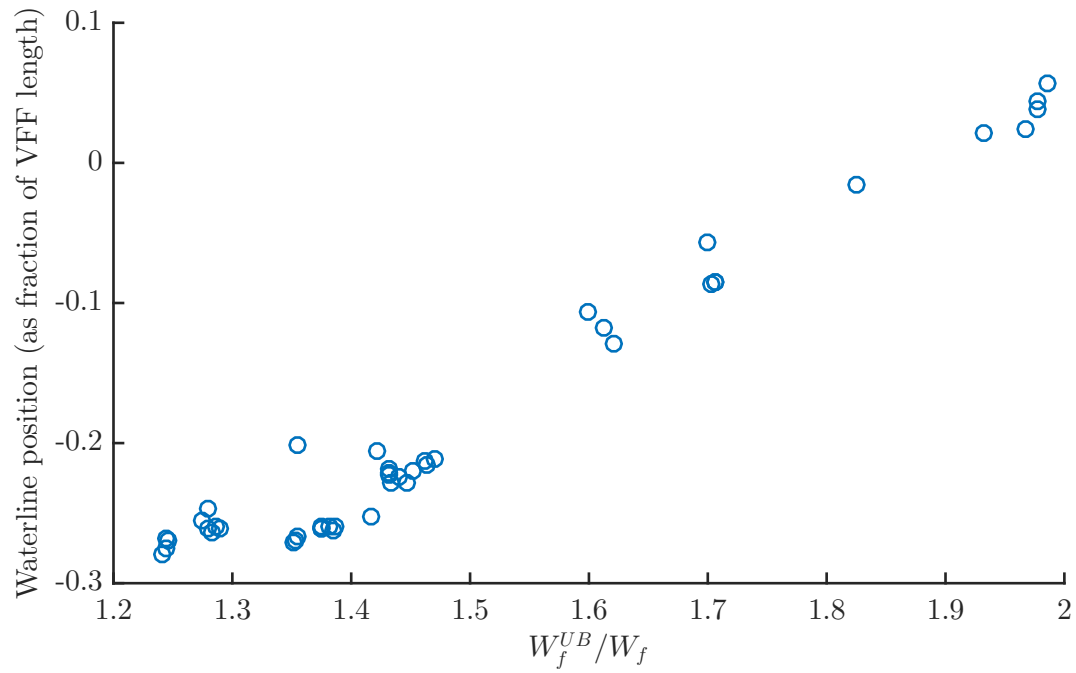

Figure 5.29: Correlation of the waterline position with the float width as a function of its upper limit. Contrast with Fig. 5.20.

5.7.3 Comparison with other devices and WaveTrain verdict

With a vast number of wave energy converter designs, and in the absence of conclusive cost figures for each, it is difficult to make clear and fair comparisons between devices. And despite the variety of metrics that have been used to try and facilitate such comparisons, a sense of comparative performance can often be insightful, even considering the caveats that apply. With particular relevance to the WaveTrain device, a numerical benchmarking study [11] assessed eight types of wave energy device, comparing their performance across four metrics, including Capture Width Ratio (CWR). Though that study used time-domain models, the accuracy of a fully linear model in modelling the WaveTrain (see the penultimate paragraph of Section 5.1) may mean a comparison is quite reasonable. Taking the characteristic width for the WaveTrain to be three times the dimension, D, of a single module, the best performing design (see Fig. 5.17) has a CWR of 0.77. Table 5.9 presents a comparison of this WaveTrain design with the eight device types from [11], as assessed in the EMEC wave climate, as this is most similar to the West Shetland Shelf climate used with the WaveTrain in the present work.

Device type	Capture Width Ratio (%)
Small bottom-referenced heaving buoy	4.2
Bottom-referenced submerged heave buoy	13
Floating two-body heaving converter	29
Bottom-fixed heave-buoy array	16
Floating heave-buoy array	11
Bottom-fixed oscillating flap	68
Floating three-body oscillating flap device	20
Floating oscillating water column	50
WaveTrain device	77

Table 5.9: Capture width ratio of the WaveTrain, and each of eight device types from [11] at the EMEC site.

Clearly, the WaveTrain performs well on this metric, aided by its high power absorption sustained over a wide range of frequencies. A further study comparing the capture width ratios for a much larger set of 156 devices [9] provides a further point of

comparison. Whilst that study used CWR values derived from numerical modelling results for some devices, and CWR values derived from physical testing results for others, the presentation of the multitude of CWRs was conveniently broken down into categories, forming a nice basis for comparison (Fig. 5.30).

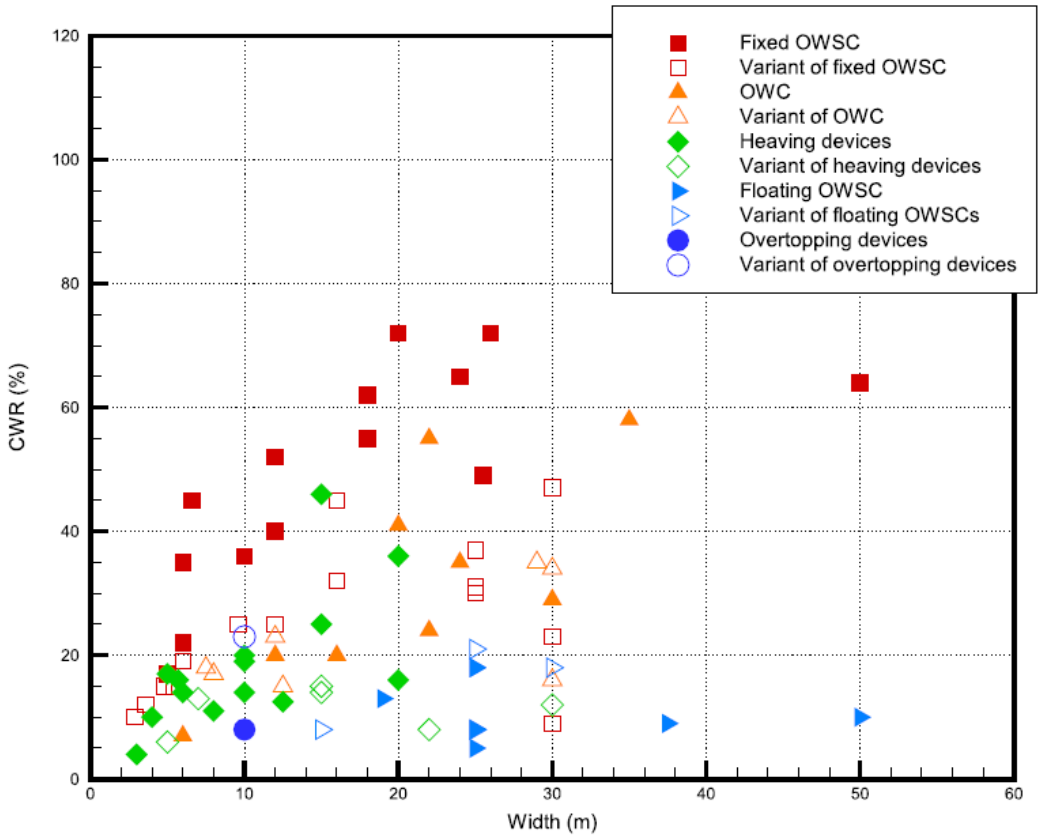

Figure 5.30: Capture width ratio as a function of the WEC characteristic dimension and the WEC category. Reproduced here courtesy of [9].

Again with the caveat of the linear model used, the indication is that the WaveTrain compares very favourably with the range of other existing device concepts. This is especially so when looking at the floating OWC category. However, the WaveTrain is thought to derive its performance from its sloped characteristics and so it may be more appropriate to categorise it as a mixture of a heaving device and a surging device (like the fixed Oscillating Wave Surge Converters, OWSCs, forming the category generally highest in CWR in Fig. 5.30).

However, whereas a single metric allows for some quantitative comparison, a range of factors undoubtedly contribute to the technical or market feasibility of a device. Whereas OWSC devices tend to experience large forces as a result of the large material surface presented to the waves, the WaveTrain is likely to achieve its CWR with much less forceful impact from the water, due to its sloped motion and slender modules. Additionally, the more highly-scoring (on CWR), fixed-bottom OWSC devices require a rigid seabed connection, which could hugely restrict their long term, large scale deployment, as it would likely be costly to install them in deep water environments, where the majority of wave energy is found. Floating OWSCs tend to score much more lowly on CWR (Fig. 5.30).

As proposed for an early full-scale rendition of the WaveTrain under the novel WEC programme of Wave Energy Scotland [2], concrete could provide a substantial proportion of the structure, vastly reducing the manufacturing cost. Therefore, the WaveTrain can score particularly well on any metrics that include a structural cost component.

Of course, the integrity of the joint-connected mechanical struts in between each pair of modules remains difficult to quantify, especially in survival conditions. But the existence of feasible devices across a range of the power- and force-based objective functions (see the well-represented Pareto fronts from Section 5.7.2) allows for some degree of control over this during the design phase. With prudent choices of further development (such as survival tests, and fatigue tests of the joints, at suitable scales), it should be possible to sustain the majority of the WaveTrain's high performance in real sea conditions. The benefits of carrying the high power extracting capability of sloped motion into a deep-water environment are likely to outweigh the complications introduced by the connecting struts and joints between modules.

Chapter 6

Duck Spine Device

6.1 Introduction

It is well known that the shape of the Edinburgh duck allows very efficient absorption of wave energy (see Chapter 1), but as part of a full spine, some coordination amongst the various degrees of freedom is required for maximal power extraction. This problem of how best to actively control a spine of ducks was first approached by Young and Pollock [10], using a pitch-heave-surge rig in a narrow wave tank (Fig. 6.1) to mimic the behaviour of a single member of a full spine of ducks. An automated machine learning technique was used to tune seven control force coefficients for maximal power extraction in a selection of irregular sea states. Power could be extracted through all three degrees of freedom, akin to the manner in which power would be extracted by a member of a full spine via the flexure of the joints and the pitching of the ducks. A key finding was that the optimisation process often led to increased proportions of the total power deriving from the heave and surge motions, especially in longer period waves. This suggests that significant power extraction from the joints of a full spine can be expected. Related work by Salter [71] on long spines of cylindrical modules, not optimised for power extraction, found that oblique wave directions led to much larger bending moments at the down-wave end of the spine. It was believed that flexural waves travelling along the spine were a precursor to this phenomenon, and only occurred with specific heading angles of the waves. It was also suggested that these features could perhaps be exploited by the control moments to yield increased power

extraction, such as was subsequently achieved with Pelamis [72]. The complexities encountered in these two studies shed some light on the expected behaviour, but it is not clear how these phenomena would manifest in a full spine of ducks optimised for power extraction. Bridging the gap between the two aforementioned studies is the primary focus of this chapter, using efficient numerical models and a frequency-domain control technique to investigate the dynamics, loadings and power production of an operational long spine of Edinburgh ducks, with both regular and irregular wave conditions.

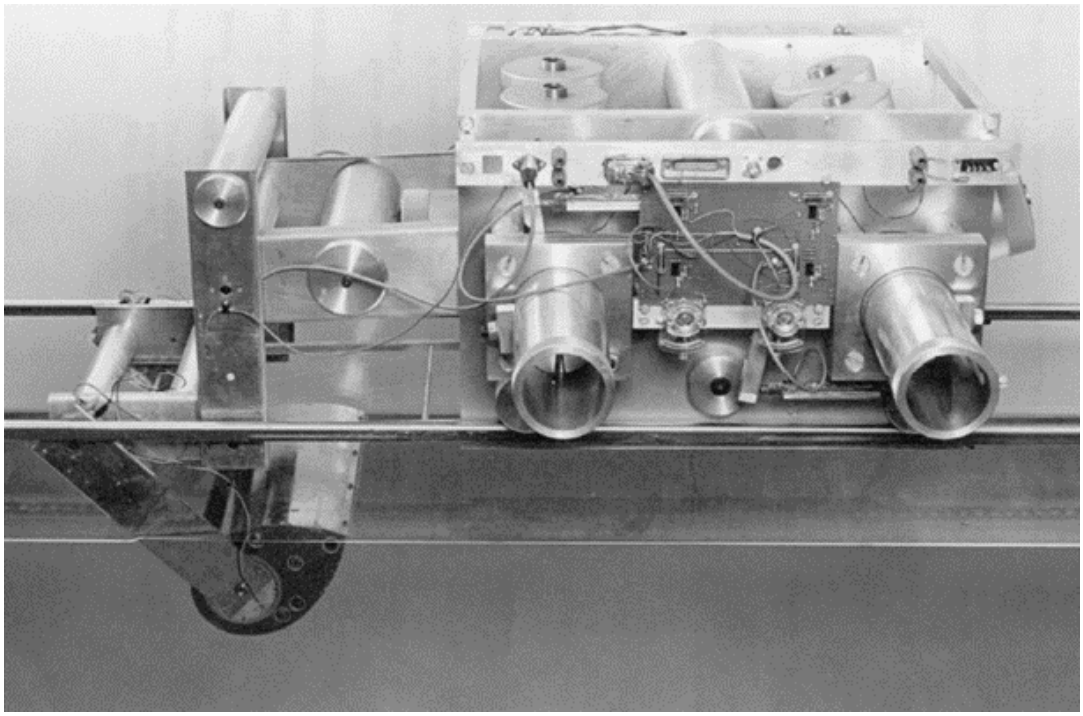

Figure 6.1: A solo duck model connected to the pitch-heave-surge rig. Courtesy of [10].

Whilst benefits only arise from numerical models by extending their range of applicability into the unknown, validation of some base cases can at least help to increase the confidence in the model outcomes. Pizer [44] compared his linear, frequency-domain numerical model of a solo duck with the experimental results of Skyner [24]. Whilst there was a good level of agreement for the hydrodynamic and hydrostatic impedance and particularly the excitation forces, Skyner's experimental results were

intentionally restricted to conditions of linearity. Wu [26] similarly found good agreement between a linear numerical model and experimental results for a solo duck in monochromatic waves, but also found that the nonlinear regimes encountered experimentally do not significantly deviate from the linear regimes, at least for wave periods and heights towards those commonly encountered in real wave climates. The extension of a solo duck to a full spine of ducks does not obviously add any nonlinear behaviour; under the influence of a freak wave, the flexure angle of a physical model of a long spine peaked at only 4°, and under normal conditions was found to be much lower [71]. Considering also that suitable motion constraints imposed through the control strategy (e.g. [8]) can also to some extent prevent unrealistic results, these findings build confidence in the ability of a linear frequency-domain model to explore the dynamics and performance of a full spine of Edinburgh ducks under conditions of optimal power extraction.

6.2 Development of an efficient hydrodynamic model

Using a single geometry and mass distribution for each duck, the full spine can be modelled efficiently in the frequency-domain using generalised modes of motion. As with the corresponding section of the previous chapter, the reader should consult [55] or [28] for further detail regarding the theory or implementation of the hydrodynamic modelling methods described in this section.

6.2.1 Duck design

The duck design used in this study is based on the cross-sectional shape of the D0018 Medium Beak Duck from Jeffrey et al. [73], which was designed to be similar to a member of a full spine. The six ballast tubes from that design are augmented here by a seventh, located much lower in the duck body to help achieve the desired mass distribution (Fig. 6.2).

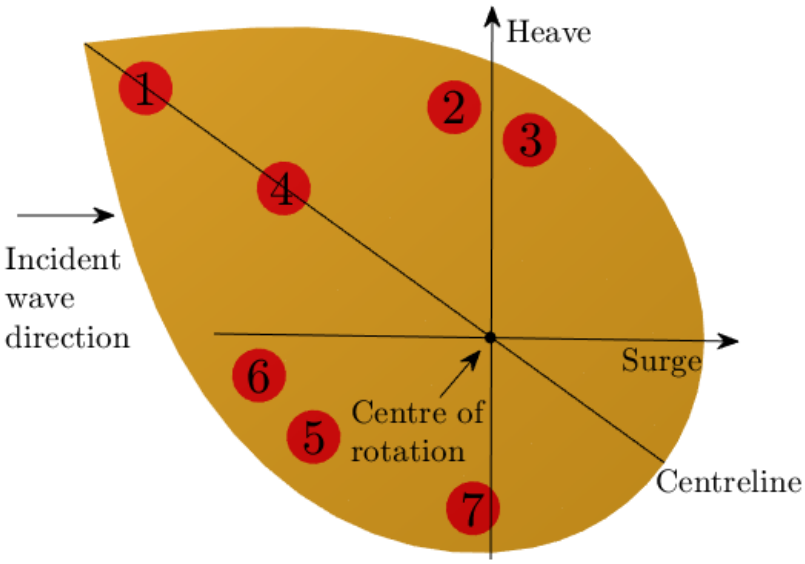

Figure 6.2: Cross-section of a single member of the full spine of ducks, with the seven ballast tubes displayed. Sway is defined into the page, with the axes centred halfway along the spine length.

The ballast tubes are each of constant density and are 1.27m in diameter. Their masses must be selected such that a suitable waterline height and an appropriate centre of gravity location are achieved, whilst satisfying the constraint that the centre of gravity and centre of buoyancy both lie on the same vertical line (Eq. 5.1). The masses used (Table 6.1) result in a waterline height of 4.12m above the centre of rotation, and a centre of gravity 1.65m radially outwards from the centre of rotation, at an angle of 4° anticlockwise from the centreline. This angle is much smaller than that used by Skyner [24], but is closer to the value of around 10° recommended for good capsize recovery [74]. The ballasts are fully defined in Table 6.1, with the radial positions defined from the centre of rotation, and the angular positions defined clockwise from the part of the centreline joining the centre of rotation and the beak tip (the pointed edge of the duck).

Ballast index	Mass (kg)	Radial position (m)	Angular position (°)
1	0	10	0
2	456000	5.5	45
3	312000	4.75	65
4	134000	6	0
5	0	4.75	-65
6	56000	5.5	-45
7	752500	4	-120

Table 6.1: Ballast tube masses and positions.

In its equilibrium position, the centreline is orientated at 36° to the horizontal (as used by Skyner [24] for a solo duck), and the distance from the centre of rotation to the beak tip along the centreline is 11.8m. A width of 29.5m is used for each duck, with a 10.5m spacing between each pair of adjacent ducks, similar to early models [71],[74]. The individual duck used here is statically stable in both pitch and roll (Eqs. 5.2, 6.1), ensuring that the whole device is statically stable.

$$(S_{22}/\forall) + z_b - z_g > 0 \tag{6.1}$$

6.2.2 Full spine and geometry definition

The full spine investigated herein consists of ten ducks, which is deemed the minimum number to achieve adequate stability by spanning multiple wave crests [3]. In practice however, provided that there is space to adjust the axial spacings between ducks as desired, the spine should extend as far as shipping lanes allow in order to maximise the absorbed energy. To visualise the device studied herein, first consider a rigid spine with 5 degrees of freedom - surge, sway, heave, roll and yaw, but not pitch. Adding to this spine 10 ducks, each of which can undergo pitch rotation, and 9 joints, each of which enables rotation in the roll and yaw directions, results in a 33 degree of freedom system (5 + 10 + (9 x 2)). In practice it may be beneficial to allow axial motions between each pair of adjacent ducks in order to maintain the correct separation even under bending of the spine, but this is not relevant to the linear problem investigated in this work. Information on how this system can be modelled using generalised modes

is given in the following section. Figure 6.3 shows the front and plan views of the ten-duck spine, along with the numbering conventions for the ducks and joints, and the definitions of the axes and wave direction.

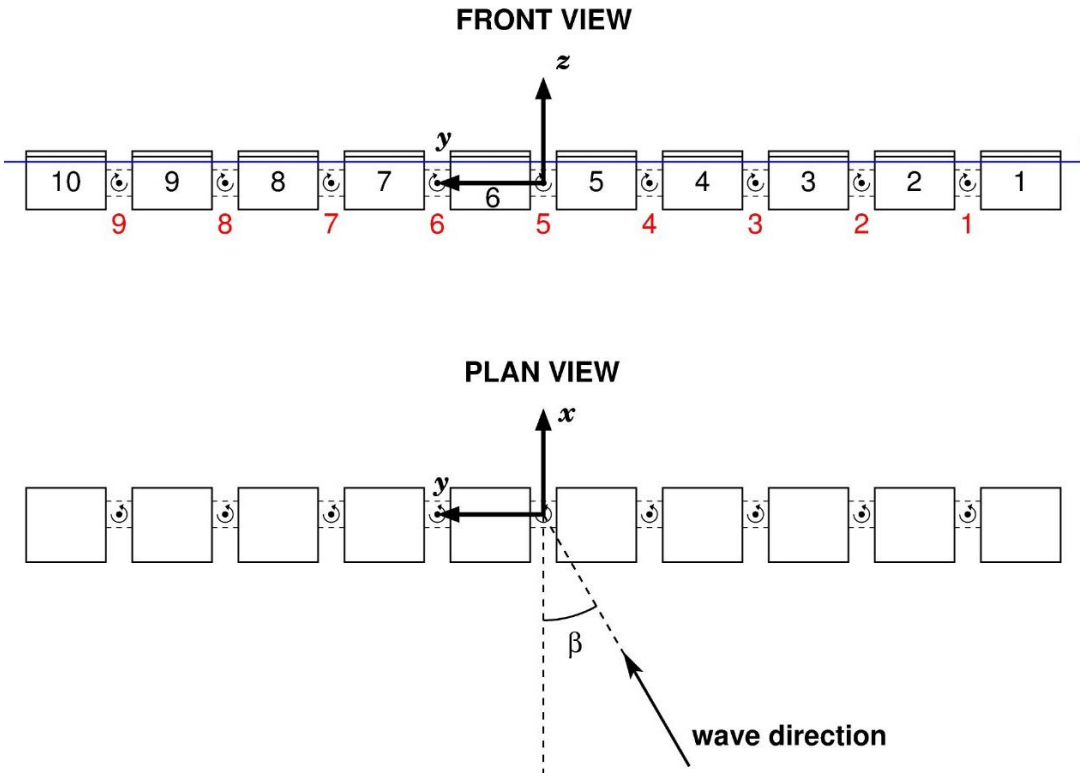

Figure 6.3: Front and plan views of the ten-duck spine, including its two degree of freedom joints. The numbering convention is indicated for the ducks and joints.

The hydrodynamic and inertial properties of the connections between ducks are neglected, and so the discretised mesh (Fig. 6.4) for the whole spine only needs to take into account the shape of the ducks and the spacings between them. WAMIT's 'low-order' method is used for this.

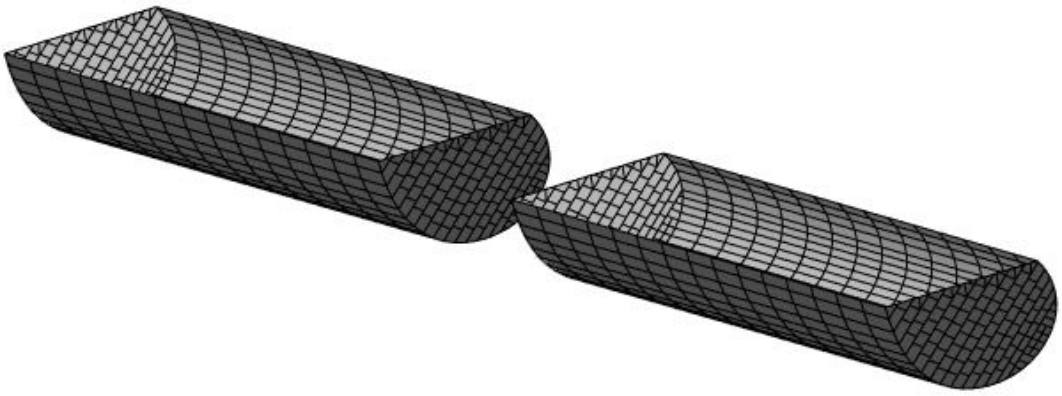

Figure 6.4: A section of the discretised mesh used to compute the hydrodynamic forces that act on the submerged part of the ten duck spine.

6.2.3 Defining the device motions

Given the internally-housed power take-off systems, each of the ten ducks can be modelled as if able to react against a rigid reference frame in the pitch direction, using the assumption that the internal mechanism can always provide the desired torques. Hence it is most convenient to define a generalised mode describing a pitch rotation about the centre of rotation for each duck, whilst locking ('fixing') the rigid body pitch mode (which is associated with the entire assembly of ducks). This ensures that pitch motions of each duck are defined relative to a stationary reference frame, so that any damping or stiffness forces are applied as they would be by an internal power take-off. (See Appendix E for more information regarding this type of decision on the mode definitions.)

Conversely, any forces applied about a spine joint must involve equal and opposite reaction forces applied to the ducks either side. The most convenient way to do this is to define the generalised modes relative to the rigid body yaw and roll modes, which define the motions of the entire freely-floating assembly as if it were rigid. The couplings (inertial, gravitational, hydrodynamic and hydrostatic) amongst all 33 modes of motion govern the effects of all the PTO moments on the spine.

Since all nine joints lie in line with the centre of rotation, the location of each is defined by just its y-coordinate, b_i, as are the modes associated with the pitching

of each duck. Reserving the first five modes ($1 \leq i \leq 5$) for the rigid body motions (surge, sway, heave, roll and yaw), defined over the entire spine as if it were rigid, the shape functions for the pitching of each duck are given by Eq. 6.2.

$$\mathbf{S}_i(\mathbf{x}) = \begin{bmatrix} z \\ 0 \\ -x \end{bmatrix} \text{ for } y \in V_i \text{ and } 6 \leq i \leq 15 \tag{6.2}$$

where V_i denotes the volume associated with duck i.

The shape functions for the joint rotations about the x-axis (akin to roll) are given by Eq. 6.3, whilst those for the joint rotations about the z-axis (akin to yaw) are given by Eq. 6.4.

$$\mathbf{S}_i(\mathbf{x}) = \begin{bmatrix} 0 \\ \mp z \\ \pm(y - b_i) \end{bmatrix} \text{ for } y \lessgtr b_i \text{ and } i \in I_r := [16, 18, 20, 22, 24, 26, 28, 30, 32] \tag{6.3}$$

$$\mathbf{S}_i(\mathbf{x}) = \begin{bmatrix} \mp(y - b_i) \\ \pm x \\ 0 \end{bmatrix} \text{ for } y \lessgtr b_i \text{ and } i \in I_y := [17, 19, 21, 23, 25, 27, 29, 31, 33] \tag{6.4}$$

As for the WaveTrain application from the previous chapter, some complexity lies within the inertial and gravitational restoring terms, especially given the shape for the duck taken from Jeffrey et al. [73], which requires conversion from the non-orthogonal coordinate system into parametric coordinates for the integrals to be evaluated. Nonetheless, the calculations proceed in the same manner as for the WaveTrain application (see Section 5.2.5), using the methods described in Chapter 4. The coordinate transformation for the duck spine between the fixed and displaced reference frames is required for computation of the c_{ij}^g entries. For example, given a coordinate on the duck furthest upstream (duck 1), the transformation is given by Eq. 6.5. Note that $i = 5$ denotes the rigid body yaw mode in this example, followed by $i = 6$ for the generalised mode describing pitching of duck 1.

$$\mathbf{x} = \begin{bmatrix} x' + \xi_1 - \xi_5 y' + \xi_6 z' - \sum_{i \in I_y} \xi_i (y' - b_i) \\ y' + \xi_2 - \xi_4 z' + \xi_5 x' - \sum_{i \in I_r} \xi_i z' + \sum_{i \in I_y} \xi_i x' \\ z' + \xi_3 + \xi_4 y' - \xi_6 x' + \sum_{i \in I_r} \xi_i (y' - b_i) \end{bmatrix} \tag{6.5}$$

Whilst the transformation comprises ten piecewise continuous descriptions along the spine due to the nine joints, each c_{ij}^g and M_{ij} element is dependent on only two discontinuities at most.

6.2.4 Shear forces at the joints

Whilst the spine can flex freely in the rotational degrees of freedom along its sections, translational motions are forbidden in this model, other than those corresponding to movement of the entire spine as a whole. (In a real nonlinear system, it may be practically beneficial to allow some surge translation at the joints, primarily to maintain the horizontal module spacings.) By setting up three additional, 'fixed' generalised modes for each joint (defined by the shape functions in Eq. 4.11), the shear forces can be analysed. (See Sections 3.4 and 4.4 for more details.)

This gives 60 modes in total, for which the radiation potentials (and diffraction potential) are solved. Table 6.2 gives a summary of these modes.

Mode type, free	Quantity	Mode type, fixed	Quantity
Rigid body	5	Joint shear forces, surge	9
Duck pitch	10	Joint shear forces, sway	9
Joint flexure (in roll & yaw directions)	18	Joint shear forces, heave	9
Total:	33	Total:	27

Table 6.2: Summary of the modes (rigid body and generalised) used in the duck spine hydrodynamic model.

6.2.5 Verification of modelling approach

Again, due to the complexity in computing the inertial and gravitational properties of the full duck spine, further verification has been carried out using the alternative approach in the time domain (see Section 3.6). To shorten the runtime of the time-domain model, a spine of only three ducks has been considered. As the computation of the c_{ij}^{g} and M_{ij} coefficients is scripted in a general manner, allowing the selection of any number of ducks, this still strongly verifies the implementation of the more efficient method. Figure 6.5 shows a comparison between the magnitudes of the RAOs

(normalised by wave amplitude) obtained from both methods, for an undamped spine of three ducks, with an incident wave heading of 30°.

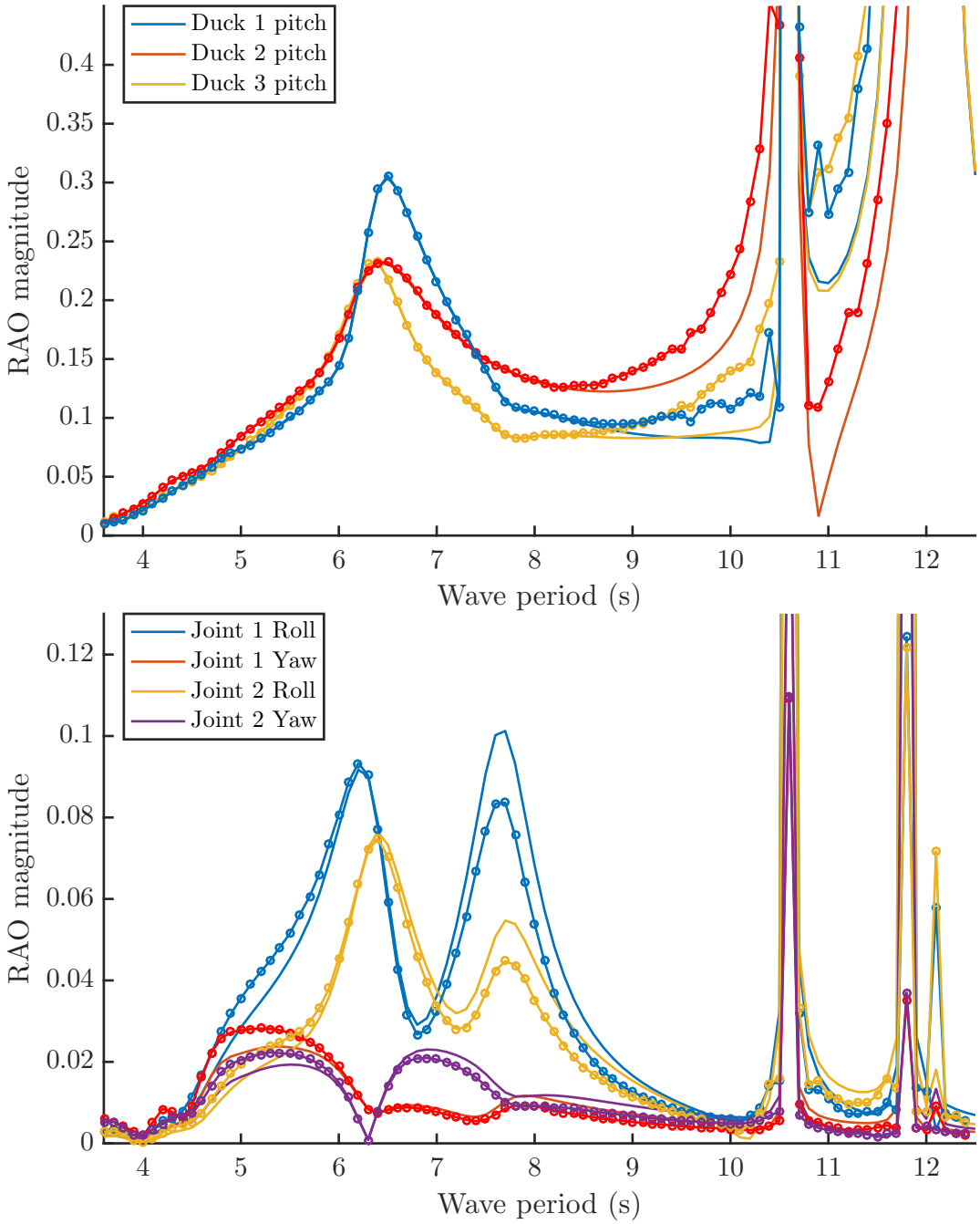

Figure 6.5: Verification of the modelling approach. Solid lines with circles: time-domain approach. Solid lines: frequency-domain approach using generalised modes. The RAO magnitudes are measured in radians per metre of incident wave amplitude.

A lack of runtime of the time-domain model explains the discrepancy for higher wave periods. In the case of the joint RAOs, the discrepancy at lower wave periods could be explained by the numerical differences in modelling the two systems, especially given the lower absolute values.

6.3 Complex conjugate control - using motion constraints

Fundamentally, complex conjugate control (CCC) is the process of optimising the absorbed power by tuning the applied PTO forces and/or moments in the frequency-domain. A component 90° out of phase with the body velocity (often provided as stiffness forces, proportional to the body displacement) enables a cancelling of the phase difference between the wave forces and the body velocity. A second, in-phase component of the forces/moments damps the body velocity so as to tune the magnitude of the body velocity. Both force components together enable the optimal power absorption, and can analytically be derived for the case of monochromatic incident waves, in terms of the hydrodynamic, inertial, gravitational and hydrostatic properties.

Since the time-averaged power is only dependent on the damping coefficients and the body velocities, it is convenient to express the equations of motion in terms of those velocities (Eq. 6.6, 6.7). Eq. 6.6 also defines the control matrix, $\hat{\mathbf{C}}$, proportional to the velocity, so that its real part corresponds to the PTO damping and the imaginary part to a PTO stiffness (or alteration of the mass or added mass).

$$\mathbf{F}_c = \mathbf{Z}\mathbf{U} - A\mathbf{X} = -\hat{\mathbf{C}}\mathbf{U} \tag{6.6}$$

$$\mathbf{Z} = \mathrm{i}\omega(\mathbf{A} + \mathbf{M}) + \mathbf{B} - \frac{\mathrm{i}}{\omega}\mathbf{C} \tag{6.7}$$

The absorbed power is given by the product of the instantaneous control force and the instantaneous velocity, for each degree of freedom. With both the control forces and velocities of sinusoidal form, this can be separated into a constant component, and an oscillatory component with twice the wave frequency. Over periods of time much

greater than the wave period, the mean power is given by just the first component (Eq. 6.8). († denotes complex conjugate transpose)

$$\mathbf{P}(\mathbf{U}) = \frac{1}{2} Re\{\mathbf{U}^\dagger \mathbf{F}_c\} \tag{6.8}$$

By substituting the control forces, $\mathbf{F}_c$, from Eq. 6.6 into Eq. 6.8, algebraic manipulation then enables the time-averaged power to be reexpressed as Eq. 6.9.

$$\mathbf{P}(\mathbf{U}) = \frac{A^2}{8}\mathbf{X}^\dagger \mathbf{B}^{-1}\mathbf{X} - \frac{1}{2}(\mathbf{U} - \frac{A}{2}\mathbf{B}^{-1}\mathbf{X})^\dagger \mathbf{B}(\mathbf{U} - \frac{A}{2}\mathbf{B}^{-1}\mathbf{X}) \tag{6.9}$$

The first term represents the power in the incident, diffracted waves, whilst the second term of opposite sign represents the power radiated away by the body. The optimal power absorption is given when this second term vanishes. The velocities (of the body) under this condition are given by Eq. 6.10.

$$\mathbf{U}^{opt} = \frac{A}{2}\mathbf{B}^{-1}\mathbf{X} \tag{6.10}$$

By substituting these optimal velocities back into Eq. 6.6, the control matrix is determined to be the complex conjugate of $\mathbf{Z}$ - hence the name of this control technique.

$$\hat{\mathbf{C}} = \mathbf{Z}^* \tag{6.11}$$

This control technique is underpinned by the assumptions of linear wave theory, and by the very nature of maximising the absorbed power under these conditions, unrealistically large body motions can result, especially for longer wave periods. In order to retain the use of complex conjugate control, without admitting unrealistic motions, a constraint must be enforced. Eq. 6.12 [8] defines the constraint relative to the velocities, with the diagonal matrix, $\mathbf{\Gamma}$, comprising the weightings, γ_i, associated with each degree of freedom i. As it is the combination of the body motions over which the restriction applies, this is perhaps best described as a 'linearity constraint'.

$$\mathbf{U}^\dagger \mathbf{\Gamma}^{-2} \mathbf{U} \leq 1 \tag{6.12}$$

Using the method of Lagrange multipliers, maximising the absorbed power subject to the motion constraint is equivalent to solving Eq. 6.13, given the auxiliary function

$\mathbf{Q}$ (Eq. 6.14). The partial derivative with respect to the complex vector, $\mathbf{U}$, is defined as the partial derivatives with respect to both the real and imaginary parts of $\mathbf{U}$.

$$\begin{bmatrix} \frac{\partial \mathbf{Q}}{\partial \mathbf{U}} \\ \frac{\partial \mathbf{Q}}{\partial \mu} \end{bmatrix} = 0 \tag{6.13}$$

$$\mathbf{Q}(\mathbf{U}, \mu) = \mathbf{P}(\mathbf{U}) - \frac{1}{2}\mu(\mathbf{U}^{\dagger}\boldsymbol{\Gamma}^{-2}\mathbf{U} - 1) \tag{6.14}$$

Evaluating the top row of Eq. 6.13 and rearranging for $\mathbf{U}$, gives the optimal velocities (subject to the constraint) in terms of the positive Lagrange multiplier, μ (Eqs. 6.15, 6.16).

$$-\mathbf{B}(\mathbf{U} - \frac{A}{2}\mathbf{B}^{-1}\mathbf{X}) - \mu\boldsymbol{\Gamma}^{-2}\mathbf{U} = 0 \tag{6.15}$$

$$\mathbf{U}^{opt} = \frac{A}{2}(\mathbf{B} + \mu\boldsymbol{\Gamma}^{-2})^{-1}\mathbf{X} \tag{6.16}$$

Substituting these optimal velocities into the second row of Eq. 6.13 yields a scalar equation, from which μ can be obtained (Eq. 6.17). See [8] for more details regarding the solution of this equation.

$$\mathbf{X}^{\dagger}\boldsymbol{\Gamma}(\boldsymbol{\Gamma}\mathbf{B}\boldsymbol{\Gamma} + \mu\mathbf{I})^{-2}\boldsymbol{\Gamma}\mathbf{X} = \frac{4}{A^2} \tag{6.17}$$

Similarly to unconstrained CCC, substituting the optimal velocities into Eq. 6.6 yields the control matrix (Eq. 6.18).

$$\hat{\mathbf{C}} = \mathbf{Z}^{*} + 2\mu\boldsymbol{\Gamma}^{-2} \tag{6.18}$$

Note that this comprises extra positive damping terms, in order to maintain body motions within the confines of the motion constraint. This over-damped case would not necessarily be the optimal strategy in the corresponding real, nonlinear system, but it at least gives a less inaccurate analysis by excluding control cases that depend on unrealistic motions.

Throughout this section so far, in both the unconstrained and constrained cases, it has been assumed that power can be extracted via all degrees of freedom. This may not always be the case; some degrees of freedom (DoFs) may be uncontrolled. In those

systems, the equations of motion can be written explicitly in terms of the controlled and uncontrolled (or 'free') degrees of freedom (Eq. 6.19).

$$\begin{bmatrix}\mathbf{F}_c \\ \mathbf{0}\end{bmatrix} = \begin{bmatrix}\mathbf{Z}_{cc} & \mathbf{Z}_{cf} \\ \mathbf{Z}_{fc} & \mathbf{Z}_{ff}\end{bmatrix}\begin{bmatrix}\mathbf{U}_c \\ \mathbf{U}_f\end{bmatrix} - A\begin{bmatrix}\mathbf{X}_c \\ \mathbf{X}_f\end{bmatrix} \tag{6.19}$$

where A is the wave amplitude, subscripts c and f are used to denote components relating to the controlled and uncontrolled modes, respectively, $\mathbf{X}$ denotes excitation forces, $\mathbf{F}$ the control forces, and $\mathbf{Z}$ is the intrinsic impedance defined relative to the velocities, $\mathbf{U}$.

It is necessary to use the control forces to optimise the controlled velocities, $\mathbf{U}_c$, in order to maximise power extraction. However, coupling between the controlled and free DoFs encapsulates a dependence of the motions of the controlled modes on the motions of the free modes. The equations of motion of the free modes can be used to rewrite the equations of motion of the controlled modes (Eqs. 6.20, 6.21, 6.22).

$$\mathbf{F}_c = \mathbf{Z}_{cc}^m\mathbf{U}_c - A\mathbf{X}_c^m \tag{6.20}$$

$$\mathbf{Z}_{cc}^m = \mathbf{Z}_{cc} - \mathbf{Z}_{cf}\mathbf{Z}_{ff}^{-1}\mathbf{Z}_{fc} \tag{6.21}$$

$$\mathbf{X}_c^m = \mathbf{X}_c - \mathbf{Z}_{cf}\mathbf{Z}_{ff}^{-1}\mathbf{X}_f \tag{6.22}$$

As stated in [44], Eq. 6.20 can then be subjected to the same method presented in [8], provided that the motion constraint applies only to the controlled modes of motion. The power is of the same form as for the case with no uncontrolled degrees of freedom (Eq. 6.23). ($\mathbf{B}_{cc}$ is the real part of $\mathbf{Z}_{cc}^m$.)

$$\mathbf{P}(\mathbf{U}_c) = \frac{A^2}{8}\mathbf{X}_c^{m\dagger}\mathbf{B}_{cc}^{-1}\mathbf{X}_c^m - \frac{1}{2}(\mathbf{U}_c - \frac{A}{2}\mathbf{B}_{cc}^{-1}\mathbf{X}_c^m)^\dagger\mathbf{B}_{cc}(\mathbf{U}_c - \frac{A}{2}\mathbf{B}_{cc}^{-1}\mathbf{X}_c^m) \tag{6.23}$$

From Eq. 6.19, the uncontrolled velocities, $\mathbf{U}_f$, are dependent on the controlled velocities, $\mathbf{U}_c$ (Eq. 6.24). Since the controlled velocities are optimised without consideration for the uncontrolled velocities, unrealistically large motions could still result in those 'free' modes.

$$\mathbf{U}_f = \mathbf{Z}_{ff}^{-1}(A\mathbf{X}_f - \mathbf{Z}_{fc}\mathbf{U}_c) \tag{6.24}$$

For completeness, the optimal velocities (of the controlled modes) in this case are given by Eq. 6.25 and the control matrix by Eq. 6.26.

$$\mathbf{U}_c^{opt} = \frac{A}{2}(\mathbf{B}_{cc} + \mu\boldsymbol{\Gamma}_c^{-2})^{-1}\mathbf{X}_c^m \tag{6.25}$$

$$\hat{\mathbf{C}} = \mathbf{Z}_{cc}^{m*} + 2\mu\boldsymbol{\Gamma}_c^{-2} \tag{6.26}$$

Under certain wave conditions, the constraint may not be active (for instance, when the wave amplitude is very small), in which case the multiplier vanishes. The optimal velocities and control matrix in that case are given by Eqs. 6.27 and 6.28.

$$\mathbf{U}_c^{opt} = \frac{A}{2}\mathbf{B}_{cc}^{-1}\mathbf{X}_c^m \tag{6.27}$$

$$\hat{\mathbf{C}} = \mathbf{Z}_{cc}^{m*} \tag{6.28}$$

Whilst it may be useful in practice to diagonalise the control matrix (for purposes of not requiring communication between spatially separated degrees of freedom, as in a WEC array), the control matrix is, in general, fully populated. However, it may be possible to diagonalise the control matrix in specific applications, but that is beyond the scope of the present work.

6.4 Duck spine dynamics under optimal power generation

(Note that the work in this subsection forms a substantial part of a recent paper that was presented at the European Wave and Tidal Energy Conference, held in Naples [75].) Constrained complex conjugate control is applied to only the 28 controlled degrees of freedom, using either Eq. 6.26 or Eq. 6.28 to define the control matrices, depending on whether the wave amplitude, period and heading angle combine to cause excess of the motion constraint in the unconstrained case.

For further verification that the control method is implemented correctly, the power was computed for a solo duck in waves of 1m amplitude and a 40° heading, and compared to the equivalent result from [8] (Fig. 6.6). The plots are very similar, despite a slightly broader plot for the duck used in the present study. Maximal performance

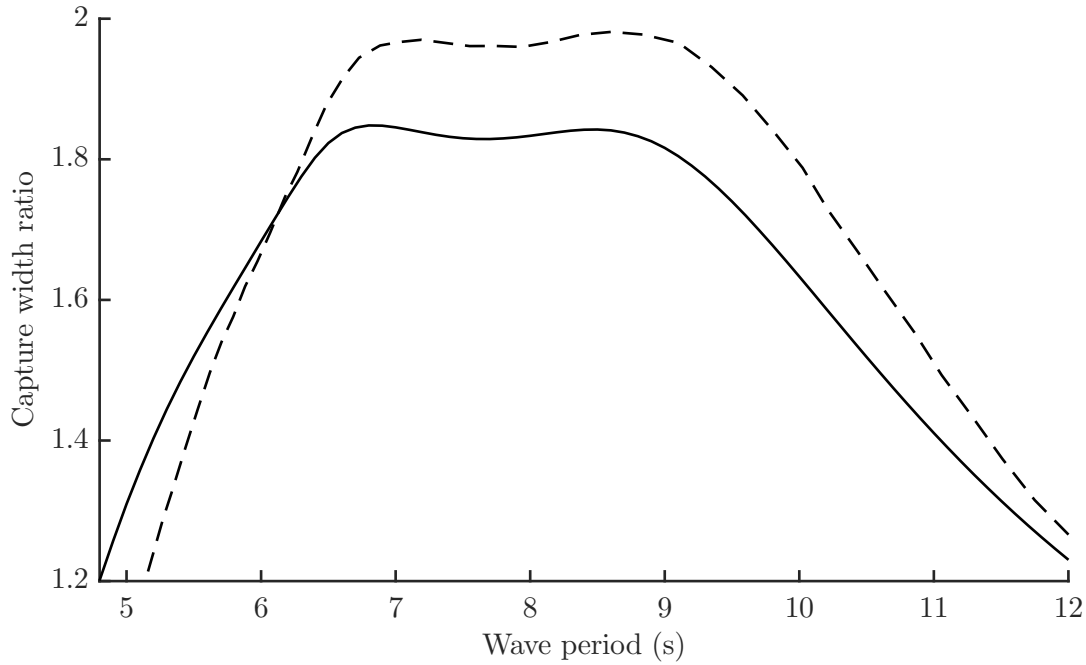

Figure 6.6: Efficiency of single duck in 40° oblique waves, 1m wave amplitude, with motion constraints. Dotted line: Result from [8]. Solid line: Result from the present study. Data is only available from both sources for the variable ranges indicated on the axes.

differs a little due to the different geometries and mass distributions, but is deemed similar enough to substantiate the use of the duck design introduced in this study.

The full spine of ducks was analysed in monochromatic waves over a range of wave periods (4 to 15s in 0.1s increments) and incident wave angles (0 to 90° in 10° increments). 0° corresponds to the case where the incident wave direction is perpendicular to the spine, and at 90° the wave direction is parallel to the spine. Though the range of wave periods likely to be encountered in a real sea may go beyond the upper limit of 15s, this is deemed large enough to gain useful insight into the behaviour of a full duck spine in this study. The weighted global constraint was set following the example given by Pizer [8]. Motion constraint weightings of $\beta_i = 0.5$rad for the pitch angle of each duck and $\beta_i = 0.2$rad for each joint degree of freedom are set. These are related to the velocity constraint weightings (the elements of $\mathbf{\Gamma}$) by the wave frequency: $\gamma_i = \omega\beta_i$. These provide a particularly conservative case in this application, given that a larger number of degrees of freedom increases the severity of

the constraint, when using the same constraint weightings. The wave amplitude was set to 1m for all wave conditions.

Devising a fair measure of performance for a device based on multiple operating principles (i.e. extracting power through different types of degrees of freedom) is not trivial. Capture Width Ratio (CWR) provides insight into the efficiency of a device, but the spine of ducks can extract power through acting both as a terminator (ducks pitching) and as an attenuator (joints flexing). Both these modes of operation can readily occur simultaneously, especially in oblique waves. Considering its operation as a terminator device, when the primary power generation will be due to the ducks pitching, it is also not clear what to set as the characteristic length for the CWR. The duck spine is somewhat like a tightly-packed, one-unit-deep array of devices, albeit with jointed connections to stabilise their locations relative to one another. The question remains whether it is fairer to use the entire spine length or just the width spanned by the ducks themselves. It is also unclear as to whether CWR can fairly be used to compare the inherent value of the duck pitch motions with that of the joint flex motions. Despite these doubts, CWR can give a useful indication of performance. The total length of the spine is adopted here as a conservative characteristic length, for all modes of power generation, but it should be borne in mind that in general it is not appropriate to compare the CWR used in this thesis to CWRs of other devices. The metric is simply used to give a better indicator of performance in sea states of different energies, than power alone would. Fig. 6.7 shows good performance over a wide range of wave periods and angles. The highest efficiencies can be maintained for a wide range of wave periods, especially if the orientation of the spine can adapt sufficiently as the predominant wave period changes. The results here suggest that a duck spine may yield optimal performance when angled away from the incoming wave direction by somewhere between 10° and 30°, and perhaps even more for wave periods longer than 10s. However, enlarging the ducks could mitigate any further required increase in the orientation angle of the spine. A zigzag spine configuration may also be able to achieve the higher performance, whilst avoiding the need to skew the overall orientation of the

spine. Additionally, the motion constraints impact the power extraction most heavily for the lowest wave angles, particularly 0° and 10°. Since these are the regions in which more power comes from the duck pitch motions, it is clear that the overly restrictive constraints bias against the duck pitch power extraction. Whilst it was not in the scope of the present study to assess the full power generating potential of the duck spine, future work should investigate the appropriateness of the motion constraints, and indeed duck shape and design.

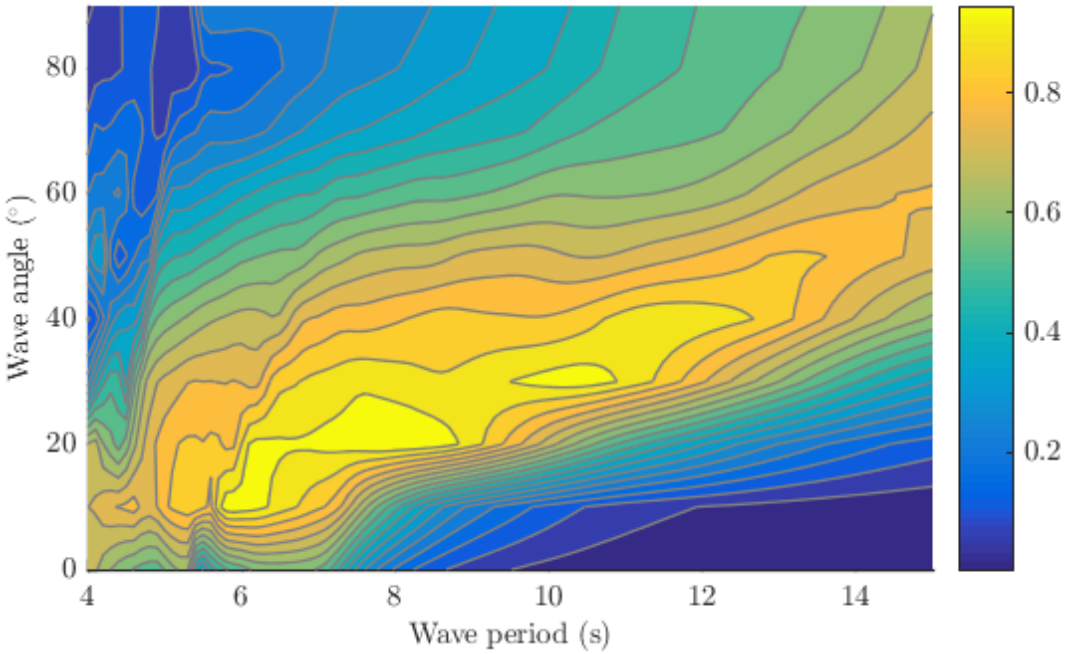

Figure 6.7: Total capture width ratio of the duck spine system under constrained optimal power generation.

This performance profile is provided by the complementary power extraction through the three types of rotation (duck pitch, and roll and yaw about each joint). In general, the ducks provide more power than the joints at lower wave periods, even for the most oblique of wave angles (Fig. 6.8). Beyond a wave period of around 8s, the ducks produce a much diminished amount of power, even for 0° waves (Fig. 6.9). This suggests that the scale of the ducks chosen here would be too small for many sea states, in which more energy is contained in wave components of period greater than 8s. One

must also bear in mind the previously noted point on the stringency of the motion constraints.

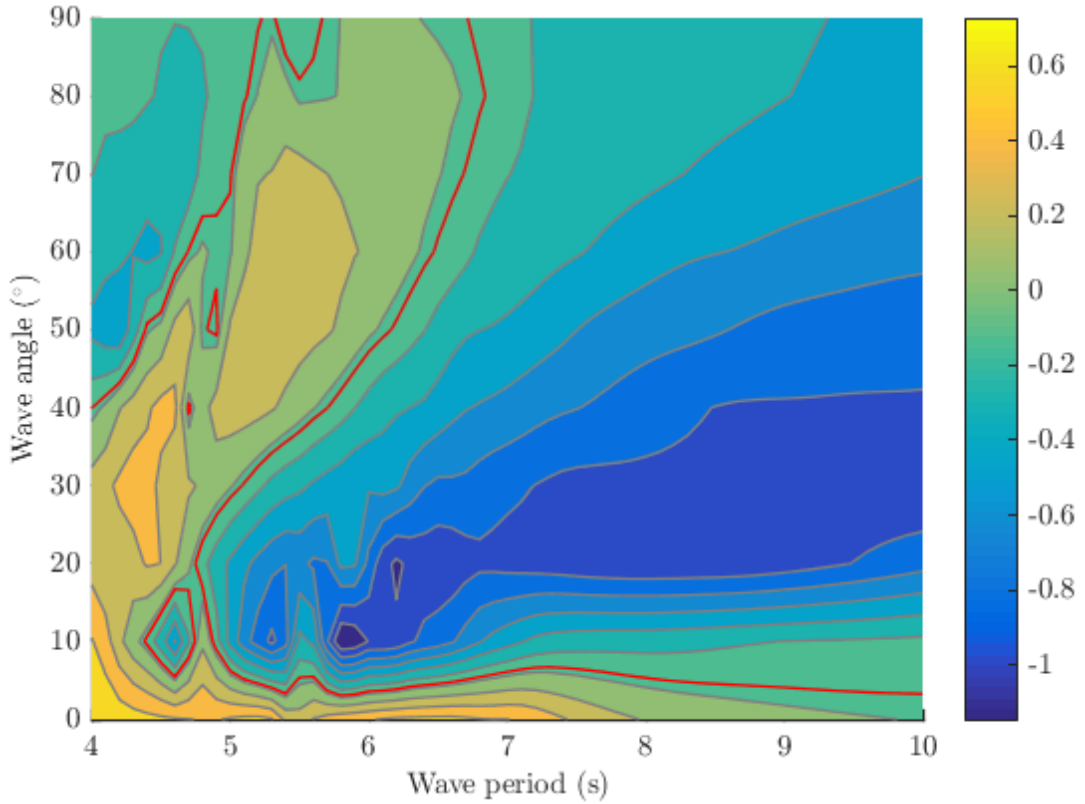

Figure 6.8: Difference in capture width ratio contributions from duck pitching and joint flexing. In yellow regions, more power is extracted through pitching of the ducks than by the flexing of the joints. The red line shows the boundary along which capture width contribution of duck pitching and joint flexing is equal.

Whilst the peak in power extracted through the ducks pitching is achieved with 0° incident waves (Fig. 6.9), the joints tend to require obliquity of the incoming waves for significant power extraction (Figs. 6.10, 6.11). Through the yawing of the modules about the joints, the most significant amounts of extracted power occur for longer wave periods and heading angles around 45° (Fig. 6.11). As the wave period becomes much longer and as the heading angle approaches 90°, the amount of power extracted through the roll motions about the joints increases (Fig. 6.10). In the upper right corner of Fig. 6.10, very large amounts of power are generated, with the duck spine more optimally configured to operate as an attenuator device, e.g. Pelamis

[72]. However, the efficiency is lower in these higher wave periods (Fig. 6.7), and so the device is better operated in a region where the ducks are designed to pitch more significantly.

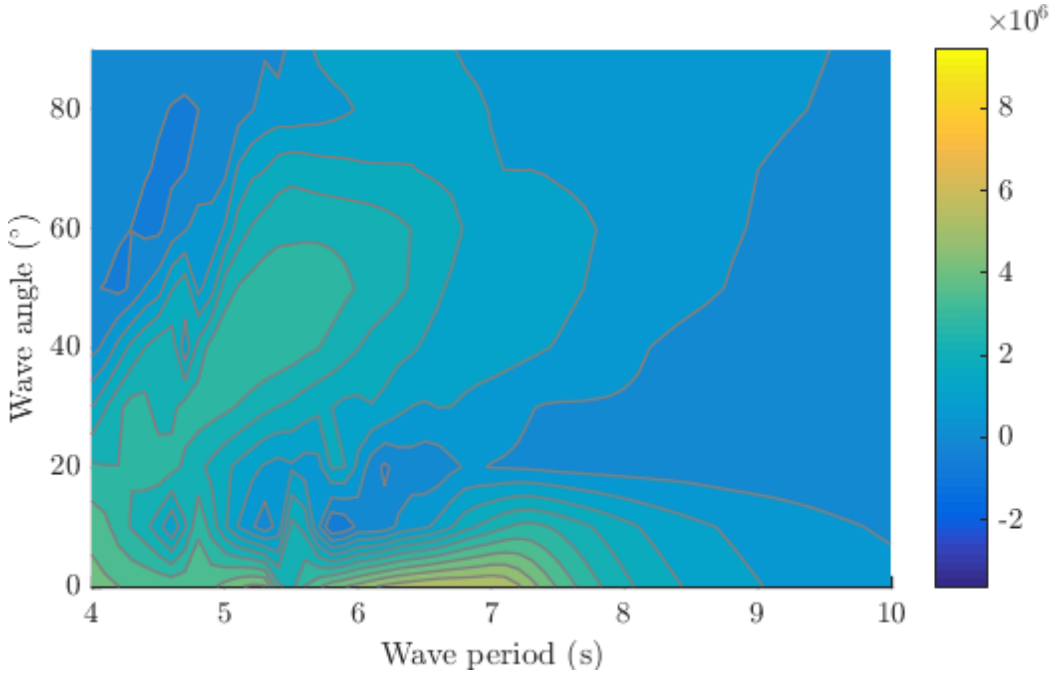

Figure 6.9: Power extraction through duck pitch motions, measured in Watts. Duck dimensions are those given in Section 6.2.1.

Under the current control strategy, net power is often input to various degrees of freedom, in order to increase the net power extraction through other degrees of freedom. This can even be seen over groups of degrees of freedom. At a wave angle of 10° and wave periods below 6s, the power extracted by the joint flexure in roll is particularly high (Fig. 6.10). Those three peaks in power extraction are mirrored by peaks of net power input (i.e. negative power extraction) through the duck pitch and joint yaw degrees of freedom. In other words, the high amount of power extracted at low wave periods through the joint roll modes must be accompanied by large power input into the joint yaw and duck pitch modes.

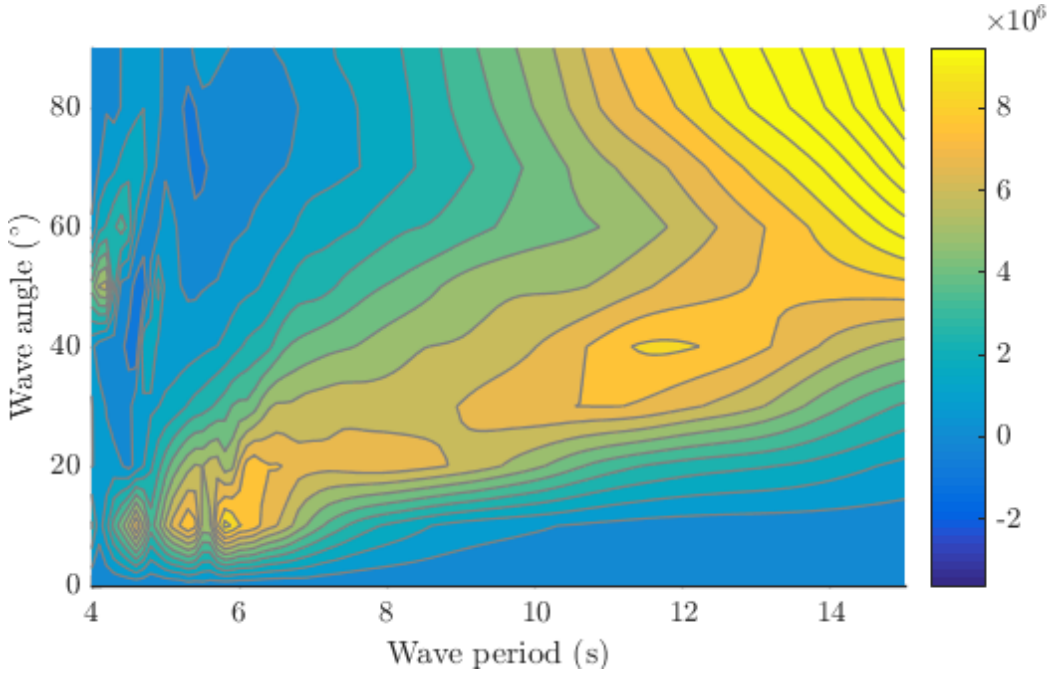

Figure 6.10: Power extraction through joint roll motions, measured in Watts. Duck dimensions are those given in Section 6.2.1.

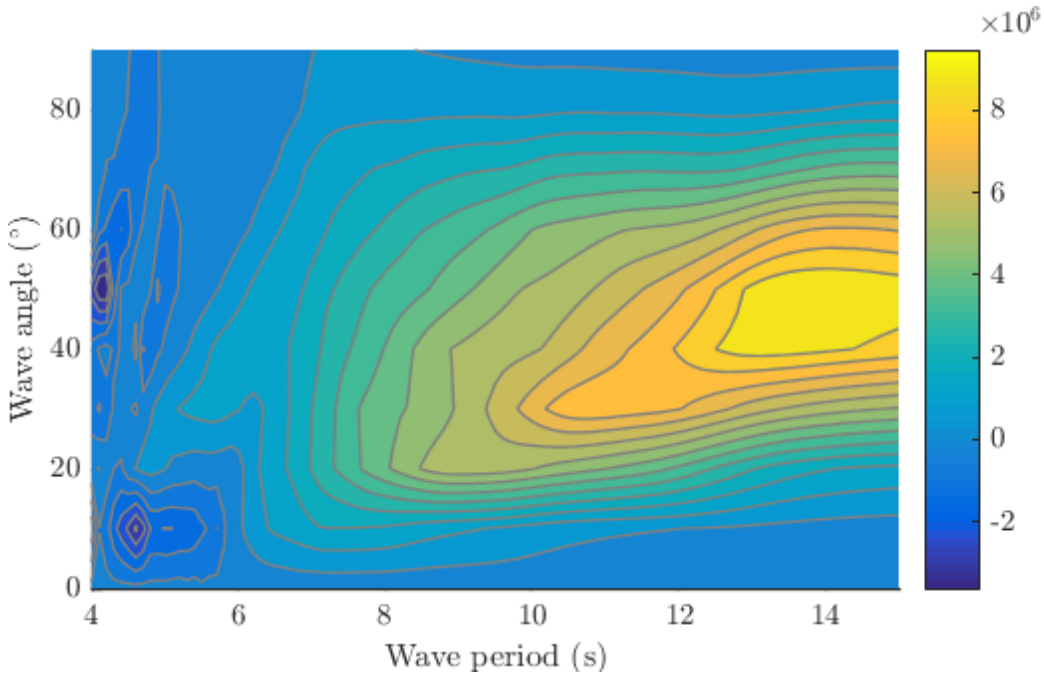

Figure 6.11: Power extraction through joint yaw motions, measured in Watts. Duck dimensions are those given in Section 6.2.1.

Hence, one cannot make any inferences about the relative importance of the various degrees of freedom on the basis of the breakdown of the power extraction alone; higher powers extracted through one type of degree of freedom may only be possible in the presence of strong coupling with other degrees of freedom. Nonetheless, it is evident that significant amounts of power can be derived from the spine joints, even when considering just small incident wave angles, which may be expected in the directional spread of a full sea state.

As a result of the control strategy, some interesting trends emerge regarding the relative amount of power extraction via different degrees of freedom. The power extraction of joints closer to the centre of the spine is often more dominant in different types of sea state to the power extraction by joints toward the ends of the spine (Fig. 6.12 shows an example of this). A positive difference in power corresponds to more power being extracted through the end joints than central ones. A series of bands are present in the example of Fig. 6.12, corresponding to complementary behaviour of the outermost and innermost spine joints. In other words, there are regions in which power is injected into the outermost joints, for the benefit of increased power extraction via the central joints, and there are regions in which the opposite is true (the inner joints act as power injectors for increased extraction through the end joints). These two regimes alternate as the period-angle space is traversed. With a 3D view, this is seen as a series of waves in the period-angle coordinate space. This behaviour is accompanied by much higher peak power extraction through the innermost joint roll modes, demonstrated by the blue and green regions of Fig. 6.12 (also note the difference in scale for the extremes in colour). As shown by the complementary orange and yellow regions, however, the power extracted via the outermost joint roll modes is much lower, but more consistent across all sea states. The high difference in these regions is thus mainly caused by greater power input to the innermost joint roll modes, for the benefit of greater power extraction elsewhere.

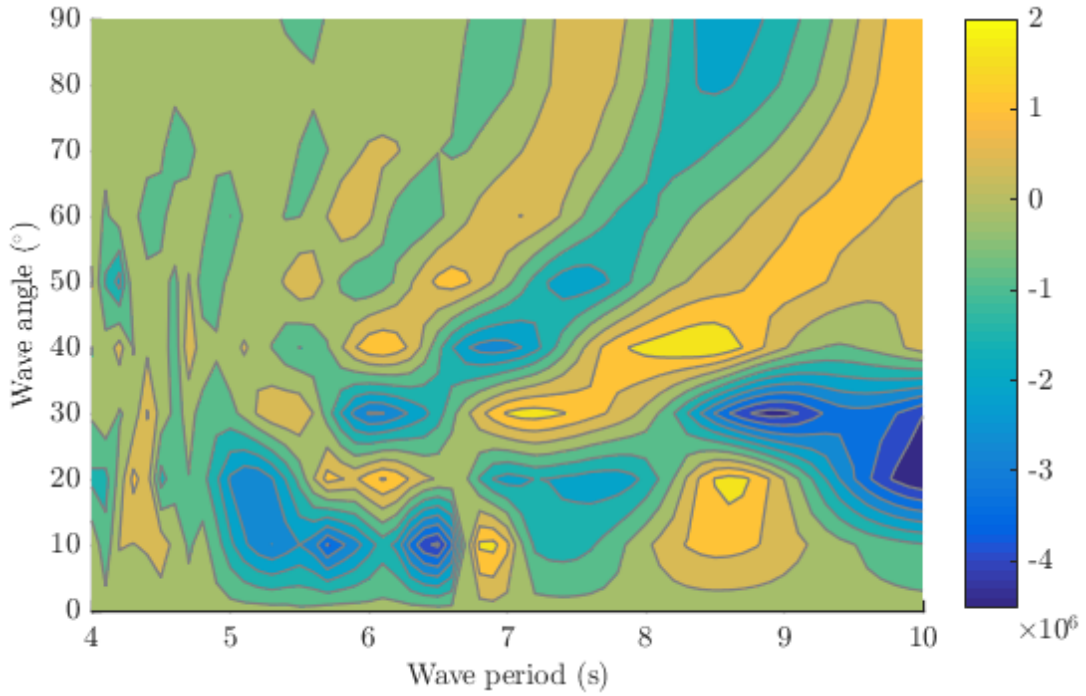

Figure 6.12: Difference in power extraction through roll degrees of freedom of joint 9 (aft joint) and joint 5 (central joint); Power (joint 9 roll) – Power (joint 5 roll). Measured in Watts. Note the difference in the sizes of the positive and negative extreme values.

Trends along the spine in the power extraction from duck pitch modes are more elusive, with the behaviour appearing to contain more complexity. Peak power extraction by ducks closer to the downstream end of the spine occurs at an angle of 0°, whilst for ducks at the upstream end, this occurs at 10° (e.g. Fig. 6.13). For most ducks, there are sea states in which they are net power extractors, and others in which they are net power injectors. Often, this sink-source type of behaviour occurs in closely separated regions of the period-angle space (e.g. Fig. 6.13).

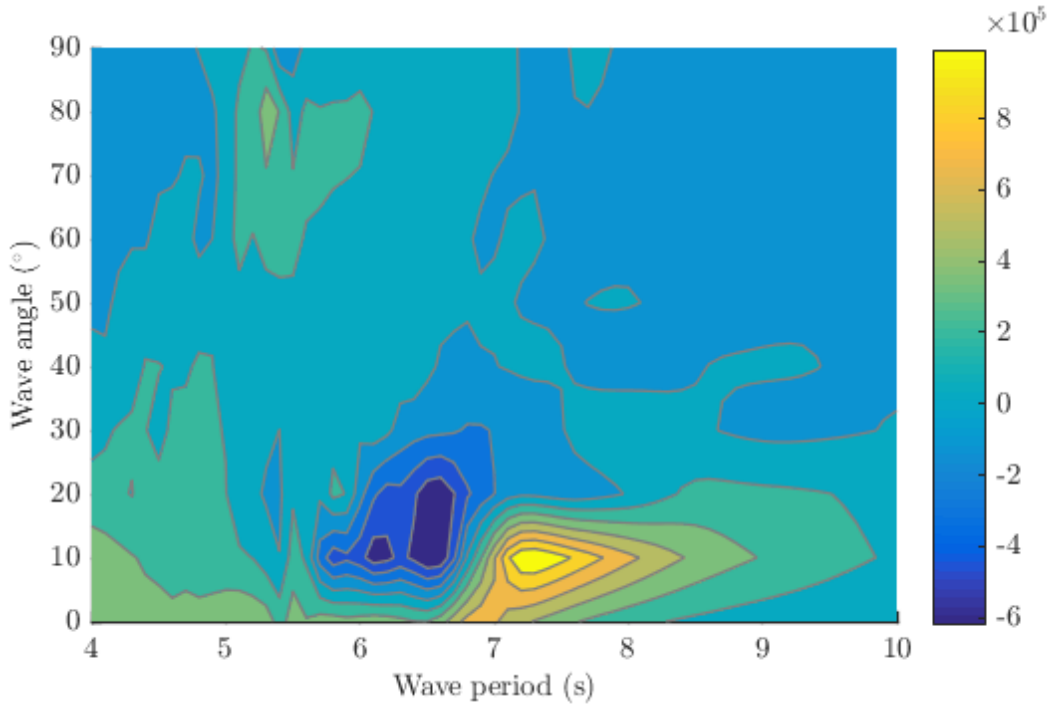

Figure 6.13: Power extraction via pitching of duck 1 (upstream end of spine), measured in Watts.

Also of interest are the shear forces and control moments involved in the power-extracting duck spine. For joint roll degrees of freedom and small wave angles (0° to 20°), the moments required by the control strategy tend to be greater towards the centre of the spine (Fig. 6.14). Similar trends hold for the control moments imparted at the joints in yaw.

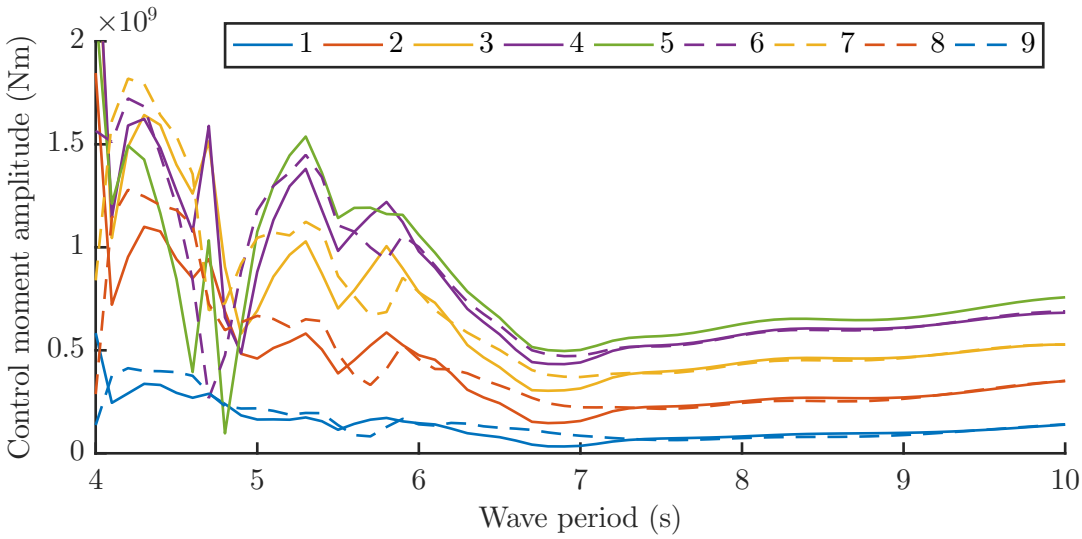

Figure 6.14: The moments demanded by the control strategy for the joint roll degrees of freedom, with a wave heading of 10°. Joints are numbered from fore to aft (see legend).

At lower wave periods, more complex behaviour emerges, and for greater wave angles, the demanded moments significantly increase at these low wave periods. This raises questions over the practical feasibility of maintaining high efficiencies for low wave periods and higher wave angles. Shear forces at the joints in sway (along the spine) are at least an order of magnitude lower than those in the surge and heave directions. For almost all wave angles and periods, the shear forces at the joints in the heave and surge directions are greatest at the outermost joints. Only for lower wave angles is this accompanied by lower control moments in the joints. Perhaps in these cases, the greater control forces have some causal relation with the reduction in the shear forces at the nearby joints. However, this argument does not hold for higher wave angles, where the control forces do not differ significantly along the length of the spine, yet shear forces do. Between periods of around 5 to 7s and angles of 10 to 60°, the heave shear forces are greater at the most downstream joint than at the most upstream one (e.g. Fig. 6.15). This trend reverses for wave periods above about 7s.

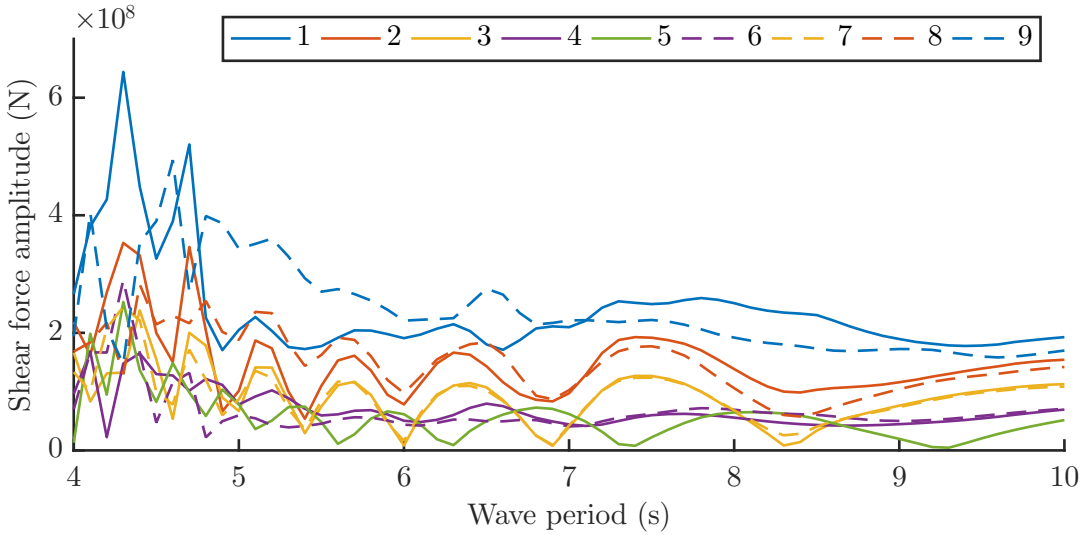

Figure 6.15: Shear forces in the heave direction at each of the nine spine joints, with a wave heading of 40°. Joints are numbered from fore to aft (see legend).

This asymmetry in the shear forces on the joints in either half of the spine is most pronounced in wave headings of 80° and 90°, where the heave shear forces are by far the greatest at the one or two most downstream joints (e.g. Fig. 6.16).

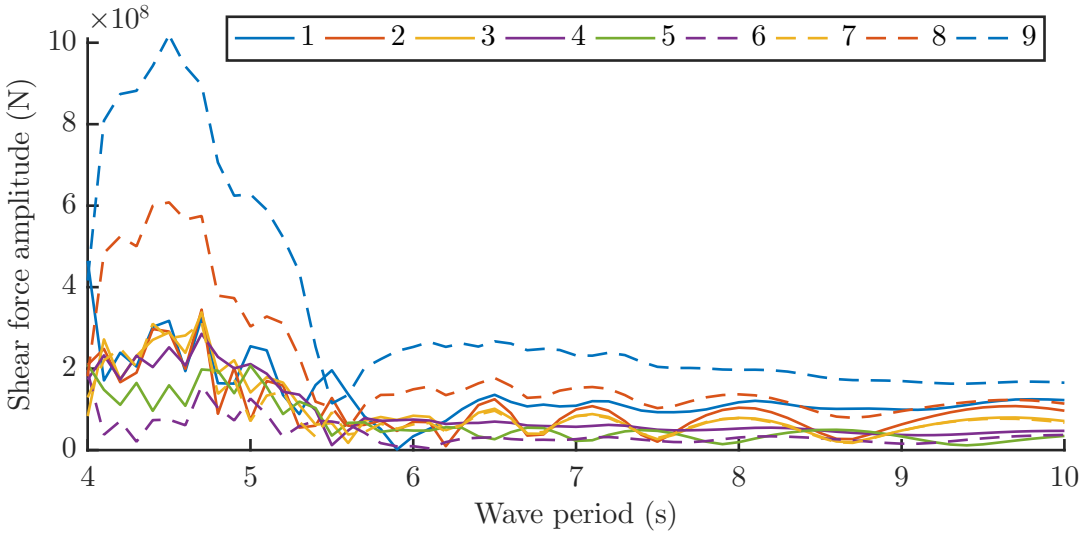

Figure 6.16: Shear forces in the heave direction at each of the nine spine joints, with a wave heading of 80°. Joints are numbered from fore to aft (see legend).

These trends bear resemblance to findings from [71]. Despite the conservative motion constraints employed here, there is also evidence of motions akin to those

produced by the proposed phenomenon of a "flexural wave". The motions of the joint flexure in roll are greatest at the outermost joints for periods between 7 and 10s and angles between 10 and 50° (Fig. 6.17 shows the effect at the central point of this range). Furthermore, the motions of the most downstream joint are greater than those of the most upstream joint.

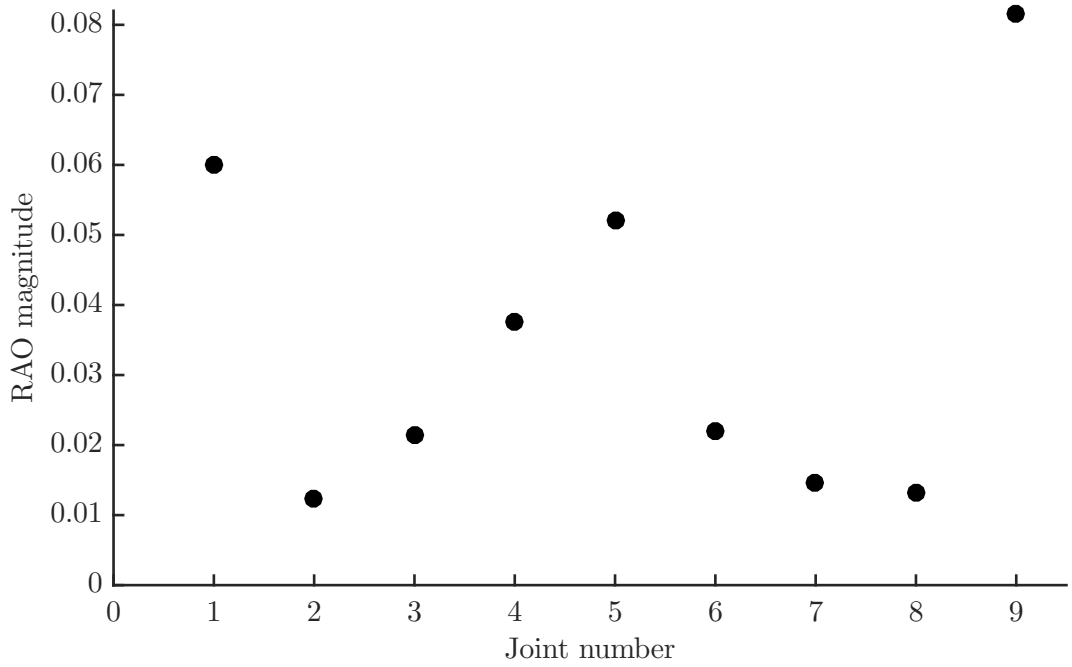

Figure 6.17: Amplitudes of the motion of each of the nine joints in roll, relative to the incoming wave motion (measured in radians). Wave period: 8.5s, wave angle: 30°.

Many of the results presented in this section offer hints of phenomena similar to those encountered in the early spine tests documented in [71], but given the complexity of the dynamics of the power-extracting spine of ducks modelled in this work, much further work is needed to clarify the exact nature of these phenomena.

6.5 Complex conjugate control - extending the motion constraint

6.5.1 Theory

6.5.1.1 Formulation

Provided there exists strong enough coupling between the controlled and uncontrolled modes of motion, control forces applied through the controlled DoFs could be used to some extent to effect the motions of the uncontrolled DoFs, $\mathbf{U}_f$. This motivates an extension of the weighted global velocity constraint to include contributions from the uncontrolled DoFs (Eq. 6.29). Of course, $\mathbf{U}_f$ can be expressed in terms of $\mathbf{U}_c$, meaning that the additional term actually increases the restriction on $\mathbf{U}_c$, which are effected directly via the control forces, $\mathbf{F}_c$.

$$\mathbf{U}_c{}^{\dagger}\boldsymbol{\Gamma}_c^{-2}\mathbf{U}_c + \mathbf{U}_f{}^{\dagger}\boldsymbol{\Gamma}_f^{-2}\mathbf{U}_f \leq 1 \tag{6.29}$$

If the inequality given by Eq. 6.29 is not satisfied by the velocities demanded by unconstrained complex conjugate control, then $\mathbf{P}(\mathbf{U}_c)$ (Eq. 6.23) should be maximised subject to $\mathbf{U}_c{}^{\dagger}\boldsymbol{\Gamma}_c^{-2}\mathbf{U}_c + \mathbf{U}_f{}^{\dagger}\boldsymbol{\Gamma}_f^{-2}\mathbf{U}_f = 1$. Using the method of Lagrange multipliers (akin to the method used by Evans [43]), this is equivalent to solving Eq. 6.30, given the Lagrangian expression in Eq. 6.31. The partial derivative with respect to the complex vector, $\mathbf{U}_c$, is defined as the partial derivatives with respect to both the real and imaginary parts of $\mathbf{U}_c$.

$$\begin{bmatrix} \frac{\partial \mathbf{Q}}{\partial \mathbf{U}_c} \\ \frac{\partial \mathbf{Q}}{\partial \mu} \end{bmatrix} = 0 \tag{6.30}$$

$$\mathbf{Q}(\mathbf{U}_c,\mu) = \mathbf{P}(\mathbf{U}_c) - \frac{1}{2}\mu\Big(\mathbf{U}_c{}^{\dagger}\boldsymbol{\Gamma}_c^{-2}\mathbf{U}_c + \big[\mathbf{Z}_{ff}^{-1}(A\mathbf{X}_f - \mathbf{Z}_{fc}\mathbf{U}_c)\big]^{\dagger}\boldsymbol{\Gamma}_f^{-2}\big[\mathbf{Z}_{ff}^{-1}(A\mathbf{X}_f - \mathbf{Z}_{fc}\mathbf{U}_c)\big] - 1\Big) \tag{6.31}$$

Evaluating the top row of Eq. 6.30 and rearranging for $\mathbf{U}_c$, yields the optimal velocities in terms of the Lagrange multiplier, μ (Eqs. 6.32, 6.33).

$$-\mathbf{B}_{cc}(\mathbf{U}_c - \frac{1}{2}\mathbf{B}_{cc}^{-1}\mathbf{X}_c^m) - \mu\big[\boldsymbol{\Gamma}_c^{-2}\mathbf{U}_c - (\mathbf{Z}_{ff}^{-1}\mathbf{Z}_{fc})^{\dagger}\boldsymbol{\Gamma}_f^{-2}\mathbf{Z}_{ff}^{-1}(A\mathbf{X}_f - \mathbf{Z}_{fc}\mathbf{U}_c)\big] = 0 \tag{6.32}$$

$$\mathbf{U}_c^{opt} = \frac{A}{2}\Big(\mathbf{B}_{cc} + \mu\big[\boldsymbol{\Gamma}_c^{-2} + (\mathbf{Z}_{ff}^{-1}\mathbf{Z}_{fc})^{\dagger}\boldsymbol{\Gamma}_f^{-2}(\mathbf{Z}_{ff}^{-1}\mathbf{Z}_{fc})\big]\Big)^{-1}\Big(\mathbf{X}_c^m + 2\mu(\mathbf{Z}_{ff}^{-1}\mathbf{Z}_{fc})^{\dagger}\boldsymbol{\Gamma}_f^{-2}\mathbf{Z}_{ff}^{-1}\mathbf{X}_f\Big) \tag{6.33}$$

Substituting Eq. 6.33 into the second row of Eq. 6.30, yields a scalar equation for μ (Eq. 6.34). The power is thus determined by Eqs. 6.33 and 6.34, along with Eq. 6.23. Eqs. 6.35 and 6.36 define quantities introduced in Eq. 6.34.

$$\frac{A^2}{4}\boldsymbol{\Theta}^\dagger\boldsymbol{\Psi}(\boldsymbol{\Psi}\mathbf{B}_{cc}\boldsymbol{\Psi}+\mu\mathbf{I})^{-1}\boldsymbol{\Psi}\boldsymbol{\Gamma}_c^{-2}\boldsymbol{\Psi}(\boldsymbol{\Psi}\mathbf{B}_{cc}\boldsymbol{\Psi}+\mu\mathbf{I})^{-1}\boldsymbol{\Psi}\boldsymbol{\Theta}$$
$$+A^2\Big(\mathbf{X}_f{}^\dagger-\frac{1}{2}\boldsymbol{\Theta}^\dagger\boldsymbol{\Psi}(\boldsymbol{\Psi}\mathbf{B}_{cc}\boldsymbol{\Psi}+\mu\mathbf{I})^{-1}\boldsymbol{\Psi}\mathbf{Z}_{fc}{}^\dagger\Big)\mathbf{Z}_{ff}^{-1\dagger}\boldsymbol{\Gamma}_f^{-2}\mathbf{Z}_{ff}^{-1}\Big(\mathbf{X}_f-\frac{1}{2}\mathbf{Z}_{fc}\boldsymbol{\Psi}(\boldsymbol{\Psi}\mathbf{B}_{cc}\boldsymbol{\Psi}+\mu\mathbf{I})^{-1}\boldsymbol{\Psi}\boldsymbol{\Theta}\Big)$$
$$-1=0 \tag{6.34}$$

$$\boldsymbol{\Psi}^{-2}=\boldsymbol{\Gamma}_c^{-2}+(\mathbf{Z}_{ff}^{-1}\mathbf{Z}_{fc})^\dagger\boldsymbol{\Gamma}_f^{-2}\mathbf{Z}_{ff}^{-1}\mathbf{Z}_{fc} \tag{6.35}$$

$$\boldsymbol{\Theta}=\mathbf{X}_c^m+2\mu(\mathbf{Z}_{ff}^{-1}\mathbf{Z}_{fc})^\dagger\boldsymbol{\Gamma}_f^{-2}\mathbf{Z}_{ff}^{-1}\mathbf{X}_f \tag{6.36}$$

6.5.1.2 Numerical solution

Whereas the optimal velocities and power within the constrained systems considered by Pizer [8] depend only on the radiation damping coefficients, $\mathbf{B}$, and the excitation forces, $\mathbf{X}$, the systems under consideration in this paper are dependent additionally on hydrostatic and inertial properties, due to the interaction of the controlled motions with the uncontrolled motions (Eqs. 6.19 - 6.22). Whilst the inertial properties derive from the mass distribution of the body (or collection of bodies) under consideration, the hydrodynamic and hydrostatic properties may be obtained from physical experiments, or as is now increasingly common, numerically by use of a radiation/diffraction code, such as WAMIT [28], which is used in the present work. Generalised modes allow this technique to be applied to a collection of mechanically interlinked bodies, or a collection of purely hydrodynamically-interacting bodies, such as a wave energy converter array.

As with the analysis given by Pizer [8], it is useful to diagonalise the symmetric matrix $\boldsymbol{\Psi}\mathbf{B}_{cc}\boldsymbol{\Psi}$, using its matrix of eigenvectors, $\mathbf{V}$ (Eq. 6.37), which results in Eq. 6.38. Since $\mathbf{B}_{cc}$ and $\boldsymbol{\Psi}$ are symmetric, positive definite matrices, the elements of $\boldsymbol{\Lambda}$, $\lambda_i > 0$ for all i. Therefore, the poles of Eq. 6.38 all occur at negative μ values, which

means there exist at most $2N$ real roots, of which one at most is real and positive.

$$\mathbf{\Lambda} = \mathbf{V}^\dagger \mathbf{\Psi} \mathbf{B}_{cc} \mathbf{\Psi} \mathbf{V} \tag{6.37}$$

$$\begin{aligned} g(\mu) \equiv & \frac{1}{4}\mathbf{\Theta}^\dagger \mathbf{\Psi} \mathbf{V} (\mathbf{\Lambda} + \mu \mathbf{I})^{-1} \mathbf{V}^\dagger \mathbf{\Psi} \mathbf{\Gamma}_c^{-2} \mathbf{\Psi} \mathbf{V} (\mathbf{\Lambda} + \mu \mathbf{I})^{-1} \mathbf{V}^\dagger \mathbf{\Psi} \mathbf{\Theta} \\ & + \Big(\mathbf{X}_f{}^\dagger - \frac{1}{2}\mathbf{\Theta}^\dagger \mathbf{\Psi} \mathbf{V} (\mathbf{\Lambda} + \mu \mathbf{I})^{-1} \mathbf{V}^\dagger \mathbf{\Psi} \mathbf{Z}_{fc}{}^\dagger \Big) \mathbf{Z}_{ff}^{-1\dagger} \mathbf{\Gamma}_f^{-2} \mathbf{Z}_{ff}^{-1} \Big(\mathbf{X}_f - \frac{1}{2}\mathbf{Z}_{fc} \mathbf{\Psi} \mathbf{V} (\mathbf{\Lambda} + \mu \mathbf{I})^{-1} \mathbf{V}^\dagger \mathbf{\Psi} \mathbf{\Theta} \Big) \\ & = \frac{1}{A^2} \end{aligned} \tag{6.38}$$

When $\mu = 0$, Eq. 6.33 reverts to the optimal velocities for the unconstrained case. As defined in Eq. 6.31, $\mu > 0$, which can only be the case when $A > A_c = \sqrt{\frac{1}{g(0)}}$; the constraint only becomes active when $A > A_c$. In this case, of the $2N$ complex roots of Eq. 6.38, still one at most can be real and positive, corresponding to a valid solution. As $\mu \to \infty$, $g(\mu) \to A^2 \mathbf{X}_f^\dagger (\mathbf{Z}_{ff}^{-1})^\dagger \mathbf{\Gamma}_f^{-2} \mathbf{Z}_{ff}^{-1} \mathbf{X}_f \equiv C$, and if $C > 1$, $\mathbf{U}_c{}^\dagger \mathbf{\Gamma}_c^{-2} \mathbf{U}_c + \mathbf{U}_f{}^\dagger \mathbf{\Gamma}_f^{-2} \mathbf{U}_f > 1$ for all $\mu > 0$, signifying that the constraint (6.29) cannot be satisfied. In physical terms, this corresponds to an insufficient strength of coupling between the controlled and uncontrolled modes of motion; the motions of the uncontrolled modes will always lead to violation of the constraint, regardless of the forces applied through the controlled modes of motion. Therefore, it is imperative that the nature of the application is considered in choosing the weightings, $\mathbf{\Gamma}_f$, before applying constraint (6.29). It is interesting to note that the presence of a solution is directly dependent only on properties of the uncontrolled modes, and the wave amplitude. However, the equations of motion (Eq. 6.19) link these properties of the free modes to the coupling between the controlled and free modes. Whilst Eq. 6.38 is a scalar equation, for systems with large N it is most practical to solve for μ numerically.

6.5.2 Application to a solo duck

To recap, the solo duck is a single body wave energy device, derived from the originally proposed spine-based system [22]. Whilst originally designed to extract power through its pitch rotations, allowing power extraction via multiple degrees of freedom can benefit the total power, whilst reducing the cost of rigidly fixing degrees of freedom in

a harsh sea environment. Furthermore, it may reduce costs further to concede control of certain degrees of freedom, especially if there were no significant negative impact on the power extraction. In this section, the methods introduced in the previous section are applied to the solo duck in order to highlight the pertinent details of its implementation. The method is then applied towards optimising the set of controlled degrees of freedom.

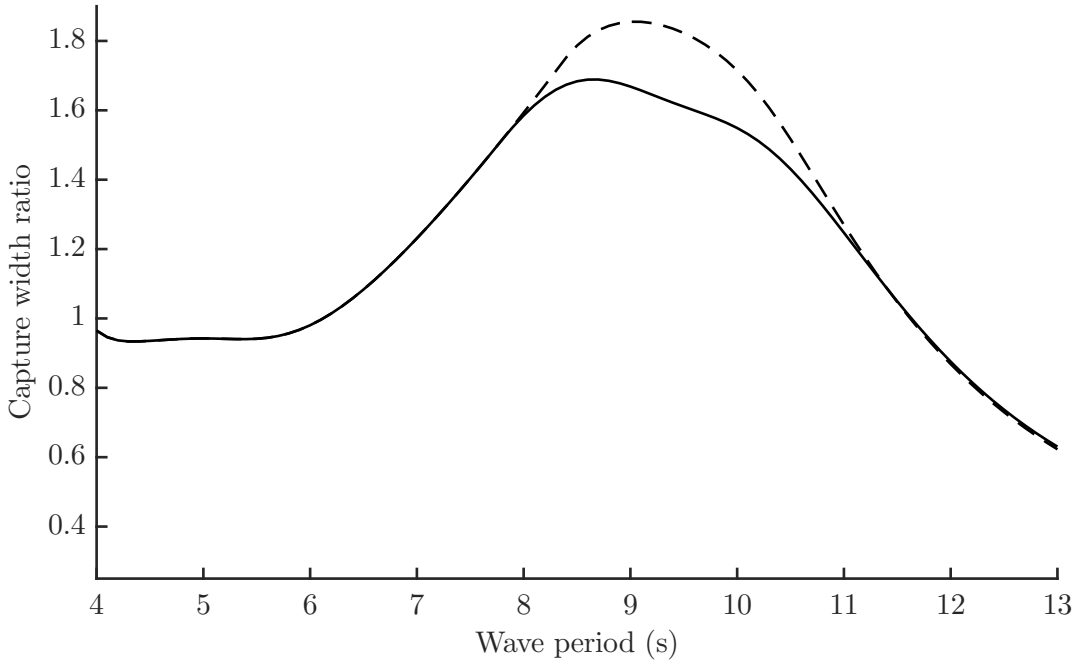

Figure 6.18: The impact of extending the motion constraint to uncontrolled degrees of freedom on the capture width ratio for a solo duck. Surge and heave motions controlled, 1m wave amplitude. Dotted line: Constraint applied only to controlled modes. Solid line: Constraint applied to all modes.

As before, β_i is set to 0.5rad for the pitch angle of each duck and 0.2rad for each joint degree of freedom. Under head-on waves, the symmetry of the device is reduced to a three degree of freedom system. Studying a similar solo duck system, Pizer [44] noted that releasing control of the surge degree of freedom resulted in a larger reduction in power than by releasing heave or pitch, for whom the reduction was small. Consequently, a solo duck with control over just surge and heave motions may provide comparable performance to a system with pitch also controlled. We adopt

this example to highlight the potential importance of using the extended constraint introduced in Section 6.5.1.1. Surge and heave are controlled, whilst the pitch degree of freedom is uncontrolled. Wavefronts are parallel to the axis of pitch rotation, and 1m and 2m wave amplitudes are considered.

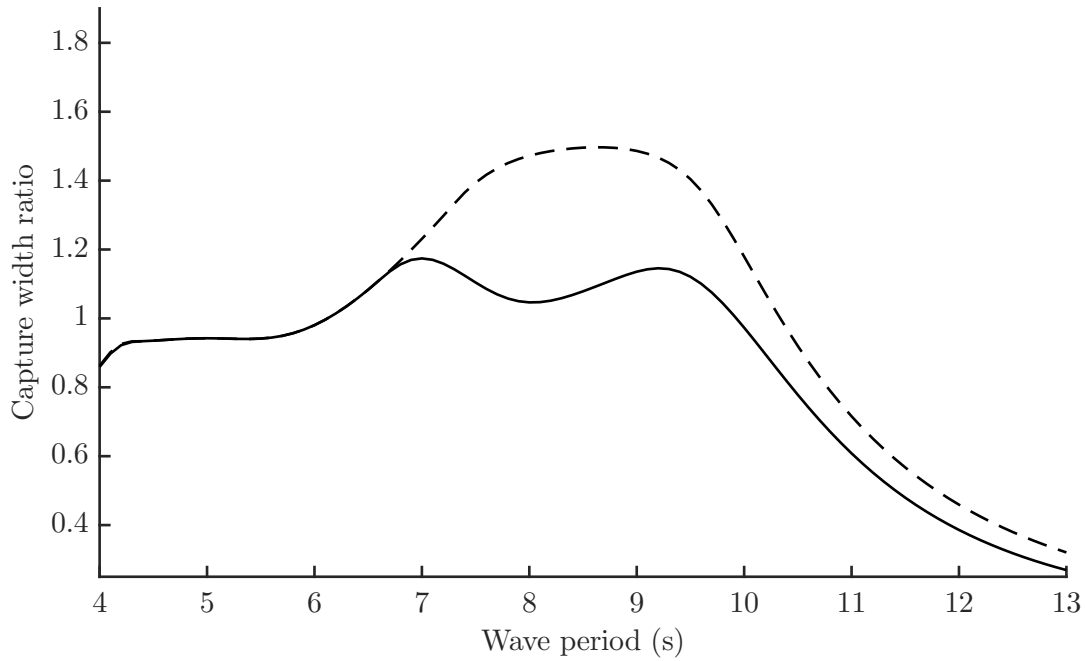

Figure 6.19: The impact of extending the motion constraint to uncontrolled degrees of freedom on the capture width ratio for a solo duck. Surge and heave motions controlled, 2m wave amplitude. Dotted line: Constraint applied only to controlled modes. Solid line: Constraint applied to all modes.

Especially around the peak in capture width ratio, whether or not the motion constraint is enforced on all degrees of freedom, or just those of surge and heave, makes a significant difference. Under 1m incident waves, a small difference in capture width ratio is present between 8 and 11s wave periods (Fig. 6.18). For 2m wave amplitudes, which are not unlikely to be encountered in a real wave climate, the difference extends to a much wider range of wave periods, and is more significant (Fig. 6.19). Capture width ratio is reduced from a peak value of around 1.5 to a peak value around 1.2. In the case following the constrained method from Section 6.3, the unconstrained pitch motions reach unrealistically high values (around 2rad for a wave period of 9.6s),

which violates the assumption of linearity (Fig. 6.20). Extending the constraint to also restrict the pitch motions unsurprisingly results in reduced pitch motions for wave periods above 7s, with surge excursions reduced similarly. Interestingly, heave motions actually increase slightly for wave periods above 8.5s.

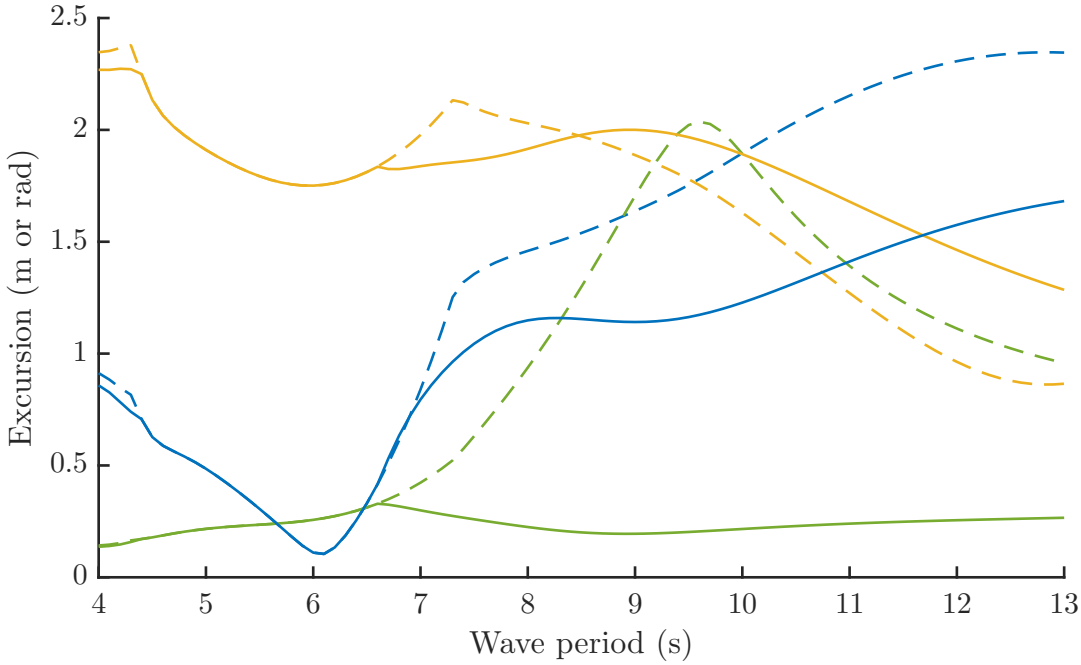

Figure 6.20: The impact of extending the motion constraint to uncontrolled degrees of freedom on motions on the surge, heave and pitch body motions. Surge and heave motions controlled, 2m wave amplitude. Dotted lines: Constraint applied only to controlled modes. Solid lines: Constraint applied to all modes. Blue: Surge; Yellow: Heave; Green: Pitch.

In general, the extended constraint (6.29) can only be satisfied if the controlled modes have enough influence on the uncontrolled modes via the hydrodynamic, hydrostatic and inertial coupling, to restrict the motions sufficiently. In the case of the solo duck under head-on waves considered above, the constraints on the out-of-plane motions (in sway, roll and yaw) are trivially satisfied since they are not excited by the waves. The constraints on the in-plane motions can be satisfied because coupling between the pitch degree of freedom and the surge and heave degrees of freedom is sufficiently strong. However, oblique waves excite the out-of-plane motions, sometimes to the extent that no amount of force imparted through the surge and heave motions

is sufficient to restrict the out-of-plane motions in accordance with the weighted constraint. Fig. 6.21 shows that between 7 and 8s wave periods, and for wave angles greater than 10°, a solution satisfying the extended constraint does not exist when only surge, heave and pitch are controlled. In this case, the constraint violation is due to resonant response in sway and roll, which are not coupled strongly enough to surge, heave and pitch.

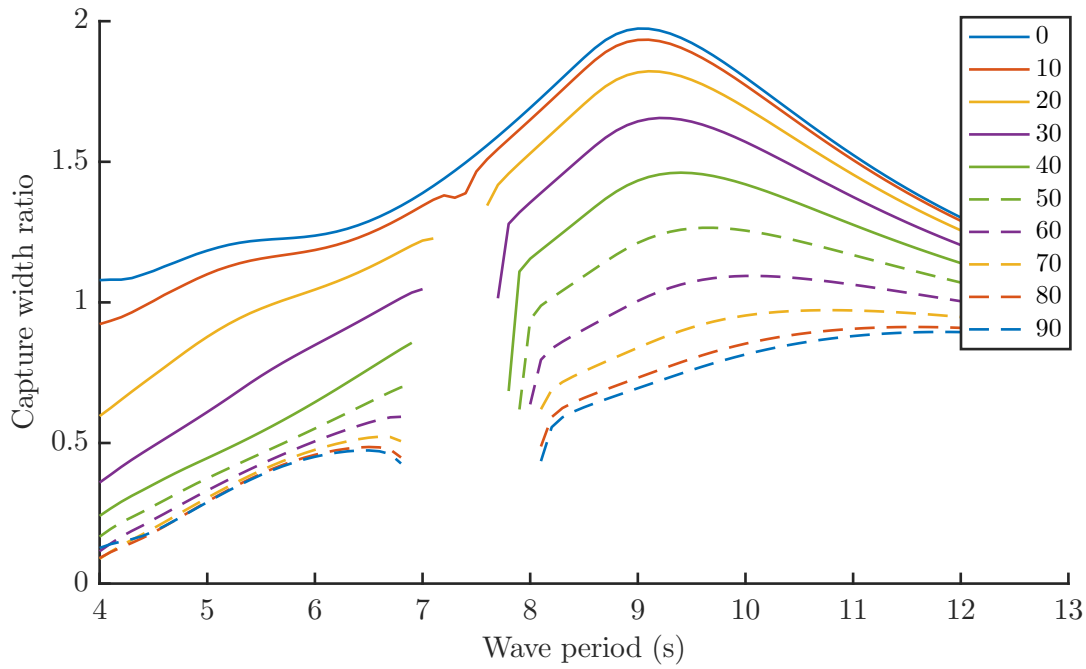

Figure 6.21: Capture width ratio of a solo duck with uncontrolled sway, roll and yaw modes. Legend defines the data lines for each wave heading, in degrees.

Bolstering this strategy with control over the sway motions increases the degree of control (direct or indirect) over the sway and roll motions. Solutions are now found for all wave periods, with heading angles up to and including 60°, but there still remain regions in which no solution exists for greater wave angles (Fig. 6.22).

The greater range of solutions is largely due to the hydrodynamic coupling between the sway and roll modes, enabling control forces applied through sway to restrict the motion in roll. However, this strategy results in larger sway excursions, which ultimately cause constraint violation for wave angles above 60°. Fig. 6.23 shows the limiting case with 60° waves, in which control forces are just about able to sufficiently

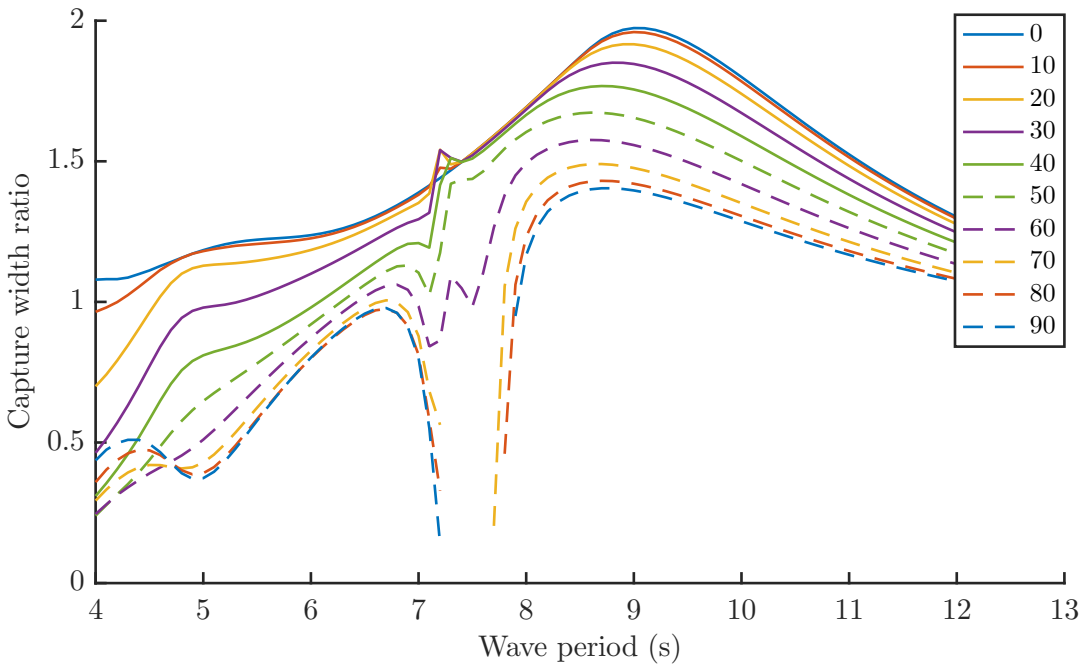

Figure 6.22: Capture width ratio of a solo duck with uncontrolled roll and yaw modes. Legend defines the data lines for each wave heading, in degrees.

restrict the roll motions at the expense of increased sway excursions, without violating constraint (6.29). Fig. 6.24 shows the motion amplitudes of the undamped and unstiffened system with a 60° wave heading. In particular, the roll amplitude exceeds its individual weighting (β) between 7 and 8s wave periods, indicating constraint violation, whilst the sway excursion is considerably below its corresponding weighting. Fig. 6.22 also highlights that the power tends towards a large negative value either side of the region containing no solutions to the Lagrange problem. As this region is neared from lower or higher wave periods, the approaching resonance of the roll motions increasingly necessitates counteractive force provision in order to satisfy the weighted global constraint. This comes at the expense of power generation, but prevents the constraint being violated. In turn, this causes increased sway excursions, and further reduces power generation until eventually, there are no solutions to the constraint, regardless of the decrease in power that is tolerated.

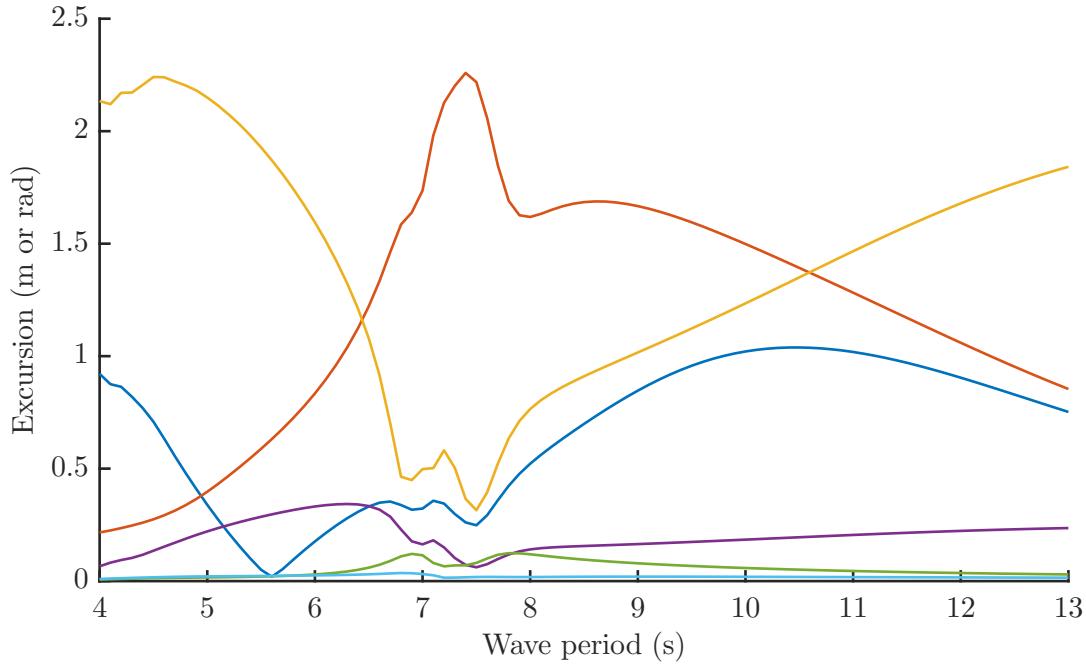

Figure 6.23: Motions of the solo duck in 60° oblique waves, optimised for power under the extended global motion constraint. Controlled modes: surge, sway, heave, pitch. Blue line: surge; red: sway; yellow: heave; purple: roll; green: pitch; light blue: yaw.

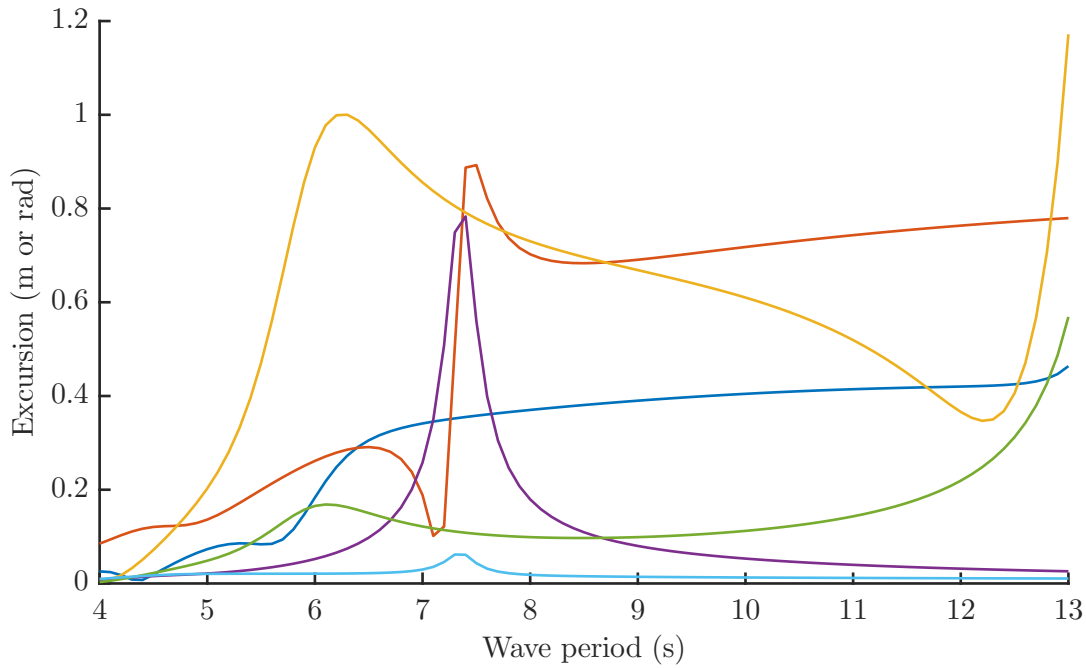

Figure 6.24: Motions of the undamped and unstiffened solo duck in 60° oblique waves. Controlled modes: surge, sway, heave, pitch. Blue line: surge; red: sway; yellow: heave; purple: roll; green: pitch; light blue: yaw.

Of the 62 combinations of controlled modes of the solo duck (excluding the cases where all are controlled or all are uncontrolled), the non-existence of solutions has been found at most to involve a narrow range of wave periods and less than the full range of wave angles. In those cases, the peaks in capture width ratio generally lie outside the period-angle combinations of the non-existence regions.

Under head-on waves where the simplified system has three degrees of freedom, locking a degree of freedom does not necessarily cause a significant reduction in performance [8]. From a two degree of freedom system, releasing (i.e. changing it from fixed, to free but uncontrolled) the third degree of freedom results in a loss in power, which is much greater when surge is released rather than heave or pitch [44]. Of course, that study [44] left open the possibility of large motions in the uncontrolled degree of freedom. However, a similar trend is found in the six degree of freedom system studied here under the impact of the extended motion constraint. Under head-on waves (a wave heading of 0°), conceding control of surge results in a greater loss of power than conceding control of heave or pitch (Fig. 6.25). The peak capture width ratio value of 1.97 reduces only to 1.79 in conceding control of heave. Despite some additional loss of bandwidth, this may still provide an advantage if the systems required to control the heave (or pitch) degree of freedom are costly.

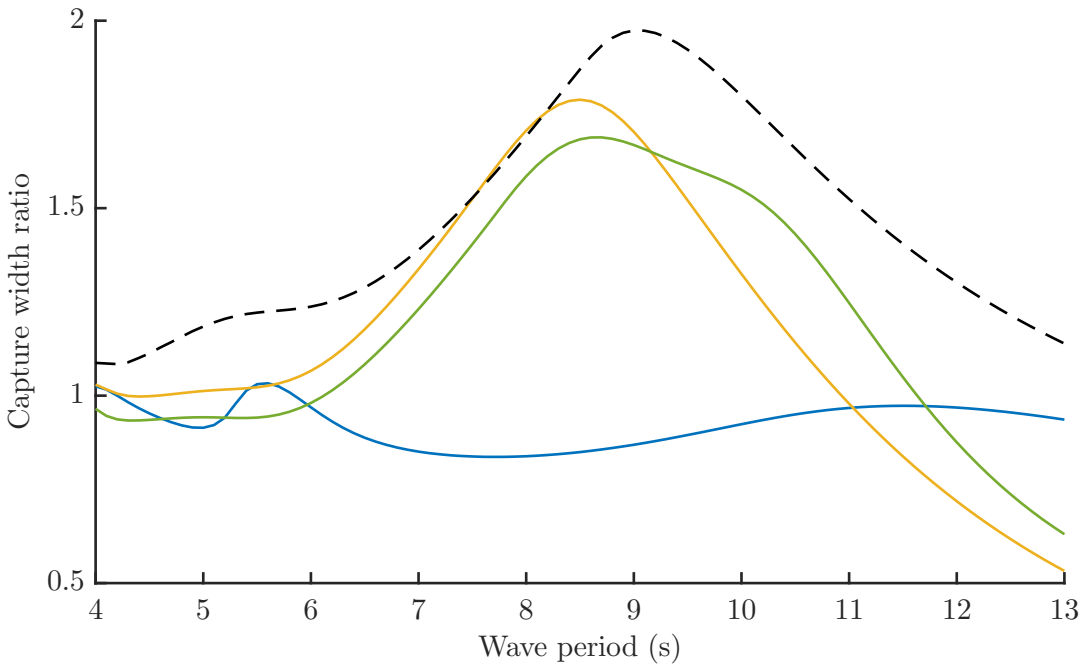

Figure 6.25: Capture width ratio of the solo duck in head-on waves, with control of each in-plane degree of freedom conceded in turn. Wave angle: 0°. Dotted line: all 6 degrees of freedom controlled. Solid lines: blue - surge uncontrolled, yellow - heave, green - pitch.

Whilst out-of-plane degrees of freedom (sway, roll and yaw) do not affect the power capture with a 0° wave heading due to the plane of symmetry of the duck, it is not the case that the in-plane degrees of freedom do not affect the power capture with a 90° wave heading. In transitioning between 0° and 90° wave headings, the roles of surge and sway broadly interchange. In head-on waves, conceding control of surge results in a significant power reduction across a wide range of wave periods, whilst conceding control of sway has no effect. Conversely, in 90° waves, conceding control of sway reduces power significantly, whereas little effect is had by conceding control of surge (Fig. 6.27). Conceding control of heave or pitch diminishes the power across the full range of wave angles, especially in longer wave periods, but the power reduction is relatively insignificant. Conceding control of yaw or roll does not have any significant impact on power in wave angles close to either end of the range (Figs. 6.25, 6.27), and causes only modest reductions in power for intermediate wave angles, the majority of which occurs at lower wave periods. In fact, conceding control of roll actually increases

power for wave periods between 7.3 and 8.5s, and intermediate angles, compared to the case in which all degrees of freedom are controlled. Considering that a real deployment location may only experience a small range of incident wave angles, the device is likely to be set at an angle of around 30° since this enables a very wide bandwidth, without sacrificing much in peak power (Figs. 6.25, 6.26, see also [8]). In this light, conceding control of heave, pitch or roll would be least detrimental to performance.

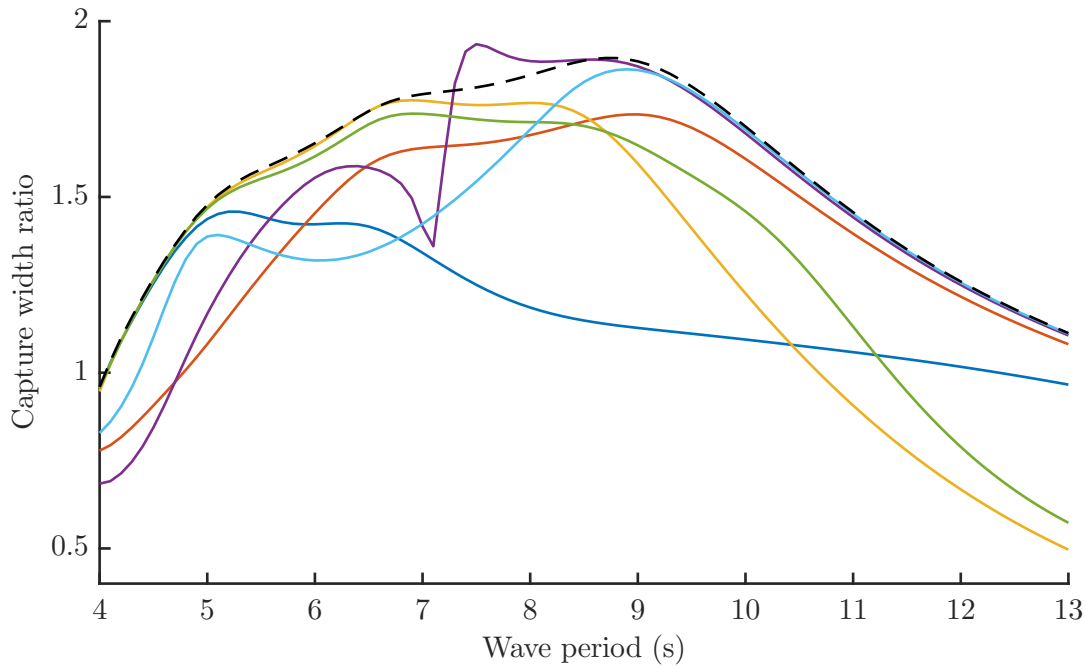

Figure 6.26: Capture width ratio of the solo duck in 30° incident waves, with control of each degree of freedom conceded in turn. Dotted line: all 6 degrees of freedom controlled. Solid lines: blue - surge uncontrolled, red - sway, yellow - heave, purple - roll, green - pitch, light blue - yaw.

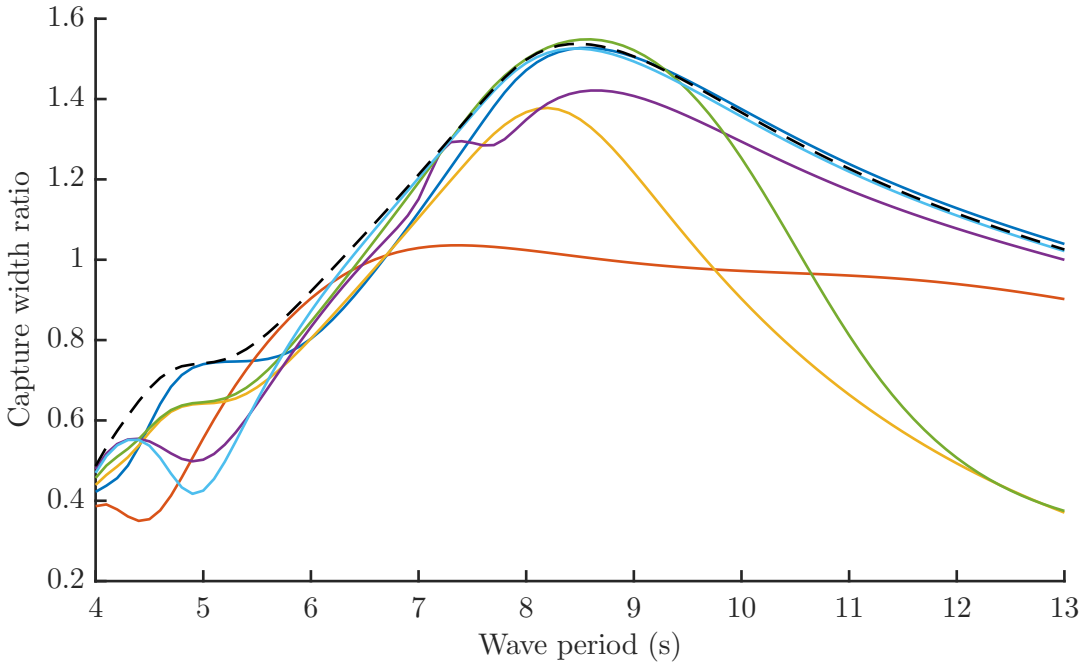

Figure 6.27: Capture width ratio of the solo duck in 90° incident waves, with control of each degree of freedom conceded in turn. Dotted line: all 6 degrees of freedom controlled. Solid lines: blue - surge uncontrolled, red - sway, yellow - heave, purple - roll, green - pitch, light blue - yaw.

Furthermore, conceding control of two degrees of freedom can even retain the majority of the power capture across a slightly narrowed band of wave periods (Fig. 6.28). Sacrificing control of heave and pitch together results in a much reduced capture width ratio, inferring that when just heave or pitch is uncontrolled, control of the other is necessary to compensate. Should it be desired that three degrees of freedom are uncontrolled, it is best to retain control over the translational degrees of freedom. This case compares favourably to the one in which all degrees of freedom are controlled (Fig. 6.28). Conversely, conceding control of the translational degrees of freedom, but retaining control of the rotational degrees of freedom, results in a large loss of power across a wide range of wave periods.

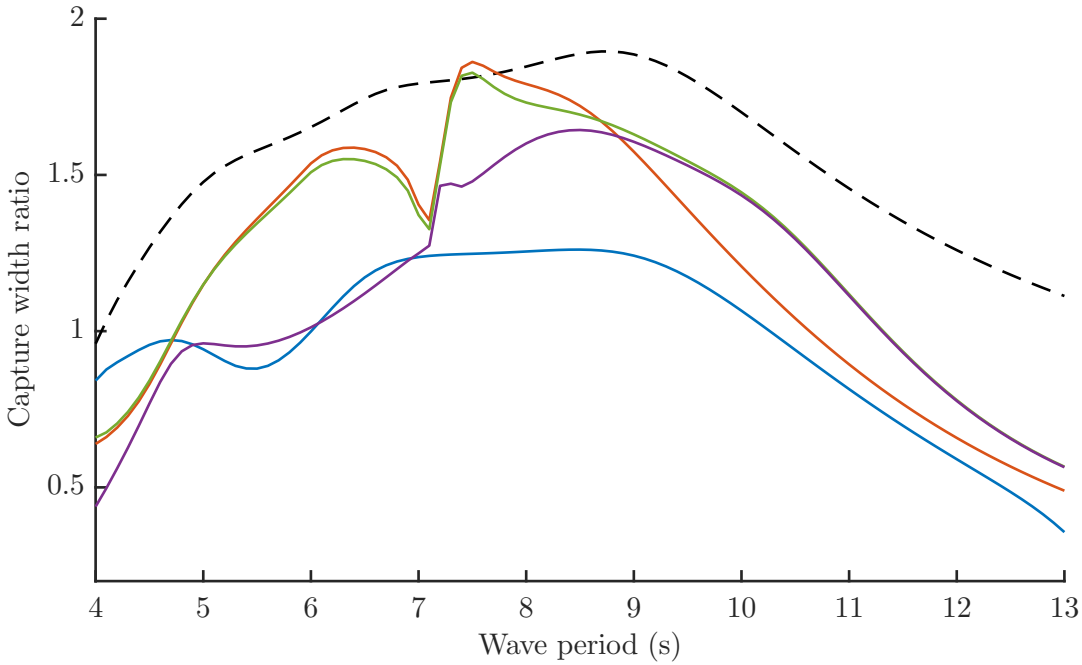

Figure 6.28: Capture width ratio of the solo duck in 30° incident waves, with a selection of better performing combinations of uncontrolled modes. Dotted line: all 6 degrees of freedom controlled. Solid lines: blue - heave and pitch uncontrolled, red - heave and roll, green - roll and pitch, purple - roll, pitch and yaw.

6.5.3 Application to a spine of ducks

The impact of the uncontrolled rigid body motions on the findings presented in Section 6.4 can now be assessed using this extended version of the motion constraint. As before, the constraint weightings are set using displacements of 0.5rad for the pitching of the ducks, 0.2rad for the body rotations about each joint and for the rigid body roll and yaw motions, and 2.5m for the heave, surge and sway rigid body motions.

Of the five uncontrolled, rigid body modes of motion, clearly unrealistic motions are only present in the surge and heave modes (see Appendix J for more details). The highest RAOs, exceeding 20, are attained with a 40° wave heading for both surge and heave. Under the extended constraint, the (significantly reduced) motions are largest in surge and heave for low heading angles between 6 and 7s periods, and for the lowest periods with wave angles towards 90°.

However, despite the large difference in the surge and heave motions of the entire

spine between the two control cases, the power absorption is not greatly affected. At greatest, the difference in CWR is around 0.06 - much less than the greatest CWRs attained (see Fig. 6.7). This figure holds even less significance when it is considered that for wave angles below 60° across the full range of wave periods, where the highest CWRs are achieved, the relative difference does not greatly exceed 10%, and is much lower than 10% in general.

The level of indifference of the power absorption to the severity of the constraint applied to the uncontrolled modes is perhaps not surprising; in contrast to the solo duck (see Section 6.5.2), the full spine is long enough to span multiple wave crests, giving greater control of and greater ability to detune the spine translational motions by way of the joint and duck properties. From another perspective, by spanning multiple wave crests, very precise tuning of the joint and duck properties is required for the manifestation of large translational motions of the entire spine. Hence, one would expect the requirement of only small changes in the joint and duck properties in order to prevent this type of resonance, without necessarily diminishing the power-generating capability. This is indeed reflected in the control moments provided, which are very similar between the two cases. The upper plot of Fig. 6.29 displays the control moments applied at the joints in the roll direction for the case of the extended motion constraint, which are almost identical to those for the less severe constraint (see Fig. 6.14).

Whilst the shear forces acting at the joints in the sway direction are almost identical with each of the two control cases, enforcing the motion constraint on the surge and heave spine motions significantly affects the joint shear forces in those directions. The net effect of extending the constraint is to lower the surge and heave joint shear forces, but the effect is more pronounced at the lower wave angles (peaking at about a factor of four difference for certain wave periods at 0°), reducing to around a factor of two at 60° headings. This reduction in surge and heave but not sway bears direct relation to the fact that the body motions are only significantly reduced by the extended constraint in the surge and heave (but not sway) directions. For wave angles at which

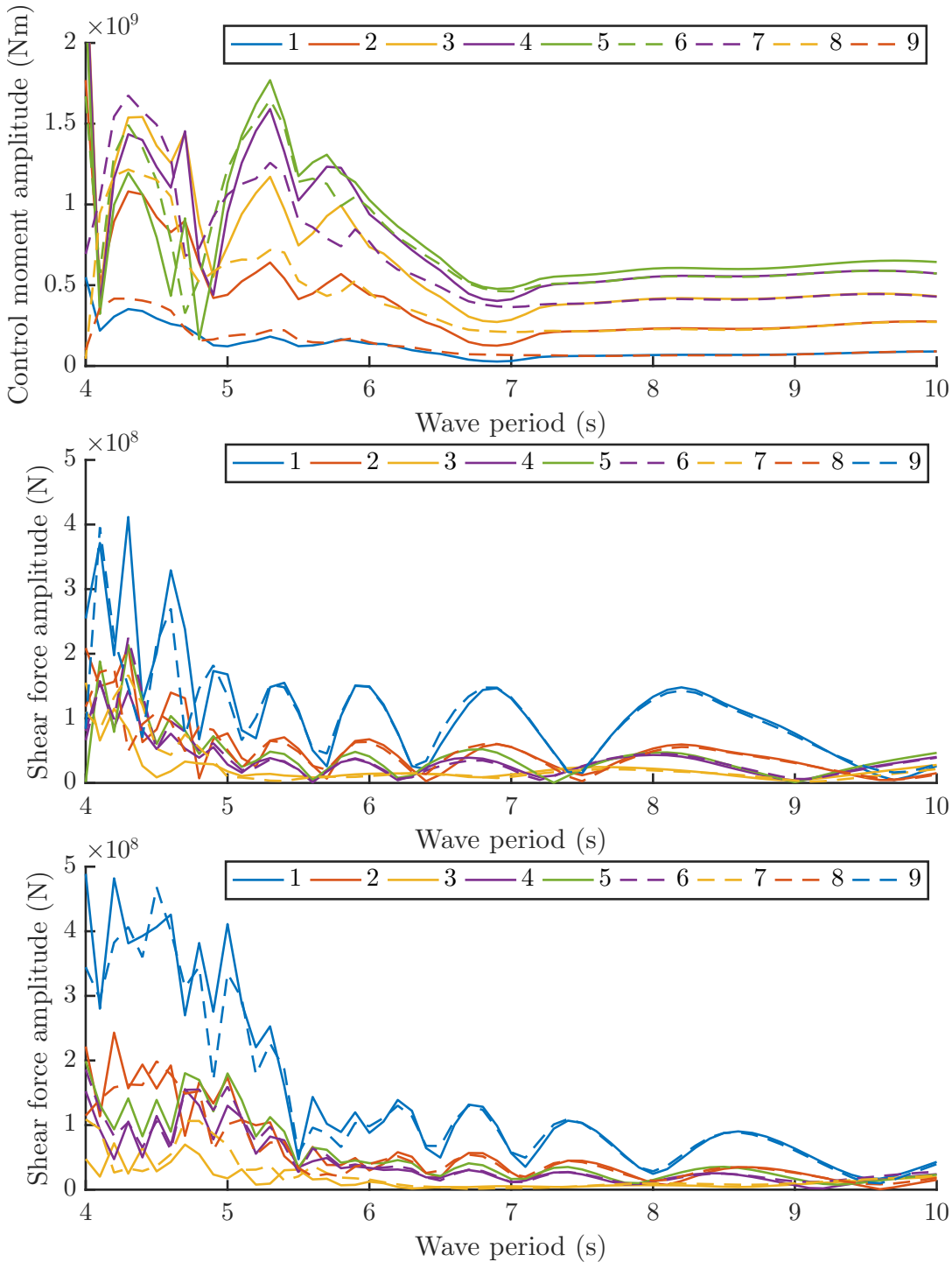

Figure 6.29: Control forces of joint roll motions with a 10° heading (upper), joint shear forces in the heave direction with a 40° heading (central), and with an 80° heading (lower). All motions are constrained - see Figs. 6.14 - 6.16 for comparison. Joints are numbered from fore to aft (see legend).

the extension of the motion constraint has a significant effect on the surge and heave motions, an extra oscillatory component of the shear forces (with respect to wave period) is introduced, particularly for the joints at either end of the spine (see the central and lower plots of Fig. 6.29 compared to Figs. 6.15 and 6.16), reflecting the peaks and troughs (or 'bands') present in the surge and heave motions (see Appendix J for more information). Evidently, larger variations in the shear force result from the tightened constraint on the surge and heave spine motions. However, the effect is still a net reduction in the magnitudes of the shear forces. Also note that the lowest shear forces are now experienced by joints 3 and 7, which lie halfway between the central and end joints of the spine. This is in contrast to the case with the uncontrolled degrees of freedom unconstrained, where these joints experienced greater forces on average (across all wave periods) than the more centrally located joints.

Whilst motions akin to the 'flexural wave' phenomenon were seen in Section 6.4 to occur at certain wave periods and angles in the roll directions, the dynamics of the full spine are complex. Just as the extended version of the constraint affects the rigid body surge and heave motions, so too does it affect the motions in the other degrees of freedom. For example, the previously seen occurrence of the 'flexural wave' is no longer present (see Appendix J for more details).

This section, along with Section 6.4, has merely touched upon some of the clearest features, somewhat with respect to investigating the impact of extending the motion constraint. There remains a multitude of complexities in the behaviour of the duck spine that could be analysed using the hydrodynamic and control model employed in these sections. These are discussed further in Section 7.3.2.

To summarise, the extension of the motion constraint that is applied to the full duck spine has little effect on the power absorption or control moments, despite significant changes in the device motions (particularly the surging and heaving of the entire spine) and the shear forces acting at the joints.

6.6 Power extraction of duck spine in uni- and multi-directional irregular waves

Whilst the monochromatic analysis in the preceding sections allows useful insight into the behaviour of the optimised duck spine, an extension to irregular seas allows for a more realistic assessment of the performance and dynamics. Still based on linear hydrodynamics from the frequency-domain model, superpositions of the body responses weighted by representative wave spectra enable prediction of the power extraction in a real sea climate. Though similar to the method used in Section 5.3.4, the use of complex conjugate control requires some further deliberation, and in order to analyse the duck spine performance in multi-directional wave conditions, the method must be extended.

6.6.1 Method

Whilst truly optimal performance would require real-time control within each sea state (perhaps deriving the specific strategy from some form of machine learning algorithm), optimising the control strategy in monochromatic waves of the energy period (and predominant wave heading) of each sea state can give an indication of performance. Further, computational advantages are derived from the efficiency of both the entirely frequency-domain hydrodynamic models and the analytical control method. Contrary to the case in Chapter 5, where only diagonal damping coefficients were controlled, complex conjugate control is predisposed to often demand large motions. Therefore, some restrictions must be imposed on the body motions. This is achieved using a combination of a clipping of the time series (following McCabe's approach [6]), and the use of a constrained form of the complex conjugate control algorithm.

Using the same West Shetland Shelf wave climate (see Appendix G), the method from Section 5.3.4 requires just minor adaptations in order to simulate the ten-duck spine extracting power from these unidirectional waves. The body response time series can be computed from the wave spectrum and frequency-domain hydrodynamic behaviour as before, using Eqs. 5.18 - 5.23. For the body response in each sea

state, the power must then be computed using the fully-populated damping matrix given by the complex conjugate control algorithm. This, along with the fact that an appropriate motion cap must also be applied, alters the required form of Eq. 5.27. Eqs. 5.28 - 5.30 can then be used as before to compute the annual mean power, but over the 28 power-extracting DoFs instead of the WaveTrain's three. Since the extension to a multidirectional wave climate is more complicated but builds upon these same adaptations, that context will be used to formally define these required changes.

It is commonly assumed that the directional component of a wave spectrum is independent of the wave frequency, allowing the multidirectional spectrum to be expressed as $S(\omega_k, \theta_l) = S(\omega_k)D(\theta_l)$, where $S(\omega_k)$ can be given by a unidirectional spectrum (in this case by Eq. 5.18), and $D(\theta_l)$ is a directional spectrum, whose definite integral over the full angle range is equal to unity. In this section, the directional spectrum is given by Eq. 6.39 (p.35, [76]), where Γ is the Gamma function, θ_P is the predominant wave direction, $n = 4$, and $|\theta_l - \theta_P| \leq 90°$.

$$D(\theta_l) = \frac{\Gamma(1 + \frac{n}{2})}{\sqrt{\pi}\Gamma(\frac{1}{2} + \frac{n}{2})} cos^4(\theta_l - \theta_P) \tag{6.39}$$

The amplitudes of the component waves within the spectrum are then given by Eq. 6.40.

$$\alpha(\omega_k, \theta_l)^2 = 2S(\omega_k)D(\theta_l)\Delta\omega_k\Delta\theta_l \tag{6.40}$$

Using random phases generated for each of the frequency and angular components, ω_k and θ_l, the elevation of the incident irregular waves is given by Eq. 6.41.

$$\eta_q(t) = \sum_{l=1}^{L}\sum_{k=1}^{K} \alpha(\omega_k, \theta_l) cos(\omega_k t + \psi_{k,l,q}) \tag{6.41}$$

The frequency-domain RAOs are then required for each degree of freedom in order to construct the irregular, body response time series. The excitation forces are dependent on the wave heading angle, and so the body motions now are too. Eq. 5.21 is used to compute the RAOs of each degree of freedom, j, at each wave frequency,

ω_k, and wave direction, θ_l. These RAOs are then used with Eqs. 6.42 and 6.43 to compute the body response time series.

$$\chi_j(\omega_k, \theta_l) = \alpha(\omega_k, \theta_l)\xi_j(\omega_k, \theta_l) \tag{6.42}$$

$$x_{j,q}(t) = \sum_{l=1}^{L}\sum_{k=1}^{K} |\chi_j(\omega_k, \theta_l)| cos(\omega_k t + \psi_{k,l,q} + \angle\chi_j(\omega_k, \theta_l)) \tag{6.43}$$

The motion limits used to clip the time series of motion for each degree of freedom are inspired by the values used in Section 6.4 for the motion constraint. Note that 'motion limits' or 'limiting' relate to the clipping of the time series of the body motions, whilst 'motion constraints' or 'constraining' relate to the complex conjugate control strategy used to obtain the RAOs. The motion limits, X_j^{lim}, are set to 0.2rad for joint flexure modes of motion, and 0.5rad for the duck pitch modes of motion.

For each degree of freedom, j, and the random phase index, q, (each index corresponds to a set of random phases) the power is dependent upon the motions of every DoF via the damping coefficients that couple DoF j to each other DoF, and is determined by Eq. 6.44.

$$P_{j,q}(t) = \begin{cases} \sum_{i=1}^{N} \dot{x}_{j,q} B_{ji}^{pto} \dot{x}_{i,q} \text{ for } |x_{j,q}(t)| \leq X_j^{lim} \text{ and } |x_{i,q}(t)| \leq X_i^{lim} \\ 0 \text{ otherwise} \end{cases} \tag{6.44}$$

The mean power extracted from each sea state is obtained by Eq. 5.28. Averaging over the 10 random phase sets, then summing over the 28 degrees of freedom gives the total mean power in each sea state (Eq. 6.45). Weighting by the annual occurrence of each sea state then gives the annual mean extracted power (Eq. 5.30).

$$\bar{P}(H_{m0}, T_z) = \sum_{j=1}^{28} \frac{1}{10} \sum_{q=1}^{10} \bar{P}(H_{m0}, T_z, j, q) \tag{6.45}$$

6.6.2 Results and discussion

The complex conjugate control algorithm is implemented at each of the 14 energy periods for each predominant wave angle, giving a PTO damping and PTO stiffness matrix for each sea state. First, three variations of the control strategy have been analysed,

for two sizes of duck spine, and for cases with both 0° and 20° unidirectional waves (Figs. 6.30 & 6.31). The motion constraints are 0.5rad for duck pitch rotations, 0.2rad for joint flexure and rigid body roll and yaw angles, and 2.5m for translational degrees of freedom. Note that in this section, 'performance' relates to capture width ratio, as this allows a distinction between designs of different spine lengths but congruent duck cross-sections, and also comparison of differently sized spines. The Capture Width Ratio (CWR) is obtained by dividing the annual mean extracted power by the annual mean power in waves that span a full spine length (see Table 6.3). Further discussion of the limitations of this metric in facilitating comparison to other types of WEC is given in Section 6.4.

Scale multiplier	Annual mean power (W)
1	2.55×10^7
1.4	3.57×10^7
2	5.10×10^7

Table 6.3: Power in the incoming waves across the total length of the spine.

Of the three forms of constraint, unconstrained control produces the least amount of power. This is because the lack of any motion constraint allows a control strategy which is often reliant on large motions. In comparison with a case where motions are constrained, smaller damping forces are expected in general, to compensate for the larger motions. However, the motion limits then imposed on the time series of the power negate any advantage this strategy may have had; the time series of the power is heavily clipped as a result of the inappropriately large motions.

Applying the motion constraint to the controlled modes of motion yields an increase in power, as in general, higher damping forces are selected, which reduce the impact of the motion limits in clipping the time series of the power.

Additionally, constraining the five rigid body modes (the uncontrolled modes) can result in a small increase in power (Fig. 6.30), but can also have the converse effect (Fig. 6.31). This method is also more computationally intensive. As such, the motion constraint is only applied to the controlled degrees of freedom for the rest of this study.

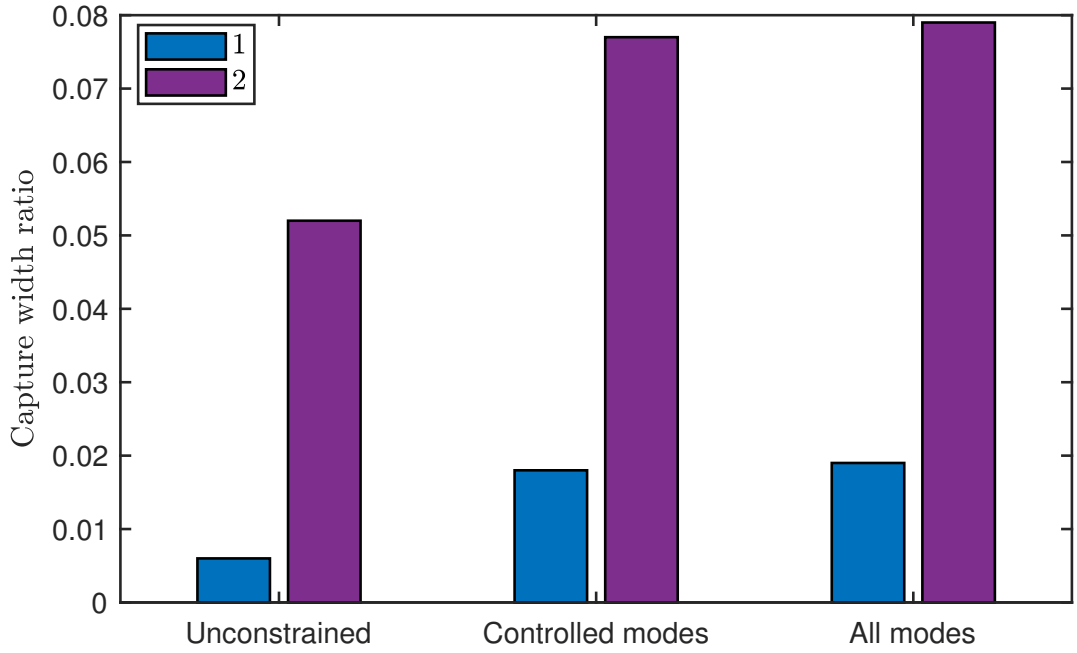

Figure 6.30: Unidirectional seas, 0° wave heading. Annual mean capture width ratio for the three control cases. Legend indicates the scale multiplier.

As previously noted in Section 6.4, the scale of the duck spine is critical in maximising performance in a given sea climate. For low wave angles, the yellow regions in Figure 6.34 are situated below the most prevalent and energy intensive wave periods of the West Shetland Shelf wave climate (see Appendix G). Increasing the device size increases the CWR for multi- and uni-directional waves, particularly for smaller wave angles (Figs. 6.32 & 6.33), and with the exception of unidirectional waves incident at an 80° angle. The proportional increase is greatest for head-on waves - a 4.3x increase of CWR in unidirectional waves with a doubling of scale. The increase is much less significant for more oblique wave headings - barely a 10% increase in CWR with a doubling of scale, for unidirectional waves of a 60° heading. This trend can be explained by consideration of the distinct types of motion involved with different wave angles. Performance in 90° waves is most dependent on the longitudinal properties of the spine, whilst performance in head-on waves is dependent solely on the scale of the duck cross-section - this is further evidenced by the indifference of the CWR to a change in spine length (see the equivalent height of the red and yellow bars for

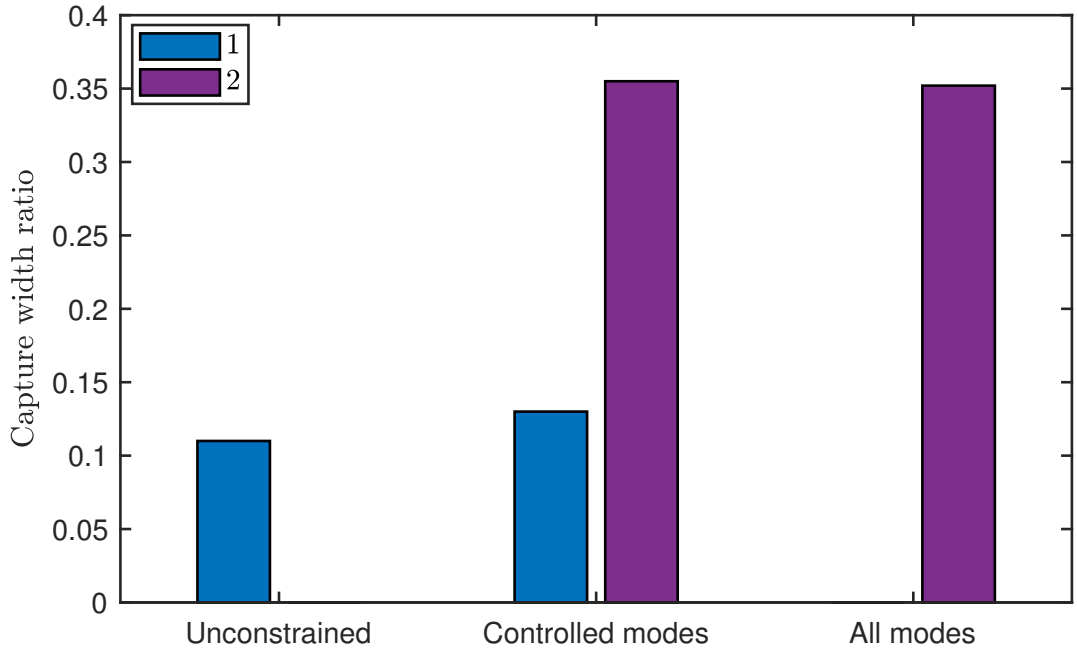

Figure 6.31: Unidirectional seas, 20° wave heading. Annual mean capture width ratio for the three control cases. Legend indicates the scale multiplier.

head-on waves in Figure 6.32). The fact that the peak CWR for wave angles between 60° and 90° occurs at a wave period of around 16s suggests that the spine of the original-scale ('x1') device is long enough for the more oblique wave directions. Given the increases in CWR achieved with an increase in the scale of the entire device, it is (at least to a large extent) the duck cross-section that is too small to tune effectively to the prevalent wave periods, which is the reason for the limited CWRs in irregular seas of small heading angles (Fig. 6.32). The increase in CWR with scale is even more pronounced in multidirectional seas with a 0° predominant wave angle, as the directional spread is taken into account (Fig. 6.33).

As a result of the undersized duck cross-section, the smallest duck spine considered (with a scale multiplier of 1) produces increasing amounts of power as the (predominant) wave angle increases towards a maximum value of 90° (see the blue bars of Figures 6.32 & 6.33). Again, this is explained by noticing that as the wave angle increases, the peak in CWR shifts towards periods more likely to be encountered in the wave climate (Fig. 6.34). With a doubling of the scale of the spine, the band of

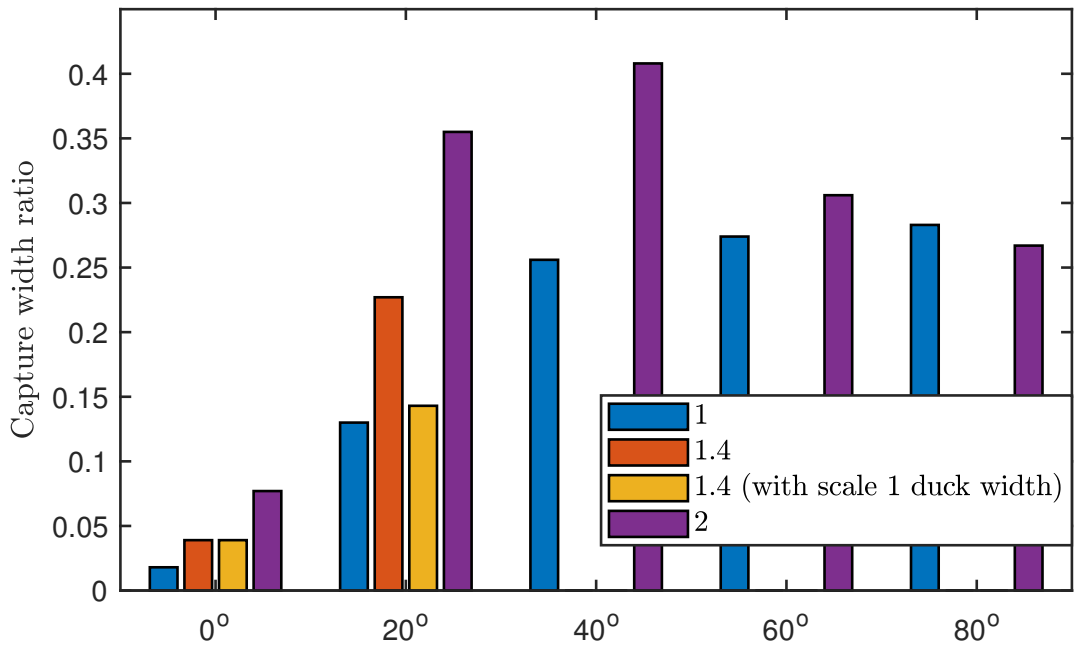

Figure 6.32: Unidirectional, irregular seas, constrained complex conjugate control. Annual mean capture width ratio of various scales and with various heading angles. Legend indicates the scale multiplier, note that the yellow bars involve a duck cross-section scale of 1.4, with a scale of 1 along the axis of the spine.

peak CWR is shifted and stretched towards higher wave periods (Fig. 6.35), reducing the angle at which peak CWR occurs in the irregular seas. (That band also extends over a wider range of wave periods than before.) In unidirectional waves, the greatest CWR of the double-scale device is achieved with a 40° heading angle, whereas in multidirectional waves, the peak lies at a predominant heading of around 60°. This is likely because of the steeper decrease in CWR below the band of peak CWR than above it (Fig. 6.35). The dwarfing of the unidirectional CWR achieved in head-on waves (0.077) by the CWR achieved with even a small increase in angle (0.355 at 20°), indicates that the ducks are still undersized (in terms of their cross-sectional area) for this particular wave climate - with a 0° wave angle, peak CWR of around 0.6 is only achieved at wave periods between 6s and 10s.

However, even if the duck cross-sections were enlarged whilst preserving the duck widths and spacings, performance may be degraded if peak CWR were to occur at the same wave period for every wave angle, since that would prevent the retention of

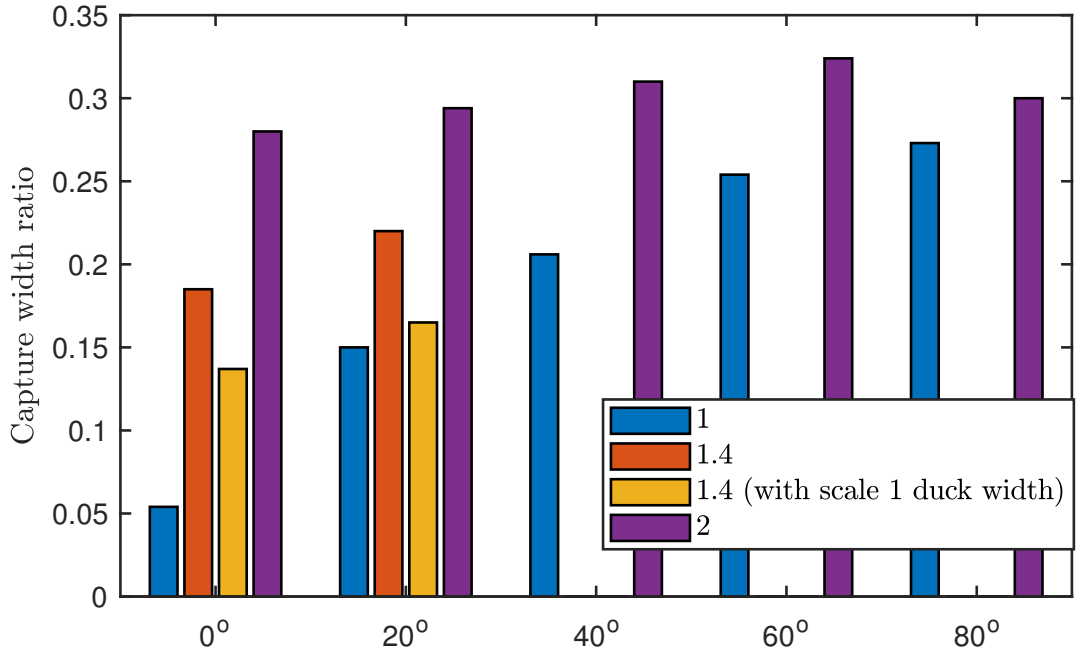

Figure 6.33: Multidirectional, irregular seas, constrained complex conjugate control. Annual mean capture width ratio of various scales and with various predominant heading angles. Legend indicates the scale multiplier, note that the yellow bars involve a duck cross-section scale of 1.4, with a scale of 1 along the axis of the spine.

peak CWR that is afforded by adjustment of the spine orientation as the predominant wave period changes. In any case, a small amount of directional spreading may be enough to eliminate the necessity of a much larger (and potentially less stable) duck - contrast the purple bars of both Figure 6.32 and Figure 6.33: as a function of the (predominant) wave angle, the CWR is much more narrow-banded in unidirectional seas. In multidirectional seas the double-scale duck spine enables an almost constant CWR across the full range of wave angles, a feature which could be beneficially exploited (using the device sizing) in more variable wave climates. Of course, the peak value of the CWR (with respect to predominant wave angle) would be lower in a wave climate with more spreading, but with the benefit of mitigating either the need for larger duck cross-sections, or for greater demands placed on the control system in order to avoid head-on waves.

It is important to bear in mind that though the ducks may be too small (in terms of cross-section) to extract power most efficiently in the absence of connecting joints

(or in head-on waves), it is the joints and ducks in unison that enable the higher CWR values. Whilst it is the addition of the connecting joints that allows the spine to achieve such high CWR values in slightly oblique sea states, it does not follow that the removal of the duck pitching (leaving a hinged-rafter type of device) would necessarily retain such performance. Further discussion regarding the inferences that can be made about different degrees of freedom on the basis of the breakdown of power extraction is given in Section 6.4.

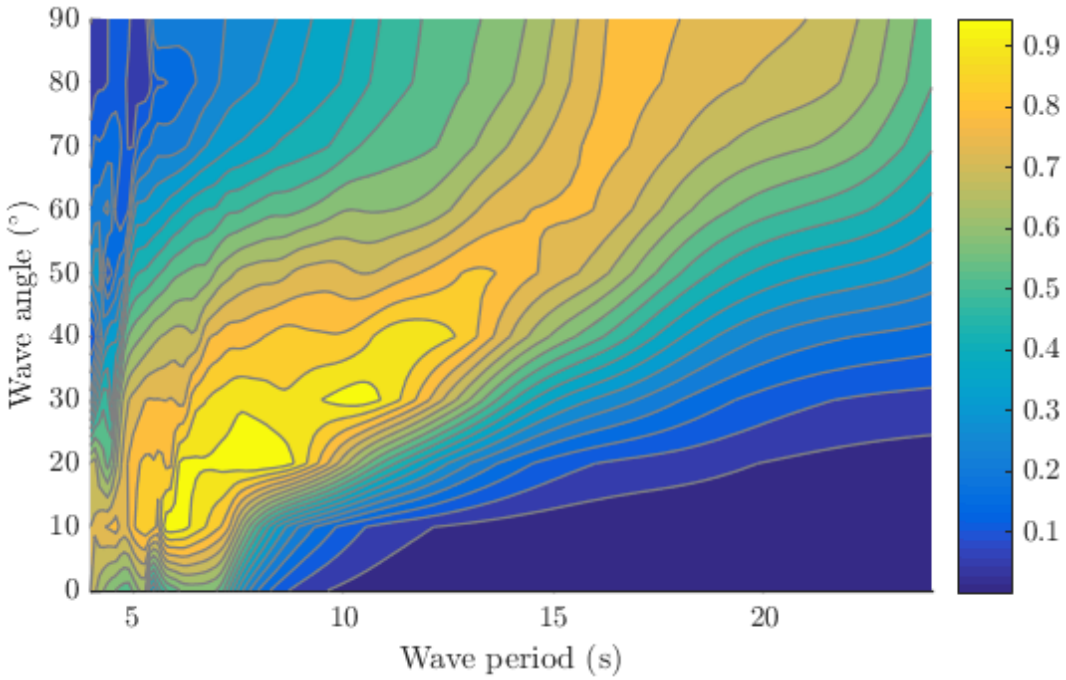

Figure 6.34: Capture width ratio of the original-scale ('x1') duck spine in regular waves.

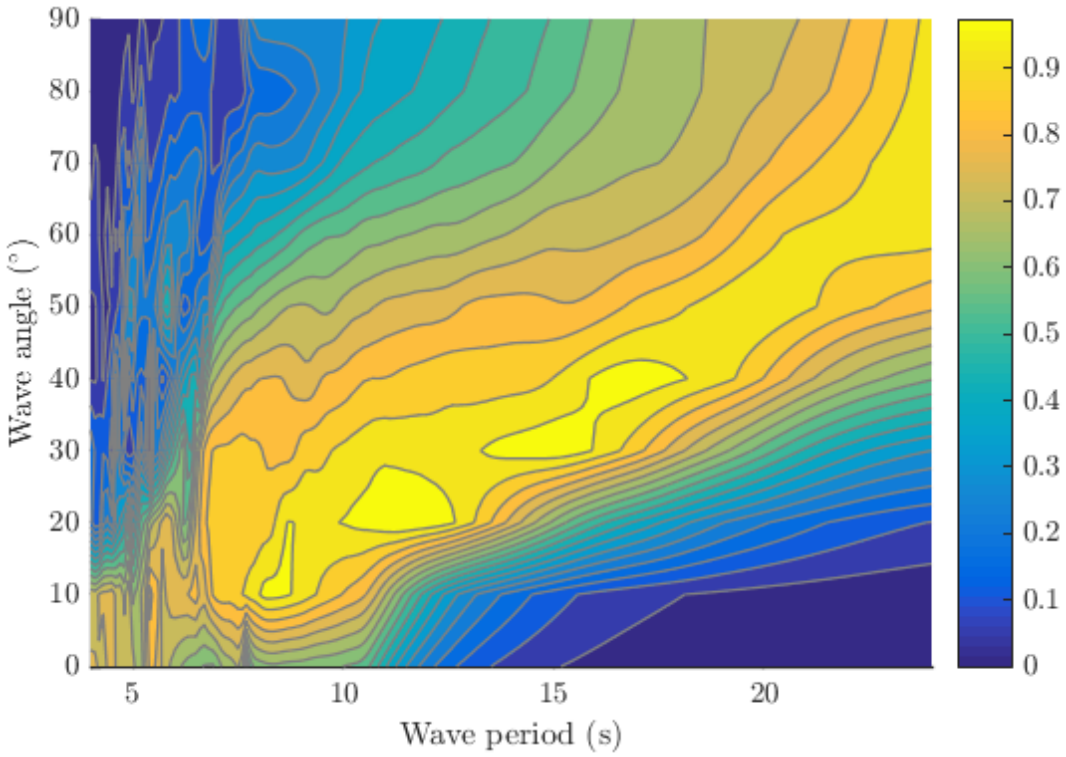

Figure 6.35: Capture width ratio of the double-scale ('x2') duck spine in regular waves.

Chapter 7

Conclusions and Further Work

Whilst the results of the optimisation studies are presented and discussed in Sections 5.7, 6.4, 6.5.3 and 6.6.2, this section collates the main findings specific to each device, and discusses some recommended areas for further work, motivated by the limitations of the current work. Conclusions from the illustrative example of the extended complex conjugate control method featuring the solo duck (Section 6.5.2) are also presented for completeness.

7.1 The WaveTrain device

7.1.1 Conclusions

With maximal power extraction as the only objective (see Section 5.7.1), it was discovered that there does not exist any single design that significantly outperforms all others. Despite this, five key design criteria have been found, all of which appear as necessary but not sufficient conditions.

The ratio of the mass of the internal water column to the mass of the surrounding module must be sufficiently large, in order to space the resonant response of those two elements appropriately in wave frequency. The exact value of the ratio required is somewhat dependent on the geometric and mass parameters chosen, but a value of at least five is recommended. Should stronger low density materials become available in the near future, even greater mass ratios would be better advised. It must also

be borne in mind that a wave climate experiencing a narrower range of frequency components would likely require lower mass ratios than those recommended here.

The optimal inclination angle of each WaveTrain module lies around 36°, but significant powers and CWRs can still be obtained between 27 and 37°.

The final three criteria are more evidently dependent on one another. The thickest floats (W_f closest to the upper limit enforced by L_f) tend to be required to produce the best performance, whilst the waterline in those designs must be low enough that it leaves a sufficient amount of bulk above the water surface. In these designs, the best waterline position is around halfway down the Vertical Float Face (VFF). In summary, the optimal configurations involve an almost maximal vertical float face length (provided by maximal W_f), with a waterline intersecting very close to halfway down the VFF. However, provided that a sufficient amount of bulk is retained above the water surface, slightly less-than-optimal designs exist with float widths as narrow as half the maximum allowed value, and with waterlines intersecting positions all the way up to the top of the VFF. Significant power reductions can be expected with floats any narrower than this, and with waterlines intersecting any higher than the VFF.

To summarise, the five key criteria, with their optimal values found by optimising power extraction where appropriate, are as follows:

1. Module inclination angle (36°)
2. Ratio of the entrained water mass to the module mass (> 5)
3. Waterline height relative to the vertical float face (halfway up)
4. Float width relative to float length (the maximum possible - so that float is triangular in cross-section)
5. Amount of 'bulk' above water (allows for minimal drop in performance with sub-optimal combinations of 3. and 4.)

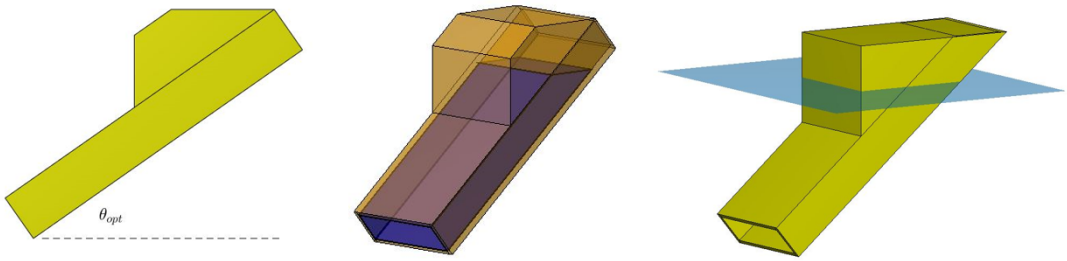

Figure 7.1: A graphical representation of the five key design criteria. Left: module inclination angle; centre: mass ratio; right: waterline height, relative float width, and amount of 'bulk' above water.

These five criteria (mass ratio, θ, waterline height, relative float width, and the amount of 'bulk' above water) vastly narrow the remaining area of design space. However, there remains flexibility in the choice of the remaining parameters (Table 7.1), providing some scope for practical considerations relating to the available materials and construction techniques. Whilst for the highest power-extracting designs, the upper bounds of W, D, and L were pushed up against, the remaining four parameters were not so tightly constrained: L_f ranged between 30 and 65m (between 0.22 and 0.45 of the module length, L), W_f ranged from 10 to 28m, ρ_t ranged from the lower bound of 1000kgm^{-3} up to values approaching 4000kgm^{-3}, and ρ_f ranged somewhere between 90 and 300kgm^{-3}.

Variable	Recommended value
θ	$27 - 37°$
W	$\geq$ 25m
D	$\geq$ 30m
L	$\geq$ 150m
L_f	$30 - 65$m
W_f	$10 - 28$m
W_f/L_f	$0.22 - 0.45$
ρ_t	$<$ 4000kgm^{-3}
ρ_f	$90 - 300$kgm^{-3}

Table 7.1: The recommended parameter values based on the single-objective optimisation of power extraction.

The inclusion of the second, force-based objective function (see Section 5.7.2) results in Pareto fronts that are inherently of a discontinuous nature, due to the

physical constraints. These discontinuities can be exploited, along with the curvature of particular sections of the Pareto fronts, to elect certain designs as more favourable, despite the inability to quantify the trade-off between the two objectives. From the Pareto fronts and the more favourable designs within them, some key trends emerge from the use of the three variants of the objective functions.

As when tending towards the designs of highest $\bar{P}$, as those with lowest $\bar{G}$ are approached, the waterline height decreases towards a limit around halfway down the vertical float face. In contrast to the highest $\bar{P}$ designs, which are also accompanied by a maximal float width, it is just sufficient that the float width of the lowest $\bar{G}$ designs is greater than around two-thirds of its maximal value. In between the two ends of the Pareto front, the waterline heights generally do not exceed the top of the vertical float face - almost all optimal design candidates have a waterline intersecting the upper half of the vertical float face.

Whilst high $\bar{P}$ values can be achieved to either side (particularly to the lower side) of the optimal inclination angle (36°), generally higher $\bar{G}$ values result as the inclination angle dips below, rather than above, 36°. A small number of designs may provide an exception to this rule, offering minor benefits in terms of the objective functions. However, any improvements may be outweighed by the difficulty in retaining feasibility as the design is practically engineered, since the physical constraints are increasingly severe at lower inclination angles.

For the Pareto front designs, the correlation of the power-based objective function with θ, is much stronger with the normalised objective functions ($\bar{P}/D$ and $\bar{G}/D$) rather than the unnormalised objective functions ($\bar{P}$ and $\bar{G}$). Whilst still not a sufficient condition for high $\bar{P}/D$, the Pareto front cannot be traversed without altering θ.

Maximising $\bar{P}/D$ requires an increase of D to around 9m. In contrast to the case with unnormalised objective functions, this is far below the upper bound, which suggests that perhaps this width of design is able to benefit most from some kind of beneficial diffraction effect.

As a result of the reduced values of D explored by the genetic algorithm with these objective functions, the panel size required for accurate results is reduced, in addition to the worsened solver convergence properties. This increases the computational requirements (or decreases the accuracy of the results), by decreasing the rate of convergence of the genetic algorithm, and by increasing the number of panels required for the meshes of the hydrodynamic models. These effects are seen in transitioning from objective functions $\bar{P}$ and $\bar{G}$ to $\bar{P}/D$ and $\bar{G}/D$, but they are particularly prominent with objective functions $\bar{P}/M$ and $\bar{G}/M$, at least partly because of the tendency for low values of D, W and W_f to prevail. Though an increased number of generations partly alleviates the problem, computational limits have restricted the level of certainty in the conclusions relating to these objective functions. Thus, they are presented with a lower level of confidence, more as insights that could prompt further investigation.

A square tube cross-section may be beneficial for objective functions normalised by the module mass. Whilst there is no clear trend in the waterline locations or float thicknesses, the two are very strongly correlated, indicating a much stricter dependence on the amount of bulk above water than with the other variants of the objective functions.

To summarise the main design trends discovered from the multi-objective optimisations, in the form of design recommendations:

(Objective functions $\bar{P}$ and $\bar{G}$)

- A waterline intersecting halfway up the vertical float face is required for the optimal designs at either end of the Pareto front.
- For the lowest $\bar{G}$ designs, W_f only needs to be greater than two-thirds of its maximal value.
- Regardless of the subjective level of importance of the two objectives, the waterline should always intersect the upper half of the vertical float face.

- Inclination angles (θ) below 36° should not be considered unless they are accompanied by major cost savings, since the joints will always incur more damage (with no benefits to power extraction) than the designs with θ above 36°. Manufacturing complexity is also likely to increase with θ values much below 30°.

(Objective functions $\bar{P}/D$ and $\bar{G}/D$)

- The inclination angle, θ, must be changed in order to traverse the Pareto front - i.e. in order to achieve optimal designs with different levels of importance ascribed to power extraction and to the force acting at the joints.

- Capture width ratio appears to be optimised with D around 9m.

(Objective functions $\bar{P}/M$ and $\bar{G}/M$)

- If high device mass is a concern, it may be beneficial to employ a square tube cross-section (i.e. $W = D$).

The Pareto sets for the three multi-objective cases are also characterised by certain parameter ranges. The designs optimised for $\bar{P}/M$ and $\bar{G}/M$ tend to have short modules (50m $< L <$ 65m) and relatively high inclination angles ($47° < \theta < 56°$), whereas the designs optimised for $\bar{P}$ and $\bar{G}$ and for $\bar{P}/D$ and $\bar{G}/D$ span wider ranges of module lengths and inclination angles - from just over 30° up to 54°, and from around 65m up to the upper bound of 150m. In all cases, the designs with the highest values of the power-based objective functions are characterised by low θ and high L, with some level of correlation along the Pareto fronts towards the designs with the lowest force-based objective function values, which tend to have high θ and low L values.

For designs optimised for $\bar{P}$ and $\bar{G}$ and for $\bar{P}/D$ and $\bar{G}/D$, W is never lower than 13m, and the upper bound (25m) is pushed up against for the designs with highest $\bar{P}$ and $\bar{P}/D$. In both cases, the ratio of the float length to the tube length, L_f/L, is split into two regions - for the highest $\bar{P}$ or $\bar{P}/D$ designs, the float length is somewhat less than half the tube length, whilst it is somewhat greater than half the tube length for

the designs at the opposite end of the Pareto front. The float width (W_f) is always greater than 12m, and lies somewhere between a quarter and half of the float length (L_f).

The trends for the two densities differ somewhat between these two pairs of objective functions. Designs optimised for $\bar{P}$ and $\bar{G}$ are split into two groups in terms of float density, ρ_f. When $\bar{P}$ <2MW, 50kgm^{-3} < ρ_f < 125kgm^{-3}, and for $\bar{P}$ >2MW, 200kgm^{-3} < ρ_f < 380kgm^{-3}. The full range of tube densities is spanned by the Pareto front individuals, but a high ρ_t is always complemented by a particularly low ρ_f value. Likewise, the higher ρ_f values must be accompanied by lower ρ_t. To a large extent mirroring the trend in waterline height, both the highest and lowest $\bar{P}$ designs have ρ_t values approaching the lower bound of 1000kgm^{-3}. To accompany this, the designs placing more importance on high $\bar{P}$ have relatively high ρ_f values, and the designs placing greater importance on limiting $\bar{G}$ have lower ρ_f values. By contrast, the designs optimised for $\bar{P}/D$ and $\bar{G}/D$ exhibit little correlation with ρ_f, but it spans 150 - 400kgm^{-3} for all designs. There is little constraint on the pairings of tube and float densities. The designs with highest $\bar{P}/D$ have ρ_t values towards the lower bound, as before, but the designs with lowest $\bar{P}/D$ have higher ρ_t values, around 3000kgm^{-3}.

All three objective function pairings share the conclusion that a mass ratio in excess of 10 is generally required for the designs with highest values of the power-based objective function. Conversely, this mass ratio should be much lower if more emphasis is placed on obtaining low values of the force-based objective function.

Whilst the optimal designs vary quite widely across the choice of objective functions, and within each Pareto front, a number of more general recommendations can be made on the basis of the findings from the previous four paragraphs:

- If high power extraction is given most importance, the device should be characterised by low *theta* and high L values; if low joint forces are prioritised, the device should have higher θ, with lower L.

- The tube width, W, should not be smaller than 13m.

- Higher prioritisation of power extraction should be accompanied by shorter floats (lower L_f) relative to the tube length (L).
- In general, the entrained water mass should be at least 10 times larger than the module mass.

7.1.2 Limitations and further work

Despite the efficient hydrodynamic model, various avenues of investigation were rendered inaccessible by their high computational requirements. As such, the study has been partly sculpted by these limitations. As available computer power continues to rise in the subsequent years (see Appendix H), it may be possible to extend the current work to build greater breadth and certainty of the conclusions, perhaps strengthening the endeavour by intertwining the numerical work with further physical testing. A number of specific areas for further work follow directly from the conclusions in the previous section, whilst others are more directly related to the methodology.

Whilst Section 5.6 enabled some insight into the effect of the constraints on the parameter space, the complexity could be further explored in order to better distinguish between the influences of the physical and computational constraints. Making the optimisation runs with different panel (patch subdivision) sizes could help clarify if the results are in any way dependent on the discretisations. This would lower the dependency on the added mass matrix symmetry metric as a filter for inaccuracy, but the sensitivity of the results to various thresholds of this metric could also be quantified. Whilst certain constraints on the physical design are absolutely necessary to the WaveTrain concept (e.g. freely-floating, static stability), others could be changed in an attempt to unlock further areas of parameter space. For instance, trialling various float shapes (see the absence of points in the top left corner of Fig. 5.16), modifying the joint attachment points, changing the number of modules, etc. Relating to the trends in Section 5.6, for instance, the bias against designs with low θ may be alleviated by a change in the float shape and a relaxation of the constraint on float thickness (Eq. 5.5). Where possible, these investigations should be motivated by consideration

of the underlying physics. Thirdly, the genetic algorithm parameters that govern the search routine could be tuned towards the goal of reducing the required computational resources. It should also be checked to what extent the genetic algorithm search itself shapes the obtained trends, and whether there are still better performing designs that a tuned GA could aim to find. Fourthly, zeroing the power at frequencies for which the solver fails to converge can result in indications of poorer hydrodynamic model accuracy than is really the case; with cubic spline order (as opposed to quadratic), the solver can be particularly prone to failure, despite a very close comparison of the response amplitude operators at frequencies where the solver succeeds.

It was noted in section 5.1 that spectral domain models could offer an efficient way of incorporating nonlinear behaviour into the numerical models for use in an optimisation scheme. Given that the objective functions used in this optimisation study were only dependent on quantities averaged over each sea state, the lack of time series information provided by a spectral model poses no issues. It would be interesting to approach the challenge of determining suitable coefficients for the nonlinear forces in this kind of model, particularly with respect to an optimisation study. Because of the variation in designs, it may be most reasonable to have these coefficients dependent on the geometric parameters. However, it would be interesting to contrast the results of a study in which a constant viscous drag coefficient (e.g. taken from previous WaveTrain work [2], [20]) were employed within a spectral domain model, with the results in the present work.

Similarly to in a spectral domain model, the motion limits could have alternatively been enforced by assuming that the wave components within an irregular spectrum obey a Gaussian distribution, and so simply removing a certain fraction of the total power, based on the motion limit. This would have been simpler than the alterations of the time series used in this work, but would not have removed the need to integrate over the time series. To do this, a spectral domain approach would be required.

The approaches mentioned so far can also be applied to investigate questions more specifically relating to the obtained results. For instance, the validity of the trends

obtained for objective functions $\bar{P}/M$ and $\bar{G}/M$ should be investigated, along with the underlying causes of, for example, the benefits of a square tube cross-section (if these conclusions hold true). Relating to the relative effects of the physical and computational constraints, the amount to which they are responsible for the discontinuities in the Pareto fronts could be investigated. The beneficial diffraction effect hypothesised from the use of objective functions normalised by the characteristic device width, D, should be investigated. A physical explanation for this may enable a conclusive determination of this parameter, regardless of the rest of the design configuration.

How the simplified module design (including the point mass) can be translated into appropriate engineering designs, whilst retaining the key criteria for performance, should also be investigated. Based on the limitations that may be imposed by the manufacturing and construction processes, design tolerances could be introduced in order to quantify the level of uncertainty in the performance of the optimal design candidates when they are realised physically. Depending on the robustness (with regards to performance) of the optimal design features discovered in this work, robustness could be included in the optimisation scheme as an additional objective function. Given sufficient computing resources, this could be achieved by assessing a small set of designs around each design candidate in order to extract a distribution of the sensitivity of the power or fatigue damage, whose standard deviation could then be minimised.

In the configuration of the optimisation routines, some consideration was given to allowing a range of designs with the spacing between modules equal to half a wavelength. Despite the use of irregular seas comprising not just a single wavelength, the module spacings of the candidates for optimal design should be investigated, in order to understand the range of conditions over which this hypothesis holds true.

Finally, physical testing of some of the optimal configurations in a tank may help to somewhat validate the outputs of the optimisation routines (i.e. the design trends and best-performing configurations), and could be used to obtain physical understanding that could be used, in turn, to inform the design of the optimisation algorithms. Some empirical measurements of the stress cycling at the joints could also enable the

expression of the force-based objective function absolutely, in terms of the lifetime. Comparable economic data could even extend this to a monetary cost, enabling the two objective functions to be combined into a single objective function.

7.2 The solo duck

Conceding control of some degrees of freedom may provide cost savings that outweigh the loss in power. In head-on waves, conceding control of heave reduces the peak value of capture width ratio from 1.97 only to 1.79. A similarly mild reduction in performance is achieved by conceding control of pitch, but significantly worse performance results if surge becomes uncontrolled. Conceding control of roll can actually result in increases in capture width ratio for certain wave period ranges and intermediate heading angles, over the case where all degrees of freedom are controlled. In 30° oblique waves, there are several key combinations of control concessions, which result in only small performance reductions: conceding control of heave, roll or pitch (5 controlled modes), conceding control of heave and roll or pitch and roll (4 controlled modes), conceding control of roll, pitch and yaw (3 controlled modes). Control of only one of the heave and pitch modes at most should be sacrificed; conceding control of both results in significantly lowered capture width ratio.

7.3 The duck spine device

7.3.1 Conclusions

From the frequency-domain analysis of the ten-duck spine in various wave periods and angles (see Section 6.4), there are some key conclusions regarding the design and behaviour, that are independent of the control strategy:

- A significant contribution to the total power extraction should be expected from the joints, except perhaps when the wavefronts are parallel to the spine.
- Optimal power extraction will likely require a small angle of orientation between the spine and the incoming wavefronts.

- Optimal power extraction may require significant amounts of power being injected into certain degrees of freedom, in order to increase the extraction through others.

- The dynamics of the duck spine under the constrained optimal power take-off conditions are complex.

- Outer and inner spine joints can benefit the entire spine through their complementary dynamics and power extractions.

- Similarly, upstream ducks should have different power extraction profiles to downstream ducks.

- Shear forces acting on the joints in the sway direction (along the spine) are significantly lower than shear forces on the joints in the heave and surge directions (perpendicular to the spine).

- Surge and heave shear forces can be expected to be greater on joints at either end of the spine.

- The moments on the joints, input as part of the control strategy (in yaw and roll directions), generally correlate inversely with the joint shear forces (in heave and surge directions), but only for conditions with small wave heading angles.

Whether or not the motion constraint for the complex conjugate control strategy is applied to the uncontrolled degrees of freedom does not heavily impact the predicted power extraction or the demanded control moments (see Section 6.5.3). This is perhaps physically due to the spine spanning multiple wave crests. However, the shear forces and motions are somewhat different between the two cases:

- Whilst the shear forces in the sway direction are largely unchanged, the surge and heave shear forces at the joints are in general reduced, with the reduction more significant at lower wave angles.

- Less asymmetry (with respect to the spine) in the shear forces is present under the extended motion constraint, but the joints at either end of the spine tend to always undergo the largest shear forces.

- As well as the overall reduction in heave and surge shear forces, the extended constraint also introduces an oscillatory component of the shear force amplitudes with respect to wave period, so that the proportional reduction is much greater at certain wave periods than others.

- With the extended motion constraint, the shear forces (at least in heave and surge) are lowest at joints 3 and 7, halfway between the middle of the spine and the joint at each end.

- The motions of the spine are complex, and seem largely dependent on both the type of constraint and the weightings. Despite this, hints of 'flexural wave' type behaviour can be observed for certain degrees of freedom at certain wave periods and angles - i.e. where motions of the spine are larger towards the downstream end (at least for certain degrees of freedom).

Finally, the simulation of the ten-duck spine in irregular waves (see Section 6.6.2) provides additional insights. Of the three complex conjugate control variants, applying the motion constraint to only the controlled degrees of freedom has been found to be most appropriate for the time-series analysis. The size of the duck spine can be critical to performance, with respect to which the wave direction must be considered, because of its determination of the relative importance of the spine length and the duck cross-sectional size. Based on the typical dimensions used to achieve a stable design (as in this work), undersized duck cross-sections are perhaps more likely than too short a spine.

If there exist significant limitations on the mechanism used to tune the spine orientation in each sea state, the presence of directional spreading may be beneficial, by reducing the dependence of the CWR on the orientation angle; despite its lineal

design, the duck spine may perform favourably in sea climates with spreading and where the predominant wave direction changes significantly. The spreading may also reduce the need for further and potentially destabilising enlargement of the duck cross-sections. If there exists an asymmetry in the rate of decline of the monochromatic CWR above and below the peak CWR band, the directional spreading is also likely to change the required orientation angle with respect to the predominant direction of the incoming waves.

7.3.2 Limitations and further work

Despite the breadth of conclusions drawn about the behaviour of the duck spine under likely operational conditions, the modelling analysis used in this thesis has provided a vast quantity of data, from which many more observations could be made. There are also further dependencies that should be investigated. It was noted that the motion constraint weightings were taken from prior studies and may be overly-conservative, particularly in the context of the larger numbers of degrees of freedom. The impact of increasing the lenience of the weightings should be investigated, especially regarding the fact that the motion constraints most heavily affect the power extraction at the smallest wave heading angles. In this work, the motions of each degree of freedom have been constrained through the use of modes of motion amongst which there is significant coupling. In this light, the absolute body motions should be analysed for additional trends in the body dynamics, and to verify the limits of the suitability of applying the motion constraints in this way. In the frequency-domain analysis, wave amplitude should be added to period and angle as a third variable, in order to expand the understanding of the dynamics and performance to conditions expected in a real sea climate. In order to maximise the potential of the spine, the dependence of the optimal spine sizing on the wave climate should be investigated, with a view to quantifying the relationship. The hints of 'flexural waves' should be investigated further, in order to understand whether any detrimental effects on the loadings should

be expected for the real system, and whether the control strategy could be modified accordingly.

A zigzag arrangement of duck modules along the spine would allow the provision of the necessary orientation angle of each duck with respect to the incoming waves, without the need to angle the entire spine. By reformulating the shape functions for the motions about each joint, this type of configuration should be modelled to investigate the consequences for the power absorption and the device dynamics.

A further challenge is the choice of control strategy for a real, time-domain system. A sensitivity study focused on the control moment coefficients could aim to find optimal values constrained by upper limits on the moment provision. The model could also be used to analyse the amount of power exchanged in and out of each degree of freedom that does not contribute to the average power. For a given control strategy, this would give a measure of how any power take-off system inefficiencies are likely to be amplified [44], and hence the level of robustness. With regards to facilitating a fair comparison between the duck spine (or other jointed devices) and other candidates for large amounts of wave power extraction, a suitable alternative metric to capture width ratio should be devised. Finally, physical testing of sections of a power-extracting spine may prove useful in validating the models and assessing the contribution of nonlinear behaviour under certain conditions.

Appendix A

Verification that all body motions are achievable with a given set of generalised modes

To verify that all possible configurations of a jointed body are achievable using a superposition of the modes of motion, we begin with an example case of two hinge-connected bodies. This system can be modelled using six rigid body modes, plus one generalised mode allowing for symmetric motion about the hinge. Firstly, it is trivial to see that any position of the entire body can be achieved by the rigid body motions. Now consider the absolute rotation angles of bodies 1 and 2 to be Φ_1 and Φ_2, respectively. From the mode definitions, and given that the hinge mode is defined relative to the rigid body pitch mode, these are given by superpositions of the pitch motion, ϕ_p, and the symmetric rotation about the hinge, ϕ_1:

$$\begin{pmatrix} 1 & 1 \\ 1 & -1 \end{pmatrix} \begin{pmatrix} \phi_p \\ \phi_1 \end{pmatrix} = \begin{pmatrix} \Phi_1 \\ \Phi_2 \end{pmatrix} \tag{A.1}$$

The linear independence of the premultiplying matrix implies that all possible configurations of both bodies about the hinge are achievable with this set of modes of motion. This can easily be extended inductively to n hinges connecting $n+1$ bodies, because each additional hinge provides a contribution of opposite sign to each of its connecting bodies.

Appendix B

Miscellaneous difficulties and troubleshooting points

This section gives a selection of remarks concerning miscellaneous difficulties in the implementation of generalised modes for joints.

1) WAMIT provides two methods of implementing generalised modes, characterised by their use of different pre-processing files in which the properties of the generalised modes can specified. Without venturing deeply into the functions of each, the first method uses a self-contained Fortran file, labelled 'DEFMOD'. However, in order to use the 'higher-order' method for specifying the distributions of the velocity potentials over the body surfaces, the second method must be used. This involves compiling the appropriate Fortran code into a Dynamic Link Library (DLL) file, labelled 'NEWMODES'.

The mesh of the submerged body portion is defined about its centre of gravity for convenience of definition of its mass properties. This means that the body then needs to be shifted down to its correct location (such that $z = 0$ at the free surface) before the velocity potentials are solved for. Coordinates for this translation are defined in the .POT file. However, it has been discovered that there exists a difference between the two methods in the coordinate frames in which the shape functions must be defined. It seems that there is no information regarding this in the WAMIT manual ([28]), and so this provides a potential source of difficulty in setting up the generalised modes.

When using DEFMOD, the shape functions should be defined in WAMIT's '*global* coordinate frame', where $z = 0$ at the free surface. This requires a shift of any occurrence of the z-coordinate downwards by the difference between the free surface position and the centre of gravity location (the mesh file is defined about the centre of gravity). However, when using NEWMODES, the shape function needs to be defined with respect to the '*body* coordinate frame', in which the mesh file is defined. Hence no coordinate shift is required in that case.

2) Computing the gravitational restoring force/moment coefficients can prove arduous and be prone to programming errors. Given the absence of any direct feedback from WAMIT on the presence of these errors, a good indicator of errors in the coefficients is provided in the Response Amplitude Operators (RAOs) - specifically, RAO magnitudes tending towards a non-zero value as the frequency tends to zero.

3) Particular care should be taken with the specification of the generalised modes when panels/patches lie particularly close to the joint location. In addition to ensuring that patches do not span the discontinuity, it must be ensured that the panels or patches are associated with the correct mode definition. Vertical panels or patches can be particularly prone to errors in this sense.

Appendix C

The use of a point mass

With only two mass components (float and tube), and the float extending downwards from the top of each module, a third mass component is necessary to enable a wide range of solutions to satisfy the equality (5.1). Physically, the point mass approximates what may be achieved with a more complicated mass distribution in practice. By placing it at the bottom of the upper face of the tube (see Fig. 5.1), the centre of gravity can easily be shifted to the left, whilst the centre of buoyancy will shift rightwards (in the module's reference frame), as more of the module becomes submerged. This is important in solving equality (5.1) because without the point mass, the centre of gravity will usually be further right than the centre of buoyancy.

Typically, the masses required are insignificant compared to the float and tube wall masses, and so are not investigated further during the optimisation study.

Appendix D

Dipole wall approximation

The test device used is described by the parameters given in Table D.1. A small range of densities is required to maintain feasibility of the device for the full range of wall thicknesses.

Parameter	Value
Module length, L	1
Inclination angle, θ	40
Float length, L_f	0.5
Float width, W_f	0.15
Tube depth, D	0.8
Tube width, W	0.15
Float density, ρ_f	200 - 350
Tube density, ρ_t	1350 - 1500
Tube wall thickness, t	variable

Table D.1: Test device parameters for dipole wall approximation study.

Five wall thicknesses have been used to test the validity of the dipole wall panels - 1, 2.1, 5, 7.5 and 10mm. A small amount of damping is applied to each water column ($5\text{Nm}^{-1}\text{s}$). The lid RAOs begin to deviate significantly around 5mm (Figs. D.1, D.2). Whilst the dipole-walled meshes are identical for each case, the mass/inertial properties of the device still vary with thickness, hence the reason that the RAOs differ.

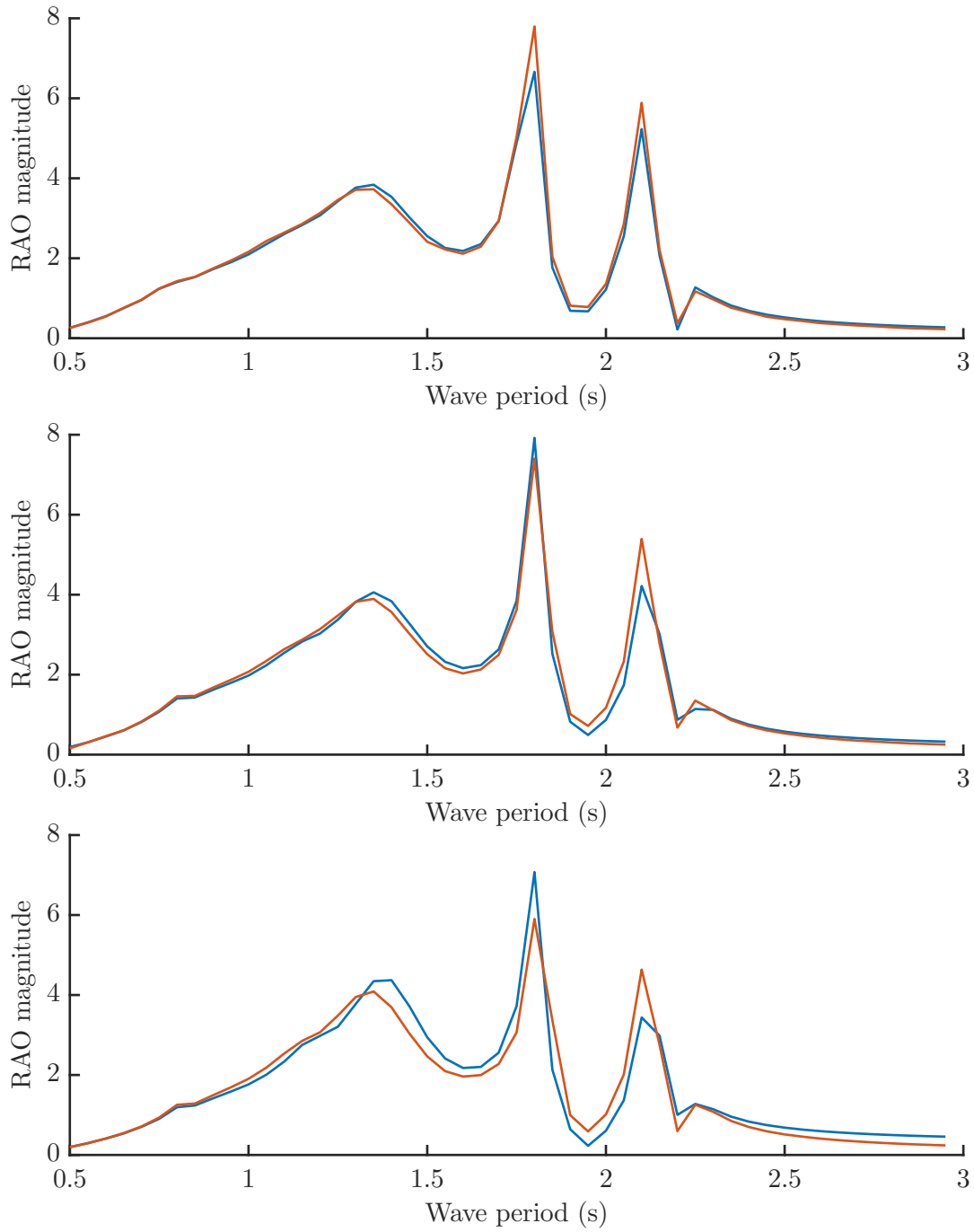

Figure D.1: RAO magnitudes of central lid, wall thicknesses of 0.001m (upper), 0.0021m (central) and 0.005m (lower). Red - thick-walled mesh; blue - dipole-walled mesh.

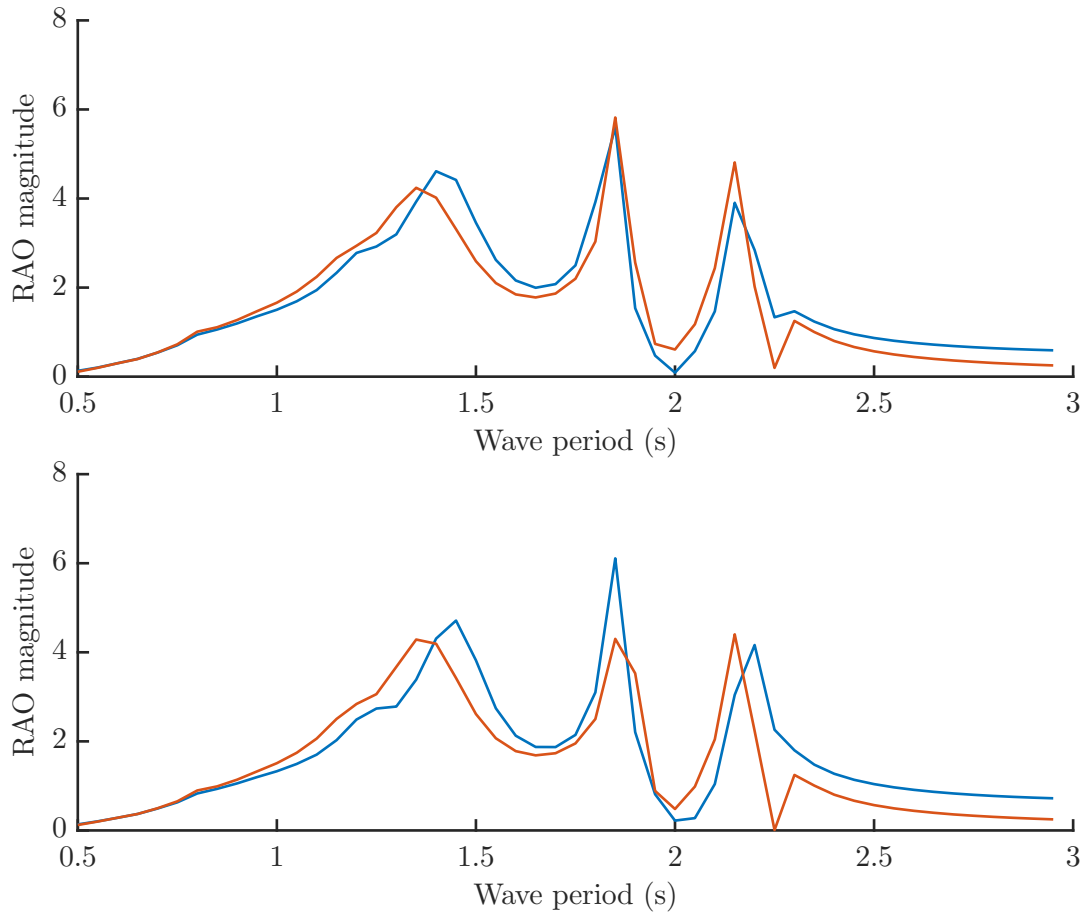

Figure D.2: RAO magnitudes of central lid, wall thicknesses of 0.0075m (upper) and 0.01m (lower). Red - thick-walled mesh; blue - dipole-walled mesh.

As expected, convergence is achieved with fewer patch subdivisions with the dipole wall representation (Fig. D.3).

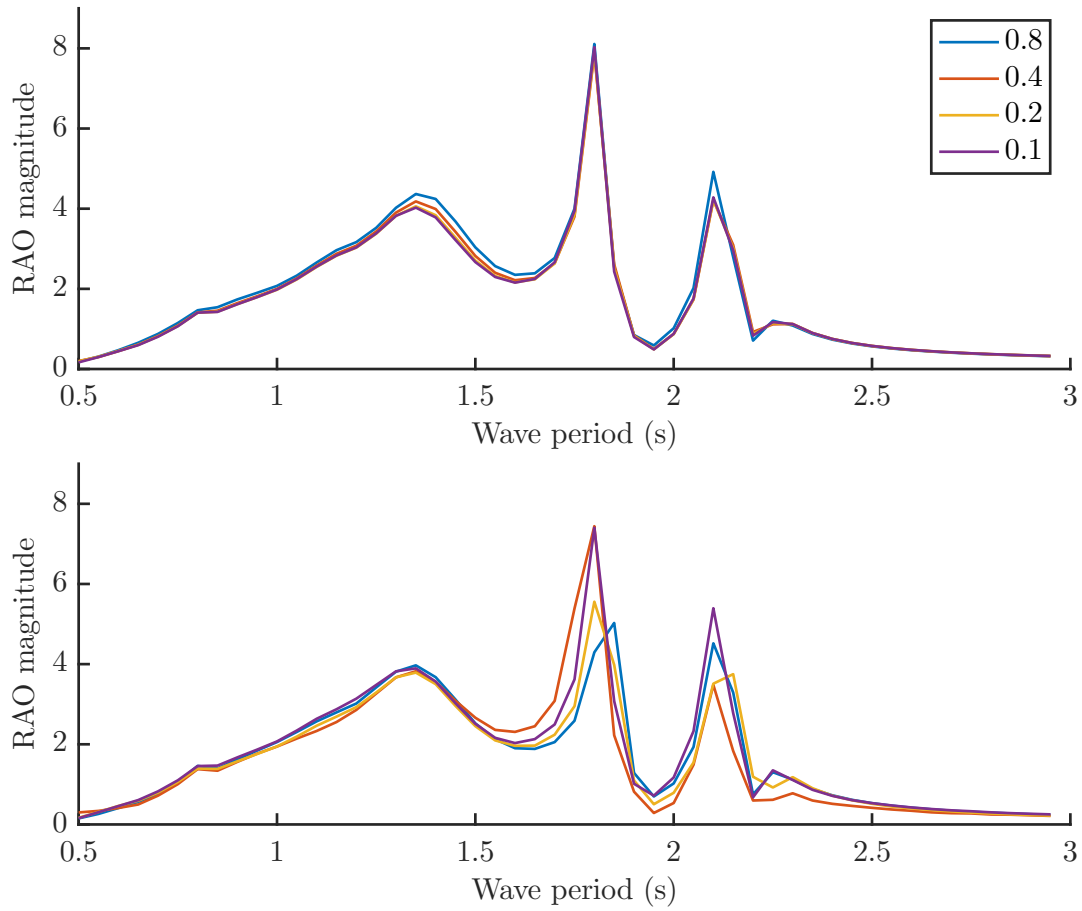

Figure D.3: RAO magnitudes of central lid, with the dipole-walled mesh (upper) and with the thick-walled mesh (lower). Legend indicates panel size as fraction of module length, L.

The use of dipole walls increase computational efficiency by both reducing the number of patches required, and by reducing the number of subdivisions required for sufficient solution accuracy.

Appendix E

Guidance on choosing form of (generalised) mode definitions

In modelling a wave energy converter, the portions over which the modes of motion are defined can influence the level of convenience involved in defining the power take-off forces/moments. Take the simple example of a two-body wave energy converter, with both bodies moving in heave, and power extracted from the relative motion of the two by an on-board PTO system. By defining the system by a heave mode of the entire assembly as if it were rigid, and a heave mode of the second body, the power take-off forces require application to only the second mode of motion. Denote this method as using *'relative' mode definitions*. If each of the modes were instead defined over each individual body, both modes of motion would require damping in order to represent the forces applied by an on-board PTO system. Characterise this method by the presence of only *'absolute' mode definitions*, for modes involving power extraction.

Alternatively, if the power were extracted by the absolute motion of the second body (e.g. by a seabed-mounted PTO system), defining the modes separately over each body enables the requirement of only a single damping coefficient. In practice, this could be a heaving device operating in the presence of a nearby floating body, or a heaving buoy whose monopile support alleviates some of the loadings by also allowing motion in pitch. Table E.1 summarises the form of the damping matrix for these cases, forming some guidance on which type of mode definitions to adopt for each kind of power extraction; if power is extracted from relative motion, use *relative*

mode definitions, if power extracted from the absolute motion of a particular degree of freedom, use *absolute* mode definitions.

	'Absolute' mode definition	'Relative' mode definition
On-board PTO	$\begin{pmatrix} B_{pto} & -B_{pto} \\ -B_{pto} & B_{pto} \end{pmatrix}$	$\begin{pmatrix} 0 & 0 \\ 0 & B_{pto} \end{pmatrix}$
Seabed-mounted PTO	$\begin{pmatrix} 0 & 0 \\ 0 & B_{pto} \end{pmatrix}$	$\begin{pmatrix} B_{pto} & B_{pto} \\ B_{pto} & B_{pto} \end{pmatrix}$

Table E.1: The required form of the PTO damping matrix for a two degree of freedom device when using each modelling approach and each form of power take-off system.

This guidance is extensible to devices with any amounts of degrees of freedom or PTO systems, applying to just the degrees of freedom involving power extraction. It should also be noted that whilst the form of the PTO damping matrix is easy to express in the example case of two heaving bodies, regardless of the approach, for larger more complex systems with various degrees of freedom, this is not necessarily so when power extracting modes are defined in the 'absolute' manner. In fact, providing the appropriate reaction forces on the rest of the bodies using this approach may require several force components acting on other modes of motion, depending on how the modes are defined.

In the case with only a single PTO system with no stiffness provision, the 'relative' mode definitions also permit the damping coefficient to be found analytically (see Section 5.3.2 and Appendix F).

Appendix F

Analytical optimisation of damping coefficients

Optimising the damping coefficient for a wave energy converter with just a single degree of freedom, for whom stiffness provision is infeasible (such as a bottom-fixed Oscillating Water Column (OWC)), is straightforward ([59], p.192). Increasing the amount of degrees of freedom, whilst maintaining power extraction through just one, increases the complexity but still permits an analytical solution. The next two sections investigate these cases, before the subsequent two sections investigate the system of polynomial equations as the number of PTOs is increased.

F.1 1 PTO, 1 other mode of motion

This case mirrors a floating OWC, with a vertical water column, and its encasing body only free to move in heave. Beginning with the frequency-domain equations of motion (F.1, F.2), using $N = 2$, the water column motion can be rearranged for and used in the expression for the average power extracted (F.3).

$$\sum_{j=1}^{N} \widetilde{D}_{ij}\xi_i = X_i \tag{F.1}$$

$$\widetilde{D} = -\omega^2(M_{ij} + A_{ij}) + \mathrm{i}\omega(B_{ij} + B_{ij}^{pto}) + C_{ij} \tag{F.2}$$

$$P_a = \frac{1}{2}\omega^2 \xi^{\dagger} \mathbf{B}^{pto} \xi \tag{F.3}$$

This yields an expression for the power in the form of (F.4), where a, b, c and d are coefficients in terms of the elements of matrices $\mathbf{A}$, $\mathbf{B}$, $\mathbf{C}$, $\mathbf{M}$, and the vector $\mathbf{X}$.

$$P_a = \frac{dB_{pto}}{aB_{pto}^2 + bB_{pto} + c} \tag{F.4}$$

Differentiating with respect to B_{pto}, and setting equal to zero, results in a quadratic equation, whose solution is given by (F.5) and (F.6). Interestingly, the optimal B_{pto} in this case is independent of the excitation forces, X.

$$B_{pto}^{opt} = \sqrt{\frac{c}{a}} \tag{F.5}$$

$$B_{pto}^{opt} = \sqrt{\begin{aligned} &\{[-\omega^2(M_{11}+A_{11})+C_{11}][-\omega^2 A_{22}+C_{22}] \\ &-\omega^2 B_{11}B_{22}+\omega^2 B_{12}B_{21} \\ &+[-\omega^2 A_{12}+C_{12}][\omega^2 A_{21}-C_{21}]\}^2 \\ &+\omega^2\{B_{11}(-\omega^2 A_{22}+C_{22}) \\ &+B_{22}(-\omega^2(M_{11}+A_{11})+C_{11}) \\ &+B_{12}(\omega^2 A_{21}-C_{21}) \\ &-B_{21}(-\omega^2 A_{12}+C_{12})\}^2 \end{aligned}}{\omega^4 B_{11}^2 + (-\omega^2(M_{11}+A_{11})+C_{11})^2} \tag{F.6}$$

A similar procedure was used by Stappenbelt and Cooper [56] in their derivation of the optimal PTO damping for a floating OWC modelled using three modes of motion.

F.2 1 PTO, N other modes of motion

In this case still only one body motion is involved in the power production. However there are now N entries in each row of the matrix, $\widetilde{\mathbf{D}}$, reflecting the extra couplings between the PTO mode and each other mode. This means that the form of the solution will still be that of (F.5), but with coefficients a, b, c, and d now depending on additional terms due to the other modes. By noticing how they are formed, a more general form of (F.6) can be derived. The inverse of $\widetilde{\mathbf{D}}$ is required to solve for the

body motions. This inverse is equal to its adjugate matrix divided by its determinant. Hence the numerator coefficient, d, is formed by multiplying row i of matrix $\widetilde{\mathbf{D}}$ by the excitation force vector, $\mathbf{X}$, where i denotes the index of the PTO mode (F.7, F.8).

$$d = \frac{1}{2}\omega^2 |\sum_{j=1}^{N} D_{ij} X_j|^2 \tag{F.7}$$

$$\mathbf{D} = adj(\widetilde{\mathbf{D}}) \tag{F.8}$$

Denominator coefficients, a, b and c are derived from the square of the determinant of $\widetilde{\mathbf{D}}$. c is the part of $|det(\widetilde{\mathbf{D}})|^2$ that is not a function of B_{pto}, and so can be expressed in terms of a modified determinant (F.9, F.10). $\widetilde{\mathbf{C}}$ is given in (F.10) for the case where the power extraction is associated with the last mode index.

$$c = |det(\widetilde{\mathbf{D}} - \widetilde{\mathbf{C}})|^2 \tag{F.9}$$

$$\widetilde{\mathbf{C}} = \begin{bmatrix} 0 & \dots & 0 & 0 \\ \vdots & \ddots & \vdots & \vdots \\ 0 & \dots & 0 & 0 \\ 0 & \dots & 0 & \mathrm{i}\omega B_{pto} \end{bmatrix} \tag{F.10}$$

In a similar fashion, a is the component of $|det(\widetilde{\mathbf{D}})|^2$ that is a function of B_{pto}^2 (F.11, F.12). In this case, the coefficient must locate only the terms in the determinant of $\widetilde{\mathbf{D}}$ comprising B_{pto}, that when squared, yield all terms proportional to B_{pto}^2.

$$a = |\frac{M_{ii}(\widetilde{D} - \widetilde{C}_c)_{ii}}{B_{pto}}|^2 \tag{F.11}$$

$$\widetilde{\mathbf{C}}_c = \begin{bmatrix} 0 & \dots & 0 & 0 \\ \vdots & \ddots & \vdots & \vdots \\ 0 & \dots & 0 & 0 \\ 0 & \dots & 0 & (D_{ii} - \mathrm{i}\omega B_{pto}) \end{bmatrix} \tag{F.12}$$

M_{ii} denotes the minor matrix of element D_{ii}, where i is the mode index of the PTO. In other words, remove row i and column i from matrix $\mathbf{D}$, and take the determinant of that resulting matrix.

Equations (F.5, F.9, F.10, F.11, F.12) now embody the solution for this case, with an arbitrary amount of other modes of motion. Thus the system can be solved analytically when power is extracted through only a single mode of motion.

F.3 2 PTOs, N other modes of motion

This yields the power (F.13) expressed by the summation of two terms, each of which is in a similar form to the case with one PTO mode. In this case though, a_i, b_i, c_i and d_i for $i = 1, 2$ are each a quadratic function of the other B_{ptoi}. For example, $d_1 = e_1 B_{pto2}^2 + e_2 B_{pto2} + e_3$, where e_1, e_2 and e_3 are constants in terms of the mass, damping and stiffness matrices, and the excitation forces.

$$\begin{aligned} P_a = & \frac{d_1 B_{pto1}}{a_1 B_{pto1}^2 + b_1 B_{pto1} + c_1} \\ & + \frac{d_2 B_{pto2}}{a_2 B_{pto2}^2 + b_2 B_{pto2} + c_2} \end{aligned} \tag{F.13}$$

F.3.1 Case 1: Restricted damping coefficient values

For the case where all B_{ptoi} values are equal ($B_{pto1} = B_{pto2}$), differentiating with respect to B_{pto} and setting the resultant expression equal to zero yields a 14th order polynomial equation. To prove this (F.14), we first notice that the power (F.13), with $x = B_{pto1} = B_{pto2}$, is a pair of terms whose numerators are third order in x, and whose denominators are fourth order in x. Differentiating each term using the quotient rule results in an increase in the order of the numerators and denominators. Since the coefficients involved in each of the two terms are different, to combine them into a single term, each denominator must be multiplied top and bottom by the other term.

$$\begin{aligned} P_a &= \frac{O(x^3)}{O(x^4)} + \frac{O(x^3)}{O(x^4)} \\ \frac{dP_a}{dx} &= \frac{O(x^2)O(x^4) + O(x^3)O(x^3)}{O(x^8)} \\ &+ \frac{O(x^2)O(x^4) + O(x^3)O(x^3)}{O(x^8)} \\ &= \frac{O(x^6)}{O(x^8)} + \frac{O(x^6)}{O(x^8)} \\ &= \frac{O(x^{14})}{O(x^{16})} = 0 \end{aligned} \tag{F.14}$$

F.3.2 Case 2: Unrestricted damping coefficient values

For the case where each of the $x_i := B_{ptoi}$ values is free to vary, we obtain a similar expression by differentiating with respect to x_2, but from here we need to differentiate again with respect to x_1. This gives a polynomial equation, which is 15th order in each variable, but 29th order (F.15).

$$\begin{aligned} \frac{d^2 P_a}{dx_1 dx_2} &= \frac{d}{dx_1}\left(\frac{O(x_1^8)O(x_2^6) + O(x_1^7)O(x_2^7)}{O(x_1^8)O(x_2^8)}\right) \\ &= O(x_1^{15})O(x_2^{14}) + O(x_1^{14})O(x_2^{15}) = 0 \end{aligned} \tag{F.15}$$

In both cases here, the resulting equations are far beyond analytical solution methods, and in fact the second case is a function of two variables anyway, so does not necessarily have a unique solution.

F.4 M PTOs, N other modes of motion

Extending this analysis to the general case of M PTOs, it quickly becomes clear that the complexity of the equations increases hugely with increasing values of M. To summarise these results, for case 1, with all B_{ptoi} equal, the polynomial to be solved is of order $(4M^2 - 2)$. For case 2, with all B_{ptoi} free to vary, the polynomial is of order $P = (2M^3 - 2M^2 + 4M - 1)$ in each of the variables, and total order $(P + 1)/M$.

For three PTO modes in the case of the WaveTrain, case 1 results in a 34th order polynomial equation, and case 2 results in a 140th order polynomial equation. As an optimistic estimate for case 1, the computational expense involved in generating the coefficients of the 34th order equation terms may well be minimal given that they would mainly involve algebraic manipulations. Additionally, numerical solvers may well be able to provide accurate solutions in a reasonable amount of time. The major downside to this method lies in the difficulty required to program a routine to derive the coefficients of the 34th order polynomial equation, in terms of the entries in the matrices shown in equations (F.1, F.2).

Appendix G

West Shetland Shelf wave climate

The scatter table for a West Shetland Shelf wave climate, around 40km west of the Shetland Islands, is given in Table G.1 [6].

With reference to practical measurements of waves, it is important to note that energy period and root-mean-square wave height are more appropriate indicators; the zero-crossing periods and significant wave heights measured are by their definitions completely dependent on the resolution of the wave recorder.

Mean zero-crossing period, T_z (s) $\rightarrow$ Significant wave height, H_{m0} (m) $\downarrow$	4.5	5.5	6.5	7.5	8.5	9.5	10.5	11.5	12.5	13.5	14.5	15.5	16.5	17.5
0.25	0	2	2	0	0	1	0	0	0	0	0	0	0	0
0.75	36	89	147	128	95	44	18	10	1	4	4	1	0	0
1.25	51	229	228	306	339	215	82	42	12	6	6	1	0	0
1.75	2	115	184	208	302	269	177	92	24	14	4	2	1	1
2.25	0	21	165	184	202	231	205	115	67	26	18	8	1	1
2.75	0	1	63	153	158	142	193	142	84	47	21	11	1	1
3.25	0	0	5	105	147	103	125	136	92	58	30	10	5	1
3.75	0	0	1	31	113	100	89	92	79	48	33	12	3	1
4.25	0	0	0	5	51	86	77	69	53	42	33	14	6	3
4.75	0	0	0	0	20	62	65	51	43	39	31	17	6	2
5.25	0	0	0	0	2	22	59	47	36	28	23	13	2	4
5.75	0	0	0	0	0	5	38	45	23	16	25	10	2	0
6.25	0	0	0	0	0	1	14	39	17	15	21	5	1	1
6.75	0	0	0	0	0	0	4	24	21	13	11	4	2	0
7.25	0	0	0	0	0	0	1	14	17	11	6	2	2	0
7.75	0	0	0	0	0	0	0	8	16	11	4	2	1	0
8.25	0	0	0	0	0	0	0	4	14	10	3	2	1	1
12.00	0	0	0	0	0	0	0	2	19	26	26	11	2	2

Table G.1: West Shetland Shelf occurrence matrix ($\hat{O}$, hours).

Appendix H

Computing resources

The hardware used in this work for the numerical computations comprised an Intel Core i7-6700 quad-core 3.4GHz processor, with 32 Gigabytes of RAM, and was purchased for only a few hundred pounds towards the beginning of 2017. Particularly with a view to any future work, either looking to expand on the results in this thesis or to develop similar optimisation studies, it is useful to document the approximate runtimes relating to parts of the numerical work carried out in this thesis.

The 24 runs of the single-objective genetic algorithm (as documented in Section 5.7.1) took approximately 7 days of computing time. A run of the multi-objective genetic algorithm (as documented in Section 5.7.2) with 121 generations, each of 100 individuals, took around 5 days of computing time. The two most major constituents of this were the solution of each individual's hydrodynamic model using WAMIT and the objective function evaluations, which contributed to the total runtime in similar proportions. Both of these were heavily optimised for the hardware - the WAMIT runs maximally used the system's cores and RAM, the number of frequencies were kept to a minimum (see Section 5.3.4.5), the plane of symmetry was exploited, in addition to using the 'higher order' panelling method and dipole wall panels; parallel processing and the vectorisation of 'for loops' enabled a degree of optimality for the given computing architecture in computing the objective functions. Note that the computation of the elements in the mass matrices and in the gravitational restoring force matrices did not contribute substantially to the total runtime - this was a result

of manually performing the integrations, so that the coded expressions for these matrix entries could be expressed as a set of purely algebraic operations. In any future work, the effort required on the part of the modeller to do this must be considered.

In the work on the duck spines (Chapter 6), the greater numbers of degrees of freedom and the use of the 'lower order' panelling method led to greater runtimes for each hydrodynamic model - taking around 30 minutes for 100 frequencies. If geometric optimisation were desired with current computing resources (see above), the 'higher order' method would certainly be required. Within Chapter 6, by far the most computationally intensive were the results of Section 6.6.2. Each entry in Tables 6.32 and 6.33 took around 3 hours of computational time, giving a total of around 84 hours for both tables. This included around an hour for each WAMIT run, 8 minutes for each power calculation, and 40 minutes to compute the mass matrix and gravitational restoring matrix entries using symbolic algebra. There also existed further opportunity for runtime reductions in the storing and accessing of the arrays used for both the hydrodynamic models and the objective function computations.

Applied to the 10 duck spine with its 33 degrees of freedom, a great difference in runtime was seen between the two forms of constrained complex conjugate control (see Sections 6.3 and 6.5). When the constraint was applied only to the controlled degrees of freedom, solving for the Lagrange multipliers over 61 frequencies and 10 angles (610 Lagrange multipliers in total) took around 20 minutes, whilst applying the extended constraint to the same problem took around 20 hours. These differences should be considered with a view to applications of high complexity and where many sea conditions are to be analysed.

Assuming a doubling of computing power every two years in accordance with Moore's law, significant extensions to the results presented in this thesis may be possible within the next 5-10 years. Regarding this, see also Sections 7.1.2 and 7.3.2.

Appendix I

3rd International Conference for Offshore Renewable Energy publication

The following paper, which was presented in 2018 by the lead author at the International Conference for Offshore Renewable Energy in Glasgow, is reproduced here in full. Of particular importance to this thesis is section 3.3 of the paper, where the physical model test results are used to assess the validity of the numerical models with and without quadratic damping forces applied.

NUMERICAL AND PHYSICAL MODELLING OF A NOVEL, SLOPED MODULE, MULTIBODY WAVE ENERGY CONVERTER

A. Cotten, J. van 't Hoff & D. Forehand, *University of Edinburgh, UK*
N. Wells, *Joules Energy Efficiency Services Ltd., UK*

ABSTRACT

Building upon the previously demonstrated promise of sloped buoy concepts, the WaveTrain device concept is introduced and its main design features and operational principles explained. The construction of a bespoke time-domain model of the system is presented, in particular giving details on the inclusion of the oscillating water column contained within each power module. A couple of stages in the verification process of this model are presented. A thorough description of the set-up of a physical WaveTrain, 1:35 scale model is provided, which is then used with a selection of irregular seas to calibrate quadratic coefficients that aim to represent the effects of viscous drag. The resulting nonlinear numerical, linear numerical and physical models are then used to assess the suitability of such numerical methods, leading to an indication that full system optimisation may be possible with a purely linear model. Finally, some key development stages towards an efficient frequency-domain model of the WaveTrain device are presented, placing particular emphasis on the treatment of hinges using generalised modes of motion.

NOMENCLATURE

A_{ij}	Added mass matrix
A_{ij}^{∞}	Infinite frequency added mass matrix
B_{ij}	Radiation damping matrix
B_i^E	Quadratic viscous drag coefficients
C_{ij}	Hydrostatic stiffness matrix
C_{ij}^E	External stiffness matrix
D_{ij}	Power take-off damping matrix
F_i	Wave excitation forces
G_i	Elevation to force impulse response function
$K_{ij}(t)$	Radiation impulse response function
M_{ij}	Mass matrix
N	Number of modes of motion
x_j	Positions
$\dot{x}_j$	Velocities
$\ddot{x}_j$	Accelerations
t	Time
η	Surface elevation
ξ_i	Frequency-domain motions
ω	Frequency

1. INTRODUCTION

The WaveTrain Wave Energy Converter (WEC) is an evolution of the IPS Buoy concept [1]. The IPS Buoy was a heaving point absorber consisting of a hollow tube with a piston inside. The system was designed for the piston to react against the inertial water mass inside the tube. Provision of a mass from the WEC itself (or from the surrounding water) to act as a reaction mechanism for the Power Take-Off eliminates the need for rigid attachment to the seabed, avoiding use of costly support structures and increased loading on the mooring system. This is a practical requirement for the utilisation of the substantial offshore wave energy resource. The IPS Buoy also had the benefit of requiring no physical end-stops, the tapered tubing allowing water to rush around the piston as it nears its motion limits. Combining this form of PTO with a buoy operating with sloped motion led to the development of the Sloped IPS Buoy [2].

For heaving buoys to be well-tuned to the waves in real sea conditions, either a large mass is required to counteract the hydrostatic forces, or an elaborate control system is needed to lengthen the natural period. An alternative solution is provided by tilting the axis of motion towards the horizontal, thus reducing the hydrodynamic stiffness, and lengthening the natural period without a significant increase in the device mass.

As part of the development of the Sloped IPS Buoy, it was found that constraining the motion of a WEC to an inclined axis can result in a very high and broad power absorption bandwidth [3]. Unfortunately, testing of freely-floating versions unveiled a collapse of this feature [4], as pitching motion tended to cause dissipation of much of the energy [5]. The WaveTrain concept presented herein provides a potential solution to this problem, enabling retention of the good power absorption

characteristics, whilst avoiding the need for any kind of rigid connection to the seabed.

2. THE WAVETRAIN CONCEPT

Originally conceived of by Dr. Nicholas Wells [6], this concept comprises multiple sloped modules, connected in series with mechanical struts and rotational joints [Fig. 1]. The design of each module is partially inherited from the Sloped IPS Buoy, though not identical. Although the device is still in an early stage of development, some key features are established.

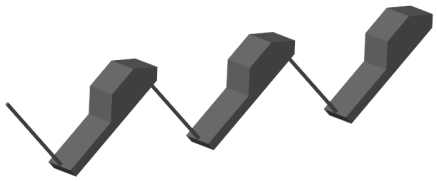

Figure 1: Stationary configuration of the three module WaveTrain device.

2.1 INTERCONNECTION OF MULTIPLE MODULES

The interconnection of multiple modules aims to prevent excessive amounts of pitching, whilst still allowing free motion of each module along the inclined axis. Restorative forces from neighbouring modules, provided through the struts, ensure that only a small amount of pitching is possible.

In still water, each module resides at its intended inclination angle, with the top of each module piercing out of the water surface. In this stationary reference frame, the rigid struts are connected from the bottom of one module to the underside of the top of the next module. Struts are connected at right-angles to the inclined plane, to ensure that the maximum restorative forces are provided.

The struts are connected to the modules using rotational joints - for purposes of energy extraction, to permit rotations in the plane of symmetry of the device. These joints could also allow some limited out-of-plane motions to alleviate loadings.

Note that no optimal number of modules has been determined, but three modules are used for initial models, since it provides the simplest case that is representative of the system dynamics (i.e. it includes a module with neighbours either side).

2.2 POWER TAKE-OFF SYSTEM

As with the IPS Buoy, it is desired that the PTO mechanism reacts against the inertial mass of the surrounding water. Hence, each module has a base consisting of a hollow tube, which is open-ended at the bottom to the surrounding water. Unlike the IPS buoy though, the WaveTrain proposes to use a pneumatic turbine atop each module to facilitate power extraction. Consequently, each module is essentially a floating oscillating water column device, with each interior body of water pushing or drawing air through a turbine.

2.3 FLOAT SHAPE

In order to achieve motion along the inclined axis, a vertical face is provided to the incoming waves. As long as a sufficiently large amount of this float face is submerged, the module should exhibit the correct motions, given a suitable mass distribution. The float is also used for buoyancy, and is anticipated to be constructed from a lighter material than the tube walls. Thus the float should be shaped so as to incorporate both of these features adequately.

3. NUMERICAL AND PHYSICAL MODELLING

3.1 TIME-DOMAIN MODEL CONSTRUCTION

The numerical model described in this section involves setting up and solving a series of ordinary differential equations that encapsulate the device dynamics. Linear hydrodynamic behaviour is obtained using a boundary element method (WAMIT [7]) to compute frequency-domain coefficients, which can then be transformed into the time-domain. The SimScape Multibody package [8] within Simulink is used to model the mechanical behaviour of the multibody system, including the rotational joints.

It is assumed that the hydrodynamic interactions of the connecting struts are negligible compared to those of the modules. Due to the two-dimensional nature of the design, motions of the bodies outwith the plane of symmetry are assumed to be insignificant to the overall behaviour of the device. As a result, motions in sway, roll and yaw can be

neglected. Since the hinges are incorporated as a form of post-processing in Simulink, the hydrodynamic coefficients must be computed for the case of three separate, unconnected modules, each free to move in surge, heave and pitch. The three modules are modelled together to capture the hydrodynamic interactions between them. A discretised surface mesh must be defined for solution by the boundary element method [Fig. 2]. The presence of the water columns inside each module tube means defining this is not as straightforward as it would be for a solid (i.e. not hollow) object.

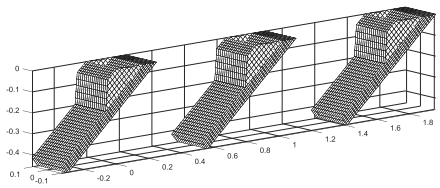

Figure 2: Discretised mesh for input to the boundary element method software.

Since the tube walls are thin, a large number of normal surface panels may be required to ensure accurate results [7]. Alternatively, dipole panels can be used, approximating the tube walls as infinitely thin. This increases computational efficiency, but requires that walls are suitably thin.

In order to conveniently facilitate calculation of power extraction from the water columns, additional panels are required on the free surface of each water column, effectively adding a 'massless lid' to the water surface. In order to permit this 'lid' to accurately track the water surface, suitable generalised modes need to be defined [9]. The water columns of the WaveTrain modules are thin compared to the wavelength of any incoming waves, which means that sloshing of the internal water surface can be assumed to be minimal. Therefore, just a single translating, 'piston' mode is sufficient to capture the motion of this surface. In order to model the effect of power extraction on the body motions, damping can then later be applied directly to the 'lid'. These additional modes of motion are defined relative to the corresponding module, but enable hydrodynamic coefficients to be found in the same manner as the rigid body modes.

The boundary element method solves for the hydrodynamic and hydrostatic coefficients in equation (1), for all i and j. N is the total number of modes, twelve, which includes the generalised 'lid' modes, representing the motion of the water column surfaces. The hydrodynamic coefficients reflect the interaction between all of these modes.

$$\sum_{j=1}^{N}[(M_{ij} + A_{ij}(\omega))\ddot{x}_j(\omega) + B_{ij}(\omega)\dot{x}_j(\omega) + C_{ij}x_j(\omega)] = F_i(\omega) \quad (1)$$

With a quadratic drag term and PTO damping included, the full set of time-domain equations for the hydrodynamics is given by (2), for all values of i.

$$\sum_{j=1}^{N}[(M_{ij} + A_{ij}^{\infty})\ddot{x}_j(t) + \int_0^t K_{ij}(t-\tau)\dot{x}_j(\tau)d\tau + C_{ij}x_j(t) + D_{ij}\dot{x}_j(t)] + B_i^E\dot{x}_i(t)|\dot{x}_i(t)| = \int_{-\infty}^{\infty} G_i(\tau)\eta(t-\tau)d\tau \quad (2)$$

The radiation convolution term contains the radiation impulse response function, $K_{ij}(t)$, and each convolution integral is calculated using direct numerical integration. The damping matrix, D_{ij}, represents the forces exerted by the PTO system on the body motions. The quadratic terms are used to incorporate empirical corrections to the system dynamics, emulating the effects of viscous drag (calibration of these is discussed in the next section). The excitation forces driving the device motions are dependent on the waves encountered, and have been formulated as a convolution of the surface elevation and the force impulse response function, $G_i(t)$, which is derived from the frequency-domain excitation forces. The mass properties of the device must also be provided to the solver, though with the hydrodynamic analysis performed with respect to the centre of gravity of each module, this only requires the mass and pitch moment of inertia of each module.

In (2), the first four equations (i = 1 – 4; surge, heave, pitch, lid translation along the column) correspond to the first, leftmost module, the second four (i = 5 - 8) to the central module, and the final four (i = 9 - 12) to the rightmost module. The hinge interactions are incorporated within the Simulink environment by using the SimScape package's pre-built 'blocks' to apply the appropriate constraint equations between modules. Since only in-plane motions are to be considered, each joint is given just a single, rotational degree of freedom. Though a full scale model will not have any rigid tethering, a fixed hinge is connected to the top of the strut at the front of the device to mimic the effect of a buoy keeping the device in position. At the time of construction, WEC-Sim [10] had no capability to deal with the oscillating water columns, hence the use of Simscape Multibody instead. In this environment, only the three rigid body motions of each module are connected to the hinges, and coupled directly to the joint constraints. Since each water column is coupled directly only to its encasing sloped module, the hydrodynamic force acts directly on the column mass. However, because its motion is modelled using a massless element, the 'self-added mass', A_{44}, A_{88}, or $A_{12\,12}$, is removed from the main hydrodynamics solver and used in place of the zero value in the mass matrix, in order for the hydrodynamic force to induce an acceleration.

3.2 VERIFICATION OF NUMERICAL MODEL

In the course of development of the model, various tests were performed to verify the modelling procedures. As such, the complete model was built up in stages, beginning with a single, untethered module, simply solving the equations of motion given in (2), for just four modes of motion. By deriving the Response Amplitude Operators (RAOs) from this time-domain analysis, comparison with the corresponding frequency-domain model, (1), verified correct operation.

A further key step was the reformulation of this single WaveTrain module model using the Simscape Multibody software. This includes the use of the self-added mass of the lid mode for computing the acceleration of the water surface at each time step. A good match was achieved between the frequency-domain model and the Simscape Multibody time-domain model. Figure 3 shows this comparison for the case of the amplitude of the water column motion, in a range of regular seas.

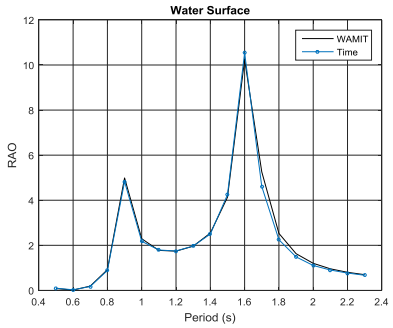

Figure 3: Response amplitude operators for the motion of the water column free surface, for a single, freely floating WaveTrain module.

A second key stage in the modelling process was the extension of the model from just a single module, to the full, interconnected, three module device. One test that can be applied to the model involves analysing the physical behaviour of the device under certain sea conditions. When the spacing between adjacent modules is equal to half the wavelength of the incoming waves, adjacent modules should exhibit motions in antiphase with one another. This will also lead to strong reaction forces between modules, therefore maintaining movement of each module along its inclined plane. This is clearly seen in the motions of the device in unidirectional sea states with a peak period that corresponds to this half-wavelength separation criterion. Figure 4 shows the heave displacements of the first and second modules under these sea conditions. The negative linear correlation represents antiphase motions. This correlation is not perfect due to the nature of the irregular sea, with the presence of some waves shorter or longer than the predominant wavelengths.

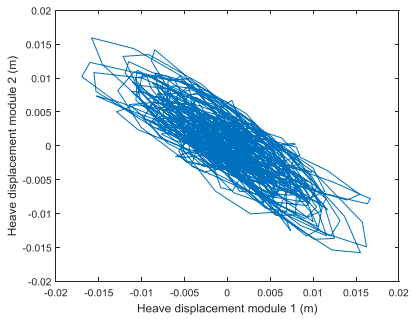

Figure 4: Heave displacements of the first and second modules in near-resonant conditions.

Adding further confidence in the model, in a sea state with a much longer predominant wavelengths, no such correlation is observed [Fig. 5].

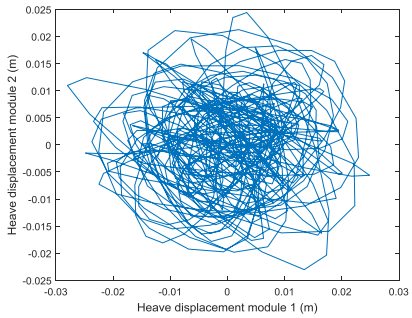

Figure 5: Heave displacements of the first and second modules in far-from-resonant conditions.

3.3 CALIBRATION USING PHYSICAL MODEL

The physical model was designed to be tested in the FloWave Test Tank at The University of Edinburgh, in 2m water depth, and at 1:35 scale. Since the device needs to float at the correct height for the float to be partially submerged, and for each module to reside at the desired angle of inclination (40º to the horizontal in this model), the mass distribution has to be precise. When balanced against the needs of structural integrity and manufacturability, this results in a set of quite specific design criteria.

In the interests of manufacturability and structural properties, the internal water column of each module has been divided amongst five separate PVC tubes, which are sandwiched between two polycarbonate sheets. Fine sand mortar fills the interstitial space between the tubes, helping to keep a low centre of gravity relative to the centre of buoyancy, which is crucial for stability of the device. Holes were drilled such that the air flow from each of the tubes can enter an air chamber at the top of the module, where it is then passed through a valve constriction to simulate the effects of a PTO system.

The float consists of shaped blocks of closed cell polyurethane structural foam, whose submerged portions are rounded off to minimise any viscous eddy generation, which is particularly significant at model scale. This assembly is then sealed with sheets of polycarbonate.

Two tubular struts are connected between adjacent modules in a triangular arrangement, with the two meeting at the top of the underside of one module with a ball joint, and connected to either side of the polycarbonate sheet atop the row of PVC tubes with hinge joints. This configuration ensures appropriate module spacing restraint, whilst allowing some out-of-plane rotation to prevent the build-up of significant lateral loads on the device. The ball joint at the top of the front two struts is attached to a mooring buoy, itself connected to the base of the tank via catenary mooring chains.

Internal wave probes sit inside two of the tubes, and a sensor is positioned atop each module for pressure measurement inside the air chamber, and subsequent computation of the absorbed power. A Qualisys capture system was used for measuring the motions of the device, with the markers placed on stalks mounted on top of each module.

The base unit comprising the tubes measured 1.185m x 0.34m, with an individual tube outer diameter of 68mm. The float is 0.6m long, with a height of 0.165m, and 0.278m wide, including the rounded edges. The struts have a total length of 0.92m, and the total mass per module (including two connecting struts) is 17.1kg. Figure 6 shows the full construction assembled prior to submersion and testing.

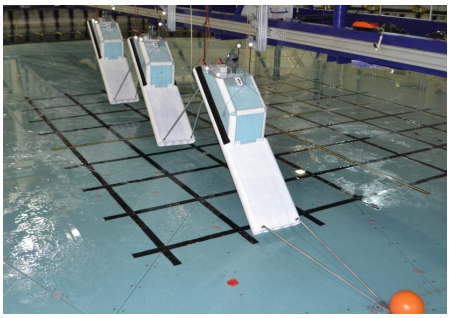

Figure 6: WaveTrain model prior to testing in the FloWave Test Tank.

One of the aims of this physical model was to enable calibration of the quadratic drag coefficients for the numerical model, and of course assess the suitability of such an empirical correction. With the design emphasis placed on power absorption, perhaps the most appropriate method is to tune the coefficients in order to try and match the predicted power absorption of the numerical and physical models. This procedure was carried out in a range of irregular sea states based on a JONSWAP spectrum (with $\gamma = 1$), representative of a generic potential deployment location [Table 1].

Table 1: The twelve unidirectional, irregular sea states used for testing the physical model.

Sea state no.	Full scale T_p / s	Full scale H_s / m
1	7.7	1.5
2	10.5	1.5
3	13.3	1.5
4	14.7	1.5
5	12.6	2.0
6	7.7	2.5
7	9.9	2.5
8	9.1	3.5
9	10.5	4.5
10	11.9	4.5
11	13.3	3.5
12	10.5	3.5

The absorbed power values for each sea were obtained using the pressure measurements and water column velocities relative to the corresponding body. They were averaged over the sea run time of 512s. The PTO damping values for the numerical model were taken from measurements of those used in the physical model. These values were sought to maximise power production, and were based on a set of tests of the physical model in each sea state.

Table 2 shows the power absorption in each sea state, based on three model cases, two numerical and one physical.

Table 2: Comparison of the mean absorbed powers (model scale, measured in Watts) in the twelve irregular sea states, given by the numerical model with no viscous drag (VD), the numerical model with VD, and the physical model.

Sea state no.	Numerical - No VD	Numerical - VD	Physical model
1	0.27	0.25	0.27
2	0.21	0.19	0.23
3	0.12	0.11	0.13
4	0.09	0.08	0.10
5	0.25	0.22	0.26
6	0.96	0.66	0.67
7	0.66	0.55	0.61
8	3.09	1.21	1.22
9	5.05	2.41	1.58
10	3.89	1.46	1.24
11	0.66	0.55	0.65
12	1.35	0.95	1.04

The fully linear numerical model (with no viscous drag) makes good predictions of the power in sea states 1-5,7 and 11 – the differences are well below 10% in many of these cases. The addition of viscous drag worsens the predictions slightly for these sea states, but makes significant improvements in the predictions in sea states 6, 8, 10, and 12. There is still a relatively large difference in the power values for sea state 9. These trends display rough alignment with the level of wave steepness expected to be found in those sea states. The linear model performs well in the least steep of the seas, whilst the addition of the quadratic drag terms enables the model to quite accurately predict the power absorption in all but one of the steeper seas too.

Though the wave steepness is observed only as an indicator of modelling requirements here, it is clearly not a perfect predictor of nonlinear behaviour. The interactions between the body and the waves are ultimately responsible for any viscous effects, not simply the nature of the waves.

This perhaps explains why the model is accurate for seas 6 and 8, but not for sea 9. A further caveat is that the steepness of waves in a given sea state is not trivial to quantify absolutely. Despite this, these results suggest that a linear model with additional viscous drag terms is likely to be adequate to predict the device performance in the majority of relevant sea states. The results also give an indication that a fully linear numerical model is likely to give reasonable performance predictions in a not insignificant proportion of sea states in a typical wave climate. This suggests a fully linear model may well be adequate for optimising the WaveTrain concept.

4. TOWARDS FULL DESIGN OPTIMISATION WITH AN EFFICIENT FREQUENCY-DOMAIN MODEL

The physical model presented in section 3 was designed around the test tank capabilities and other practical considerations relating to the construction of the device. When added to the need for a specific level of submersion, the need for each module to reside at its intended angle of inclination, and stability requirements, this results in a very restricted set of design criteria. To this end, the design of the physical model was only able to include a limited degree of tailoring towards optimal performance in specific sea conditions.

A thorough optimisation study could unveil improved designs, with increased understanding of the device dynamics in a range of sea conditions. As a consequence of the lack of available information about the gradient (with respect to the parameter space) of the objective function to be optimised, this would require a large number of device evaluations. If the parameter space is quite large and not well understood beforehand, this could entail the assessment of thousands of candidate designs. In this setting, time-domain models are quite intensive, computationally, and a frequency-domain model may be the only option. With this line of reasoning, and the understanding that fully linear results can still provide useful results, a frequency-domain model should be sought for the WaveTrain device.

In order to model the device completely within the frequency domain, the hinge motions cannot rely on the time-domain solvers as used for the models presented in the previous section. The most efficient method relies upon the use of 'generalised modes', since it only requires a number of modes of motion equal to the number of degrees of freedom of the system.

Although hinged systems have been modelled in this manner before, published studies on this topic have only presented cases with simple geometries (e.g. [11], [12], [13], [14]), and relatively few implementation details are documented therein. Hence the full WaveTrain system should be developed in stages, validating each intermediate model against an equivalent time-domain model, for whom the modelling of hinges is much better established. In this section, a couple of the intermediate modelling cases are used to highlight some potential difficulties arising in modelling hinges using generalised modes (WAMIT is the boundary element method used here), and to pave the way towards a full frequency-domain model of the WaveTrain device.

4.1 SETTING UP THE MODEL WITH GENERALISED MODES

A frequency-domain model involves solving the equations of motion for all of the rigid body motions, plus the generalised modes of motion (3).

$$\sum_{\mathrm{j=1}}^{\mathrm{N}}[-\omega^2(\mathrm{M_{ij}}+\mathrm{A_{ij}})+i\omega\mathrm{B_{ij}}+\mathrm{C_{ij}}+C_{ij}^{E}]\xi_j = F_i \quad (3)$$

For all N defined modes of motion, ξ_i, the added mass coefficients, A_{ij}, radiation damping coefficients, B_{ij}, the excitation forces, F_i, and the buoyancy components of C_{ij}, the hydrostatic forces, are naturally computed by WAMIT. For the rigid body modes, this is also the case for the gravitational components of C_{ij}, but the gravitational coefficients involving generalised modes must be computed manually, and input via the separate external stiffness matrix, C_{ij}^{E}. The mass matrix terms, M_{ij}, for all modes, must also be entered manually. It is in computing these two additional sets of terms that additional levels of complexity can enter the modelling process.

Generalised modes are defined by a three dimensional vector, specifying the distribution of the velocity normal to the body surface. Judicious choice of this 'shape function' makes for a

streamlined analysis of the model outputs, not to mention reduced effort in computing the extra terms that must be input. The most natural hinge mode shape in this case is that obtained by extending the rigid body coordinate system to allow extra, symmetric rotation about the hinge. The resulting velocity distribution is therefore discontinuous at the hinge location.

Due to the linear nature of the problem, multiple hinges simply yields a series of additive terms, arising analogously to those for a single hinge. [Note that the mode shape chosen must allow for the desired range of possible full device motions, using linear combinations of the complete set of rigid body and generalised modes.]

4.2 INTERMEDIATE MODELLING CASE 1

The model considered here uses hinge locations similar to that in the full WaveTrain device, yet with uniform, cuboidal barges of half the density of water [Fig. 7]. The assumption is again that connecting struts between each pair of hinges contribute negligibly to the hydrodynamic behaviour.

Figure 7: Schematic of intermediate modelling case 1. **Black** spots denote hinge locations, **red** line marks the mean water level.

One intricacy encountered here involves the hinge locations. Though a hinge location may be desired to be in line with the edge of a barge, an empirical result uncovers that WAMIT treats a panel with exactly the same x-coordinate as the mode definition discontinuity location, as being part of the body to the 'positive-coordinate' side of the hinge. One must be wary of this when defining the generalised modes if panel centroids are likely to be very close to the hinge locations.

The Response Amplitude Operators (RAOs) for this case, from both the time-domain and frequency-domain models, agree well in terms of peak location and height [Fig. 8]. A lack of resolution and runtime in the time-domain model explains the remaining discrepancy. Such a large runtime is required in the time-domain model for this particular configuration, most likely because of the inherently unstable locations of the hinges and struts.

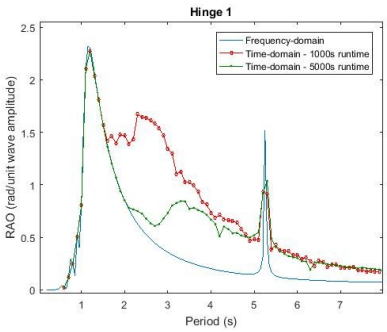

Figure 8: Comparison of RAOs of time-domain and frequency-domain models of the configuration depicted in Fig. 7.

4.3 INTERMEDIATE MODELLING CASE 2

Moving further towards the WaveTrain concept, a series of solid, sloped modules is modelled. The three modules are connected using four hinges and two struts, in locations analogous to those in the physical model in section 3.3, albeit without a front strut and a connected mooring system. From the model in section 4.2, this introduces geometry asymmetry in the direction of wave propagation, with more complex geometry and thus computation of the M_{ij} and C_{ij}^{E} terms.

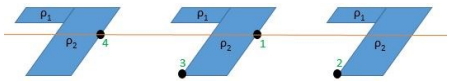

Figure 9: Schematic of intermediate modelling case 2. **Black** spots denote hinge locations, **green** numbers label each hinge, **red** line marks the mean water level.

In order to simplify the calculations required for the mass matrix coefficients and gravitational restoring forces, each sloped module is treated as two connected parallelograms, termed the 'float' (density, ρ_1) and 'body' (ρ_2), each of uniform density. In order to ensure both that the centre of gravity lies on the same vertical line as the centre of buoyancy ($x_G = x_B$), and that the device is statically stable ([15], p. 294), a set of variables was found, somewhat by trial and error, leaving the required float density to be solved for directly. To simplify the submerged portion of the body (for

ease of panelling within WAMIT), the variables were chosen such that the 'float' is completely above water, and so in this case is only helping to achieve the correct mass distribution.

Following the determination of a suitable set of geometric parameters fully describing the complete body and its mass distribution, the M_{ij} and C_{ij}^{E} terms can then be calculated for the generalised modes. Since this includes a large number of integral evaluations, care must be taken, especially as there is limited feedback from WAMIT to indicate the location of any errors. One useful marker that an error lies in the gravitational restoring terms is an RAO plot tending towards a non-zero value as the frequency tends to zero.

Slight misalignment of the outputs from the time- and frequency-domain models [Fig. 10] can be explained by numerical inaccuracies, particularly in calculating the extra coefficients, in addition to limited runtime of the time-domain model. In any case, a range of wave periods encompassing only the leftmost peak is likely to be used for analysis of absorbed power in a representative sea state, and the alignment is best at these lower periods.

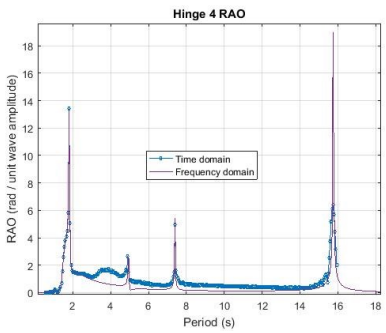

Figure 10: Comparison of RAOs of the leftmost hinge, for the time-domain and frequency-domain models of the series of sloped modules depicted in Fig. 9.

4.4 FUTURE WORK

Using massless lids to model the water columns means that these additional generalised modes of motion contribute no further non-zero mass matrix or hydrostatic terms. However, the more complicated geometry resulting from a hollow module means the process of ensuring the intended inclination angle, static stability, and a suitable water level height is not a trivial extension from the case in section 4.3. Despite this, a full, frequency-domain model of the WaveTrain device would enable the development of optimisation routines, in order to assess the full potential of the design concept.

5. CONCLUSIONS

A new concept for wave energy extraction has been introduced, describing its development from previously tested, promising sloped buoy devices. Its key features, including an interconnection of multiple sloped modules, internal oscillating water columns facilitating power take-off, and a specific float shape, have been described, along with the main operating principles.

Performed as part of the Wave Energy Scotland Novel WEC Stage 1 project, the development of a time-domain numerical model is presented, along with the construction of a physical model for testing in the FloWave Test Tank at The University of Edinburgh, at 1:35 scale. The numerical model utilises the generalised modes feature in the boundary element method, WAMIT, to model the hydrodynamic behaviour of the internal water columns. In order to integrate these frequency-domain hydrodynamic outputs into the time-domain model with the hinged connections, the model must be constructed such that the hydrodynamic force on each water column 'lid' acts on its added mass. Expected physical behaviour of adjacent models in irregular sea states, both tuned and not tuned to the module spacing, is seen in the numerical model, adding confidence in its correct operation.

Using a representative set of irregular sea states, the physical model has been used to calibrate quadratic viscous drag coefficients, based on the power absorption. Under the majority of sea conditions, the combination of quadratic drag terms with an otherwise linear model is shown to be accurate in predicting power absorption. In fact, a fully linear model does well at predicting power absorption in a range of sea conditions, and therefore could be suitable for use in an optimisation study. The comparison of the power absorption of these three models (linear, nonlinear and physical) in the twelve sea states gives an

indication that wave steepness could be used as a predictor of model adequacy.

Finally, as part of a journey towards a maximally efficient frequency-domain model of the WaveTrain, two intermediate modelling cases are presented and used to highlight some of the difficulties and considerations in using generalised modes to model hinges within WAMIT. Given constraints on water level height, module inclination angle, and static stability, time-domain motions of a series of solid, sloped modules are shown to compare well with those from the corresponding frequency-domain model.

ACKNOWLEDGEMENTS

The time-domain numerical model and the scale physical model were developed as part of a Wave Energy Scotland Novel Wave Energy Converter Stage 1 project, and the authors are grateful for this funding. The lead author would also like to acknowledge ESPRC for the studentship with award reference 1809924, provided through the Centre for Doctoral Training in Wind and Marine Energy Systems.

REFERENCES

1. Noren SA, 1982 'Apparatus for recovering the kinetic energy of sea waves', US Patent No. 4773221.
2. Salter S, Lin C-P, 1995 'The sloped IPS wave energy converter', 2nd European Wave Power Conference, pp. 337-344.
3. Lin C-P, 1999 'Experimental studies of the hydrodynamic characteristics of a sloped wave energy device', PhD thesis, University of Edinburgh.
4. Payne G, Taylor J, Bruce T, Parkin P, 2008 'Assessment of boundary-element method for modelling a free-floating sloped wave energy device. Part 2: Experimental validation', Ocean Engineering 35, pp. 342-357.
5. Parkin P, Payne G, Taylor J, 2003 'Numerical simulation and tank tests of the free-floating sloped IPS buoy', 5th European Wave Energy Conference.
6. N. Wells, B. Elsaesser, 2013 'Performance of the JOULES Wavetrain WEC', MARINET Infrastructure access report.
7. WAMIT Inc., 2016 'WAMIT user manual, Version 7.2'.
8. MathWorks, SimScape Multibody.
9. Lee C-H, Newman JN, 1996 'Wave interactions with an oscillating water column', 6th International and Offshore Polar Engineering Conference.
10. https://wec-sim.github.io/WEC-Sim/publications.html, accessed on 24/7/18.
11. Newman JN, 1994 'Wave effects on deformable bodies', Applied Ocean Research 16, pp. 47 - 59.
12. Newman JN, 1997 'Wave effects on hinged bodies: Part 1 – body motions', technical report, WAMIT.
13. McNatt JC, Venugopal V, Forehand D, 2015 'A novel method for deriving the diffraction transfer matrix and its application to multi-body interactions in water waves', Ocean Engineering 94, pp. 173-185.
14. Mathai T, 2000 'Use of generalised modes in hydrodynamic analysis of multiple bodies', 10th International Offshore and Polar Engineering Conference
15. Newman JN, 1977 'Marine Hydrodynamics', MIT Press.

Appendix J

The effect on duck spine behaviour of extending the motion constraint

This section provides extra detail concerning the application of the extended motion constraint to the full spine of Edinburgh ducks. Additional justification of many of the findings stated in Section 6.5.3 is also provided.

Relating to the heave and surge motions of the whole spine (Figs. J.1), bands of large motions are interspersed by bands of small motions, forming a pattern similar to that of Fig. 6.12. In some areas of the period-angle space, these bands are clearly oscillatory themselves, forming a series of peaks (where motions are very large) and troughs (where the motions are very small). Applying the constraint to all degrees of freedom appears to broadly retain this pattern (Fig. J.2), yet with drastically diminished variation of the RAO magnitudes over the range of periods and angles.

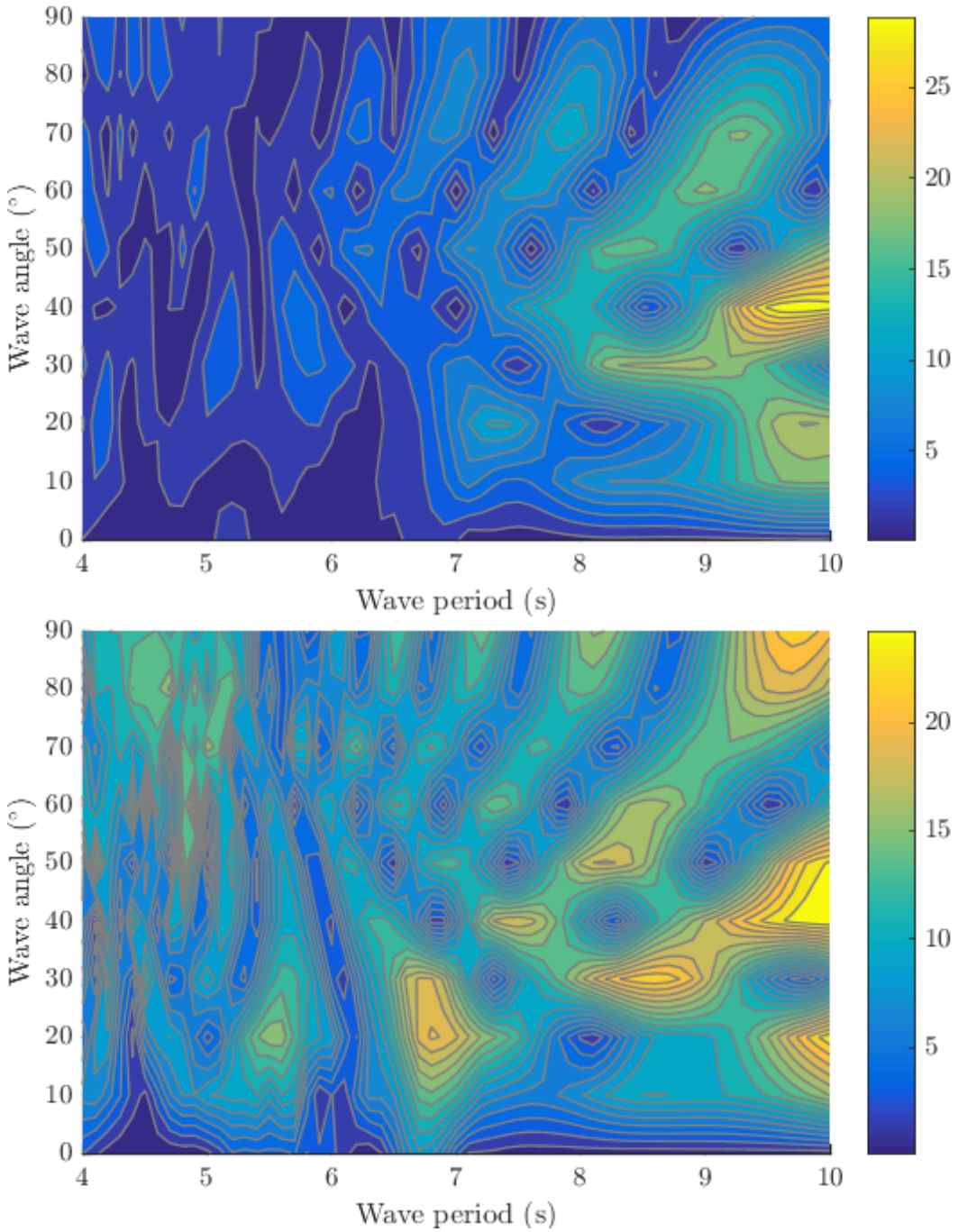

Figure J.1: RAO magnitudes of the surge (upper) and heave (lower) rigid body motions, when the motion constraint applies to only the controlled modes of motion.

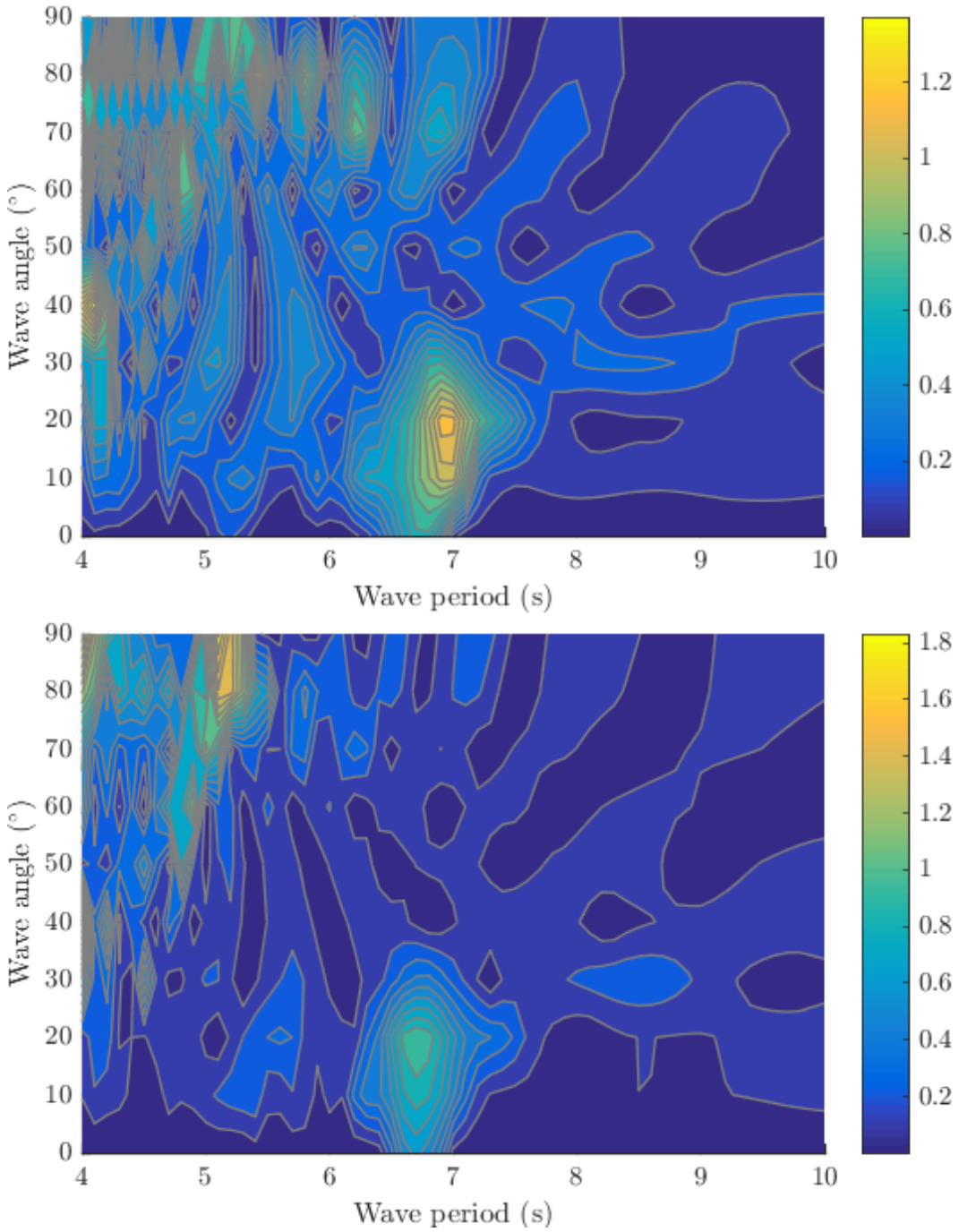

Figure J.2: RAO magnitudes of the surge (upper) and heave (lower) rigid body motions, when the motion constraint applies to all modes of motion.

The absolute and relative differences in capture width ratio between the cases of the original and the extended motion constraints are shown in Figs. J.3 and J.4. The high densities of contour lines around 8.5s periods are due to numerical issues in computing

the power using Eq. 6.23. It is important to recognise that the complexity of the terms in the equations that describe the extended constraint system (see Section 6.5), necessitates an increasing amount of numerical operations as the number of degrees of freedom is increased. This has been found to occasionally result in spurious results, such as those seen here. It may be possible to express some of the equations differently, so as to minimise this type of occurrences, but fortunately, in this example, the results are still unobscured by the numerical difficulty.

The bands of large and small motions seen in Fig. J.1 are reflected in Figs. J.3 and J.4.

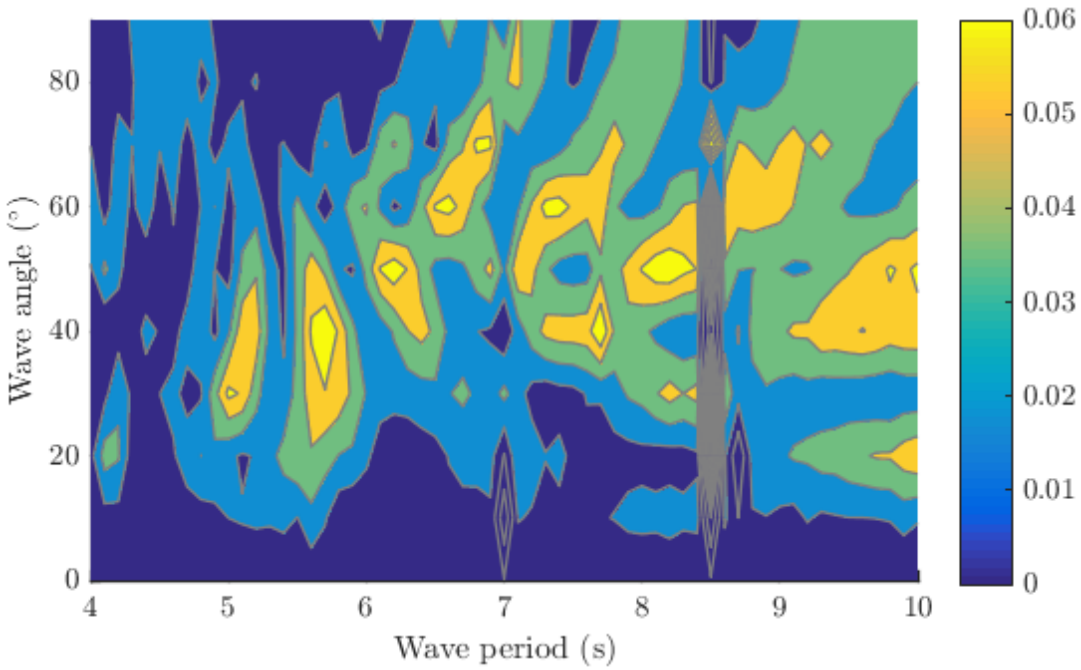

Figure J.3: Absolute difference in capture width ratio between the two control cases that use different versions of the motion constraint.

The RAOs also exhibit different patterns and trends under the extended motion constraint. The RAO magnitudes now vary in an oscillatory manner with wave period, as with the aforementioned shear forces. Another notable change is seen in the duck pitching motions - at wave headings around 50° and periods above 6.6s, the second most downstream duck exhibits much greater motions than its counterparts, particularly at wave periods of 7s and 8.4s (Fig. J.6). Finally, in the yaw directions,

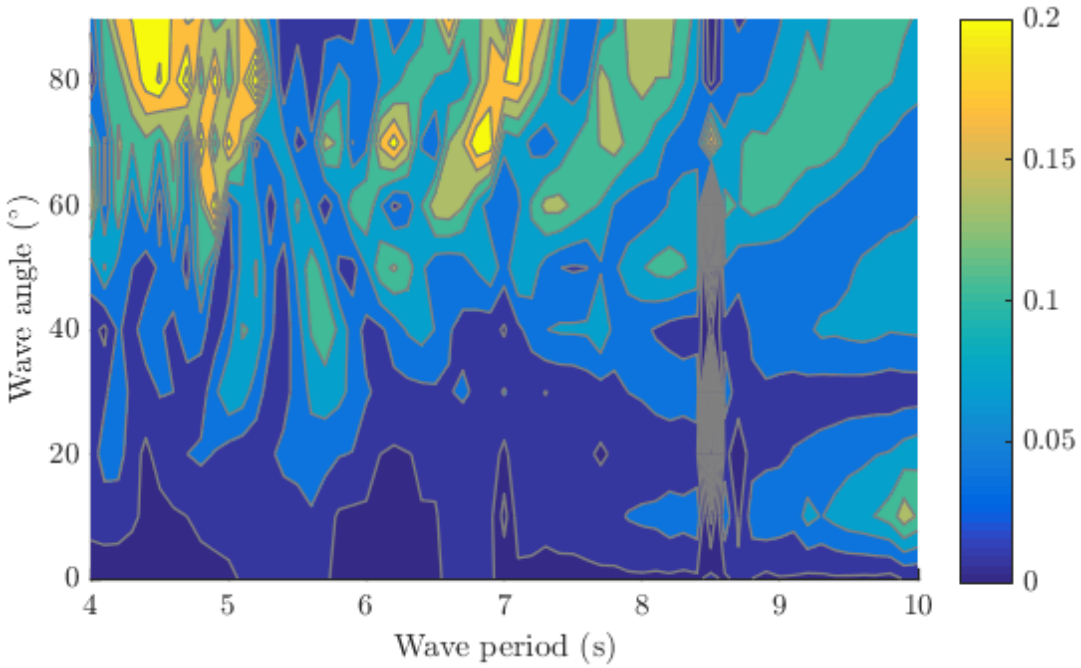

Figure J.4: Fractional difference in capture width ratio between the control cases that use different versions of the motion constraint.

the motions of the joints at either end of the spine (joints 1 and 9) are diminished compared to their neighbours, under the influence of the extended constraint (Fig. J.7). In addition to the pervasion of the oscillatory form of the RAO magnitudes with wave period, the second and perhaps third most downstream joints (joints 7 and 8) exhibit greater motions than the most downstream joint at the higher end of the wave period range.

Clearly, the dynamics of the duck spine are complex - the motions in particular.

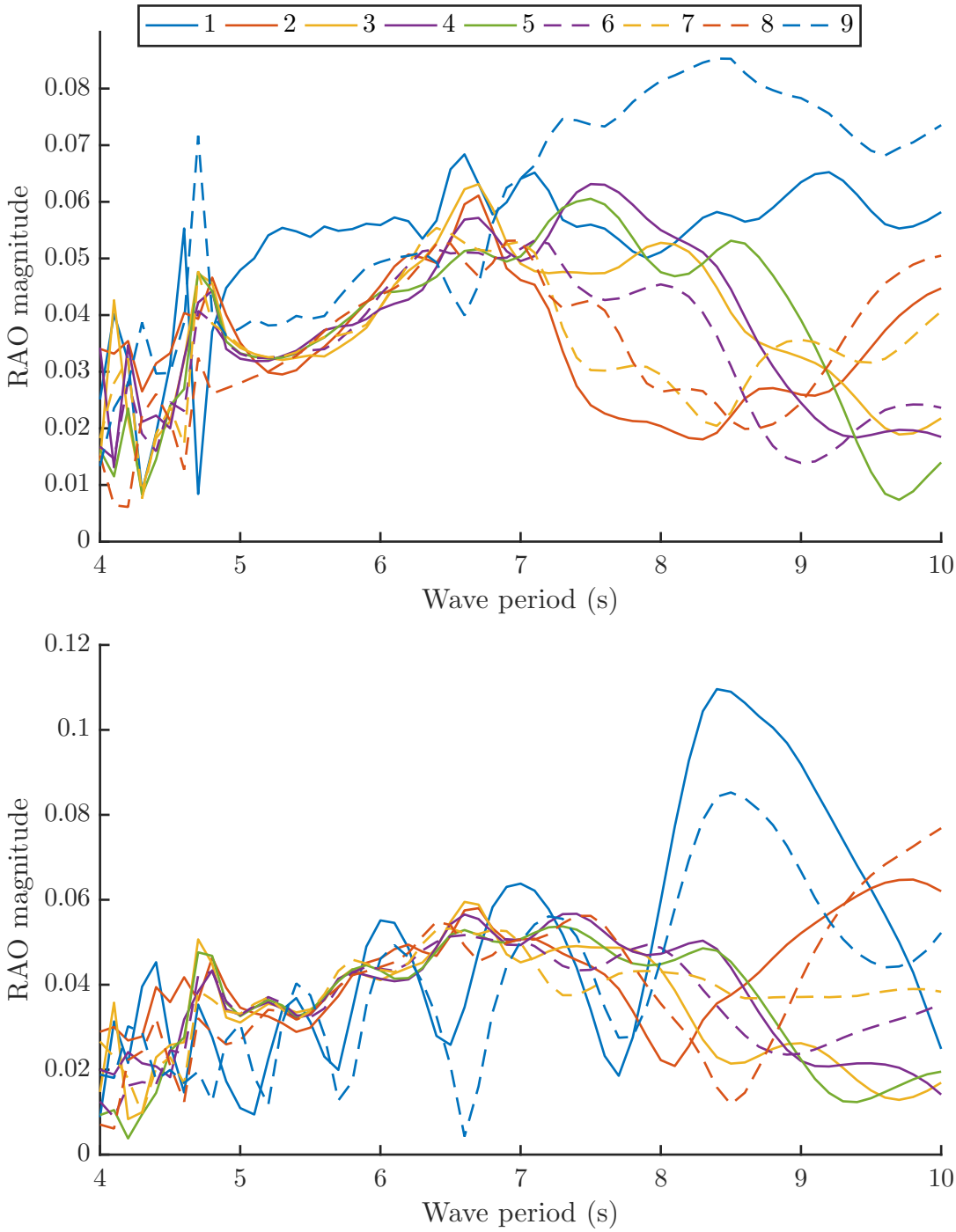

Figure J.5: RAO magnitudes of the joint flexure at each joint in the roll direction, measured in radians per metre of incident wave amplitude. Wave heading: 40°. Upper plot - only controlled modes constrained, lower plot - all modes constrained. Joints are numbered from fore to aft (see legend).

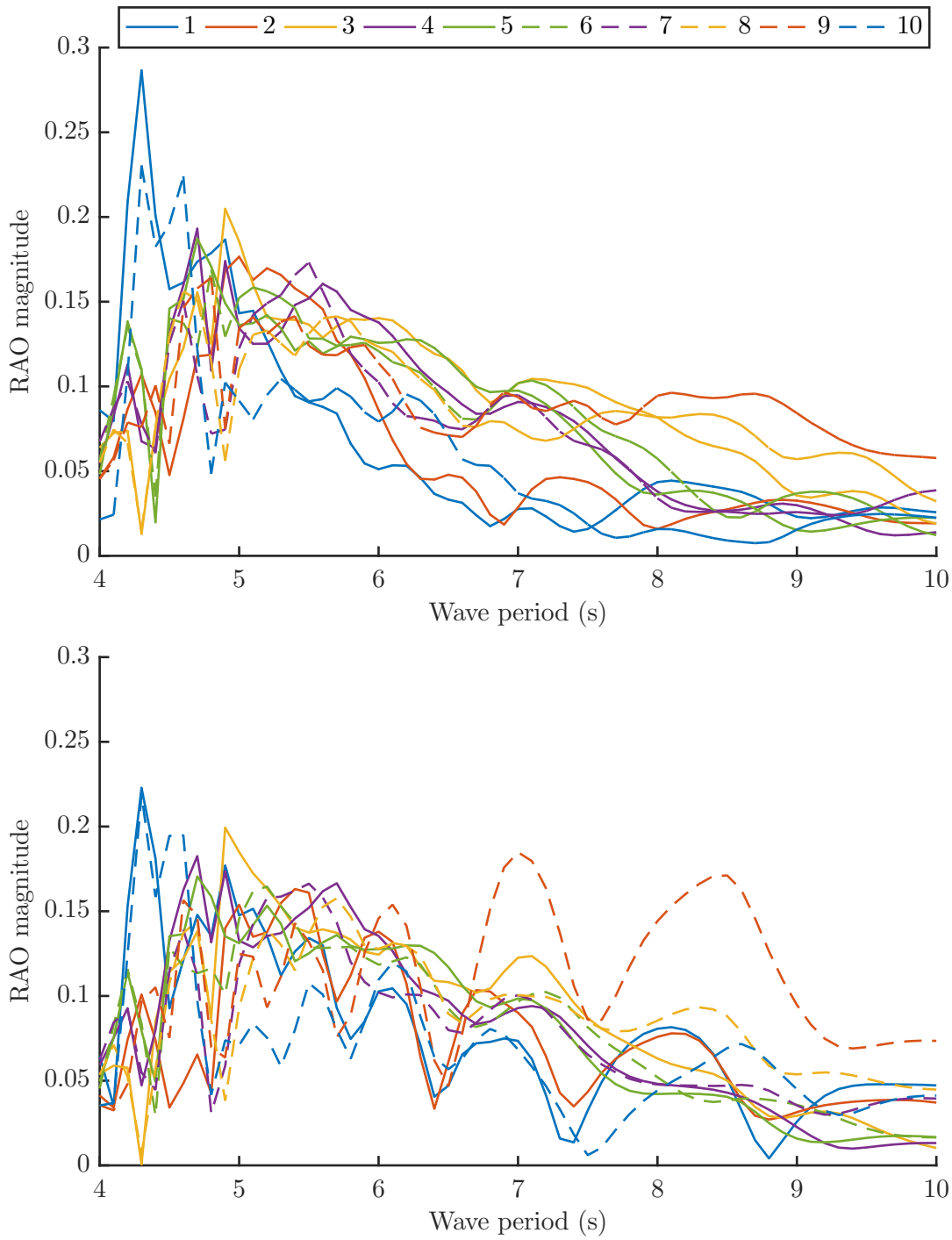

Figure J.6: RAO magnitudes of the duck pitching rotations, measured in radians per metre of incident wave amplitude. Wave heading: 50°. Upper plot - only controlled modes constrained, lower plot - all modes constrained. Ducks are numbered from fore to aft (see legend).

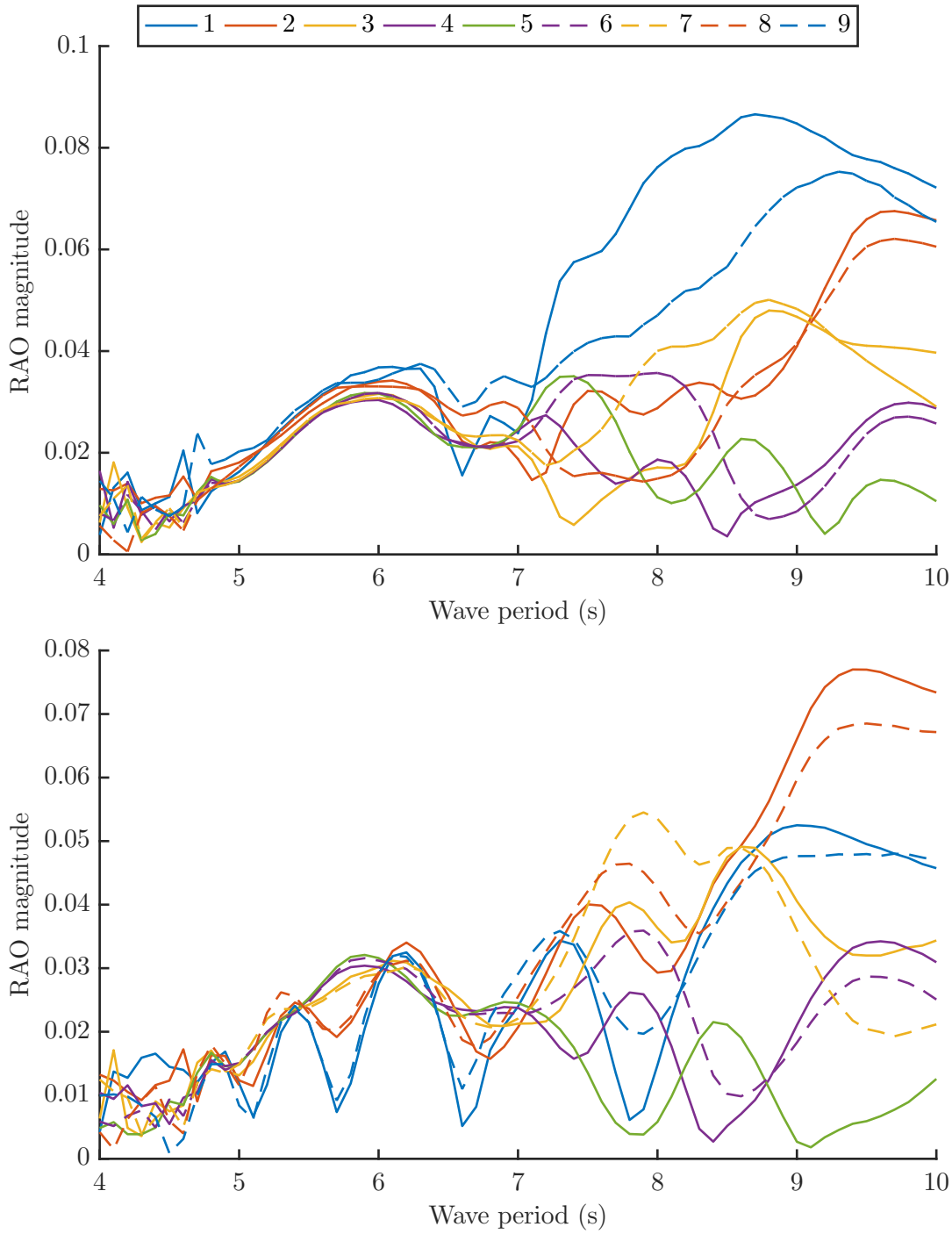

Figure J.7: RAO magnitudes of the joint flexure at each joint in the yaw direction, measured in radians per metre of incident wave amplitude. Wave heading: 40°. Upper plot - only controlled modes constrained, lower plot - all modes constrained. Joints are numbered from fore to aft (see legend).

Bibliography

[1] G. S. Payne, "Numerical modelling of a sloped wave energy device," *PhD thesis, University of Edinburgh*, 2006, available from: https://www.era.lib.ed.ac.uk/handle/1842/15607.

[2] "WaveTrain sloped pneumatic WEC, Wave Energy Scotland Novel Wave Energy Converter Programme, Stage 1," http://www.waveenergyscotland.co.uk/programmes/details/novel-wave-energy-converter/wavetrain-sloped-pneumatic-wec/.

[3] S. Salter, "Wave energy: Nostalgic ramblings, future hopes and heretical suggestions," *Journal of Ocean Engineering and Marine Energy*, vol. 2, pp. 399–428, 2016, DOI: 10.1007/s40722-016-0057-3.

[4] "Artist's impressions of a full spine of Edinburgh ducks," https://www.era.lib.ed.ac.uk/handle/1842/23489, Accessed: 05/06/2019.

[5] J. C. McNatt, V. Venugopal, and D. Forehand, "A novel method for deriving the diffraction transfer matrix and its application to multi-body interactions in water waves," *Ocean Engineering*, vol. 94, pp. 173–185, 2015, DOI: 10.1016/j.oceaneng.2014.11.029.

[6] A. P. McCabe, "Constrained optimization of the shape of a wave energy collector by genetic algorithm," *Renewable Energy*, vol. 51, pp. 274–284, 2013, DOI: 10.1016/j.renene.2012.09.054.

[7] C.-P. Lin, "Experimental studies of the hydrodynamic characteristics of a sloped wave energy device," *PhD thesis, University of Edinburgh*, 1999.

[8] D. J. Pizer, "Maximum wave-power absorption of point absorbers under motion constraints," *Applied Ocean Research*, vol. 15, pp. 227–234, 1993, DOI: 10.1016/0141-1187(93)90011-L.

[9] A. Babarit, "A database of capture width ratio of wave energy converters," *Renewable Energy*, vol. 80, pp. 610–628, 2015, DOI: 10.1016/j.renene.2015.02.049.

[10] H. E. Young and J. Pollock. (1985) "Variable coefficient control of a wave-energy device", Edinburgh Wave Power Project, University of Edinburgh. [Online]. Available: http://www.homepages.ed.ac.uk/shs/Wave%20Energy/Old%20reports/

[11] A. Babarit, J. Hals, M. J. Muliawan, T. Moan, and J. Krokstad, "Numerical benchmarking of a selection of wave energy converters," *Renewable Energy*, vol. 41, pp. 44–63, 2012, DOI: 10.1016/j.renene.2011.10.002.

[12] A. F. de O. Falcão, "Wave energy utilization: A review of the technologies," *Renewable and Sustainable Energy Reviews*, vol. 14, pp. 899–918, 2010, DOI: 10.1016/j.rser.2009.11.003.

[13] "Wave Energy Scotland programmes," https://www.waveenergyscotland.co.uk/programmes/, Accessed: 05/06/2019.

[14] "U.S. Department of Energy Wave Energy Prize," https://www.energy.gov/eere/water/about, Accessed: 05/06/2019.

[15] "Wave energy device types," http://www.emec.org.uk/marine-energy/wave-devices/, Accessed: 05/06/2019.

[16] S. Salter and C.-P. Lin, "The sloped IPS wave energy converter," *2nd European Wave Power Conference*, pp. 337–344, 1995.

[17] G. Payne, J. Taylor, T. Bruce, and P. Parkin, "Assessment of boundary-element method for modelling a free-floating sloped wave energy device. part 2: Experimental validation," *Ocean Engineering*, vol. 35, pp. 342–357, 2008, DOI: 10.1016/j.oceaneng.2007.10.008.

[18] P. Parkin, G. Payne, and J. Taylor, "Numerical simulation and tank tests of the free-floating sloped IPS buoy," *5th European Wave Energy Conference*, 2003.

[19] N. Wells and B. Elsaesser. (2013) "Performance of the JOULES Wavetrain WEC, MARINET Infrastructure Access Report". [Online]. Available: http://www.marinet2.eu/wp-content/uploads/2017/04/Wavetrain_HMRC_Infrastucture_Access_Report-1.pdf

[20] A. Cotten, J. van 't Hoff, D. Forehand, and N. Wells, "Numerical and physical modelling of a novel, sloped module, multibody wave energy converter," *3rd International Conference on Offshore Renewable Energy*, pp. 48–57, 2018.

[21] "WAVETRAIN (Research Training Network Towards Competitive Ocean Wave Energy)," https://cordis.europa.eu/project/rcn/73452/reporting/en, Accessed: 09/08/2019.

[22] S. H. Salter, "Wave power," *Nature*, vol. 249, pp. 720–724, 1974, DOI: 10.1038/249720a0.

[23] S. H. Salter, "The use of gyros as a reference frame in wave energy converters," *2nd International Symposium on Wave Energy Utilization*, pp. 99–115, 1982.

[24] D. Skyner. (1987) "Solo duck linear analysis". [Online]. Available: http://www.homepages.ed.ac.uk/shs/Wave%20Energy/Old%20reports/

[25] J. Wu, Y. Yao, W. Li, L. Zhou, and M. Göteman, "Optimizing the performance of solo duck wave energy converter in tide," *Energies*, vol. 10, p. 289, 2017, DOI: 10.3390/en10030289.

[26] J. Wu, Y. Yao, D. Sun, N. Zhonghua, and M. Göteman, "Numerical and experimental study of the solo duck wave energy converter," *Energies*, vol. 12, p. 1941, 2019, DOI: 10.3390/en12101941.

[27] D. V. Evans, "A theory for wave-power absorption by oscillating bodies," *Journal of Fluid Mechanics*, vol. 77, pp. 1–25, 1976, DOI: 10.1017/S0022112076001109.

[28] "WAMIT User Manual (v7.2), WAMIT Inc." http://www.wamit.com/manual.htm, Accessed: 09/01/2019.

[29] J. N. Newman, "Wave effects on deformable bodies," *Applied Ocean Research*, vol. 16, pp. 47–59, 1994, DOI: 10.1016/0141-1187(94)90013-2.

[30] T. Mathai, "Use of generalised modes in hydrodynamic analysis of multiple bodies," *10th International Offshore and Polar Engineering Conference*, 2000.

[31] J. N. Newman. (1997) "Wave effects on hinged bodies: Part 1 - body motions". [Online]. Available: http://www.wamit.com/Publications/Hinged1.pdf

[32] C.-H. Lee and J. N. Newman, "An assessment of hydroelasticity for very large hinged vessels," *Journal of Fluids and Structures*, vol. 14, pp. 957–970, 2000, DOI: 10.1006/jfls.2000.0305.

[33] Y. Li, H. Peng, W. Qiu, B. Lundrigan, and T. Gardiner, "Hydrodynamic analysis and optimization of a hinged type wave energy converter," *35th International Conference on Ocean, Offshore and Arctic Engineering*, 2016.

[34] S. Xu, J. M. Rodrigues, and C. G. Soares, "Hydrodynamic analysis and optimization of a wave activated device," *Progress in Renewable Energies Offshore: Proceedings of the 2nd International Conference on Renewable Energies Offshore*, pp. 285–292, 2016.

[35] A. P. McCabe, G. A. Aggidis, and M. B. Widden, "Optimizing the shape of a surge-pitch wave energy collector using a genetic algorithm," *Renewable Energy*, vol. 35, pp. 2767–2775, 2010, DOI: 10.1016/j.renene.2010.04.029.

[36] A. Garcia-Teruel and D. I. M. Forehand, "Optimal wave energy converter geometry for different modes of motion," *Advances in Renewable Energies Offshore: Proceedings of the 3rd International Conference on Renewable Energies Offshore*, pp. 299–305, 2018.

[37] A. Babarit and A. Clément, "Shape optimization of the SEAREV wave energy converter," *Proceedings of the 9th World Renewable Energy Congress*, 2006.

[38] G. S. Payne, R. Pascal, and G. Vaillant, "On the concept of sloped motion for free-floating wave energy converters," *Proceedings of the Royal Society A: Mathematical, Physical and Engineering Sciences*, vol. 471, 2015, DOI: 10.1098/rspa.2015.0238.

[39] M. López, V. Ramos, P. Rosa-Santos, and F. Taveira-Pinto, "Effects of the PTO inclination on the performance of the CECO wave energy converter," *Marine Structures*, vol. 61, pp. 452–466, 2018, DOI: 10.1016/j.marstruc.2018.06.016.

[40] J. Hals, J. Falnes, and T. Moan, "A comparison of selected strategies for adaptive control of wave energy converters," *Journal of Offshore Mechanics and Arctic Engineering*, vol. 133, p. 031101, 2011, DOI: 10.1115/1.4002735.

[41] J. Falnes, "Radiation impedance matrix and optimum power absorption for interacting oscillators in surface waves," *Applied Ocean Research*, vol. 2, pp. 75–80, 1980, DOI: 10.1016/0141-1187(80)90032-2.

[42] P. Nebel, "Maximizing the efficiency of wave-energy plant using complex-conjugate control," *Proceedings of the Institution of Mechanical Engineers, Part I: Journal of Systems and Control Engineering*, vol. 206, pp. 225–236, 1992, DOI: 10.1243/PIME_PROC_1992_206_338_02.

[43] D. V. Evans, "Maximum wave-power absorption under motion constraints," *Applied Ocean Research*, vol. 3, pp. 200–203, 1981, DOI: 10.1016/0141-1187(81)90063-8.

[44] D. J. Pizer. (1994) "Numerical modelling of wave energy absorbers". [Online]. Available: http://www.homepages.ed.ac.uk/shs/Wave%20Energy/Old%20reports/

[45] G. K. Batchelor, *An Introduction to Fluid Dynamics.* Cambridge, UK: Cambridge University Press, 2000.

[46] J. N. Newman, *Marine Hydrodynamics.* Cambridge, Massachusetts: The MIT Press, 1977.

[47] C.-H. Lee, J. N. Newman, and F. G. Nielsen, "Wave interactions with an oscillating water column," *Proceedings of the Sixth International Offshore and Polar Engineering Conference*, pp. 82–90, 1996.

[48] Folley, M. (Ed), *Numerical Modelling of Wave Energy Converters: State-of-the-art techniques for single devices and arrays.* London, UK: Elsevier, 2016.

[49] "WEC-Sim: Wave Energy Converter SIMulator," https://energy.sandia.gov/energy/renewable-energy/water-power/technology-development/wec-sim-wave-energy-converter-simulator/, Accessed: 05/06/2019.

[50] "Edinburgh Wave Systems Simulation Toolbox," https://sourceforge.net/projects/rnfoundry/, Accessed: 05/06/2019.

[51] "Simscape Multibody," https://uk.mathworks.com/products/simmechanics.html, Accessed: 05/06/2019.

[52] J. Falnes, *Ocean Waves and Oscillating Systems: Linear Interactions Including Wave-Energy Extraction.* Cambridge, UK: Cambridge University Press, 2002.

[53] "The Curved Wave Tank, University of Edinburgh," https://www.eng.ed.ac.uk/research/facilities-and-resources/small-research-facilities/curved-wave-tank, Accessed: 05/06/2019.

[54] "FloWave Ocean Energy Research Facility, University of Edinburgh," https://www.flowavett.co.uk/home, Accessed: 05/06/2019.

[55] C.-H. Lee and J. N. Newman, "Computation of wave effects using the panel method," *WIT Transactions on State-of-the-art in Science and Engineering*, vol. 18, pp. 211–251, 2005, DOI: 10.2495/978-1-85312-837-0/06.

[56] B. Stappenbelt and P. Cooper, "Optimisation of a floating oscillating water column wave energy converter," *Proceedings of the 20th International Offshore and Polar Engineering Conference*, pp. 788–795, 2010.

[57] M. Folley and T. Whittaker, "The effect of plenum chamber volume and air turbine hysteresis on the optimal performance of oscillating water columns," *Proceedings of the 24th International Conference on Offshore Mechanics and Arctic Engineering*, pp. 493–498, 2005.

[58] C.-H. Lee, J. N. Newman, and X. Zhu, "An extended boundary integral equation method for the removal of irregular frequency effects," *International Journal for Numerical Methods in Fluids*, vol. 23, pp. 637–660, 1996, DOI: 10.1002/(SICI)1097-0363(19961015)23:7<637::AID-FLD437>3.0.CO;2-3.

[59] J. Cruz, *Ocean Wave Energy: Current Status and Future Perspectives.* Berlin, Heidelberg: Springer, 2008.

[60] R. L. Haupt and S. E. Haupt, *Practical Genetic Algorithms, 2nd Ed.* Hoboken, New Jersey, USA: John Wiley & Sons Inc., 2004.

[61] A. J. Chipperfield and P. J. Fleming, "The matlab genetic algorithm toolbox," *IEE Colloquium on Applied Control Techniques Using MATLAB*, 1995, DOI: 10.1049/ic:19950061.

[62] O. M. Faltinsen, "Sea loads on ships and offshore structures," *Cambridge University Press*, 1990.

[63] A. Konak, D. W. Coit, and A. E. Smith, "Multi-objective optimization using genetic algorithms: A tutorial," *Reliability Engineering and System Safety*, vol. 91, pp. 992–1007, 2006, DOI: 10.1016/j.ress.2005.11.018.

[64] K. Deb, A. Pratap, S. Agarwal, and T. Meyarivan, "A fast and elitist multiobjective genetic algorithm: NSGA-II," *IEEE Transactions on Evolutionary Computation*, vol. 6, pp. 182–197, 2002, DOI: 10.1109/4235.996017.

[65] K. Deb and R. B. Agrawal, "Simulated binary crossover for continuous search space," *Complex Systems*, vol. 9, pp. 115–148, 1995.

[66] "Structural forces and stresses for wave energy devices," Wave Energy Scotland, Tech. Rep., June 2016, available from: https://library.waveenergyscotland.co.uk/other-activities/landscaping-studies/wes_ls02_er_forces/.

[67] R. G. Budynas and J. K. Nisbett, *Shigley's Mechanical Engineering Design, Ninth Ed.* New York, USA: McGraw-Hill, 2011.

[68] "Fatigue design of offshore steel structures," Det Norske Veritas, Tech. Rep., October 2011, available from: https://www.dnvgl.com/oilgas/download/dnvgl-rp-c203-fatigue-design-of-offshore-steel-structures.html.

[69] "Rainflow Counting Algorithm, by Adam Nieslony," https://uk.mathworks.com/matlabcentral/fileexchange/3026-rainflow-counting-algorithm, Accessed: 05/06/2019.

[70] H. D. Maniar, "A three dimensional higher order panel method based on B-splines," *PhD thesis, Massachusetts Institute of Technology*, 1995, available from: https://dspace.mit.edu/handle/1721.1/11127.

[71] S. H. Salter. (1984) "Bending moments in long spines", Edinburgh Wave Power Project, University of Edinburgh. [Online]. Available: http://www.homepages.ed.ac.uk/shs/Wave%20Energy/Old%20reports/

[72] R. Yemm, D. Pizer, C. Retzler, and R. Henderson, "Pelamis: experience from concept to connection," *Philosophical Transactions of the Royal Society A*, vol. 370, pp. 365–380, 2012, DOI: 10.1098/rsta.2011.0312.

[73] D. C. Jeffrey, D. J. E. Richmond, S. H. Salter, and J. R. M. Taylor. (1976) "Second year interim report", Edinburgh Wave Power Project, University of Edinburgh. [Online]. Available: http://www.homepages.ed.ac.uk/shs/Wave%20Energy/Old%20reports/

[74] D. C. Jeffrey, G. J. Keller, D. Mollison, D. J. E. Richmond, S. H. Salter, J. R. M. Taylor, and I. A. Young. (1978) "Fourth year report", Edinburgh Wave Power Project, University of Edinburgh. [Online]. Available: http://www.homepages.ed.ac.uk/shs/Wave%20Energy/Old%20reports/

[75] A. Cotten and D. I. M. Forehand, "Investigation into the control strategy for a long spine of edinburgh duck modules, using an efficient numerical model," *Proceedings of the 13th European Wave and Tidal Energy Conference*, p. , 2019.

[76] "Environmental conditions and environmental loads," Det Norske Veritas, Tech. Rep., October 2010, available from: https://www.dnvgl.com/oilgas/download/dnvgl-rp-c205-environmental-conditions-and-environmental-loads.html.